X-RAY PHOTOELECTRON SPECTROSCOPY ANALYSIS OF MAGNETRON SPUTTERED Cu_2ZnSnS_4 BASED THIN FILM SOLAR CELLS WITH CdS BUFFER LAYER

A Thesis Submitted to
the Graduate School of Engineering and Sciences of
İzmir Institute of Technology
in Partial Fulfillment of the Requirements for the Degree of

DOCTOR OF PHILOSOPHY

in Physics

by

Ayten CANTAŞ BAĞDAŞ

June 2017
İZMİR

We approve the thesis of **Ayten CANTAŞ BAĞDAŞ**

Examining Committee Members:

Prof. Dr. Lütfi ÖZYÜZER
Department of Physics, İzmir Institute of Technology

Prof. Dr. Birol ENGİN
Department of Physics, Dokuz Eylül University

Asst. Prof. Dr. Enver TARHAN
Department of Physics, İzmir Institute of Technology

Asst. Prof. Dr. Özgenç EBİL
Department of Chemical Engineering, İzmir Institute of Technology

Asst. Prof. Dr. Muhittin AYGÜN
Department of Physics, Dokuz Eylül University

21 June 2017

Prof. Dr. Lütfi ÖZYÜZER
Supervisor, Department of Physics
İzmir Institute of Technology

Prof. Dr. R. Tuğrul SENGER
Head of the Department of
Physics

Prof. Dr. Aysun SOFUOĞLU
Dean of the Graduate School of
Engineering and Sciences

ACKNOWLEDGEMENTS

Firstly, I would like to thank my supervisor, Prof. Dr. Lütfi ÖZYÜZER. His encouragement and support made this project possible.

I also would like to thank Assoc. Dr. Gülnur Aygün for her contribution to this thesis.

I would like to thank to TUBITAK for funding the project number of "114F341" during my thesis. I want to thank to Applied Quantum Research Center at department of Physics, Izmir Institute of Technology for the support of X-ray Photoelectron Spectroscopy analysis. I would like to thank to my colleagues Fulya Turkoglu, F. Gülsah Akca, Ece Meric and Dilara Buldu who work together in this CZTS project. I also thank to Dr. Mehmet Ali Olgar for sharing his experience with me. Thanks to all Ozyuzer research group members who made the laboratories a wonderful working environment.

I want to thank to my family especially my mother Guler Cantas who make my life easier with her support. I feel very lucky to have such a nice family. Thank you to my beloved husband for giving me his support for 16 years. Life is beautiful with him.

Last but not least, though he is not aware of those yet, I thank my little sweet son Batı for the patience he showed me in the moment when I could not be with him in writing this thesis.

ABSTRACT

X-RAY PHOTOELECTRON SPECTROSCOPY ANALYSIS OF MAGNETRON SPUTTERED Cu_2ZnSnS_4 BASED THIN FILM SOLAR CELLS WITH CdS BUFFER LAYER

Cu_2ZnSnS_4 (CZTS) is a novel quaternary compound which contains Cu, Zn, Sn and S elements. It is a p-type semiconductor which has been taken attention in the last years as an absorber layer. Since it consists of abundant, low cost and non-toxic elements, it is one of the most promising candidate as an absorber layer for thin film photovoltaic (PV) application. Having high absorption coefficient, low bandgap value which is theoretically in desired range make this material attractive for solar cell application. In this thesis, CZTS absorber layers were grown using two stages which are the magnetron sputtering of metallic precursors, followed by a heat treatment under sulfur vapor atmosphere. Two types of CZTS were grown such as SLG/Mo/Cu (55nm)/Sn/Zn/Cu (120nm) and SLG/Mo/Cu (120nm)/Sn/Zn/Cu (55nm). For the same stacking order, the effect of Cu thickness sequentially grown with Sn layer on the film quality were investigated. The optical properties, microstructure, surface and bulk composition of CZTS films were investigated in detail. This study revealed a correlation between the CZTS stacking order having different thickness of Cu layer and the improvement of film quality, which was also confirmed by the photo-conversion efficiency of the fabricated devices. In this work, the other investigated layer is CdS which is an n-type semiconductor with bandgap energy of 2.4 eV. Since CdS has well lattice match with the heterojunction between CdS and CZTS, it is one of the most preferred material as a buffer layer for solar cells. In this work CdS buffer layers were deposited by chemical bath deposition technique. The optimization of CdS layers were occurred and optical, structural, bulk and surface compositions were investigated in detail. Finally, SLG/Mo/CZTS/CdS/i-ZnO/AZO devices were fabricated. The effect of structure properties of CZTS films and the thickness of CdS buffer layer on efficiency of fabricated solar cells were investigated.

ÖZET

CdS TAMPON KATMANLI MIKNATISSAL SAÇTIRILMIŞ Cu_2ZnSnS_4 TABANLI İNCE FİLM GÜNEŞ HÜCRELERİNİN X-IŞINI FOTOELEKTRON SPEKTROSKOPİ ANALİZİ

Cu_2ZnSnS_4 (CZTS), Cu, Zn, Sn ve S elementleri içeren yeni dörtlü bir bileşik olup son yıllarda soğurucu katman olarak dikkat çeken p-tipi yarıiletkendir. Bol, düşük maliyetli ve toksik olmayan elementlerden oluştuğu için ince film fotovoltaik (PV) uygulamalarda emici katman olarak en umut verici adaydır. Yüksek absorpsiyon katsayısına sahip olması, teorik olarak arzulanan aralıkta düşük band katsayısı değeri bu malzemeyi güneş pilleri uygulaması için çekici hale getirir. Bu çalışmada, CZTS soğurucu tabakalar, metalik öncüllerin magnetron saçtırma tekniği ile büyütülmesi ve ardından sülfür buharı altında tavlanmasıyla iki aşamalı olarak büyütülmüştür. SLG/Mo/Cu (55nm)/Sn/Zn/Cu (120nm) ve SLG/Mo/Cu (120nm)/Sn/Zn/Cu (55nm) sırasında iki tip CZTS soğurucu katman büyütülmüştür. Aynı istif sırası için, Sn katmanı ile ardışık olarak büyütülen Cu katman kalınlığının film kalitesi üzerindeki etkisi araştırılmıştır. CZTS filmlerin optik özellikleri, mikroyapı, yüzey ve yığın kompozisyonu ayrıntılı olarak incelenmiştir. XPS analizi ile iki dizilimde büyütülen CZTS filmlerin elementel yüzey bileşimleri kıyaslanmıştır Bu çalışmada, farklı kalınlıklarda Cu tabakasına sahip olan CZTS istifleme sırası ile film kalitesinin iyileştirilmesi arasında bir ilişki olduğu gösterilmiş ve üretilen güneş hücrelerinin ışık-dönüştürme verimlilikleri ile doğrulanmıştır. Bu çalışmada, incelenen diğer katman, 2.4 eV'lik yasak enerji band aralığına sahip, n-tipi yarıiletken olan CdS'dir. CdS ile CZTS'nin oluşturdukları arayüzeyin iyi bir örgü eşleşmesine sahip olması nedeniyle, CdS güneş pilleri için bir tampon katmanı olarak en çok tercih edilen malzemelerden biridir. Bu çalışmada CdS tampon tabakaları kimyasal banyo tekniği ile kaplanmıştır. CdS katmanlarının optimizasyonu yapılarak optiksel ve yapısal özellikleri, yığın ve yüzey bileşimleri detaylı olarak incelenmiştir. Bu optimizasyonlar sonucunda SLG/Mo/CZTS/CdS/i-ZnO/AZO yapısında güneş pilleri üretilmiştir. CZTS filmlerin yapısal özelliklerinin ve CdS tampon tabakasının kalınlığının, büyütülen güneş pillerinin verimliliği üzerindeki etkisi araştırılmıştır.

To my sweet son Batı

TABLE OF CONTENTS

LIST OF FIGURES

Figure **Page**

LIST OF TABLES

CHAPTER 1

INTRODUCTION

1.1. Renewable Energy Sources

The growth in economy, increase in the populations and structural changes are the main parameters that effect the energy consumption in a world. While the countries are developing, along with accompanying the living standards get better, the demand in energy rises proportionally. With respect to recent investigations, the worldwide energy demand is assumed to increase by approximately 48% within the next 24 years. At the present time, 78% of the world's energy demand is supplied by fossil fuels. Account of the detrimental emissions of burning fossil fuels such as coal, oil, and natural gas, high prices of oil in a world, the increase in the threats of global warming and the expansion of energy need, non-fossil renewable energy sources are taken into attentions in the long term support. Among all source of energy, the renewable energy, with the rate of 2.6% per year, is the fastest-extending form of energy in a world as given in Figure 1.1. In 2020, the usage in renewable energy is predicted to be 7% and it would increase to 37% in 2040. Since the renewable energy is sustainable, it will never end. Due to the fact that the natural and available resources form the fuel of them, they are cost-effective. Renewable energy is environmentally friendly because it does not produce waste products like carbon dioxide and other polluters. Renewable energy is produced from wind, solar, thermal and hydropower which are the natural resources. In this process, the energy is renewed instead of being exhausted. Hydroelectricity, geothermal, wind power and solar generate energy 0.5 TW, 12 TW, 2-4 TW and 120.000 TW, respectively.

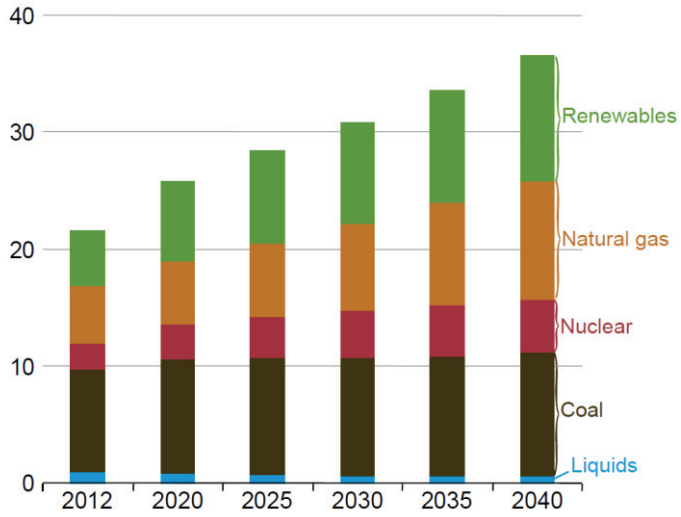

Figure 1.1. From 2020 to 2040, the world's energy source and the amount of their generated energy (trillion kilowatthours) (Source: "International Energy Outlook 2016 With Projections to 2040," 2016).

Among all renewable energy sources, solar energy has the highest contribution. In addition to this, between the different sources of renewable energy, the solar power attracts the attention due to the existence of unlimited and available energy source everywhere. It is also convenient in terms of generating the power in large and small scale. The storage and cost are the most important properties of solar power.

1.2. Solar Energy

Today, the solar energy is the most important natural renewable energy source on the Earth's surface. It has thermal application by heating the water and air and photovoltaic application by converting the solar power to electricity. An amazing amount of energy generated from the sun and received by the earth is 174,000 terawatts (TW). However, 30% of it is reflected back to the infinite whereas the left one is absorbed by land surface of Earth, clouds and oceans. The wavelengths of emitted photons from the sun is between 100 nm and 10^6 nm, which relates with the energies between 12.4 eV and 1.24 meV. But its intensity changes at different wavelengths as seen in Figure 1.2.

The blue line is the black body irradiance at 5900 K, which relates with the sun irradiance. After the photons enter the atmosphere some of them are absorbed by ozone and water vapor so, spectrum of irradiance is given with air mass (AM) 0 and 1.5 which depend on zenith angle.

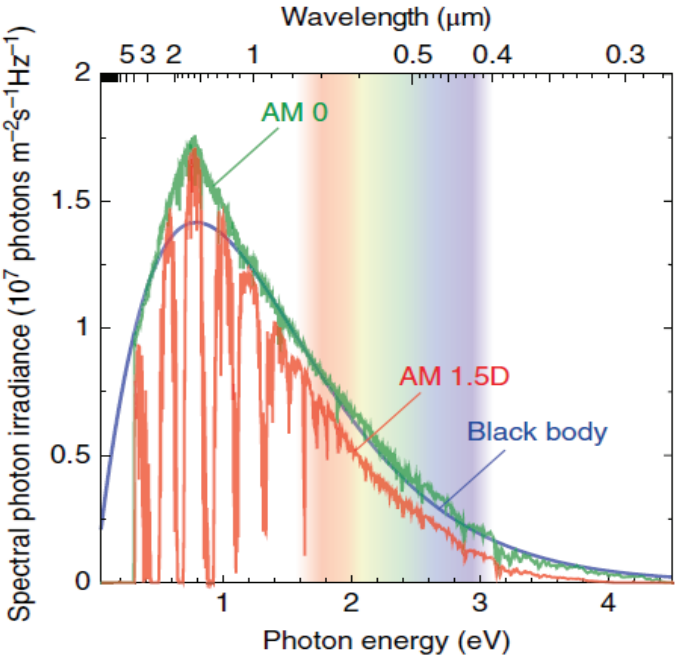

Figure 1.2. Solar Radiation
(Source: Ito, 2014)

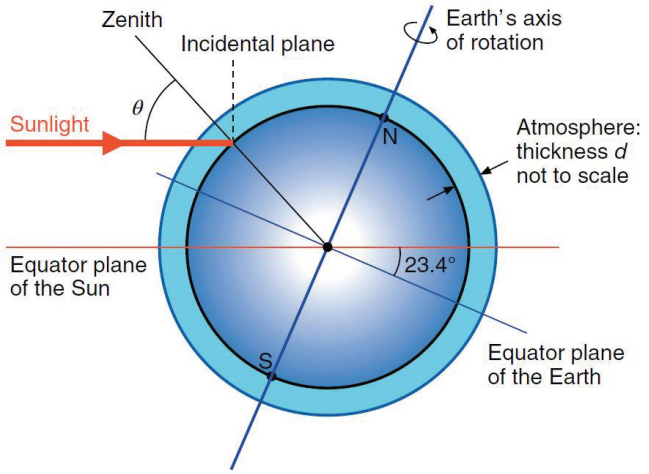

Figure 1.3. The path of sun light through the atmosphere
(Source: Ito, 2014)

Figure 1.3. demonstrates the way of solar radiation to reach the Earth's surface after surpassing the atmosphere effective thickness. The path length of light, s, is defined as $s=d/\cos(\theta)$ which links with time and place on the Earth. The term of air mass (AM) is given by $s/d \approx 1/\cos(\theta)$. AM0 named with the extraterrestrial spectrum is the solar radiation outside the atmosphere. AM1.5 represent the incident light having an angle of 48.2° between the sun's position and the zenith.

AM1.5 radiation has the irradiance as 827 W/m^2. 1000 W/m^2 value was selected to become a standard because this irradiance value is close to the maximum irradiance value received at the earth's surface. Therefore, power of photovoltaic systems is generated under this standard AM1.5 (1000 W/m^2) radiation.

1.3. Photovoltaic Systems

Photovoltaic systems (PV) convert the solar energy to electricity. Since they are convenient and sustainable source, they are the main solution of increasing global energy demand. The cost of PV systems has decreased in last years which is the result of increment in solar cell efficiency. The development of photovoltaic materials is experiencing a huge expansion and efficiency records are continuously broken. In the next chapter, the details of photovoltaic and solar cells will be explained.

CHAPTER 2

THIN FILM SOLAR CELLS

2.1. Photovoltaic (PV) Technology

In photovoltaic technology, the solar cell systems are seperated into three parts based on the used semiconductor. First generation solar cells are the crystalline Silicon (c-Si). More than 80% of the PV industry is based on Si wafer technologies. However, these technologies base on an indirect band gap absorber material, so it requires a thick layer to absorb more incident solar radiations. Also in order to obtain high efficient solar cell, perfect crystals are necessary which makes them expensive.

The second generation solar cells use inorganic materials, are thin film solar cells which have taken increasing attention as an alternative to limitations of c-Si technology in the early stage of the 2000. Since they have high optical absorption coeefficient and consist of direct band gap materials, thinner layers absorb more incident solar radiations which makes them low cost material. Given that they can also be flexible, this allows them for large area applications. Nowadays, based on the used absorber material, there are mainly five types of inorganic solar cells which are amorphous Si (a-Si), cadmium telluride (CdTe), copper indium gallium diselenide (CIGS), copper indium diselenide (CIS) and $Cu_2ZnSnS(e)_4$ CZTS(e). Since power conversion efficiency is important parameter for PV systems to determine the device performance, the detailed investigation of these solar cells will be given in the following section.

The third generation solar cells use organic materials such as small molecules or polymers. This category also covers expensive multi-junction solar cells which has the highest performance in the world. Their trading applications are limited due to the high production cost. As third generation solar cell, perovskite solar cells demonstrate high potential with having efficiencies beyond 20%. Polymer solar cells have a simple and quick production way. They have also cheap large-scale area application.

Although third generation solar cells have some advantages, their performance and stability are still limited (Krebs et al., 2013).

2.2. Thin Film Solar Cells

Thin film solar cells are fabricated by depositing thin films of photovoltaic materials. Their thickness change from nanometers to micrometers on substrate. The main objective of PV is to economize the cost of the cell by diminishing the cost of materials. In addition to material cost reduction, most thin film PV costs are lower than those of silicon technologies when they are compared. Thin film solar cells are also available for growth on flexible substrates. Many of the thin film solar cell materials have a direct bandgap and therefore also higher absorption coefficients than Si which has an indirect bandgap. Even though thin film solar cells have potential being more efficient than crystalline silicon solar cells; this fact has not been reached, yet.

2.2.1. Amorphous Si Solar Cell (a-Si)

a-Si solar cells belong to second-generation thin film solar cell technology. Having a direct bandgap material, amorphous silicon is a non-crystalline form of silicon.

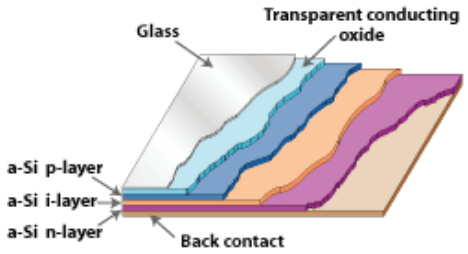

Figure 2.1. a-Si solar cell structure.

a-Si solar cells use three layersfor the structure either p-i-n or n-i-p photodiode sequence as demonstrated in Figure 2.1. These three layers consist of thin p-type layer (~20 nm), very thick undoped intrinsic layer (~100-200 nm) and thin n-type layer. a-Si solar cells can also be made flexible. Thanks to flexibility, it can be used for curved surfaces. Having low output power restricts its usage only for small applications. Although, the highest efficiency of 13.6% for a-Si has been reported by LG electronics, they have instability problems which decrease the device performance.

2.2.2. Cadmium Telluride (CdTe) Solar Cell

Cadmium telluride (CdTe) is a p-type semiconductor with a direct optical band gap of 1.45 eV. Its absorption coefficient is 5.0×10^5 cm^{-1} therefore it absorbs the most of photons in a small depth. Tellurium is obtained from the refinment of copper. Since the cadmium is more abundant than tellurium, it would be an important concern if CdTe solar cells were more prefered solar cell. In 2015, the first solar declared the 22.1% conversion efficiency for CdTe solar cell. Having toxic components, however, CdTe based solar cells have high safety and waste treatment cost.

2.2.3. Copper Indium Gallium Diselenide (CIGS) Solar Cell

Copper indium gallium diselenide (CIGS), is another p-type semiconductor absorber layer for thin film photovoltaic devices. CIGS solar cell has a direct band gap of 1.7 eV, a high absorption coefficient of 10^5 cm^{-1} which allowing to absorption 90% of incoming light. The intrinsic defects effect the electronic conductivity of this material. The vacancies of copper and indium yield p-type conductivity whereas the selenium vacancies result n-type conductivity. In at Cu antisite defect is the most crucial defect which effect the carrier recombination. CIGS has an efficiency of 21.7% which was decleared by the Centre for Solar Energy and Hydrogen Research Baden-Württemberg (ZSW) and sets a highest record in Europe. However, there are concerns about using the toxicity selenium. In addition, having expensive constitute elements as In and Ga, the mass production of CIGS is very high cost.

2.2.4. Copper Indium Disulfide (CIS)

As a ternary compound the copper indium disulfide ($CuInS_2$, CIS) looks for accomplishing the problems related with the use of gallium and selenium. CIS is taken much interest due to its optoelectronic properties. CIS has 1.54 eV bandgap value and 28.5% theoretical efficiency (Ji et al., 2013; Toyama et al., 2015). The World highest conversion efficiency of 18.7% for CIS solar cell was announced at EU PVSEC 2016 by Solar Frontier which has a potential to be replaced with CIGS solar cells.

As observed for the other solar cells, CIS has drawback, too. Due to the high price of In, CIS is blocked for mass production in the future. The removing of this drawback will cause the reduction in cost production.

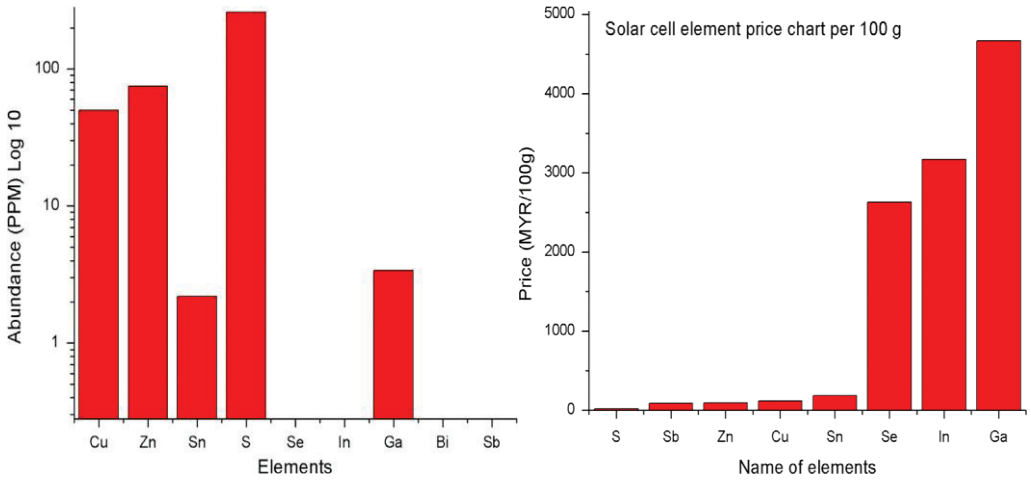

Figure 2.2. The abundance in the Earth's crust and the price of constitute elements of CZTS, CIS and CIGS (Source: Ali et al., 2016).

Beside these, copper zinc tin sulphur Cu_2ZnSnS_4 (CZTS), copper zinc tin selenium $Cu_2ZnSnSe_4$ (CZTSe) and copper zinc tin sulfide selenium $Cu_2ZnSnS(e)_4$ (CZTS(e)) are highly studied semiconductor absorber materails at last decade. In terms of earth crust content, having the low price and non-toxic constitute elements, CZTS based solar cells have great advantages for PV industry. Figure 2.2. shows the abundance and price of ingredients elements of all types of solar cells. The detail investigation of CZTS solar cell will be given in the Chapter 4.

CHAPTER 3

PHYSICS OF SOLAR CELLS

3.1. Shockley-Queisser Limit

The solar radiation that reaches the earth has various wavelengths but only some of them can create an electron-hole pairs. For a given solar spectrum, there are many factors that affect their essential efficiency limit. In the case of the photon energy below the band gap, it is not absorbed whereas the photons with energies higher than the band gap are not totally turned to electrical energy due to the thermalization of charge carriers. By considering these factors, approximately 45% of the solar power survives for semiconductors with a band gap of 1.1-1.4 eV (Polman, Knight, Garnett, Ehrler, & Sinke, 2016). The energy conversion efficiency of solar cell is given with the percentage of converted power from the sunlight to electrical energy.

In 1961, Shockley and Queisser firstly calculated the maximum theoretical efficiency limit which is the most significant parameter for solar cell production. There are primary considerations in the calculation. Figure 3.1. shows the existence of limit for the usable electrical power.

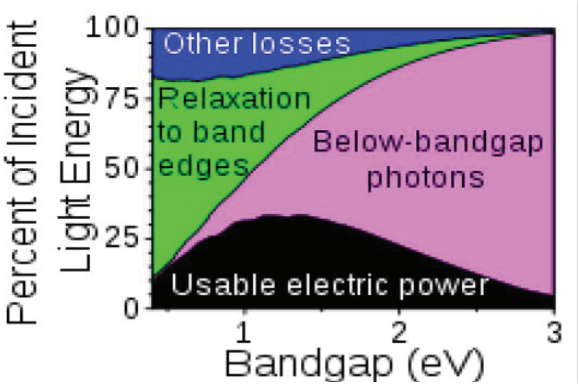

Figure 3.1. The limitations of usable electric power.

According to calculation, the highest short-circuit current density is obtained for the lowest bandgap. This assumes that each solar photon converted into an electron that flows through the circuit.

At higher bandgaps, there are fewer photons above the bandgap, and therefore the current density decreases. Figure 3.2. shows the theoretical calculation results that the open-circuit voltage increases as the band gap increases whereas the short-circuit current density (J_{SC}) decreases with increasing bandgap.

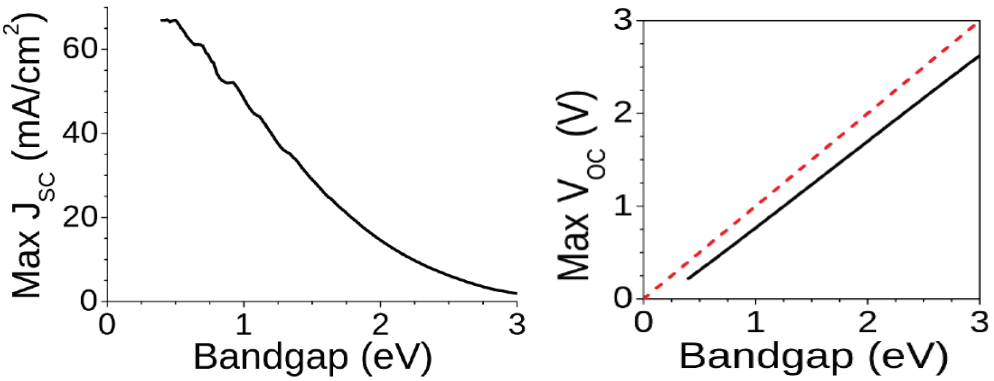

Figure 3.2. The limit for the short circuit current density (J_{SC}) and open circuit voltage V_{OC} (Source: Shockley & Queisser, 1961).

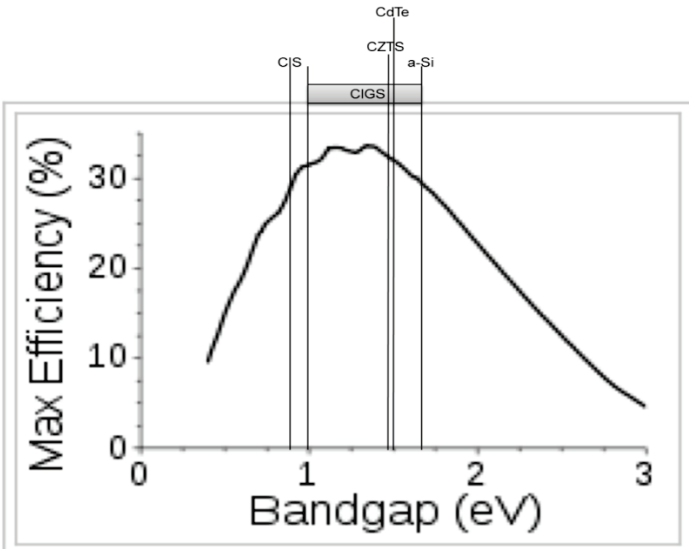

Figure 3.3. According to Shockley-Queisser limit, the efficiency limit for a single junction solar cell under "one-sun" illumination (Source: Shockley & Queisser, 1961).

They showed that by using an AM1.5 solar spectrum, it is possible to obtain the maximum solar conversion efficiency at around 33.7% for a single p-n junction with a band gap of 1.4 eV (Shockley & Queisser, 1961). Therefore, using the material with the band gap between 1-2 eV (Figure 3.3.) provide more electrical power.

So far, none of these thin film solar cells described below has led to an efficiency as expected in theoretical.

3.2. Photovoltaic Effect

Alexandre-Edmond Becquerel has been observed the photovoltaic effect (PV) for the first time in 1839. While he was trying to generate a current between platinum and gold plates which were dipped in a solution, they were exposed to light. In this case, the light energy is absorbed by the valence band electrons of metal and they are excited to the conduction band which result the free electron movements between the materials. Although the PV effect relates with photoelectric effect, the fact that they are completely different events.

In the photoelectric process, when a material is exposed to light, the electrons in a material absorb the light energy and leave the material to generate electric current. The photovoltaic effect which occurs in semiconductors is the electronic process that converts the sun light directly to the electricity. When the energy of incoming light is equal or higher than the bandgap energy of a semiconductor, the light is absorbed and an electron is excited from valence band and conduction band of semiconductor. In this process, the electrons are set free and moved through the circuit.

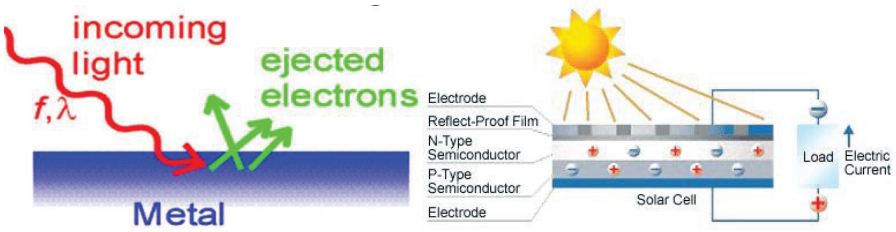

Figure 3.4. Photoelectric effect (on the left) and Photovoltaic effect (on the right).

The mechanism of photovoltaic devices base on a simple p-n junction. Therefore, it is important to understand the semiconductor types and the operation of p-n junction.

3.3. Semiconductors

The main difference between the semiconductors is the majority charge carrier types. Electrons and holes can move freely between the atoms of a semiconductor. If the majority charge carriers within a material are electrons, this material is called n-type semiconductor or donor and the conductivity of this kind of semiconductor is provided by excess electrons. On the contrary, in the case of majority charge carriers are holes this material is called p-type semiconductor or acceptor and the conductivity of this kind of semiconductor is provided by excess holes. When the number of excited electrons and holes are equal, this kind of material is named with intrinsic (undoped) semiconductor. Since it is a pure semiconductor without any dopant, it is also called as undoped semiconductor. Figure 3.5. shows the band diagram of semiconductor types.

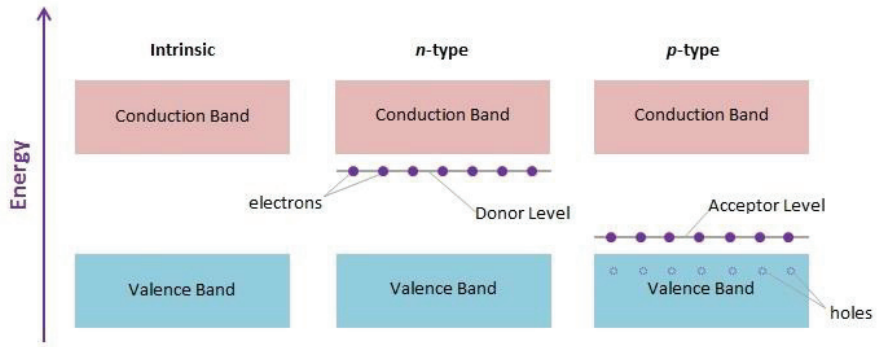

Figure 3.5. Band diagram of intrinsic, p-type and n-type semiconductors.

In the band diagram, the Fermi level energy (E_F) represents the highest occupied energy state by electrons at T=0K. The position of Fermi level lies at different position at different semiconductor types. Since there are equal number of electron and hole in intrinsic semiconductor, Fermi level stays middle of the bandgap. P-type semiconductors are electron deficient material and the Fermi level position stays close to the valence band. N-type semiconductors have excess electrons and the Fermi level stays close to conduction band so there are more electrons at those energy levels.

3.4. P-N Junction

The p-n junction in Figure 3.6. forms by bringing two semiconductors with opposite doping together. In the case of interconnection of p and n semiconductors, the excess electrons in the n-type material diffuse to the p-type material side whereas the excess holes in the p-type material diffuse to the n-type material side. As a consequence of this diffusion, the space charge (depletion) region is formed as well as electric field is generated from n-type material to p-type material at the junction.

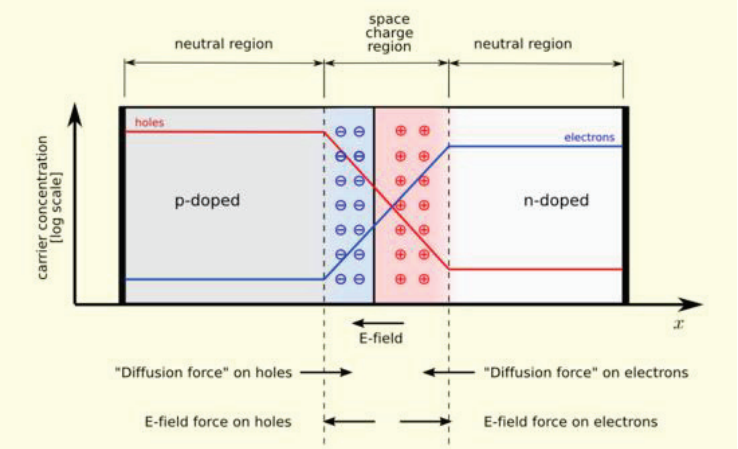

Figure 3.6. Schematic diagram of p-n junction in thermal equilibrium.

Due to the electrostatic force in the junction, some electrons and holes move back to the n and p region, respectively which causes the formation of drift current from n type to p-type. Without any voltage application, the p-n junction is in thermal equilibrium. In the case of equilibrium, the net current which consists of drift and diffusion current is zero for both electrons and holes since the magnitute of diffusion and drift currents are equal but they are in opposite direction.

3.4.1. P-N Junction Under Bias

In the condition of forward bias as shown in Figure 3.7. the positive terminal of the battery is connected to the p type and the negative terminal of the battery is connected to the n type. The positive terminal repels the holes and negative terminal repels the electrons through the junction which decrease the width of depletion region. This situation decrease the electric field at the depletion region.

The barrier height for the majority carriers decreases so diffusion current of majority carrier increases. The drift current, which oppose the diffusion current, is not relatively sensitive to the change in barrier height thus it has the same value as its thermal equilibrium.

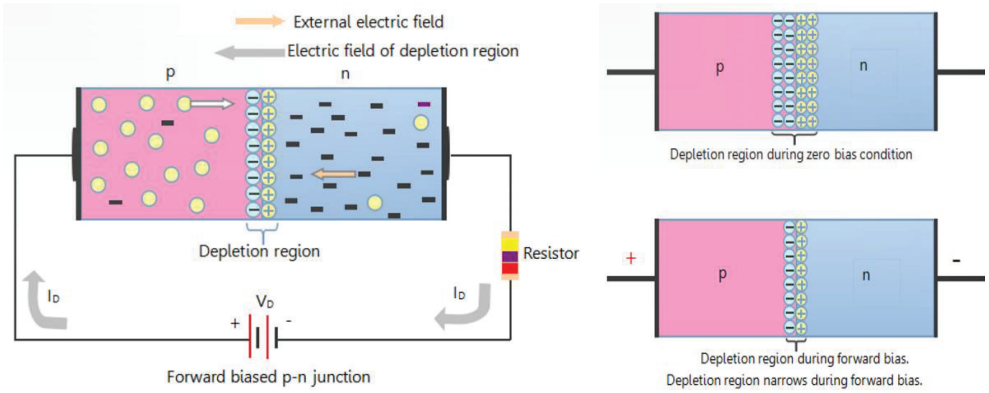

Figure 3.7. Forward bias condition of p-n junction.

In the condition reverse bias as shown in Figure 3.8. the negative terminal of battery is connected to p type and positive terminal of the battery is connected to the n type. The negative terminal attract the holes and positive terminals attract the electrons which increase the width of depletion region. This situation increase the electric field. The higher electric field in the depletion region decreases the diffusion of charge carriers from one side to the junction which results the decrement in diffusion current. Since the drift current is not sensitive to the changes in width of depletion region, it remains the same at thermal equilibrium value. Therefore, in reverse bias a small negative current flows.

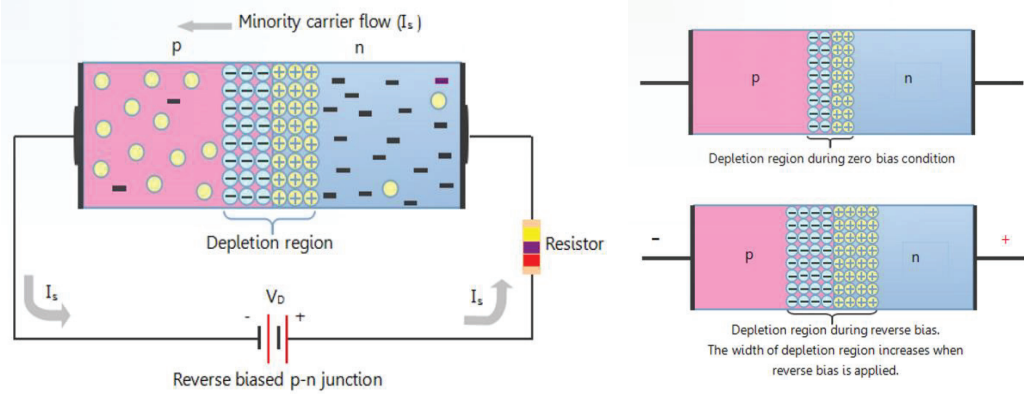

Figure 3.8. Reverse bias condition of p-n junction.

This current is generally named with reverse saturation current I_o. Since the p-n junction behaves as a diode in dark conditions, two terminal electronic component allow the current flow only in one direction. In summary, under forward bias (V>0) condition the current flows but it cannot flow under reverse bias (V<0) condition. For an ideal diode the dark current is given by the following equation 3.1.

$$I_{dark} = I_0 \left(e^{\frac{qV}{kT}} - 1\right) \tag{3.1}$$

Here, I_{dark} is the net current flowing along the diode in dark, I_0 is the dark saturation current, V is the applied voltage across the terminals of the p-n junction, q is the electron charge, k is the Boltzmann's constant and T is the absolute temperature in Kelvin. Figure 3.9. (a) demonstrates the I-V curve of pn junction under dark condition. On the I-V curve of the pn junction in dark, the left side gives the reverse bias and the right side gives the forward bias case of the junction.

3.4.2. P-N Junction Under Illumination

When the band gap energy of material is greater than the energy of incident light, no absorption as well as no electron-hole pair formation are observed. When the diode is illuminated, two different events are observed. If the photon energy is greater than the bandgap of material, the incident photons are absorbed and electron-hole pairs are generated in the junction which become a source of electricity and results a current along the junction. Electrons flow from low to high work function materials e.g., Mo→p-type→n-type→ZnO→AZO. In the case the contacts are connected, because of electron-hole pair generation under illumination a current which is called photo-current (I_L) flows in the opposite direction to the dark current. Therefore, the dark current equation of the junction should be modified for the case of illumination of the junction with the following equation 3.2.

$$I = I_0 \left(e^{\frac{qV}{kT}} - 1\right) - I_L \tag{3.2}$$

Figure 3.9. (b) demonstrates the I-V curve of pn junction in light which the left side of the curve gives the reverse bias and the right side gives the forward bias case. The Figure 3.9. (b) is different from the Figure 3.9. (a). Once there is not any light to form any current, the solar cell behaves as a diode. Since the illumination causes the photocurrent in the opposite direction of the dark current, I-V curve shifts along the negative current-axis. While the intensity of incident light is increased, the generated current by solar cell increases.

There are some important parameters such as I_{SC}, V_{OC}, FF and η which play a key role in characteristics of solar cell. All of them are defined under illumination conditions as given in Figure 3.9. (b) I_{SC} is the short circuit current which is the current value when the voltage equals to zero. For an ideal solar cell, I_{SC} is the maximum current value generated in the solar cell by excitation of photon. V_{OC} is the open circuit voltage which occurs when there is not any current passing along the solar cell. Therefore, so as to determine V_{OC}, the equation 3.2 is derived as the following.

$$\mathrm{I} = \mathrm{I}_0 \left(\mathrm{e}^{\frac{\mathrm{q}V_{OC}}{\mathrm{kT}}} - 1 \right) - I_L = 0 \tag{3.3}$$

$$V_{OC} = \frac{kT}{q} \ln\left(\frac{I_L}{I_S} + 1\right) \cong \frac{kT}{q} \ln\left(\frac{I_L}{I_S}\right) \tag{3.4}$$

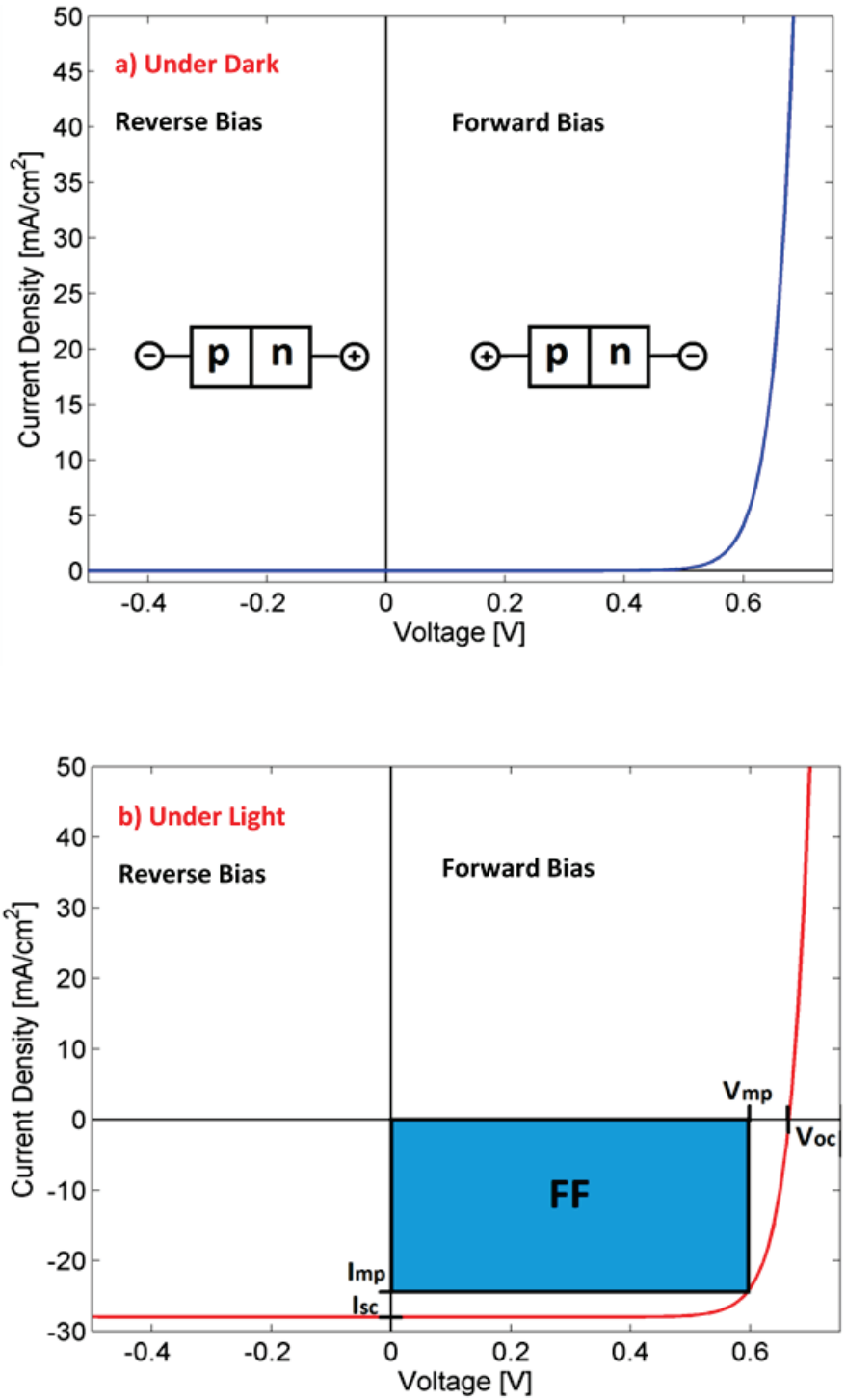

Figure 3.9. Current-voltage curve of solar cell under a) dark and b) light conditions.

The quality of the solar cell is determined by the fill factor (FF) which is calculated by the ratio of the maximum power to the output power as given with the equation 3.5.

$$FF = \frac{P_{max}}{P_{output}} = \frac{I_{MP} * V_{MP}}{I_{SC} * V_{OC}} \tag{3.5}$$

From the I-V curve of illuminated solar cell, FF can also be interpreted as the ratio of the rectangular areas shown in Figure 3.10.

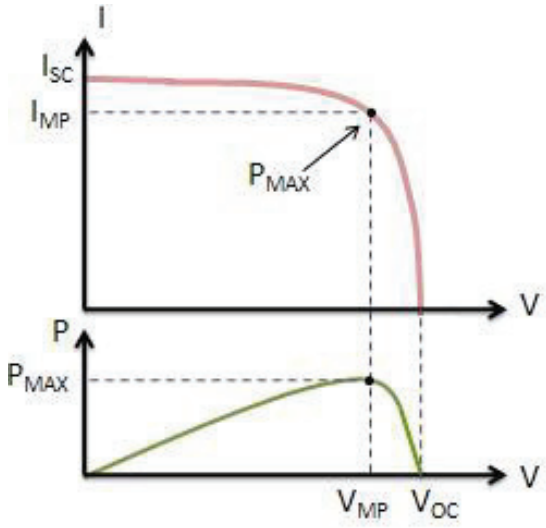

Figure 3.10. Illuminated I-V curve of solar cell.

To define the quality of solar cell and compare it with another cell, the most common used parameter is the efficiency (η) value. As given by the equation 3.6, efficiency is calculated from the ratio of output power (P_{max}) from the solar cell to the input power from the sun.

$$\eta = \frac{P_{max}}{P_{in}} = \frac{V_{OC} I_{SC} FF}{P_{in}} \tag{3.6}$$

Efficiency is also links with the spectrum and the intensity of the incident light, as well as the temperature of solar cell. Thus, conditions of efficiency measurement must be cautiously checked so as to make comparison the performance of one solar cell to another.

3.5. Equivalent Circuit of a Solar Cell

In order to understand the electronic behavior of a solar cell, the electrically equivalent model should be created. Although the ideal solar cell could be modeled by a diode in parallel with a current source, in reality there is not an ideal solar cell therefore a series resistance as well as a shunt resistance are added to the model. The schematic representation of a solar cell is given in Figure 3.11.

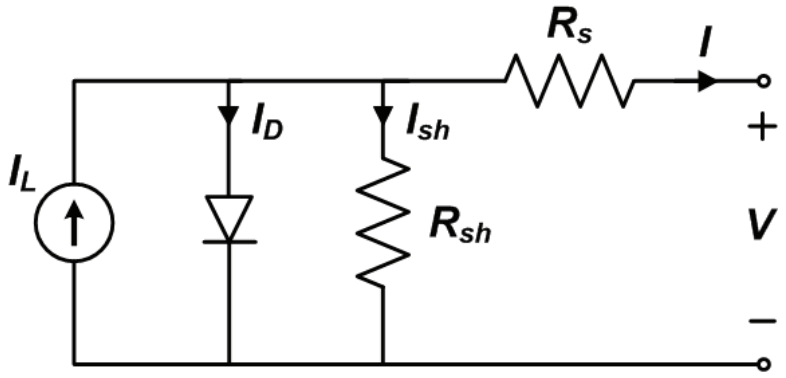

Figure 3.11. The equivalent circuit of a non-ideal solar cell.

In this circuit, I is the output current, I_L is the photo-current, I_D is the diode current, I_{sh} is the shunt current, R_{SH} is the shunt resistance and R_S is the series resistance. The output current is given with the equation 3.7.

$$I = I_L - I_D - I_{SH} \tag{3.7}$$

The potential across both the shunt resistance and the diode is V_D while the output voltage is V as given in equation 3.8.

$$V_D = I_{SH}R_{SH} \quad , \quad V_D = V + IR_S \tag{3.8}$$

For the non-ideal solar cell, the modified output current is given by the equation 3.9.

$$I = I_L - I_0\left(e^{\frac{q(V+IR_S)}{kT}} - 1\right) - \frac{V+IR_S}{R_{SH}} \tag{3.9}$$

3.6. Series Resistance

Thin film solar cells have two electrical contacts such as front and back contact. The front contact where the light penetrates to the cell consists of transparent conducting oxide (TCO) layer. Back contact forms from metal layer at the back of the solar cell. The series resistance forms due to the back contact resistance between metal and absorber interface, front contact (TCO) resistance and the bulk resistance of the photoactive material (Kavitha et al., 2016).

There is a relation between optical and electrical necessities. When the TCO is thin in order to diminish the optical loss due to absorption inside material, it causes the high sheet resistance which clearly contribute to the series resistance (Rs) (McEvoy, Castaner, & Markvart, 2012).

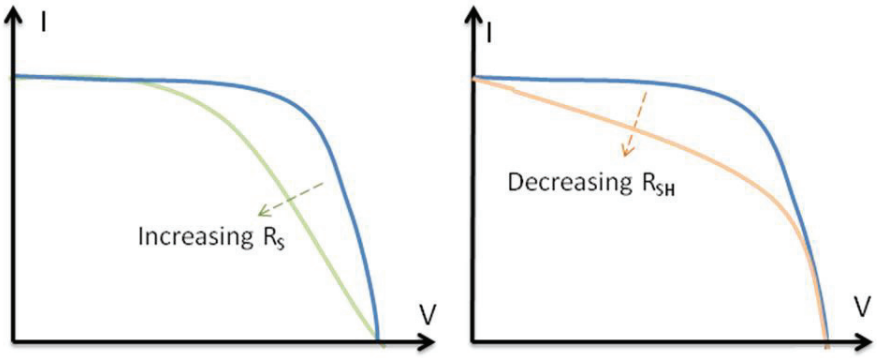

Figure 3.12. The effects of a) Series resistance (Rs) and b) Shunt resistance (R_{SH}) to the I-V curve of solar cell.

In the case TCO layer is thick which absorbs much light, the generation of photo-carrier decreases. The thickness of the back contact is less important than the front contact thickness because they are extremely conducting metal layers. Generally, sheet resistances do not induce remarkable electrical losses but it is crucial to use low sheet resistant TCO layers. The effect of series resistance to the electrical characteristics of solar cells is shown in Figure 3.12.

And also the absence or reduced amount of photon absorption in the buffer layer reduces the fill factor (FF) because of the enhancement of series resistance (Buffiere et al., 2014). The high value of series resistance decreases the short circuit current density and FF.

3.7. Shunt Resistance

In thin film solar cells, the shunt is the most commonly observed problem. Shunt is caused by the manufacturing defects in bulk and cell surface. Shunt resistance stands for a parallel high-conductivity path across the p-n junction and results the power losses. Although for an ideal solar cell the shunt resistance, R_{SH}, is thought as infinite, for the non-ideal solar cell the low value of it results power losses in solar cells by supplying an

alternate current path for the photo-generated current. For this reason, the amount of flowing current through the solar cell diminishes.

In addition, the open circuit voltage across the solar cell and the FF from the I-V curve reduce (Figure 3.12.) (Singh & Ravindra, 2012). A straight-forward method was used for estimating the series and the shunt resistance of solar cell. In this method, the slope of I-V curve at the open-circuit voltage and short-circuit current point gives the series and the shunt resistance, respectively. The deviation in I-V curve of non-ideal solar cell from the I-V curve of ideal solar cell is the result of increase and decrease in the series resistance and shunt resistance, respectively. Figure 3.13. demonstrates the determination of R_S and R_{SH} resistances.

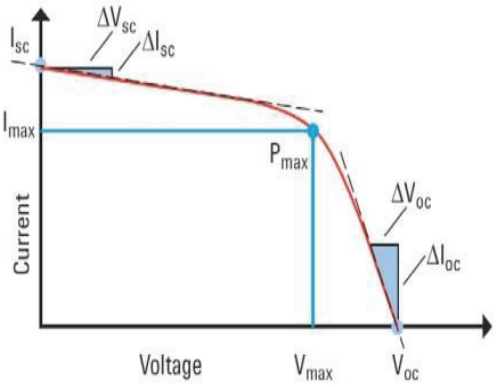

Figure 3.13. Demonstration of R_S and R_{SH} calculation.

3.8. Losses in Solar Cells

In the ideal solar cell operation, each incident photon energy is absorbed by solar cell and electron-hole pairs are created. All of the created electron-hole pairs contribute to the generation of photocurrent and in this case 100 % efficiency would be achieved. However, in real solar cell process, there are many types of loss mechanisms which effect the photo-conversion efficiency of solar cell. In Figure 3.14., the possible loss mechanisms for solar cell process are schematically listed.

Thermalization is known as the energy lost where the excess energy of photon is released as heat into the semiconductor lattice. So as to reduce thermalization effect, the band gap should be as high as possible. Absorption in window and buffer layers, incomplete in collection and absorption cause the decrement in the current. Recombination is one of the loss mechanisms for solar cells.

Some of generated charge carriers are not collected at the electrodes and electron-hole recombination occurs. Recombination forms by defects in the bulk of the absorber or at the buffer-absorber and buffer-window interfaces. All types of recombination cause open-circuit voltage losses. Moreover, I_{SC} is also limited by the recombination in the depletion region due to trapping energy levels.

Optical losses are caused by the reflection of incident light from each layers of solar cell and the non-absorption of long wavelength photons by the absorber layer. Optical losses decreases the short circuit current and the efficiency.

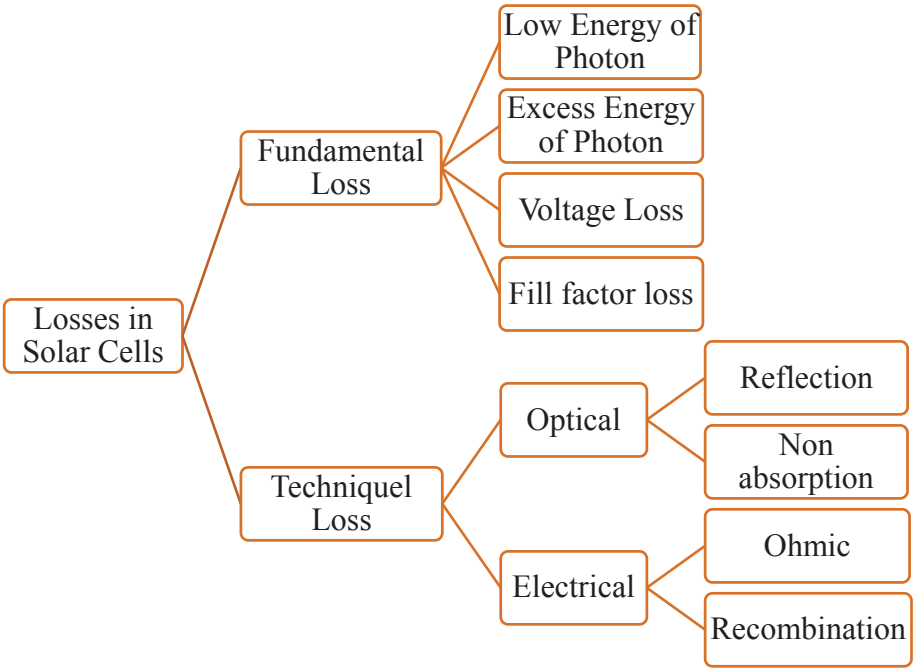

Figure 3.14. Losses in solar cells.

3.9. Aim of The Work

In spite of the fast improvement of CZTS based solar cells, their efficiency are still lower than the theoretically expected value which is higher than 30% (Shockley & Queisser, 1961) Therefore some parts of the work was devoted to optimize CZTS absorbers with the aim of obtaining sufficiently good CZTS properties for PV application. This is followed by the optimization of CdS buffer layer in the solar cell structure. The structure, chemical and optical properties of CZTS and CdS layers were investigated using a wide range of techniques. Some part of the work was devoted to fabricate SLG/Mo/CZTS/CdS/ZnO/Al:ZnO solar cell structures.

The effect of calibrated CZTS and CdS layers inside the device structure on the photovoltaic characteristics of solar cells were searched in detailed. This work has allowed for insight into the effect of sequentially grown Cu thickness with Sn layer on the CZTS structure and the thickness of CdS buffer layer on the photovoltaic performance of CZTS based solar cells. Surface composition and formation of superior phases on the surface of CZTS absorber are important for the interface between CdS buffer layer and CZTS. Therefore, in this work the quantification of CZTS surface by XPS analysis is also aimed.

3.10. Structure of The Work

This thesis consist of mainly seven chapters. In Chapter 1, a brief explanation about renewable energy and solar energy is given. Chapter 2 concerns with thin film solar cells. Chapter 3 explains the physics of solar cells and theoretical limit for single junction thin film solar cells. In Chapter 4, the review on CZTS based solar cells and information about solar cell layers are given. In Chapter 5, four main experimental processes for CZTS, CdS, ZnO and Al:ZnO layers are explained in detail and also the knowledge about characterization techniques that used in this work are also informed. In chapter 6, characterization results of CZTS absorber and CdS buffer layers are discussed. The photovoltaic response of fabricated solar cells are also discussed in this chapter. Conclusion of this work are presented in Chapter 7.

CHAPTER 4

A REVIEW OF THIN FILM SOLAR CELL LAYERS

4.1.Mo Back Contact Layer

The main requirement for the back contact is to provide a low series resistance and an ohmic contact to the absorber layer. To obtain ohmic contact, the selected metal should have work function value close to that of semiconductor. Putting the thin layer material with narrow bandgap among the metal and semiconductor may result the ohmic contact. The increment in dopped level as high as possible near the surface of semiconductor can develop the ohmic contact. The formation of ohmic back contact between absorber and substrate is as important as the stoichiometry and the quality of absorber layer which can limit the efficiency. The ohmic contact should have low contact resistance ($< 10^{-6}$ Ωcm^2) and should be thermally stable when temperature varies.

When it is compared with other back contact materials such as W, Ta, Nb, Cr, V, and Ti, Mo is unique therefore it has been widely used as back contacts for CZTS solar cells. As well as its low electrical resistivity, it has other properties which satisfy the most necessities of a good back contact. Mo is thermally stable at high processing temperatures which has resistance to make detrimental interface with Cu. Mo has perfect adhesion between soda lime glass substrates and CZTS absorber layer. Finally, Mo back contact allows Na ions to diffuse from the SLG substrate to CZTS absorber layer during CZTS deposition which has a beneficial effect on the performance of the solar cell. In the literature, it was detected a relation between the sputter gas pressure and the stress of the Mo film. The deposition of Mo films under low Ar pressure resulted a compressive stress whereas deposition under high Ar pressure resulted a tensile stress on the film (Hoffman & Thornton, 1982; Thornton & Hoffman, 1985, 1989). Afterwards, Scofield *et al* has been declared that a single pressure sputtering of Mo films do not have low resistivity and good adhesion, which are desired properties of the back contact for solar cells. They demonstrated that Mo films deposited at low sputtering pressure has low resistivity which is in close-range to the bulk values at room temperature ($\rho_b = 5.4 \times 10\text{-}6$ Ωcm), while the films deposited under high sputtering pressure has higher resistivity than the bulk values.

The reason of the relation between the deposition conditions and the electrical properties is the difference in the film morphology. These differences are the result of different sputtering pressure, having high resistivity with porous structure under high pressure deposition condition and having low resistivity with more packed morphology but bad adhesion on glass substrate under low pressure deposition condition.

In order to achieve this problem, they developed two pressure deposition steps. With this technique, it was firstly deposited thin Mo layer as an adhesion layer under high pressure and secondly, to obtain low sheet resistance Mo layer deposited under low pressure (Scofield, Duda, Albin, Ballard, & Predecki, 1995).

Generally Mo back contact layer is deposited in bilayers (with a thin layer on bottom, deposited at higher pressure, and a second thicker layer deposited at lower pressure) (Karthikeyan, Zhang, & Campbell, 2014). This technique is being adopted as a primary solution to optimize the Mo back contact in terms of electrical and adhesion characteristics.

4.1.1. MoS_2 Layer

For the Mo/CZTS type solar cells, the formation of MoS_2 interface between Mo back contact and CZTS absorber is possible. During the sulfurization process of absorber layer occurring at higher than 350 °C, the sulfurization of molybdenum can also be caused and MoS_2 can be formed (Ahmed, Deligianni, & Romankiw, 2012). However, the deeply examinations for the properties of back contact and its interface with the absorber layer are not easy works. MoS_2 interface layer grows during the absorber deposition and it cannot be seen until the growth of the absorbent layer is complete. It is thought that at high temperature such as at around 550 °C, the sulfur atmosphere effect the properties of interface existing between absorber /Mo back contact (Bär et al., 2008). Some of researchers believe the benefit of MoS_2 layer as an electrical quasi-ohmic contact whereas the others think that the only formation of MoS_2 layer does not help the ohmic contact and it depends on the semiconductor type and the thickness of this layer (Biccari et al., 2011). The bandgap of MoS_2 is 1.17 eV and the energy level difference between the vacuum level and valence band maximum is (VBM) 5.6 eV which is similar to that of CZTS. It is considered that the small valence band offset value (~ 0.1 eV) should be exist between MoS_2/CZTS interface.

Although this layer may be useful as an electrical ohmic contact and develop the adhesion between CZTS and Mo back contact, simultaneously it can results a high series resistance when it has high thickness. MoS_2 layer which has approximately 300 nm thickness forms a Schottky-type barrier and results the increment in device resistance and decrement in V_{OC}. On the contrary to this, enough thin MoS_2 layer (~100 nm) is beneficial for the solar cell performance because it forms the ohmic contact and allows the good adhesion between Mo back contact and CZTS absorber (Wang et al., 2010). It is crucial to control the formation of MoS_2, because good ohmic contact depends on having convenient properties of MoS_2 layer. For instance, owing to high compressive stress formed in the absorber layer, inside the MoS_2 layer holes can be formed which diminish the electrical contact between CZTS absorber layer and Mo back contact layer. By decreasing the whole contact area between CZTS absorber and Mo back contact layers, the series resistance of a solar cell can be increased by these holes which results the reduction in cell efficiency. Therefore, decrement in the contact resistance can increase the efficiency of solar cell (Ahmed et al., 2012).

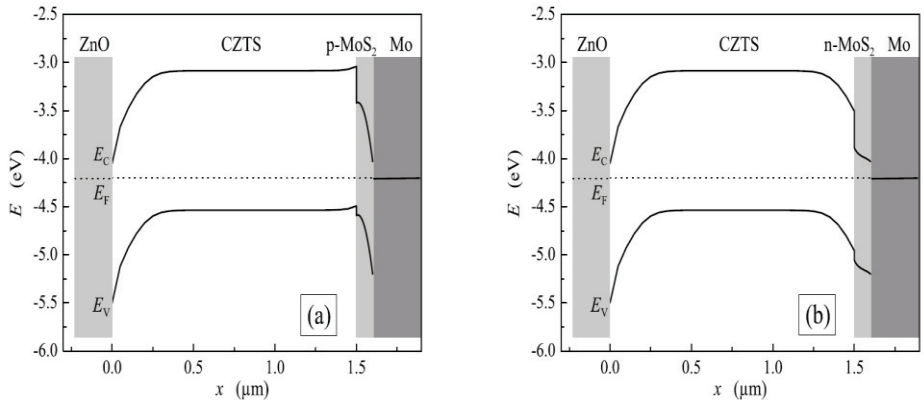

Figure 4.1. The representation of band profiles in a CZTS solar cell in the case of existing a) p-type and b) n-type MoS_2 interface layer (Source: Biccari et al., 2011).

Additionally, Biccari *et al.* think that having highly *p*-type MoS_2 might result the best situation by giving a Schottky type barrier at the Mo/MoS_2 interface as shown in Figure 4.1. (a) (Biccari et al., 2011). With the help of the tunneling, the narrow barrier which is formed in the case of high doping can be passed. In the case of formation *n*-type MoS_2 due to the work function of *n*-type MoS_2 and Mo are nearly the same, as seen in Figure 4.1. (b) barrier is positioned at the CZTS/MoS_2 interface and this results huge contact barrier which is detrimental for solar cell performance.

4.1.2. Na Diffusion in Solar Cell

While the absorber layer is grown on SLG substrate, at the annealing temperatures between 500°C and 600°C the SLG substrate exhibits some kind of transitions. By increment in the mobility of ions, Na ions can penetrate into the absorber layer. The effect of Na diffusion from the SLG substrate to the absorber layer has been investigated for different types of solar cell.

For CIGS, it has been found to be a beneficial effect of Na supplementation for solar cells. The added Na atoms improve the microstructure of the absorber layer, reduce the resistivity and increase the open circuit voltage (V_{OC}) as well as device efficiency (Nakada, Iga, Ohbo, & Kunioka, 1997). The positive effects of Na diffusion are detected for the CZTS based solar cells. It was reported by many groups that Na diffusion increases the grain size of the final film. As well as the grain size increment, it also increases the free carrier concentration (Prabhakar & Jampana, 2011). Nagaoka *et al*, demonstrated for CZTS absorber that Na diffusion increased the hole concentration diminished the thermal activation energy (Nagaoka et al., 2014). The similar effect has been observed for the CZTSe absorber that Na developed the hole density and mobility as a result V_{OC} and fill factor increased (Li, Kuciauskas, Young, & Repins, 2013).

According to the general belief in beneficial effects of Na diffusion, Na can behave as a shallow acceptor therefore it can be used to enhance the open circuit voltage V_{OC} of solar cells by increasing the acceptor density (Salomé, Rodriguez-Alvarez, & Sadewasser, 2015).

4.2. A Review of CZTS Absorber Layer

In 1978, Hall *et al.* firstly reported the X-ray diffraction pattern of natural mineral as a kesterite and stannite structure. This has revealed that CZTS had similar crystal structure but it was different material (Hall et al., 1978). Afterwards in 1988, for the first time Ito and Nakazawa published their report on the photovoltaic response of CZTS. CZTS thin films were grown by sputtering of single CZTS target on stainless steel substrate and a junction was fabricated between CZTS and cadmium tin oxide (CTO). As a result 165 mV open circuit voltage was obtained from this device (Ito & Nakazawa, 1988).

In 1997, the first device characteristic of CZTS thin film solar cell was reported by Katagiri *et al.* for the ZnO:Al/CdS/CZTS/Mo/SLG(soda lime glass) solar cell structure. The absorber CZTS layer was grown by two stages which were the electron beam deposition of a Cu/Sn/Zn stack on Mo/SLG substrate and sulfurization of this metallic precursor. They obtained 400 mV open circuit voltage and 0.66% power conversion efficiency from this device (Katagiri et al., 1997). In 2001, Katagiri published a higher efficiency of 2.63% for the sulfurization of Cu/Sn/ZnS stacks (Katagiri et al., 2001). In 2003, Katagiri increased their conversion efficiency up to 5.45% by improving sulfurization chamber to make sulfurization under higher vacuum (Katagiri, Jimbo, Moriya, & Tsuchida, 2003). In 2008, Katagiri *et al*. decleared the effect of soaking the CZTS thin films with de-ionized water on removing the metal oxide particles in the CZTS absorber. By this way, they increased the device conversion efficieny up to 6.7% (Katagiri et al., 2008). In 2010, Todorov *et al*. was constructed a solar cell with a mixed sulfoselenide CZTS(e) by hydrazine based solution on Mo coated glass substrate. They showed that the solution processed CZTSSe had a device efficiency 9.6% (Todorov, Reuter, & Mitzi, 2010). With the help of the hydrazine solution-based process, the same group achieved to increase the efficiency value to 11% by improving their device performance (Todorov et al., 2013). In 2014, Wang *et al*. by using hydrazine pure solution approach, recorded champion efficiency of 12.6% for sulfoselenide CZTSSe (Wang et al., 2014). In 2016, Tajima *et al.* reported 9.4% conversion efficient CZTS solar cells. They used two layers structure of CZTS with a total thickness of 1200 nm for these devices. In order to fabricate precursor, Cu, Sn and ZnS targets were deposited by electron-beam and RF magnetron sputtering. The absorber layers were grown on Mo coated alkali-glass.

The first CZTS absorber CZTS(1) was deposited as the order of Cu/Sn/ZnS/Mo/alkali-glass which was sulfurized under 20% H_2S and %80 N_2 atmosphere at 853K for 20 min. The second set of precursors CZTS(2) were similarly fabricated on the first one as ZnS/Sn/Cu/ CZTS(1)/Mo/ alkali-glass which were sulfurized under 20% H_2S and %80 N_2 atmosphere at 773K for 60 min. After 100 nm thick CdS buffer layer was deposited, the samples were annealed at various temperature. They obtained the highest 9.4% efficiency for the two layers structure of CZTS film annealed at 603 K which currently is the champion record efficiency for CZTS thin film solar cells (Tajima, Umehara, Hasegawa, Mise, & Itoh, 2017).

4.3. CZTS Thin Film Fabrication Techniques

The growing a four-component semiconductor CZTS at the desired properties requires a number of parameter-dependent studies. In the course of fabricating a highly complex structure of CZTS, the use of low budget film growth techniques does not mean that a low-budget solar cell will be produced (Edoff, Schleussner, Wallin, & Lundberg, 2011). For this reason, it is more appropriate to categorize CZTS thin film magnification techniques as one-step or two-step operations. Single-stage systems are systems in which all elements are simultaneously included in the system. In the two-step process, the metallic precursor is brought together at the ambient temperature and then annealed. The chalcogen material (Selenium and / or Sulfur) may be included in the system during the first stage or whilist the second stage annealing. The use of two-stage system provides faster and lower-budget CZTS thin film production. In terms of fabrication environment, the preparation of CZTS thin films can also be classified into two categories: vacuum and non-vacuum based approaches as given in Table 4.1. In the following section, it will discussed the advances of the various thin film deposition techniques and the best solar cells fabricated from each of them.

Table 4.1. CZTS thin film fabrication techniques.

Vacuum Based Technique	**Non-vacuum Based Technique**
Sputtering	Electrodeposition
Chemical Vapour Deposition	Spin coating
Pulsed laser deposition	Spray pyrolysis
Evaporation	

4.3.1. Vacuum-Based Techniques

The vacuum-based approaches mainly involve thin film deposition using sputtering and evaporation. CZTS thin films are typically fabricated by high temperature sulfurization of stacks of metals, metal sulfides, or a combination of the two.

These processes are typically slow and may require up to several hours for thin film deposition and annealing. Vacuum-based deposition techniques typically give films with controlled stoichiometry and potentially high uniformity.

4.3.2. Evaporation

The fabrication of CZTS thin films by evaporation technique were firstly decleared by Katagiri *et al.* in 1997. They evaporated Cu/Sn/Zn layers on Mo coated soda lime glass (SLG) substrates, respectively. Cu/Sn/Zn/Mo/SLG stacks were sulfurized under N_2+H_2S (5%) atmosphere at 500°C. They obtained 0.66% efficiency from these solar cells (Katagiri et al., 1997). In 2001, Katagiri *et al.* used ZnS layer instead of Zn in their stack and sulfurized it in 1h at 550°C which improved their efficiency of device performance up to 2.62% (Katagiri et al., 2001). Katagiri *et al*. made a more improvements in the sulfurization chamber by replacing the quartz glass tube furnace and rotary pump with a steel chamber and turbo pump.

They also Na dopped to CZTS films by embedding a Na_2S layer between ZnS and Mo layers. As a result of these improvements, 5.45% efficient solar cells with an open circuit voltage (V_{OC}) of 582 mV and short circuit current (J_{SC}) of 15.5 mA/cm^2 were obtained (Katagiri et al., 2003). Tanaka *et al.* fabricate the CZTS thin films by simultaneously evaporation of Cu, Zn, Sn, and S targets for 60 min on quartz substrate whose temperature was in the range of 400-600°C. They obtained the large grains for the substrate temperature was 550 °C which is necessary for obtaining of high-performance photovoltaic devices (Tanaka, Kawasaki, Nishio, Guo, & Ogawa, 2006). Subsequently, they studied the composition effect on structural properties of CZTS films fabricated by co-evaporation of Cu, Zn, Sn, and S targets for 120 min on glass substrate whose temperature was 550°C. They came to conclusion that Cu or Sn-rich films were not convenient for solar cell applications due to their low resistivity (Tanaka et al., 2010). Schubert *et al.* deposited the CZTS thin films by fast co-evaporation of ZnS, Cu, Sn, and S targets on Mo coated soda lime glass substrate whose temperature was 550 °C. They found Cu-rich CZTS films. In order to remove Cu based secondary phases, KCN treatment was applied. As a result, 4.1% efficiency was observed with a 541 mV V_{OC} and, a 13.0 mA/cm^2 J_{SC} (Schubert et al., 2011). In 2011, Shin *et al.* reported the highest efficient CZTS solar cell with 8.4% fabricated by co-evaporation technique.

The CZTS absorber was deposited by evaporation of Cu, Zn, Sn and S elements on Mo coated soda lime glass substrate. The substrate temperature was kept at 150°C during the deposition. After the evaporation, the sample was annealed under atmospheric pressure at 570°C in a short time. As a result the 8.4% power conversion efficiency was obtained (Shin et al., 2011).

4.3.3. Sputtering

First sputtered CZTS thin film has been achieved by Ito and Nakazawa in 1988 which was fabricated by an argon beam sputtering technique from pressed targets of CZTS. CZTS thin films were deposited during 2-6 h on glass slides whose temperature was less than 240°C. The p-type conductivity, large absorption coefficient and 1.45 eV bandgap value was encountered for these films.

For the first time they showed the photovoltaic properties of CZTS film and its heterojunction with cadmium tin oxide which gave a V_{OC} of 165 mV (Ito & Nakazawa, 1988). Jimbo and Katagiri *et al.* obtained the CZTS films on Mo coated glass substrates by co-sputtering of SnS, ZnS and Cu targets following the sulfurization under N_2+H_2S (20%) atmosphere at 580 °C for 3h. They recorded the 5.74% efficiency for the sample with Cu/Zn+Sn ratio 0.87 (Jimbo et al., 2007). Immediately after, Katagiri *et al*. fabricated CZTS thin films on Mo coated SLG substrate by RF magnetron co-sputtering of ZnS, Cu and SnS targets and sulfurized this CZTS precursor under 20% H_2S and N_2 atmosphere at 580°C for 3h. The only difference from the previous work was that they soaked CZTS films in deionized water for 10 min before deposition of CdS buffer layer. They predicted the atomic ratios of Cu/Zn+Sn, Zn/Sn and Metal/Zn+Sn+Cu as 0.85, 1.25 and 1.10, respectively. 6.77% efficiency with open circuit voltage (V_{oc}) 610 mV and short circuit current density (J_{sc}) 15.7 mA/cm^2 was obtained from this kind of device (Katagiri et al., 2008). In 2016, Tajima *et al*. reported the best efficient CZTS solar cell by high temperature annealing after CdS buffer layer growth. CZTS films were fabricated on Mo coated alkali glass substrates. They used two layers structure for CZTS absorber layer. The thicknesses of CZTS(1) and CZTS(2) layers were 400 nm and 800 nm, respectively. CZTS absorber layers were grown by electron-beam and RF magnetron sputtering deposition of Cu, Sn, ZnS targets on Mo/alkali glass substrates, respectively.

After 100 nm thick CdS buffer layer deposition, the CdS/ CZTS(2)/ CZTS(1)/ Mo/ alkali glass structures were rinsed in deionized water and then were annealed at 473-633 K for 20 min. For the structure annealed at 603 K, for the designated area it was obtained 9.4% efficiency with 0.70 V (V_{oc}) and 21.3 mA/cm^2 (J_{sc}) (Tajima et al., 2017).

4.3.4. Pulsed Laser Deposition (PLD)

Moriya *et al.* was firstly used PLD technique to deposit CZTS solar cell on Mo coated soda lime glass substrate. CZTS precursors were fabricated by using CZTS pellets which were synthesized from a solid state reaction between ZnS, Cu_2S and SnS_2 powders. In 2007, they annealed CZTS absorbers in a temperature of 300, 400 and 500 °C under N_2 atmosphere for 1h.

The highest efficiency of 1.74% was obtained from the sample annealed in a temperature of 500 °C (Moriya, Tanaka, & Uchiki, 2007). The same group was published a new research in 2008. At that time CZTS absorbers were annealed at a temperature of 500°C under 5% N_2+H_2S atmosphere for 1h. They obtained an efficiency of 0.64% for this device which was lower than the previous record. They claimed that the change in the compositional ratio was the reason of obtaining lower efficiency value (Moriya, Tanaka, & Uchiki, 2008). Moholkar *et al.* fabricated CZTS absorbers in a similar way with Moriya et al. The only difference was that, they annealed the CZTS films under N_2 + H_2S (5%) atmosphere at 400 °C. They obtained 3.14% efficiency for the film deposited for 30 min (Moholkar, Shinde, Babar, Sim, Lee, et al., 2011). In 2014 Nandur *et al.* were deposited CZTS absorbers on Mo coated SLG by using PLD technique from a stoichiometrically close CZTS target ($Cu_{2.6}Zn_{1.1}Sn_{0.7}S_{3.44}$). The effects of laser energy, substrate temperature, post-annealing on the surface morphology, composition and optical absorption were investigated. They recorded 5.85% conversion efficiency for the structure of SLG/ Mo/ CZTS/ CdS/ ZnO/ ITO solar cell (Nandur & White, 2014).

4.3.5. Chemical Vapor Deposition (CVD)

The CZTS thin films were deposited with chemical vapor deposition technique by Washio *et al.* in 2012. The oxide precursor thin films were sulfurized for 3h at the temperature between 520-560 °C in an N_2+H_2S (5%) atmosphere.

The best conversion efficiency of 6.03% was obtained for the CZTS with the composition ratio Cu/Zn+Sn= 0.78 and Zn/Sn= 1.29. The most important result of this research was that although the CZTS films had oxygen which was supported by the O-K_α peaks in EDS, the solar cells fabricated from these films were found to have 6.03% conversion efficiency (Washio et al., 2012).

4.3.6. Spray Pyrolysis

Spray pyrolysis is a low-cost process. The deposition rate depends on solvent material and the substrate temperature. Since this technique causes the small grain size (less than 100 nm), it has drawbacks for semiconductor applications. In 1996, Nakayama and Ito was used spray pyrolysis technique to grow CZTS films on soda lime glass substrates at the temperature range between 280 and 360°C for 90 min. The solution was prepared by CuCl, $ZnCl_2$, $SnCl_4$ and thiourea (as a sulfur source) chemicals and deionize water. Firstly, the as-deposited films were sulfur deficient. But after annealing for 2h under Ar+H_2S (5%) at 550 °C, stoichiometric CZTS films were obtained. From XRD analysis, the characteristic peaks of stannite structure were observed and the improvement in the crystallinity after heat treatment was encountered (Nakayama & Ito, 1996). They chose the substrate temperature of 320 °C for determining the influence of the zinc and copper concentrations in the solution on the electrical properties of the thin films. The influences of the spray time and the substrate temperature on the crystal structure of the CZTS films were researched by Kamoun *et al*. in 2007. For the film which substrate temperature 340 °C, they acquired the best results (Kamoun, Bouzouita, & Rezig, 2007). In 2009, Kumar *et al.* investigated the effect of substrate temperature in the range of 290 °C-450 °C on the growth of CZTS thin films by spray pyrolysis technique. The best film qualities were obtained from the films with the substrate temperatures between 370 °C–410 °C (Kumar, Babu, Bhaskar, & Raja, 2009).

In 2013, Vigil-Galán *et al.* deposited CZTS thin films on Mo coated soda lime glass substrates at different substrate temperatures by spray pyrolysis technique. During the spraying, Air, N_2 and Ar were used as a carrier gas. After the deposition, the samples were reactively sulfurized at 550 and 580 °C two different temperatures for 30 min. In order to get rid of Cu based secondary phase, the samples were exposed to 1% KCN for 2 min at room temperature.

SLG/Mo (500nm)/CZTS/CdS (60nm)/ZnO(50nm)/ZnO:Al (450nm) devices were constructed. For the films fabricated at 580°C, the Cu/Zn+Sn and Zn/Sn ratio were obtained 0.85 and 1.20 where the CZTS deposited under air atmosphere, 0.81 and 1.16 where the CZTS deposited under Ar atmosphere, respectively.

From the CZTS films annealed at 580 °C, the 1% efficiency was obtained from the film deposited under Ar atmosphere whereas 0.49% efficiency was get the deposited under air atmosphere (Vigil-Galán et al., 2013). Htay *et al.* compared the device performance of CZTS based solar cells by using CdS or ZnO buffer layers. CZTS absorbers were grown on Mo coated SLG substrate by spray pyrolysis technique. The photoconversion characteristic of SLG/Mo/CZTS/ZnO/Al:ZnO and SLG/Mo/CZTS/ CdS/ Al:ZnO device structures were examined. The efficiency of 4.29% and 4.32% were obtained for the devices with ZnO and CdS buffer layers, respectively (Htay et al., 2011).

4.3.7. Spin Coating

There are three main steps to follow for the fabrication of thin film by spin-coating technique. Firstly the precursor solution is prepared. Secondly, precursor solution is spin-coating the substrate to form the film and finally annealing the film under a certain atmosphere. In 2010, Todorov *et al.* used hydrazine based solution for CZTS based thin film fabrication. After hydrazine based solution was prepared, the Mo coated glass substrates were coated by spinning and then annealed at 540 °C. Three type of CZTS films were fabricated such as high selenium content, sulfoselenide, pure sulfide. For each case, films were prepared Cu-poor and Zn-rich composition. It was obtained the photo conversion efficiency 9.66% and 9.30% for sulfoselenide and selenium rich sample, respectively (Todorov et al., 2010). After that the same group using the hydrazine based solution fabricated sulfoselenide CZTS films by spinning on Mo coated glass substrates and then annealed at 500 °C. They decreased the thicknesses of CdS, ZnO and ITO to 25nm, 10nm and 50nm, respectively. They recorded the 12.6% efficient sulfoselenide CZTS solar cell by improving the coating uniformity and the film structure (Wang et al., 2014). This is the highest efficiency recorded for CZTSSe, so far. In 2014, Park *et al*. grown the CZTS thin film precursors by spin-coating technique on Mo coated SLG substrates. The spin-coated CZTS precursors were pre-annealed under atmospheric pressure at the temperatures of 250 °C, 300 °C, 350 °C and 400 °C for 5 min.

After annealing, the precursors were sulfurized using two-zone tubular quartz furnace under Ar atmosphere for 30 min. During the sulfurization, the sulfur zone was at 300 °C whereas the precursor zone was at 550 °C. The CZTS pre-annealed at 350°C with the atomic ratio of Cu/(Zn+Sn)= 0.72 and Zn/Sn= 1.12 showed the highest PV characteristic by having 5.29% efficiency (S.-N. Park et al., 2014).

4.3.8. Electrochemical Deposition

In 2008, Scragg *et al*. firstly fabricated and analyzed the CZTS thin films by using electrochemical deposition technique. The CZTS films were obtained by annealing of metallic precursor consisted of Zn/ Sn/ Cu/ Mo/ SLG stack in sulfur atmosphere at 550 °C for 2 hours. The solar cell constructed utilizing these films were found to have V_{oc} of 295 mV, J_{sc} of 8.7 $mAcm^{-2}$ and efficiency of 0.8% (Scragg, Dale, Peter, Zoppi, & Forbes, 2008). It was thought as a reason of low efficiency that the series resistance and shunt conductance were very high.

Jiang *et al*. obtained the metallic precursors by electrochemical deposition of Cu/Sn/Zn layers on Mo coated SLG substrates. The precursors were pre-annealed at 310 °C temperature for different time durations. After, the precursors were sulfurized by utilizing sulfur powder at 590 °C for 10min in borosilicate glass ampoule. The high quality CZTS film was obtained for the 200 min pre-annealing time. From that CZTS film, solar cell with a device structure of Al/ITO/i-ZnO/CdS/CZTS/Mo/glass was fabricated. This is the highest performing solar cell with 8.1% efficiency whose absorber layer was deposited by electrochemical deposition technique (Jiang et al., 2015).

The summary of the highest efficiency CZTS thin film solar cells with respect to utilized deposition techniques is given with Table 4.2.

Table 4.2. The highest efficiency record of CZTS thin film solar cell with respect to deposition techniques.

Technique	V_{OC} (mV)	J_{SC} (mA/cm^2)	FF (%)	η (%)	References
Sputtering	700	21.3	63.0	9.40	(Tajima et al., 2017)
Pulsed Laser Deposition	376	38.9	40.0	5.85	(Nandur & White, 2014)
Chemical Vapour Deposition	658	16.5	55.0	6.03	(Washio et al., 2012)
Spray Pyrolysis	620	15.5	45.0	4.32	(Htay et al., 2011)
Spin Coating	558	18.5	51.2	5.29	(S.-N. Park et al., 2014)
Electrochem. Deposition	705	18.0	63.2	8.10	(Jiang et al., 2015)

4.4. The Role of Point Defects in Stoichiometry of CZTS

CZTS has many advantages to use as an absorber thin film photovoltaic solar cells due to its earth abundant, nontoxic and low cost properties. CZTS has a direct bandgap of 1.45-1.50 eV and absorption coefficient higher than 10^4 cm^{-1} which are convenient for thin film photovoltaic applications (Delbos, 2012). Its *p*-type semiconductor behavior comes from its intrinsic point defects which is a result of stoichiometry changes. There are different opinions about which defect provide the dominant acceptor level (Shin, Saparov, & Mitzi, 2017). Since the number of constituents in quaternary CZTS is much, this promotes the expected point defects in the lattice and more defect-induced energy levels in the electronic band gap. In theory, 24 distinct point defects can be generated by kesterite based CZTS compounds. Nevertheless, cation-on-anion and anion-on-cation anti-site defects does not take form simply because of the huge difference in charge state and electronegativity. It was proposed that the point defects in the form of cationic substitutions are associated with off-stoichiometry in CZTS (Ito, 2014). Four distinct types of substitutions were performed which produced some point defects. It is observed in A-type formation of V_{Cu} and Zn_{Cu} and B-type formation of Zn_{Cu} and Zn_{Sn} for Cu-poor and Zn-rich CZTS whereas C-type formation of Cu_{Zn} and Sn_{Zn} and D-type formation of Cu_{Zn} and Cu_i for Cu-rich and Zn-poor CZTS.

All of these substitutions are demonstrated in Figure 4.1. and also summarized in Table 4.3. The experimental results for high-efficient CZTS-based thin-film solar cells

which are in Cu-poor (Cu/(Zn+Sn)~0.8-0.9) and Zn-rich (Zn/Sn~1.1-1.2) stoichiometry stand for the A or B-type substitution mechanism (Ito, 2014).

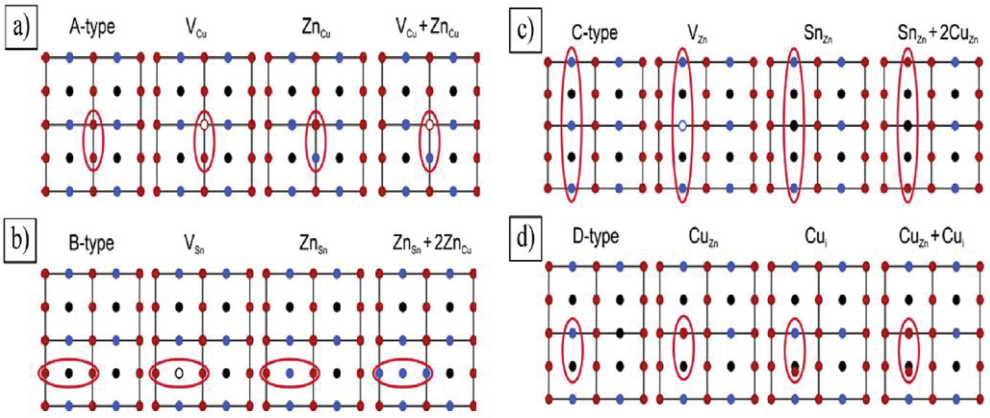

Figure 4.2. The form of a) A-, b) B-, c) C- and d) D-type non-stoichiometric CZTS resulted from cation substitution process. Within the circles copper, zinc and tin atoms are represented in red, blue and black spheres, respectively (Source: Rios, Neldner, Gurieva, & Schorr, 2016).

Table 4.3. The classification of cation substitution types with related non-stoichiometry types and cation substitution reactions (Source: Rios et al., 2016).

Type	Composition	Cation substitution reaction	Intrinsic point defects
A	Cu-poor/Zn-rich/Sn-const.	$2Cu^{+} \rightarrow Zn^{2+}$	$V_{Cu} + Zn^{2+}{}_{Cu}$
B	Cu-poor/Zn-rich/Sn-const.	$2Cu^{+} + Sn^{4+} \rightarrow 3Zn^{2+}$	$2Zn^{2+}{}_{Cu} + Zn^{2+}{}_{Sn}$
C	Cu-rich/Zn-poor/Sn-rich	$3Zn^{2+} \rightarrow 2Cu^{+}+Sn^{4+}$	$2Cu^{+}{}_{Zn} + Sn^{4+}{}_{Zn}$
D	Cu-rich/Zn-poor/Sn-const.	$Zn^{2+} \rightarrow 2Cu^{+}$	$Cu^{+}{}_{Zn} + Cu^{+}{}_{i}$

According to defect formation energy calculations in Figure 4.3., some of point defects such as four vacancies (V_{Cu}, V_{Zn}, V_{Sn} and V_S), three interstitials (Cu_i, Zn_i and Sn_i), and six anti-sites (Cu_{Zn}, Cu_{Sn}, Zn_{Cu}, Zn_{Sn}, Sn_{Cu} and Sn_{Zn}) are energetically possible to form.

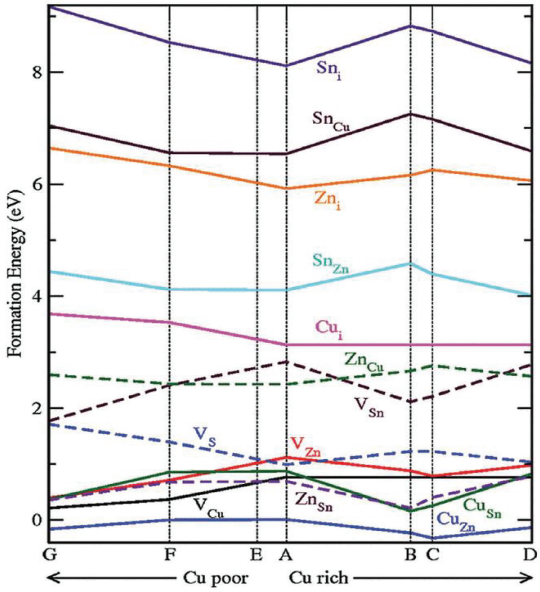

Figure 4.3. Formation energy distribution of point defects in Cu_2ZnSnS_4 as a function of Cu-rich and Cu-poor conditions (Source: Shin et al., 2017).

Between these point defects, V_{Cu}, V_{Zn}, V_{Sn}, Cu_{Zn}, Cu_{Sn} and Zn_{Sn} are negatively charged point defects which possess acceptor-like transition-energy levels in the electronic structure, whereas Zn_{Cu}, Sn_{Cu}, Sn_{Zn}, Cu_i, Zn_i, Sn_i and V_S are positively charged point defects which show donor-like transition-energy levels. In the case of Cu-poor conditions, V_{Zn}, Cu_{Sn} and Zn_{Sn} are the acceptor defects having a comparatively high formation energy. In contrast, due to the fact that Cu_{Zn} antisite and V_{Cu} have comparatively low formation energies between all possible intrinsic defects, it is more likely to encounter these point defects (Shin et al., 2017). As seen in Figure 4.4., in the energy band gap of a photovoltaic material, the formation of ionization energy levels are stimulated by intrinsic point defects. The generation probability of each defect directly associates with the formation energy of it which is affected by the chemical potential of the ingredient elements.

When the density of point defects are in adequate, localized levels at the edge of the conduction (and/or valence) band might be seen in the electronic band gap and interact to form a band. This band can combine with the conduction (and/or valence) band, and thus adjust the band structure. It was calculated that Cu_{Zn} and V_{Cu} in CZTS have the transition energy level 100 and 10 meV above the valence band maximum (VBM), respectively (Shin et al., 2017) which can be explained by the fact that the *p*−*d* coupling for Cu_{Zn} is increased, whereas it is decreased for V_{Cu} (Chen, Gong, Walsh, & Wei, 2010).

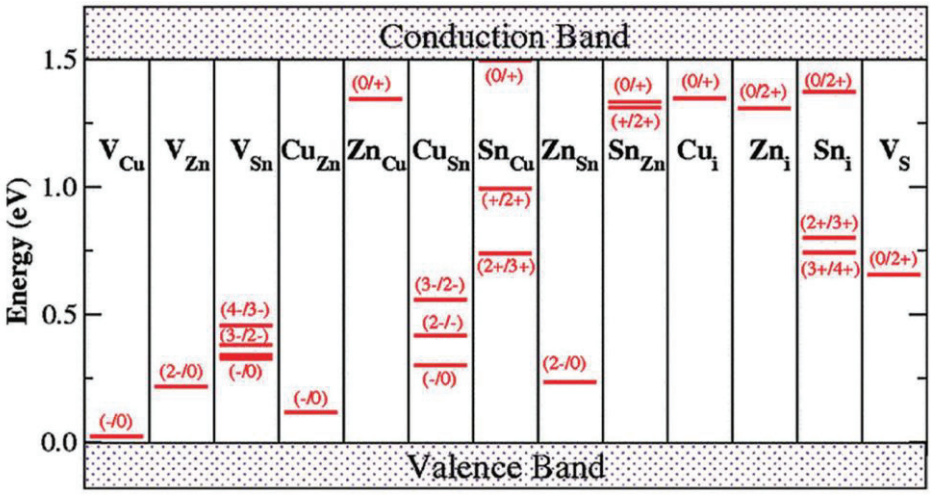

Figure 4.4. Transition energy levels belonging to intrinsic defects within the bandgap of CZTS (Source: Shin et al., 2017).

This means that V_{Cu} possess the shallowest acceptor level between the low energy intrinsic defects. Consequently, CZTS film has a p-type semiconductor's behavior and its resistivity is sensitive to Cu content. The more point defects, the more formation of defect-induced energy levels in the CZTS band gap. Between all point defects, the Cu_{Zn} and V_{Cu} which is assumed to induce the *p*-type conductivity is the most favourable defect because of having the lowest formation energy over the related chemical potential range) (Ito, 2014).

4.5. Detrimental Phase Identifications

High quality CZTS based thin film photovoltaic devices need a single phase kesterite absorber. However, the growth of pure kesterite phase without any secondary phase is difficult because of comparatively having low thermal stability and narrow single phase region of the compound. Removal or control of secondary phases is a very important point in the yield of solar cells. They can form at the interface or within the bulk and are an important problem preventing the theoretically calculated yield value from being reached. There are two reasons for the formation of secondary phases.

The first is the separation of the components of the synthesized kesterite structure during heating. Another cause of the presence of secondary phases is components that remain during the synthesis of film in the kesterite structure.

It has been proven that Sn loss in CZTS films during annealing causes the formation of secondary phases due to the low melting point (231.9 °C) of Sn element. For example, binary chalcogens do not come together to form a kesterite structure with other components (Yoo et al., 2015). Secondary phases have several effects (i.e. decrease the open-circuit voltage and photocurrent) on photovoltaic device performance.

Firstly, if the secondary phase has a wider band gap than the absorber material, the volume of absorber material and along with short circuit current are decreased. The band alignment between CZTS and the secondary phase is another important point. The trapping of charge carriers within the smaller band gap semiconductor results a type- I band alignment. In the case of type I band alignment as shown in Figures 4.5. (a) and (b), the conduction band minimum (CBM) of the secondary phase is higher (or lower) than that of CZTS, and the valence band maximum (VBM) of the secondary phase is lower (or higher) than that of CZTS. Type I band alignment bases on whether the band gap of the secondary phase is larger or smaller than that of CZTS.

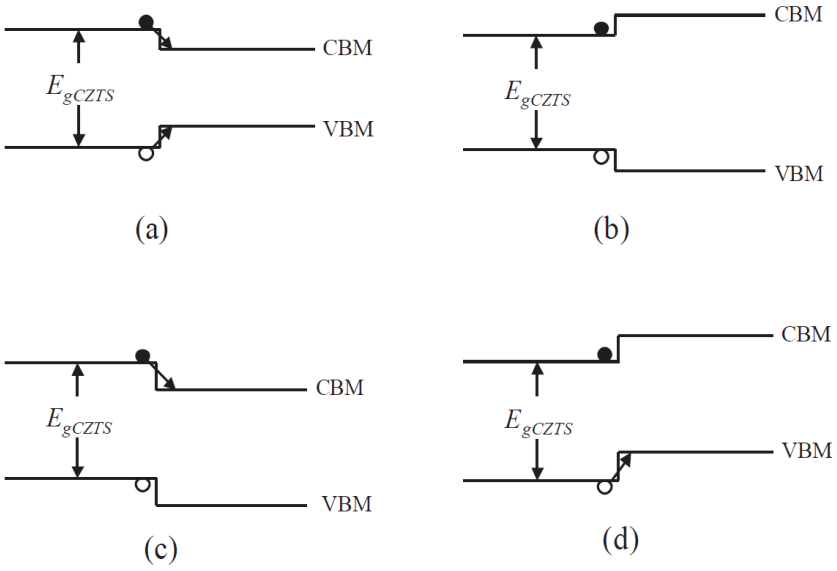

Figure 4.5. The possible band alignments at heterointerfaces between CZTS and secondary phases type I heterointerface a) with $E_g^{s.f.} < E_g^{CZTS}$ and b) with $E_g^{CZTS} < E_g^{s.f.}$, type II heterointerface with CBM and VBM in the secondary phase c) lower than that of CZTS, d) higher than that of CZTS (Source: Bao & Ichimura, 2015).

When the bandgap of secondary phase is smaller (Figure 4.5. (a)), it will ease the carrier recombination with acting as a sink for minority and majority charge carriers.

Therefore, the splitting of charge carrier is prevented and the carrier collection of the cell could be decreased. If the band gap of secondary phase is larger than that of CZTS (Figure 4.5. (b)), the band offset forms as a barrier for both of the minority and majority carriers in CZTS. Subsequently, the secondary phase just decreases the conductivity but does not enhance carrier recombination rate in the absorber layer.

On the one hand, type-II heterointerfaces act resistive barriers for one carrier type (electrons or holes) and potential wells for the other carrier type. In the case of type II band alignment as shown in Figures 4.5. (c) and (d), both of CBM and VBM for the secondary phase are lower or higher than that of CZTS. When the type II band alignment, the secondary phase behaves as a sink for only one type of carrier which means that the electrons and holes tend to be splitted. The position of the secondary phase within the absorber layer will be important providing that the interface is a resistive barrier to the minority carrier electrons in p-type CZTS. Within the space charge region, the precipitated secondary phase should act a high resistive barrier to enhance the shunt resistance of the device. However, within the quasi-neutral region the precipitated secondary phase should act low resistive barriers in order to reduce series resistance and the detrimental effects on carrier separation (Mendis et al., 2012). Thirdly, the existence of lattice mismatch between absorber layer and the secondary phase will cause interface states within the band gap which give rise to a shorter carrier lifetime.

Table 4.4. The bandgap of expected secondary phases.

Compound	Bandgap (eV)	Electric Properties	Source
Cu_2ZnSnS_4	1.5	p-type semiconductor	(Yazici et al., 2015)
Cu_2SnS_3	1.0	p-type semiconductor	(Baranowski, Zawadzki, Lany, Toberer, & Zakutayev, 2016)
ZnS	3.7	Insulator	(Bao & Ichimura, 2015)
SnS_2	2.5	n-type semiconductor	(M. Kumar, Dubey, Adhikari, Venkatesan, & Qiao, 2015)
SnS	1.0 indirect, 1.3 direct	p-type semiconductor	(Guneri et al., 2010)
Cu_2S	1.2	p-type semiconductor, metal like, highly defective	(Riha et al., 2013)

Due to the confusion of the quadruple material system, many binary and ternary sulfides, Zn_xS, Cu_xS, Sn_xS and Cu_xSnS phases, can be formed easily during the growth of CZTS films. The formation conditions of expected secondary phases and related bandgap values are given in Table 4.4. The details of formation mechanism will be given in the section 4.6.1.

Cu_2S: Copper sulphate compounds especially form in the case of Cu-rich, Zn-poor and Sn-poor conditions. They are semiconductors with low bandgap (1.2 eV) and a high absorption coefficient. Because of having metallic behavior, they can lead to shunt the solar cell. The small Cu_2S crystals behave like traps for holes and electrons and result the increment of recombination. To avoid this undesirable secondary phase, the CZTS sample is exposed to chemical etching by immersing in KCN (potassium cyanide) chemistry. As a result of this process, some inclusions or pin holes may form and result the additional problem for the absorber.

ZnS: Zinc sulphate secondary phase occurs in Sn and Cu-poor, Zn-rich regions. Due to the very high bandgap (~ 3.60 eV), it is insulative, causing the active region in the structure to shrink and block the flow of current in the absorber layer. It is detectable if exist on the surface of the absorber layer by near-resonant Raman scattering (Fairbrother et al., 2014). HCl at a temperature of 75 ° C with a concentration of 5-10% is the most suitable mixture to remove the ZnS secondary phase (Marchionna et al., 2013).

Cu_2SnS_3: It is assumed that Cu_2SnS_3 (CTS) is a tetrahedrally bonded structure as CZTS absorber (Baranowski et al., 2016) and form in Zn-poor conditions Cu_2SnS_3 has a bandgap (~1.0 eV) lower than the desired for single junction photovoltaic (Baranowski et al., 2016), they have metallic properties similar to the copper secondary phases, therefore they can increase the recombination or shunt the cell according to their amount and grain size (Wu et al., 2007).

The Cu_2SnS_3 phase can have cubic, tetragonal, monoclinic, triclinic, and hexagonal crystal structures. In order to remove Cu_2SnS_3, Bromine in a methanol solution (Br_2/MeOH) is used for etching (Wei, Newman, Tsoi, & Watson, 2016).

SnS_2: The tin sulphate is a secondary phase that occurs in the tin-rich and copper-poor conditions. It is an n-type semiconductor with band gap energy of 2.2 eV. This secondary phase which appears in the CZTS structure may casuse high photocarrier recombination by acting as an insulator or may form secondary diode inside the CZTS by acting as a semiconductor (M. Kumar et al., 2015).

The other secondary phases which observed in CZTS solar cells are SnS and Sn_2S_3. They have different properties from SnS_2. SnS is a p-type semiconductor with a direct band gap of 1.2-1.5 eV and an indirect band gap of 1.0-1.2 eV (Guneri et al., 2010). Due to having low band gap, SnS can cause a reduction in open circuit voltage. It was found that $(NH_4)_2S$ is used to remove SnS secondary phases (Wei et al., 2016). Based on the Sn and S defects, Sn_2S_3 has a mixed phase with a direct band gap of 0.97 eV and an indirect band gap of 0.82 eV (Singh, 2016). Table 4.5. gives the relation between the composition and formation of secondary phases.

Table 4.5. Different compositions and related secondary phases (Source: Scragg, 2010).

Composition description	Expected secondary phases
Cu-poor	$Cu_2ZnSn_3S_8$ + ZnS
Sn-rich	$Cu_2ZnSn_3S_8$/ SnS
Zn-poor	Cu-Sn-S + $Cu_2ZnSn_3S_8$ / Cu_2S
Cu-rich	Cu_2S
Sn-poor	Cu_2S, ZnS
Zn-rich	ZnS

As mentioned above, all secondary phases have different effects on solar cell performance. Actually, it is strongly depend on the band alignment between secondary phase and CZTS. Therefore, it is important to determine that the interface between secondary phase and the absorber is Type I or II which effect the solar cell performance.

Bao *et al.* have theoretically investigated the band alignment type between CTS/CZTS and ZnS /CZTS interface (Bao & Ichimura, 2015). They reported the result on the influence of ZnS and CTS secondary phases in CZTS absorber material by determining the band offsets using first principles calculation. For both interface, the valence band offset (ΔE_V) values were calculated. For the CTS /CZTS interface $\Delta E_V^{CTS/CZTS}$ value was calculated as a positive value which indicates that VBM of CTS is higher than that of CZTS. Similarly, for the ZnS/CZTS interface $\Delta E_V^{ZnS/CZTS}$ value was calculated as a positive value which indicates that VBM of CZTS is higher than that of ZnS. The results showed that the band alignment of ZnS/CZTS interface represents type I with large spike (>0.8 eV) for both the conduction and valence bands which create a high resistance barrier to carrier flows.

Therefore, ZnS secondary phase might prevent the flow of photo-generated carriers (electrons) and result the reduction of photo current. It also may hinder the flow of majority carriers (holes) and lead to increase the series resistance (Bao & Ichimura, 2015). Because ZnS can repel both the carriers, it can have low recombination rate. Base on this fact it can be said that in the case ZnS cover the surface or boundary of CZTS grains, recombination at the surface/boundary can be controlled. As seen in Figure 4.6. VBM of both CTS and CZTS are formed as a result of interaction between S *3p* and Cu *3d* orbital, and CBM is consisted of S *3p* and Sn *5s* orbitals (Bao & Ichimura, 2015). CTS is considered as a cluster of (Sn_{Zn} + $2Cu_{Zn}$) defect pairs in CZTS. This defect pair can move the VBM upward whereas the Cu_{Zn} antisite increases the p-d repulsion and move the CBM downward due to the wavefunction of CBM are localized on the more electronegative Sn sites by the formation of Sn_{Zn} (Chen, Yang, Gong, Walsh, & Wei, 2010; Zhai et al., 2011). Since CBM and VBM are staying within the forbidden energy region of CZTS, CTS/CZTS interface has type I band alignment which allow both minority and majority carriers flowing from CZTS to CTS. Therefore, CTS phase in CZTS will decrease the output current and voltage by acting as a recombination center. The results showed that, ZnS is being more preferable than CTS secondary phase. Although Zn-rich composition will cause the formation of highly resistive ZnS, the presence of CTS phase has absolutely more detrimental effect on the solar cell performance (Bao & Ichimura, 2015). With another aspect, due to the lattice constants of ZnS (0.541 nm) and CZTS (a = 0.551 nm) are close to each other, the interface will not contain high density of defects (Bao & Ichimura, 2015). Therefore, the CZTS/ZnS interface is expected to own a low recombination velocity (Mendis et al., 2012).

Nagoya et al. and Maeda et al. also predicted that the ZnS was the dominant impurity phase in theory when the copper-poor and zinc-rich (Maeda, Nakamura, & Wada, 2011; Akihiro Nagoya, Asahi, Wahl, & Kresse, 2010).

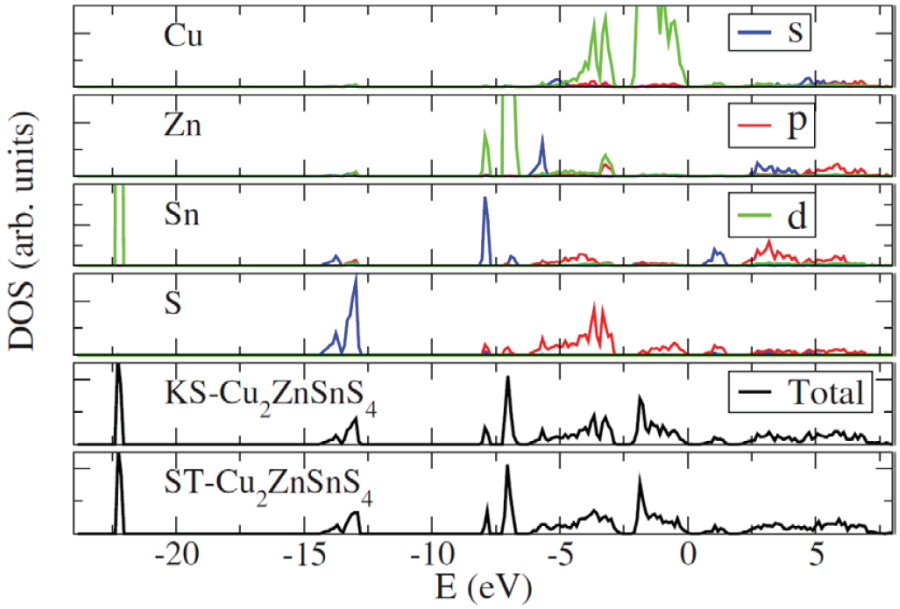

Figure 4.6. The DOS of partial KS structure as well as total KS and ST structures (Source: Chen, Gong, Walsh, & Wei, 2009).

The ZnS secondary phase has a wider band gap (3.7 eV) and generally has lower conductance. Therefore, it cannot be assumed that ZnS is responsible for the drop of open-circuit voltage or shunt resistance. However, ZnS causes high series resistance of solar cell. However, several other secondary phases such as SnS, CuS or Cu-Sn sulfide have different crystal structures from tetragonal CZTS (e.g., Cu_2S is monoclinic at room temperature while CuS is hexagonal) (Mendis et al., 2012). Therefore, they form incoherent interfaces with high recombination velocities so they are considered to be more harmful. Because these phases have lower band gap and higher conductivity, they reduce the open circuit voltage and shunt resistance and cause the cell to have very low photovoltaic performance. Because of having similar crystal structure of some secondary phases, it is difficult to differentiate all secondary phases mentioned in Table 4.5. by XRD technique. Based on the XRD sensitivity, by looking the existence of their most intense peaks, it can be identified the presence of Cu_2S (45.8°) (Cheng et al., 2011), CuS (31.8°) (Cheng et al., 2011), SnS (31.53°) (JCPDS 039-0354), SnS_2 (15.02°) (JCPDS 023-0677), Sn_2S_3 (21.49°) (JCPDS 014-0619), Cu_3SnS_4 (27.31°) (Fernandes, Salomé, & Da Cunha, 2010) and Cu_4SnS_6 (29.58°) (JCPDS 036-0053). Since their most intense peaks are not overlap with CZTS peaks. The Figure 4.7. demonstrates the XRD pattern of the some secondary phases.

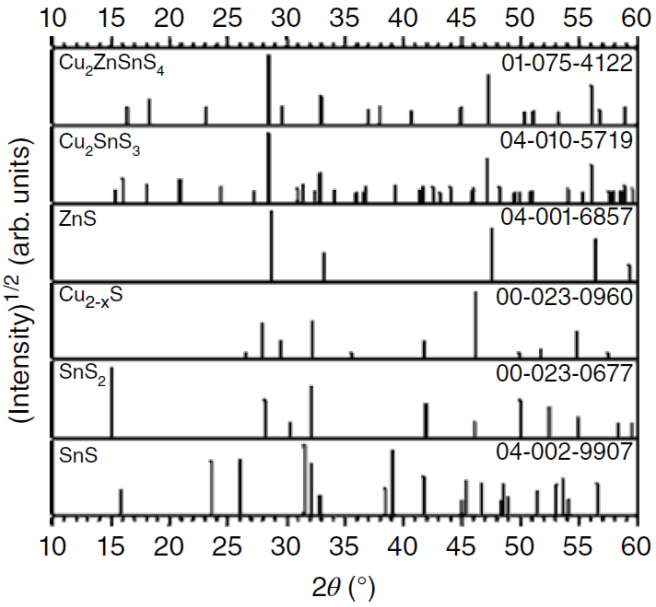

Figure 4.7. XRD peak positions of the most observed secondary phases with respect to ICDD database whose number is given in figure (Source: Ito, 2014).

On the contrary to XRD, the Raman spectroscopy is more useful to the detection of secondary phases in the CZTS absorber. Figure 4.8 shows all characteristic Raman peaks of CZTS sample as well as Table 4.6. summarizes the Raman shift of secondary phases. When the Figure 4.8. and Table 4.6. are compared, it is observed that the main vibrational peaks of ZnS and tetragonal Cu_2SnS_3 are very close to CZTS characteristic peaks. By using the laser having the energy in the infrared region, it can be difficult to clearly determine these coexistence of ZnS and CTS phases with CZTS (Malerba, 2014).

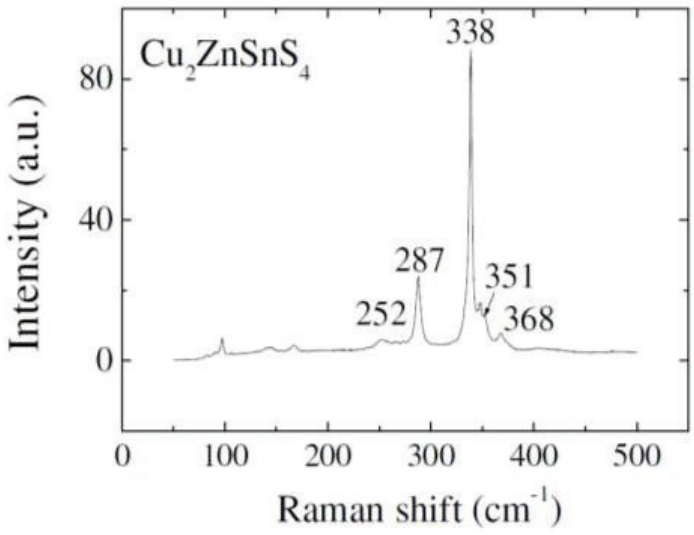

Figure 4.8. The characteristic Raman peaks of kesterite CZTS sample.

Table 4.6. Raman shift (cm^{-1}) of possible binary and ternary phases (Sources: Fernandes et al., 2010; Vigil-Galán et al., 2013).

SnS	SnS_2	Sn_2S_3	ZnS	Cu_2S	Cu_2SnS_3 Tetra.	Cu_2SnS_3 Cubic	Cu_3SnS_4 Ortho.
96	215	36-52	275	19	336-337	267	295
163	202	60-71	348-352	62-65	351	303	318
189	315	87-183	419	112/142	297	355-356	348
220	-	234-251	-	267	-	-	-
288	-	307	-	475	-	-	-

4.6. Properties of CZTS

4.6.1. Formation Mechanism of CZTS

At the early stage of sulfurization due to the penetration of sulfur atoms through the solid surface sulfide phases form. During the CZTS formation there are two ways to form CZTS absorber. In the first way, the CZTS is formed as a result of the reactions between the binary phases of Cu_2S, ZnS and SnS_2 which is given in equation 4.1.

The second way of the formation of CZTS is the reactions between these binary and ternary phases. The reaction between Cu_2S and SnS_2 form Cu_2SnS_3 (CTS) phase (Eq. 4.2.) and then the reaction between Cu_2SnS_3 and ZnS form CZTS (Eq. 4.3.).

$$Cu_2S+ZnS+SnS_2 \rightarrow Cu_2ZnSnS_4 \ (>350–400°C) \quad (4.1)$$

$$Cu_2S+SnS_2 \rightarrow Cu_2SnS_3 \ (>350–400°C) \quad (4.2)$$

$$Cu_2SnS_3+ZnS \rightarrow Cu_2ZnSnS_4 \ (>350–400°C) \quad (4.3)$$

4.6.2. The Crystal Structure of CZTS

The quaternary chalcogenide compound CZTS has three crystal structures kesterite (KS; *I*4 space group; no. 82), stannite (ST; *I*-42m space group; no. 121) or primitive mixed Cu-Au (PMCA; *P*42m space group; no. 111) (Khare, Himmetoglu, Johnson, et al., 2012). In Figure 4.9. all possible crystal structures of CZTS are presented. Although KS and ST structures both have body-centered tetragonal symmetry with eight atoms per primitive cell, the only difference between them is the placement of Cu and Zn atoms at the corners of tetragonal symmetry.

In addition, the bond characters are the same for KS and ST structures where each S atom is surrounded by two Cu, one Zn, and one Sn atoms. KS structure is described by series layers of Cu-Sn, Cu-Zn, Cu-Sn and Cu-Zn at z=0, ¼, ½ and ¾, respectively. Therefore one copper holds the 2a (0, 0, 0) position with zinc and the leftover copper orders at 2c (0, ½, ¼) and 2d (0, ½, ¾). The formation energy of the ST structure is higher than that of the KS structure, and as a result, KS is a more stable crystalline structure. As theoretically predicted, the probability of formation in the KS structure is higher than ST.

However, the fact that the band gap of the KS structure is 0.12 eV higher than that of ST which makes it necessary that the desired structure for solar cell production is the KS structure. And also the binding energy difference between KS and ST structures is 3 meV/atom (Valakh et al., 2013).

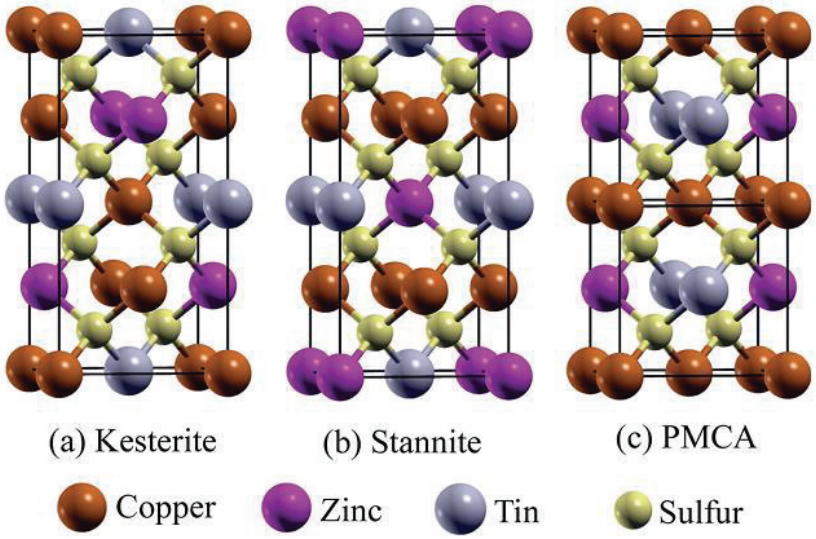

Figure 4.9. Unit cells of CZTS thin film a) Kesterite, b) Stannite, c) PMCA (Source: Khare, Himmetoglu, Johnson, et al., 2012).

Sometimes because of the antisites relates with Cu and Zn atoms, the disorder in KS structure can be observed. The existence of partially disordered kesterite structure is reported by using neutron scattering (Scragg, 2010). In the disordered KS structure the Cu and Zn atoms are randomly placed on their shared lattice plane. The occupation of lattice sites by Cu or Zn atoms in this lattice plane have equal probability which implies that disordered KS has structure close to stannite. Figure 4.10. demonstrates the KS, disordered KS and stannite crystal structures along (100) direction. The crystallinity, crystallite size, residual stress and lattice strain can be obtained by XRD. The grain size is inversely proportional with the full width at half maximum (FWHM) value of the peaks. With the help of Debye Scherer formula, it is possible to determine the grain size. The peak broadening bases on residual stress which can change the spacing between crystallographic planes in a sample.

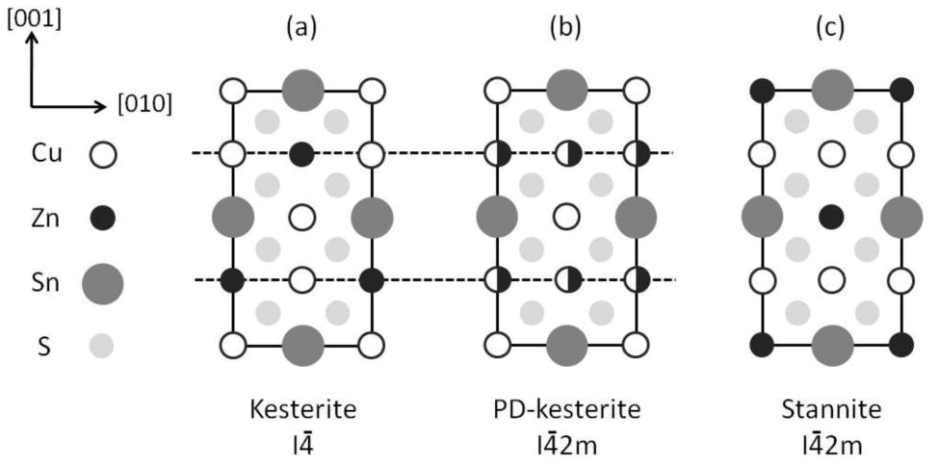

Figure 4.10. Demonstration of (a) kesterite, (b) partially-disordered kesterite and (c) stannite crystal structures. Note that the dotted line in (b) indicates the planes of Cu-Zn disorder (Source: Scragg, 2010).

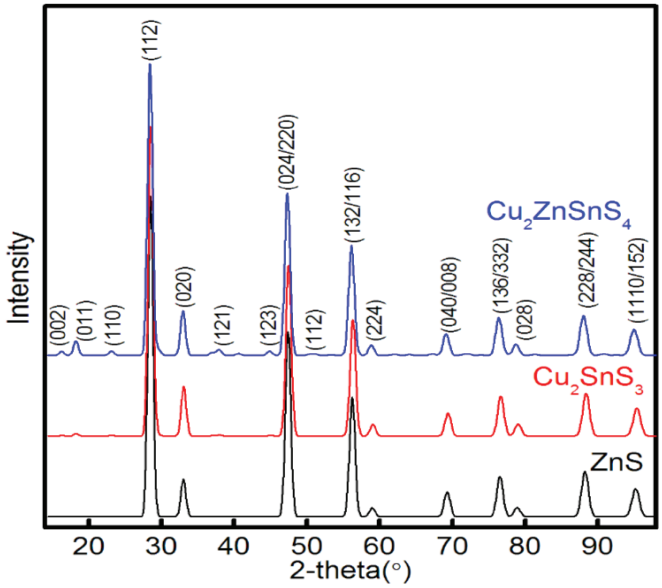

Figure 4.11. XRD patterns of kesterite CZTS, CTS and ZnS (Source: Khare, 2012).

Thus, the diffraction peak positions can be shifted by these considerations. The peaks are shifted to lower 2θ-values by tensile stress whereas they are moved to higher 2θ-values by compressive stress. In the case that both types of strain are observed at the same time, this results the broadening of the diffraction peaks. Despite the fact that XRD is an effective technique to determine the crystal structure of examined film, for CZTS it is not adequate when used alone. Because of having very similar lattice constants, there is a problem with peak overlapping when analyzing kesterite CZTS, ZnS and Cu_2SnS_3 (CTS).

The match in diffraction patterns of KS CZTS, monoclinic CTS and cubic ZnS are shown in Figure 4.11. Also in order to illustrate XRD peak positions of these phases are summarized in Table 4.7.

Table 4.7. XRD reflection positions of CZTS and some secondary phases (Source: Fernandes, Salomé, & Da Cunha, 2011).

CZTS		**Cubic Cu_2SnS_3**	**Tetragonal Cu_2SnS_3**	**Cubic ZnS**
2θ (°)	hkl	2θ (°)	2θ (°)	2θ (°)
28.44	112	28.45	28.54	28.50
32.93	200	32.96	33.07	33.03
33.02	400	-	-	-
47.33	204	47.31	47.47	47.40
56.09	312	56.13	56.32	56.24
56.20	116	-	-	-
76.41	332	76.39	76.68	76.56

4.6.3. Pseudo-Ternary Phase Diagram of Cu-Zn-Sn-S System

In order to understand the formation of a quaternary compound of Cu_2ZnSnS_4, it is necessary examining the ternary system consisted of Cu-Zn-Sn-S (Olekseyuk, Dudchak, & Piskach, 2004). The Figure 4.12. shows the pseudo-ternary phase diagram of the Cu-Zn-Sn system where the S is assumed to be exist in stoichiometric amount. The single phase CZTS forms in narrow range of phase diagram which is represented by red dot. Since CZTS has a narrow single phase region, it means that there is very low tolerance to the existence of cation deficiencies (Ito, 2014).

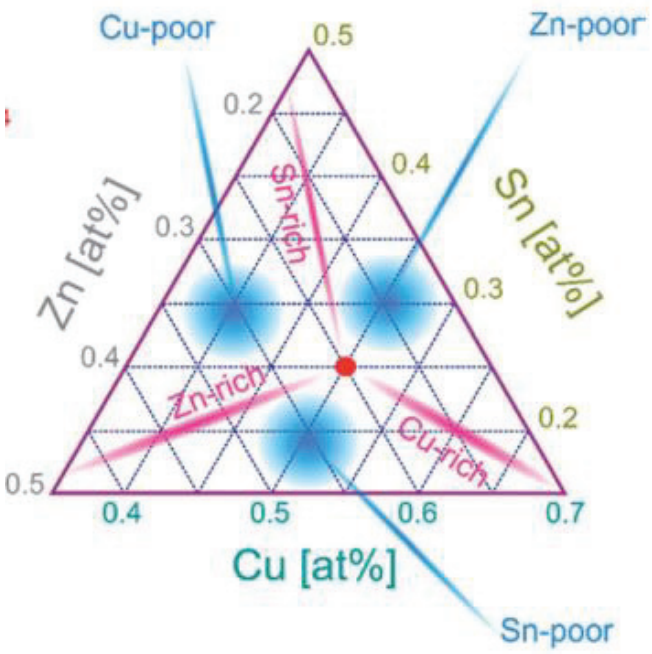

Figure 4.12. Ternary phase diagram of the Cu-Zn-Sn-S system, assumed that the S amount is stoichiometric. The red dot represents the single phase CZTS (Source: Kaur, Kumar, & Kumar, 2017).

4.6.4. Raman Analysis of CZTS

Raman spectroscopy which is a non-destructive technique is used to determine the disorder in the structure, existence of secondary phases, stress, compositional and phonon confinement effects in CZTS semiconductor (Himmrich & Haeuseler, 1991). The light penetration depth (d) and absorption coefficient (α) relation of any semiconductor is given by $d=1/\alpha$. However, using back scattering configuration when Raman scattering analysis is done, it is considered that because the light should be turn back the penetration depth relation should be $d=1/2\alpha$. With Figure 4.13., it is demonstrated the behavior of direct bandgap semiconductor having absorption coefficient below $4.0*10^4$ cm^{-1} (Fernandes et al., 2011).

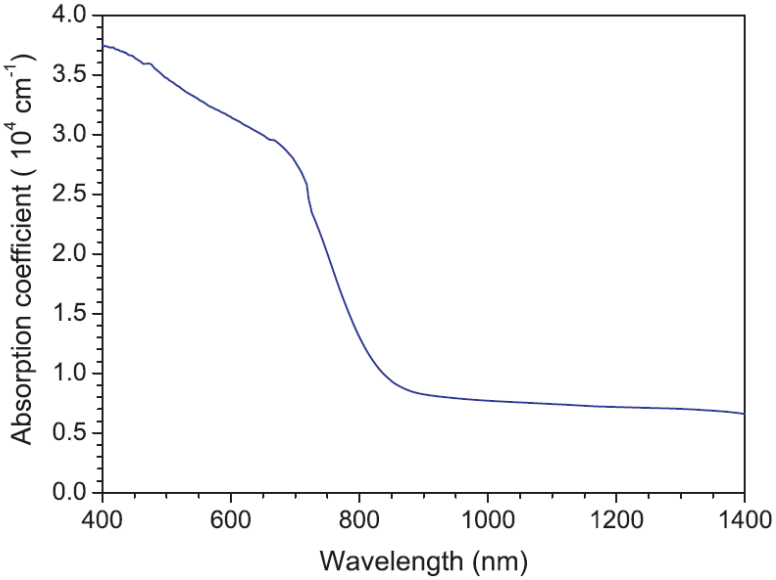

Figure 4.13. Wavelength distribution of absorption coefficient for the CZTS thin film under study (Source: Fernandes et al., 2011).

The 488, 514 and 633 nm are commonly used laser wavelengths with the penetration depths of 140, 150 and 170 nm, respectively. Yet, when the wavelength of 785 nm is used, it is possible to reach a depth of 400 nm (Fernandes et al., 2011). As mentioned before, CZTS forms in the KS, ST, or PMCA structures where the bandgap and electron affinity value difference between them are 0.15 eV. Due to this low difference, it is possible to be observed the mixture of these three crystal structures in the same CZTS absorber which limiting the power conversion efficiency of solar cell by trapping of charge carriers in domains. Therefore, high efficient solar cell should consist of a single CZTS phase. In solids, the dispersion of phonon is susceptible to the coupling between the atoms within the lattice. Therefore, KS, ST and PMCA structures can be distinguished with respect to variation of phonon distribution within these structures. In order to determine this dispersion, Raman spectroscopy can be used. Raman spectroscopy is a suitable and widely used technique due to its availability to observe the Raman scattering at frequency associated with the phonon modes at the Γ point.

In 1991, the first Raman spectroscopic studies were fulfilled for the A_2BCX_4 type compounds where **A** = Cu, Ag; **B** = Zn, Cd, Hg, Mn, Fe, Co; **C** = Si, Ge, Sn; **X** = S, Se (Himmrich & Haeuseler, 1991). For the A_2BCX_4 compounds with stannite type structure, they obtained the results from the unit cell group analysis (k=0) as $\Gamma=2A_1\oplus A_2\oplus 2B_1\oplus 4B_2\oplus 6E$. B_2 and E modes have a total of 10 vibrations of IR active,

whereas A_1, B_1, B_2 and E modes have a total 14 vibrations of Raman active (Himmrich & Haeuseler, 1991).

Raman active optical modes of CZTS for the stannite structure was firstly reported at 285, 336 and 362 cm^{-1} by Himmrich and Haeuseler (Himmrich & Haeuseler, 1991). The vibrational properties of CZTS for both KS and ST structures were calculated in theoretically with density functional theory (Gürel, Sevik, & Çağın, 2011). Because of that CZTS has eight atoms per primitive cell, 24 vibration modes are formed. The three of them are acoustic modes which equal to zero at the zone center.

For the KS structure, the Brilloun-zone-center phonon modes are given as optical and acoustic with $\Gamma_{op} = 3A \oplus 6B \oplus 6E$ and $\Gamma_{ac} = 1B \oplus 1E$, respectively. Likewise, for the ST structure optical and acoustic phonon modes are given with $\Gamma_{op} = 2A_1 \oplus 1A_2 \oplus 2B_1 \oplus 4B_2 \oplus 6E$ and $\Gamma_{ac} = 1B_2 \oplus 1E$, respectively. Among these phonon modes, A, B, A_1, A_2, B_1, and B_2 are nondegenerate whereas E modes are two-fold degenerate. In the KS structure, B and E modes are both infrared (IR) and Raman active, whereas A mode is solely Raman active. In the ST structure, B_2 and E modes are both infrared (IR) and Raman active, whereas A_1 and B_1 are merely Raman active. Since the A_2 mode of ST structure does not show both IR and Raman active, therefore, it is named the silent mode. A mode of KS, and the A_1 and A_2 modes of ST structures are formed by the vibrations of the anions. For the B_1 modes of ST structure while half of the Cu atoms move to positive z-axis, the Cu atoms left move to opposite direction. The Zn and Sn atoms are fixed in the position, the vibration of anions occurs solely in the xy plane. The vibration of cations occurs along the Z axis for the B modes of KS structure and for the B_2 modes of ST structure. For the E modes of KS and ST structures, the movement of cation occurs only within the xy plane (Gürel et al., 2011). Figure 4.14. demonstrates the atomic distribution of each vibration modes of KS and ST structures. Table 4.8. summarizes the work conducted by Gurel *et al.* on the phonon frequencies and related mode symmetry for KS and ST structures of CZTS (Gürel et al., 2011).

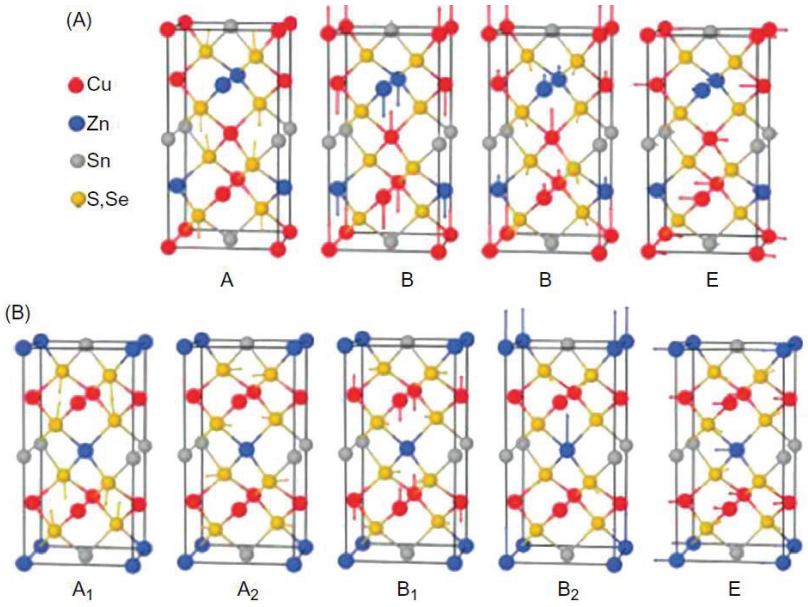

Figure 4.14. Atomic distribution of each possible vibration modes of a) Kesterite, b) Stannite structures (Source: Gürel et al., 2011).

Table 4.8. Brillouin-zone-center phonon frequencies (in cm^{-1}) and related mode symmetries for the KS and ST structures of CZTS materials (Source: Gürel et al., 2011).

Cu_2ZnSnS_4					
Kesterite			Stannite		
Sym.	This work		Sym.	This work	
A	335.2		A_1	332.7	
	309.0			309.1	
	302.1		A_2	304.3	
B(TO LO)	354.8	366.4	B_1	324.1	
	332.7	336.1		88.1	
	269.1	285.1	B_2(TO LO)	358.5	364.2
	179.6	179.9		306.2	320.6
	104.2	104.3		171.0	171.1
	92.3	93.1		96.4	96.4
E(TO LO)	341.4	353.2	*E*(TO LO)	341.3	353.7
	309.7	314.1		305.3	311.9
	278.2	289.8		268.7	283.3
	166.1	166.2		170.9	171.0
	101.4	101.4		106.9	106.9
	79.2	79.2		74.9	75.5

The electric field perturbation is the reason of TO/LO splittings in the B modes of the KS structures and the B_2 and E modes of the ST structures. Despite the covalent character of CZTS, the compounds also show ionic character. In the case of vibration of anions and cations, an electric field is created by the LO phonons throughout the vibration.

As a result of the interaction of charged electrons and holes with this electric field, which is known as a polaron effect, electrons and holes move a bit slower in the materials (Ito, 2014). The similarly Khare *et al*. reported the phonon modes of KS, ST and PMCA crystal structures as $\Gamma = 3A \oplus 6B \oplus 6E_1 \oplus 6E_2$, $\Gamma = 2A_1 \oplus A_2 \oplus 2B_1 \oplus 4B_2 \oplus 6E$ and $\Gamma = 2A_1 \oplus 2A_2 \oplus B_1 \oplus 4B_2 \oplus 6E$, respectively (Khare, Himmetoglu, Johnson, et al., 2012). Among the KS phonon modes, 15A, B, E_1 and E_2 are Raman active whereas 12B, E_1, and E_2 are IR active. Between ST phonon modes, $14A_1$, B_1, B_2 and E are Raman active whereas $10B_2$ and E modes IR active. Among the PMCA phonon modes, $13A_1$, B_1, B_2 and E are Raman active whereas $10B_2$ and E modes IR active. Table 4.9. shows the phonon frequencies of KS, ST and PMCA structures of CZTS at Γ (k=0) point. Although there are 27 possible vibrational modes of the kesterite structure, 20 modes of them are experimentally determined, so far (Guc et al., 2016). As given in Table 4.9., Raman peaks at 338 and 287 cm^{-1} are the most intense seen peaks by experimentally. The peak at 338 cm^{-1} is related to (i) the A mode of KS structure at 340.04 cm^{-1}, (ii) the A_1 mode of ST structure at 334.08 cm^{-1} and (iii) the A_1 mode of PMCA structure at 334.42 cm^{-1}. The peak at 287 cm^{-1} is linked with (i) the A mode of KS structure at 284.30 cm^{-1}, (ii) the A_1 mode of ST structure at 277.12 cm^{-1} and (iii) the A_1 mode of PMCA structure at 299.25 cm^{-1}.

Table 4.9. The phonon frequency (in cm^{-1}) of KS, ST, and PMCA structures of CZTS film (Source: Khare, Himmetoglu, Johnson, et al., 2012).

Kesterite			Stannite			PMCA			Experimental data	
Symmetry	This work		Symmetry	This work		Symmetry	This work		Raman	IR
A	340.04		A_1	334.08		A_1	334.42		338.00	
	284.30			277.12			299.25		287.00	
	272.82		A_2	263.11		A_2	266.13			
B (TO LO)	355.80	374.05	B_1	291.12			61.17		368.00	
	309.56	313.19		74.17		B_1	291.18			316.00
	238.48	254.73	B_2 (TO LO)	360.12	370.63	B_2 (TO LO)	341.77	356.57		
	166.65	168.21		277.08	291.82		278.85	288.88		168.00
	98.82	98.83		149.69	150.91		148.63	149.90		
	86.70	87.51		95.85	95.86		87.21	87.26		86.00
E (TO LO)	351.55	366.35	E (TO LO)	346.01	364.87	E (TO LO)	336.98	357.95	351.00	351.00
	281.07	293.44		264.37	275.52		277.85	284.12		293.00
	250.26	257.85		235.41	246.58		234.77	247.02	252.00	255.00
	150.53	151.05		161.68	162.63		164.81	166.56		143.00
	105.93	106.00		97.34	97.38		86.29	86.32		
	83.64	83.65		78.39	78.73		73.26	73.86		68.00

In addition to this, Khare *et al.* also reported Raman spectra of the KS, ST, and PMCA structures of CZTS in theoretical way by using density functional theory and compared them with experimental results (Khare, Himmetoglu, Johnson, et al., 2012).

The phonon dispersion curves along the symmetry points (Z-C-X-P-C-N) of CZTS in the form of KS, ST and PMCA structures are demonstrated in Figure 4.15. Although the phonon dispersion curves of this three crystal structures seems similar, the difference of them can be seen with detailed examination.

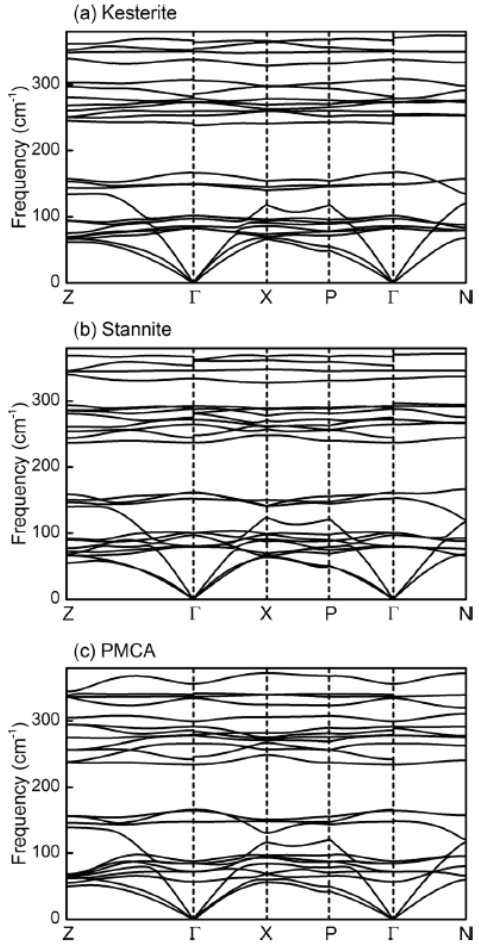

Figure 4.15. The phonon dispersion curves of CZTS a) KS, b) ST and c) PMCA structures along the Z-C-X-P-C-N symmetry points (Source: Khare, Himmetoglu, Johnson, et al., 2012).

Firstly, PMCA structure can be differentiated from KS and PMCA structures near the Γ point. For instance, the phonon dispersion graph at 365 cm^{-1} throughout the Z-Γ-X line can not appear whereas for the KS and ST structures it discontinues. The reason of the discontinuity bases on the distinction on the magnitude of LO-TO splitting along the

Z-Γ and Γ-X directions for the KS and ST structures, which resulting the phonon branches in the two directions to be separated in energy.

Secondly, the KS and ST structures can be differentiated by phonon dispersion through the Z-Γ-X line at frequencies corresponding to 165 and 150 cm^{-1}. At 165 cm^{-1}, the ST phonon dispersion curve cut the Γ point and separates into two branches which one of them goes along the Γ-Z direction. The separation is not observed for the phonon dispersion curve crossing the Γ point at 148 cm^{-1}. This event is observed reversely for the KS structure. The phonon dispersion of KS structure cut the Γ point at 145 cm^{-1} and separate into two branches which one of them goes away from the Γ point, however, this separation is not seen for the phonon dispersion curve which cut the Γ point at 165 cm^{-1}. Consequently, based on these differences, the crystal structure of CZTS can be determined (Khare, Himmetoglu, Johnson, et al., 2012).

The phonon density of states of the KS, ST and PMCA structures for each constituent elements and total composition is given in Figure 4.16. The density of states at 50-160 cm^{-1} phonon frequency range consist of the vibrations of the three metal (Cu, Zn, Sn) cations with some contribution from the sulfur anions. The density of states at around 250-300 cm^{-1} frequency are formed by the vibrations of the Zn cation, S anions and some contribution from the Cu cations. The phonon states observed between 310 and 340 cm^{-1} frequency range are the outcome of vibrations of S anions. The phonon states appeared at 340-370 cm^{-1} frequency range are the results of the vibrations of both S anions and Sn cations.

For each frequency, the phonon vibration belongs to the same atoms of KS, ST and PMCA structures. Therefore, the Figure 2.16. advocates the likeness of phonon modes for three CZTS structures (Khare, Himmetoglu, Johnson, et al., 2012). Although the most intense peak is observed at 337-338 cm^{-1} for kesterite CZTS, sometimes it is detected at 329-331 cm^{-1} which is linked with the existence of local non-uniformities with a high degree of disorder in the cation sub-lattice of CZTS. The main difference between the kesterite and the disordered kesterite structures is in the arrangement of the cations. In theoretical way, kesterite structure is more stable. It was demonstrated that the z=1/4 and z=3/4 planes of well-ordered kesterite CZTS film consists of Cu and Zn ordered at the 2c and 2d which are called as Wyckoff positions (Hall et al., 1978). However, this perfect array is not encountered in synthetical samples.

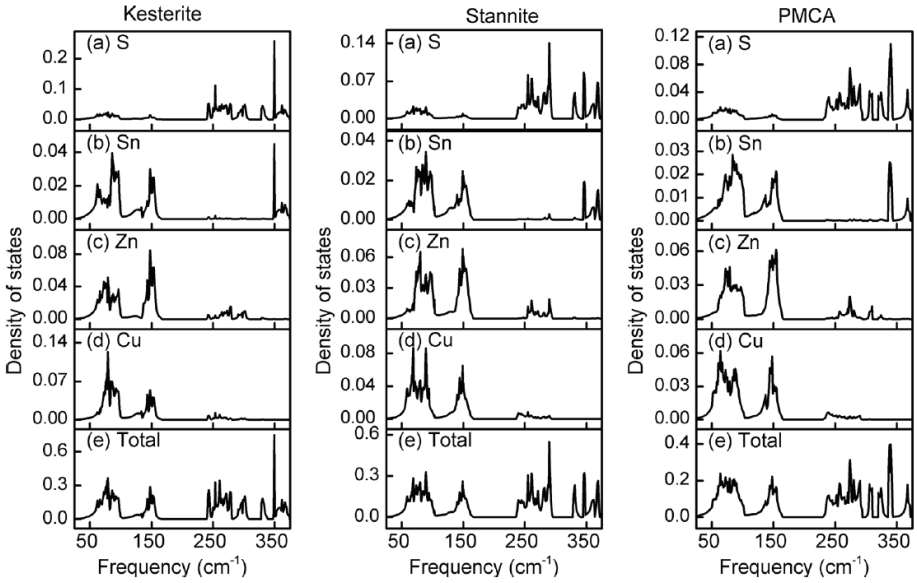

Figure 4.16. The phonon density of states of the KS, ST and PMCA structures for each constituent elements and total composition (Source: Khare, Himmetoglu, Johnson, et al., 2012).

In the case of disordered distribution of Cu and Zn atoms, a high content of Cu_{Zn} and Zn_{Cu} antisite defects are formed which reduce the quality of crystal structure of these regions. Therefore, for the domains where the disordered distribution of cations exist in a high amount, the Raman peaks shift towards lower frequency side (Fontané et al., 2012). This peak is defined as an A_1 symmetry mode of the disordered kesterite phase which results the change in group symmetry to the stannite-alike. It is possible to encounter this disordered kesterite phase while working under non-stoichiometric conditions. On the contrary to XRD, Raman spectroscopy is also efficient characterization technique for discriminating between CZTS, ZnS and Cu_2SnS_3 (Khare, Himmetoglu, Johnson, et al., 2012).

4.6.5. Electrical Properties of CZTS

CZTS is an intrinsic p-type semiconductor. Crystal defects which occur during the formation of the CZTS cause this material to exhibit a self-doped semiconducting property. The Cu atoms in the CZTS crystal are located at the lattice points where the Zn atoms must be present, forming a Cu_{Zn} antisite defects in the crystal. The absence of Cu atoms at its lattice points results Cu vacancies (V_{Cu}).

The formation of these crystal defects allows this material to gain the *p*-type semiconductor property (Chen, Yang, et al., 2010). Since these antisite defects are exceedingly stable, it is nearly impossible to form n-type CZTS.

For p-type conductivity of CZTS, Cu vacancies are more preferred than Cu_{Zn} antisite defects. Since V_{Cu} forms shallow level acceptors which increases p-type conductivity. Thus, Cu/Zn and Cu/Sn atomic ratio decides the majority charge carrier concentration in CZTS. The resistivity, mobility and carrier concentration values are important parameters for electrical properties of CZTS and they are obtained from Hall measurements. Depending on the growth technique and CZTS composition, a variable conductivity and mobility values can be encountered in the literature. Since free carrier mobility is influenced by scattering mechanisms, the density of defect and the existence of secondary phases which affect the quality of material cause the different results.

There are many different results in the literature for the CZTS's resistivity. It has been indicated that this value should be in the range of 10^{-3} to 10^{-1} Ω cm for highly efficient CZTS solar cells (Katagiri et al., 2001). The majority carrier concentration is reported in the literature as 10^{16}-10^{18} cm^{-3} (Fernandes et al., 2011; Scragg et al., 2008), but values below or above this value are also found. The mobility values are given in the range of 1.0 to 10.0 cm^2 V^{-1} s^{-1}.

4.7. Cadmium Sulfide (CdS) Buffer Layer

Cadmium sulfide (CdS), belonging to the II-IV group, is an n-type semiconductor with direct band gap value E_g=2.42 eV (in bulk at room temperature) (Lisco, Kaminski, Abbas, Bowers, et al., 2015), high absorption coefficient, a good transparent in region of visible light and being easily ohmic contact to various materials. In recent years, CdS films have extensively application areas in photodetectors, solar cells and thin film FET transistors. Because of its absorption property, it is used in Cu_2ZnSnS_4 (CZTS) (Tajima et al., 2017), CdTe (Mathew, Enriquez, Romeo, & Tiwari, 2004) and $Cu(In,Ga)Se_2$ (CIGS) (Salome et al., 2017) solar cells as a buffer layer.

There are many techniques to prepare CdS films such as chemical bath deposition (CBD) (Mazón-Montijo, Sotelo-Lerma, Rodríguez-Fernández, & Huerta, 2010), thermal evaporation (Khan, Zulfequar, & Khan, 2010), spray pyrolysis (Ravichandran & Philominathan, 2009), deep coating (Oladeji et al., 2000), sputtering (Lisco, Kaminski,

Abbas, Bass, et al., 2015), pulsed laser deposition and SILAR (Senthamilselvi, Saravanakumar, Anandhi, Ravichandran, & Ravichandran, 2011). The sublimation and the melting temperatures of CdS are about 700°C and 1750°C, respectively. Therefore, deposition of CdS can be occured from vapor phase or from high pressure liquid phase.

The growth technique, substrate type (Fernando, Khan, & Vasquez, 2015) and temperature (Sivasubramanian, Arora, Premila, Sundar, & Sastry, 2006), S/Cd ratio (Ouachtari et al., 2011), PH value (Kariper, Güneri, Göde, Gümüş, & Özpozan, 2011) and deposition time has strong effect on the electrical, optical and structural properties of CdS films. And also type of doping element and its concentration can change the optical and electrical characteristics of CdS (Anbarasi, Nagarethinam, & Balu, 2015).

CBD is frequently preferred technique due to being low temperature process (27-80 °C), inexpensive and easy to handle, having large application area (Slonopas et al., 2016). With this technique, it is also possible to control the deposition rate as well as the thickness of the film by pH, bath temperature and molar concentrations of the reactants in the bath solution. In this technique, the growth kinetic is highly important in terms of the optical and structure quality of grown films. There are mainly two CdS growth process by CBD technique ion-by ion, cluster by cluster and mixed of them (Mazón-Montijo et al., 2010). Ion-by ion process which the grown films are in cubic phase, bases on the condensation of Cd^{2+} and S^{2-} ions on the substrate. Cluster by cluster mechanism bases on the absorption of CdS or $Cd(OH)_2$ colloidal particles formed in the solution on the substrate. The ion by ion deposited CdS films have high reflection, perfect adherence to the substrate whereas with the cluster mechanism the films have less adherent and inhomogeneous layer on the substrate. Depending on the growth process and substrate temperature, CdS films have hexagonal (wurtzite), cubic (zincblende) or mixed of them crystal structure as shown in Figure 4.17. At low substrate temperature CdS grows as a cubic phase and at high temperature hexagonal phase occurs. By heating the cubic phase, the hexagonal phase can be obtain (Sivasubramanian et al., 2006). Although the hexagonal phase is thermodynamically more stable than the cubic phase (Abd-Elkader & Shaltout, 2015), its band gap energy is lower than the cubic one.

Since the most intense diffraction angle position of wurtzite and zincblende structures match within 1%, determination of exact crystal structure by XRD became a difficult work.

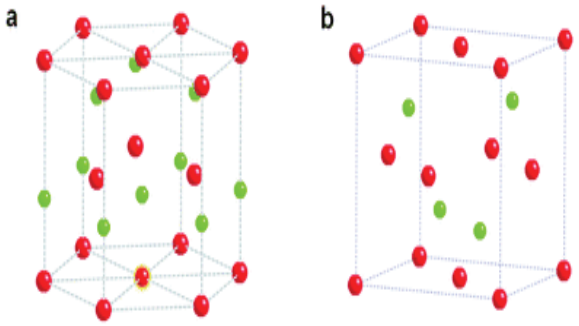

Figure 4.17. Crystal structure of CdS a) hexagonal (wurtzite), b) cubic (zincblende).

Generally the grain size of CdS films changes between 0.3 and 0.5 μm and their size can be increased with annealing treatment at high temperature. Annealing treatment also results the recrystallization of CdS films. The composition ratio of Cd and S elements (Cd/S) is important in terms of conductivity of CdS. There are many reports that the excess of cadmium plays a donor role and causes the n-type conductivity (Alexander, Higashiya, Caskey, Efstathiadis, & Haldar, 2014; Ouachtari et al., 2011). Since sulfur vacancies are donor type defects, they improves the n-type conductivity (Alexander et al., 2014). Due to the self-compensation effect created by sulfur vacancies, the obtaining p-type CdS is very hard.

In terms of photovoltaic application as a buffer layer, there are some requirements such as buffer layer should have high bandgap to diminish the high energetic photon absorption, the thickness of it should be less than 100 nm to increase the light transmission as well as device performance. There are alternative buffer layers for CdS such as Zn(O,S) and ZnS with wider bandgap. However, the cell efficiencies of CZTS with these buffer layers are still lower than the using of CdS buffer layer (Tajima et al., 2017). CdS has well lattice match with the heterojunction interface and it is possible to form epitaxial junction at the interface between CdS and CZTS; so the formation of recombination at the interface is unessential when compared with that at the interface of CZTS with wide E_g buffer layers (Alexander et al., 2014; Tajima et al., 2017).

In the literature, the highest solar cells of CIGS and CZTS were achieved using CdS buffer layer with 22.8% (Salome et al., 2017) and 9.4% (Tajima et al., 2017) photo-conversion efficiency, respectively.

4.8. ZnO Window Layer

Zinc oxide (ZnO) is II–VI semiconductor material which is used as a window layer for photovoltaic applications. ZnO is an intrinsically n-type semiconductor. In semiconductors, there exist various defects which change the electronic and optical properties of related semiconductor. While the some defects decrease the lifetime of the device, some of them enhance the quality of materials. Therefore it is crucial to control the defects. For the ZnO the observed intrinsic defects are oxygen vacancies, Zn interstitials, oxygen interstitials, Zn vacancies and antisite oxygen. The n-type semiconductor character of ZnO comes from the oxygen vacancies. In the literature, it is possible to encounter the oxygen rich p-type ZnO (Ilyas et al., 2011).

ZnO has wide and direct bandgap of 3.37 eV at room temperature (Wei et al., 2007) which makes this material available for solar cells. Being non-toxic, cheap and compatible with manufacturing process of semiconductors, ZnO has wide range of applications. Because of its unique properties, ZnO material has been taken much attention. Depending on doping, it shows n-type and p-type conductivity and high transparency. It also has many potential application in short-wavelength optoelectronic devices such as solar cells, ultraviolet (UV) laser and thin film gas sensor.

ZnO has three types of crystal structures which are wurtzite (hexagonal), zinc blende (cubic) and rocksalt (in Figure 4.18.). At environmental conditions, wurtzite structure is thermodynamically stable phase (Espitia et al., 2012).

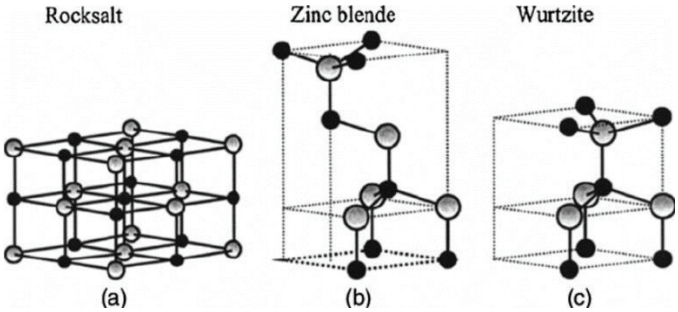

Figure 4.18. Crystal structures of ZnO
(Source: Özgür et al., 2005).

ZnO is used as a window layer for solar cell applications. ZnO is deposited on buffer layer in order to prevent the reduction in the V_{OC}. When ZnO makes a contact with buffer layer, it should be very resistive or almost insulating.

CHAPTER 5

EXPERIMENTAL PROCEDURE

5.1. Growth Method of CZTS Absorber

In this work, CZTS absorber layers were fabricated by two-step process. In the first step, metallic precursor containing Cu, Zn and Sn metallic layers, named with CZT, are deposited by magnetron sputtering technique. This step is followed by a heat treatment of metallic precursors under a sulfur atmosphere which is called a sulfurization process. Sulfurization process is required to convert metallic stacks CZT to CZTS absorber film. The details of growth process will be given in the following sections.

5.1.1. Deposition of CTS Metallic Precursor

1 μm thick Mo back contact which was coated on soda lime glasses (SLG) are used as a substrates. Substrates are cleaned by ultrasonication in acetone, ethanol and distilled water, respectively and then dried under a nitrogen stream. As demonstrated in Figure 5.1. multi-target DC magnetron sputtering system was used to deposited CZT metallic precursor which were deposited sequentially on Mo coated SLG substrates. Muti-target DC magnetron sputtering system consist of 2-inch targets of Cu (99.999%), Zn (99.99%), and Sn (99.999%). Target to substrate distance was fixed at 8 cm and for deposition of each metal layer substrate holder was rotated to related target. Before the sputtering, the vacuum chamber was evacuated at around 10^{-6} Torr by Turbo Molecular Pump (TMP) and heating was not applied to the substrates in the course of sputtering. After reaching to the required pressure, a constant amount of 30 sccm Ar gas was sent into the chamber as long as the deposition process. The operating pressure was 1.5×10^{-2} Torr and it was constant throughout the deposition. Since the thickness of each metallic precursor layer plays an important role in the formation of CZTS structure. In this study, it was desired to obtain 630 nm thick CZT metallic precursor.

Therefore, thickness calibration of each metallic layer was occurred using molecular weight and density of each element before the deposition. Thanks to regulation of the thickness of each element, the compositional ratio can be easily checked. Since in the literature high efficient solar cells are mentioned with having Cu-poor and Zn-rich composition, in this work it was also calibrated to obtain this composition.

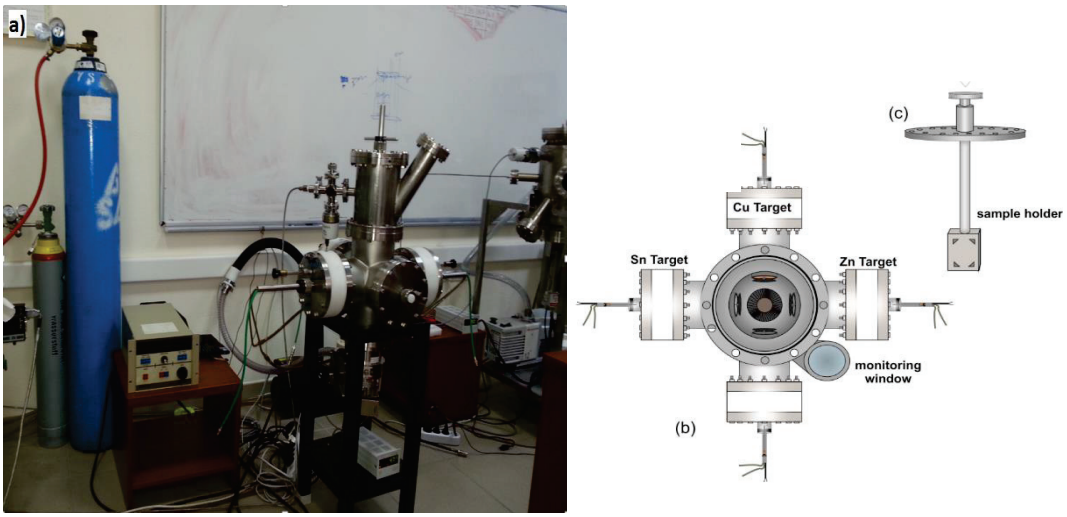

Figure 5.1. a) Magnetron sputtering system of metallic CZT precursors, b) top view of the system, c) rotating sample holder.

DC supply was used to deposit each metallic layer at 41 W, 40 W and 20 W power for the Cu, Sn and Zn targets, respectively. Thickness of Cu, Sn and Zn layers were 175, 165 and 290 nm, respectively. As given in Figure 5.2. two types stacking order were used. Type I is Mo/SLG/Cu (55 nm)/Sn/Zn/Cu (120 nm) and Type II is Mo/SLG/Cu (120 nm)/Sn/Zn/Cu (55 nm). There are many reasons to select this stacking order such as; *i*) because of easily diffusion of Cu from bottom to top layer, the middle Zn layer can prevent to formation of vacancies which resulted the diffusion of Cu, *ii*) having low melting point (231.93 °C) Sn easily evaporate, so with this stacking order the Sn loss can be minimized, *iii*) due to the easily volatility of Zn, the middle Zn layer can prevent the ZnS phase formation at the surface.

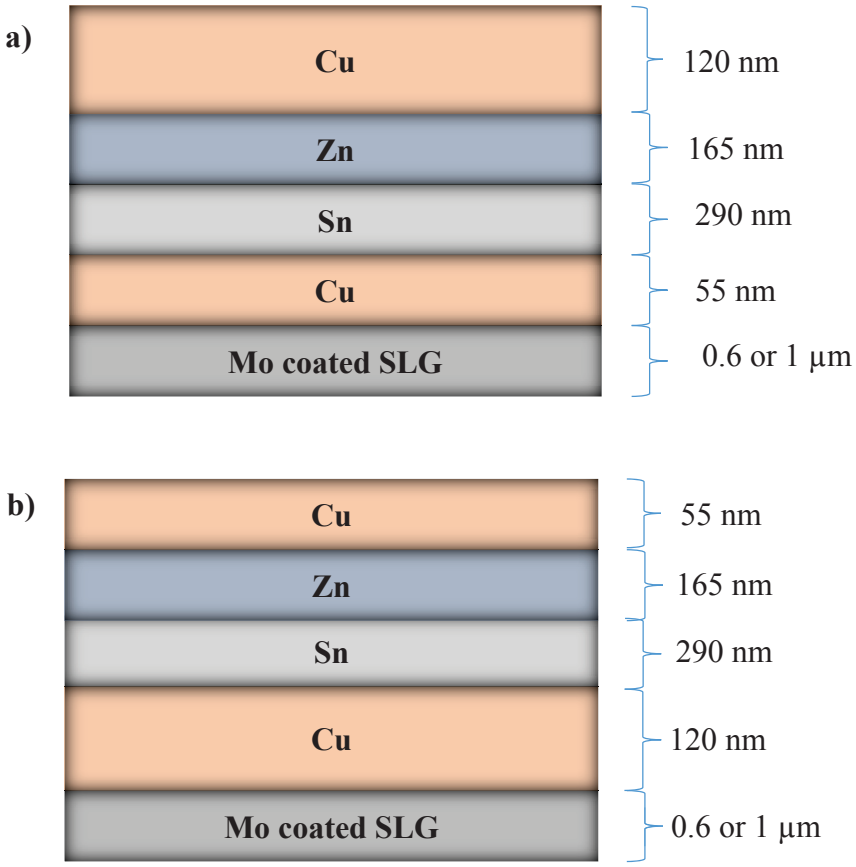

Figure 5.2. a) Type I and b) Type II stacking order of metallic precursor.

Figure 5.3. and 5.4. show the SEM image and EDX result of CZT metallic precursor, respectively, before the sulfurization. Although there are some differences in height on the film surface, it generally contains particles of the same size. And also it was not encountered any void on the CZT surface. EDX analysis revealed 42.5, 30.65 and 26.85% Cu, Zn and Sn elements, respectively. For the CZT precursor Cu/Zn+Sn and Zn/Sn ratio were 0.74 and 1.14, respectively which has Cu-poor and Zn-rich composition.

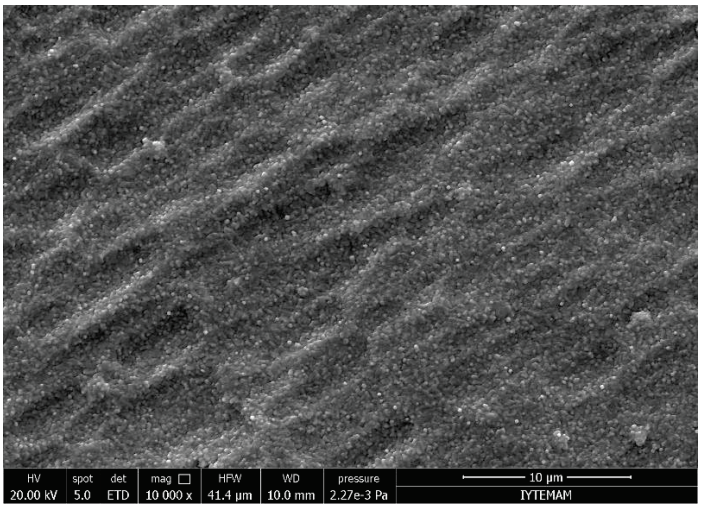

Figure 5.3. SEM image of CZT metallic precursor.

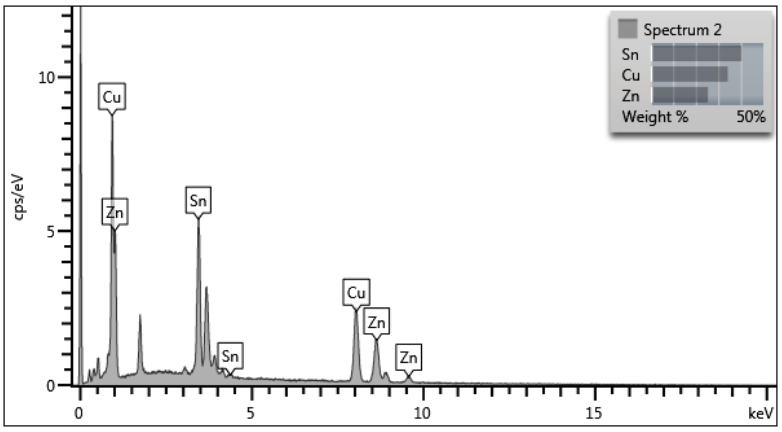

Figure 5.4. EDS result of CZT metallic precursor.

5.1.2. Sulfurization of CTS Precursor

To obtain CZTS p-type absorber layer, CZT precursors were annealed under S vapour and Ar atmosphere. The sulfurization procedure was performed with a quartz glass tube in a furnace. CZT precursor was putted the center of the furnace while the 600 mg sulfur powder (99.98%) was placed 18 cm away from the precursor. Both sulfur and the sample were inside a two different graphite boxes whose covers were not closed.

The evaporated sulfur and the hot metallic precursor have a reaction during the sulfurization. Figure 5.5. demonstrates the sulfurization system.

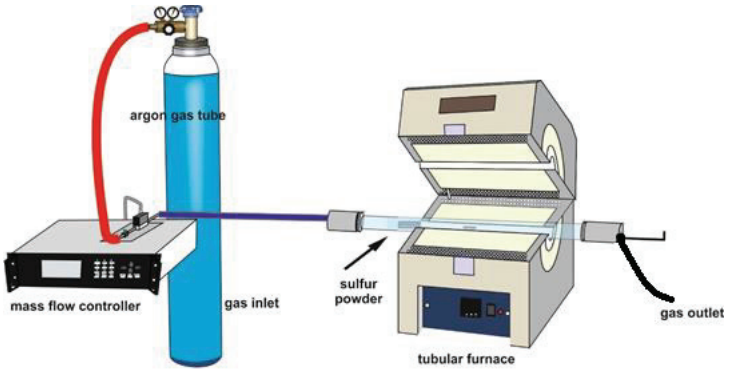

Figure 5.5. Sulfurization System.

Using a MKS 647C mass flow controller, 100 sccm Ar was sent into the quartz tube as a carrier gas and the pressure was kept at atmospheric pressure during the sulfurization. Figure 5.6. shows the sulfurization process graph of sample. The temperature of the furnace reached to 270 °C in 5 minutes and stayed at this temperature for 3 minutes. Then it was risen to 550 °C within 5 minutes. The sulfurization of CZTS metallic precursors were done at 550 °C for different sulfurization time

The length and the temperature of heat treatment are important because during the process a liquid phase might form and this might result the formation of de-wetting, accumulation of melted film to the edge of the substrate and phase segregation. Three sulfurization durations, 30, 45 and 60 min, were tried to understand how the CZTS growth process advances at 550 °C.

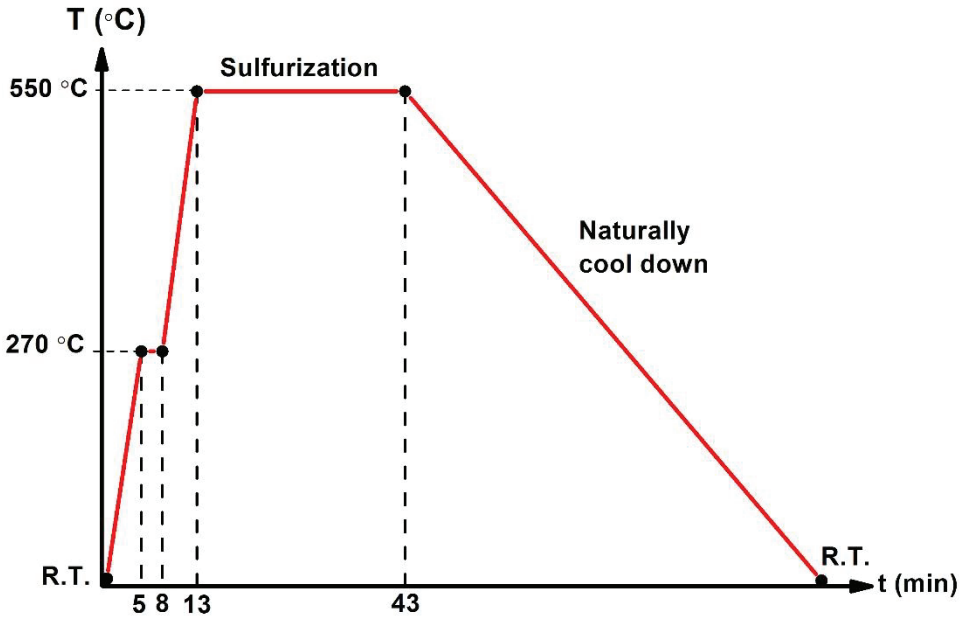

Figure 5.6. Sulfurization process parameters of a) sample box and b) sulfur box.

5.2. Chemical Bath Deposition (CBD) of CdS Buffer Layer

The CdS thin films were deposited on glass substrates with chemical bath deposition (CBD) technique. Soda lime glass substrates are cleaned by ultrasonication in acetone, ethanol and distilled water, respectively and then dried under a nitrogen stream. The bath solution contained 1.2 ml of 0.5 M cadmium acetate ($Cd(CH_3CO_2)_2$), 6 ml of 2M ammonium acetate ($NH_4CH_3CO_2$), 7 ml of 0.5 M thiourea $SC(NH_2)_2$ and 12 ml of 14.4 M (25% of NH_3 solution) ammonium hydroxide (NH_4OH) and 270 ml de-ionized water.

The cadmium acetate and thiourea employ as the cadmium and sulfur sources, respectively. NH_3 has a role as a complexing agent in order to prevent the metal hydroxide precipitation. It also effect the growth rate of CdS. In order to control the release of ions and to obtain slow deposition rate, ammonium acetate is used as a buffer solution. Figure 5.7. shows the CBD system. In the system two different size beakers were used. The big one served as a water bath tank and the small one was used for the chemical bath deposition.

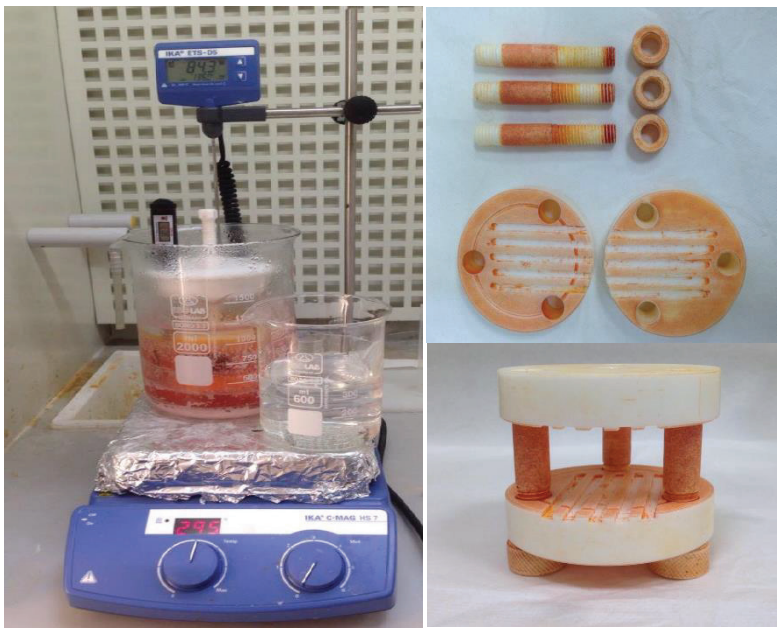

Figure 5.7. Chemical Bath Deposition System.

When the big beaker reached to the 85°C temperature, the small beaker containing 270 ml de-ionized water was placed into this and waited until the thermal balance reached.

When the thermal equilibrium was satisfied at 85°C, the glass substrates were immersed into the water. After the water and substrate system reached to 85°C, cadmium acetate, ammonium acetate and ammonium hydroxide were added to the beaker, respectively. In the course of the CdS thin film forms, the reaction process is considered as follows;

$$NH_4^+ + OH^- \leftrightarrow NH_3 + H_2O \quad (5.1)$$

$$Cd^{2+} + 4NH_3 \leftrightarrow (Cd(NH_3)_4)^{2+} \quad (5.2)$$

$$(NH_2)_2CS + OH^- \leftrightarrow SH^- + H_2O + CN_2H_2 \quad (5.3)$$

$$SH^- + OH^- \leftrightarrow S^{2-} + H_2O \quad (5.4)$$

$$Cd^{2+} + S^{2-} \leftrightarrow CdS \quad (5.5)$$

In this stage, Cd^{2+} ions were adsorbed on the surface of glass substrates (Eq. 5.2). As soon as the final system was heated to desired temperature (85°C), thiourea was added to the beaker and deposition time was started. Equation 5.3 and 5.4 represent the thiourea decomposition which is sensible to the OH^- concentration and temperature. The high concentration of OH^- makes easy the decomposition of thiourea (Fernando et al., 2015). During the deposition, the cation (Cd^{2+}) coated glass substrates adsorbed anionic S^{2-} ions (Equation 5.5). While the deposition, the bath solution was stirred at constant speed with the aid of magnetic stirrer and PH value of the solution between 9 and 10. The films were deposited at 85°C for 15 min time increments.

After the growth process, the substrates were first rinsed with deionized water at temperature 60 °C in order to remove CdS precipitation or un-reacted sulfide ions and then rinsed again with deionized water at room temperature and dried in air. The grown films in Figure 5.8. were yellow (thin) or orange (thick) in colour depending on the thickness of films and displayed well adherence to the glass surfaces.

Figure 5.8. CdS coated glass substrates; the yellow one (on left) is thin and the orange one (on right) is thick film.

5.3. Growth of ZnO Window Layer

The ZnO is an n-type semiconductor and it was used as a window layer in this work. RF magnetron sputtering system with single ZnO target was used to deposit 40 nm thick ZnO window layer. The base pressure of the system was 1.8×10^{-6} Torr and working pressure was 5.7×10^{-3} Torr. Figure 5.9. shows the deposition system. The depositions were achieved by using 50W RF power and 80 sccm Ar gas.

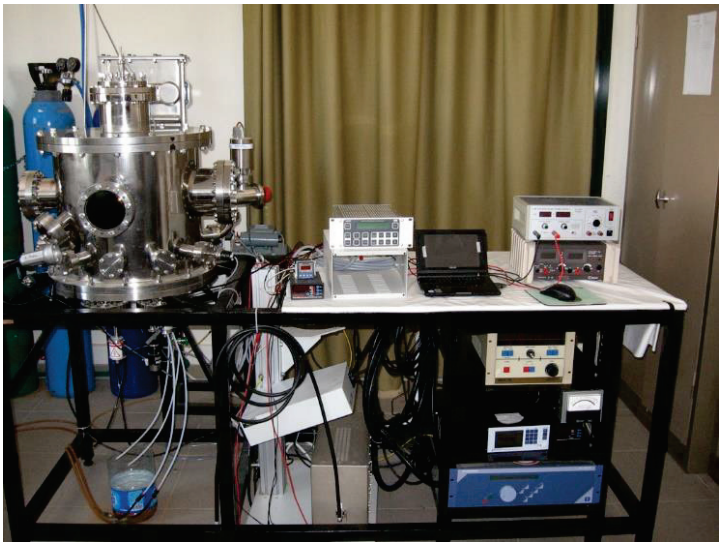

Figure 5.9. Magnetron sputtering system of ZnO and Al-ZnO layers.

5.4. Growth of Al-ZnO (AZO) Transparent Conducting Oxide

The Al-ZnO is an n-type semiconductor and it was used as a transparent conducting oxide layer in this work. RF magnetron sputtering system with single and 2%

Al dopped ZnO (Al-ZnO) target was used to deposit approximately 250-300 nm thick AZO transparent oxide layer. The base pressure of the system was 1.8×10^{-6} Torr and working pressure was 5.7×10^{-3} Torr. Figure 5.9. shows the deposition system. The depositions were achieved by using 50W RF power and 50 sccm Ar gas.

5.5. Device Fabrication

The solar cells were fabricated on Mo coated soda-lime glass substrates. The CZTS absorber layer growth is performed as described in the Chapter 5.1. After the CZTS growth, it was not performed any KCN etching because it seemed giving harm to the samples surface. CdS buffer layer was deposited on CZTS absorber layer with different thickness as mention in Chapter 5.2. The cell was completed by growing intrinsic ZnO layer (40 nm) and Al dopped ZnO (~250-300 nm) layer as explained in Chapter 5.3 and 5.4, respectively. Finally the cell areas were defined and contacts were taken to collect the carrier. In the SLG/Mo/CZTS/CdS/ZnO/AZO solar cell structure, each layer has a different kind of role in the working cell. Figure 5.10. demonstrates the device structure of solar cell. All the devices in this study did not have anti-reflective coating.

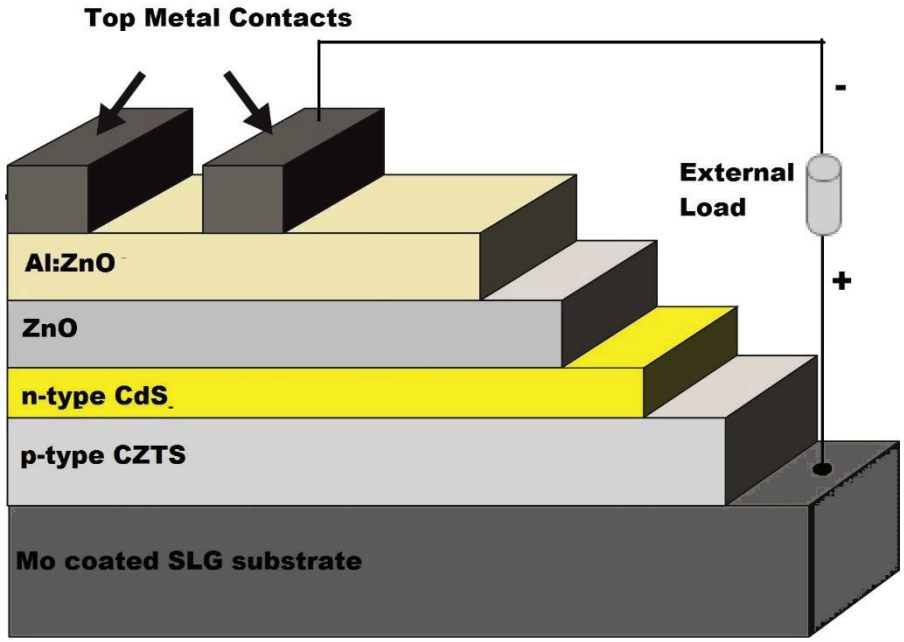

Figure 5.10. Device structure of CZTS thin film solar cell.

5.6. Samples Characterization Techniques

5.6.1. X-Ray Diffraction (XRD)

X-ray are electromagnetic waves with wavelength between 0.02 and 100 A. They are used to determine the structural arrangement of atoms and molecules of material. X-ray interacts with electrons of atoms and the penetration depth depends on the density of matter. After the interaction of X-ray with electrons, some of incident beam is deflected away from the incident direction. In the case of ordering periodically of atoms, the deflected waves will give sharp interference peak. The Bragg's Law define the condition of constructive X-Ray diffraction as $2d \sin(\theta) = n\lambda$, where n is the integer and represents the order of diffracted beam, λ is the wavelength of X-Ray, d is the distance between adjacent crystal planes and θ is the angle of incidence as well as that of reflected beam (see Figure 5.11.)

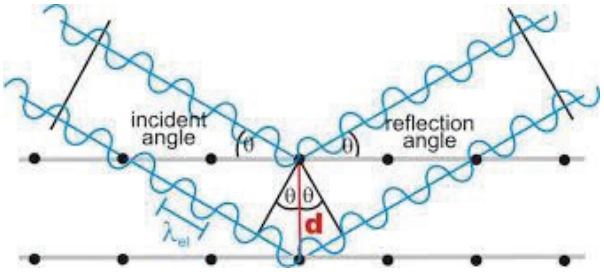

Figure 5.11. X-Ray Diffraction Pattern.

From the intensity, position and width of the output peaks, the crystal structure and its quality can be determined. In this work, Philipps X'Pert Pro X-Ray diffractometry with Cu K_α radiation (λ = 1.5406 Å) and using a step size of 0.03° and a step time of 1.1 s. was used to analyze the crystal structure.

5.6.2. Raman Spectroscopy

Raman spectroscopy is used for microstructural characterization and enable the information about molecular vibration which identify the sample. Raman spectroscopy has sensitivity to the local atomic environment.

The symmetry of the crystal structure, chemical bonds strength, mass and charge of constituent elements effect the Raman spectrum (Scragg, Choubrac, Lafond, Ericson, & Platzer-Björkman, 2014). Monochromatic light source such as a laser with different wavelength is used on the characterized sample and the scattered light is detected. The most of the scattered light has the same frequency with the excitation laser which is known as Rayleigh or elastic scattering. Since the interactions among the incident electromagnetic waves and the vibrational energy levels of the molecules which are inside the sample, the shift in energy of small amount of the scattered light is observed. As a result of this phenomenon, the plot of the intensity of shifted light versus frequency is given. Since the back scattering configuration is used in Raman scattering analysis, the penetration depth (d) of the incident light should be $d=1/2\alpha$ where α is the absorption coefficient of the examined sample. The 488, 514 and 633 nm are commonly used laser wavelengths with the penetration depths of 140, 150 and 170 nm, respectively. Yet, when the wavelength of 785 nm is used, it is possible to reach a depth of 400 nm (Fernandes et al., 2011).

In this thesis, the microstructural characterization was performed using Raman scattering. The high resolution micro-Raman instrument (Princeton Instruments, Acton SP2750 0.750 mm Imaging Triple Grating Monochrometer) was used at room temperature. The Raman measurements of CZTS films were taken with the Ar and HeNe lasers with excitation wavelength of 514.5 and 632.8 nm, respectively. The Raman measurement of CdS films were occurred by the Ar laser with wavelength of 488 nm. For all films, 100X objective and 600 grating were used. Calibration was performed using the Si main mode at 521 cm^{-1}.

5.6.3. Scanning Electron Microscopy (SEM)

The scanning electron microscopy uses electrons which interact with the sample' atoms to form an image. As a result of electron-sample interaction, the secondary electrons, backscattered electrons and characteristic X-rays are produced as given with Figure 5.12. and their signals are detected by suitable detectors and generate images which are seen on the computer screen. The penetration depth of electron beam when hit the sample surface depends on accelerating voltage and the density of the sample.

It is also possible to determine the chemical composition of selected area on the sample surface by using Energy Dispersive Spectroscopy (EDS).

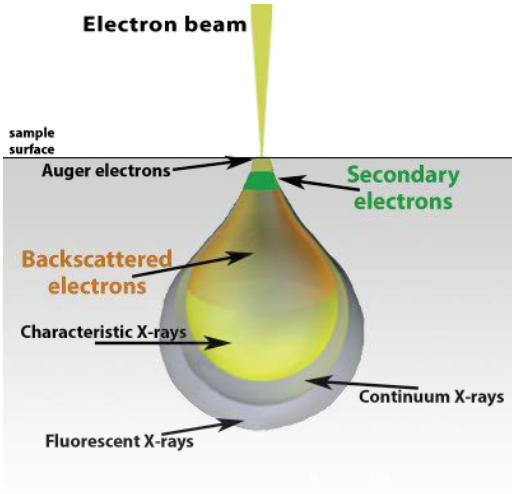

Figure 5.12. Illustration of electron beam-sample interaction.

In this study, the surface morphology of CZTS absorbers were investigated by using a scanning electron microscope (SEM; FEI-QuantaFEG 250) equipped with Energy Dispersive Spectroscopy (EDS; Oxford X-act). Surface topography was taken with 5 kV acceleration voltage at different magnifications under high vacuum with ETD detector and 3 spot size.

For cross section measurements, LV detector (BSED) and 5 spot size were used during the measurement. To determine the atomic concentration of constituent elements, EDS analysis was used.

5.6.4. X-Ray Photoelectron Spectroscopy (XPS)

In X-Ray Photoelectron Spectroscopy analysis the X-ray sources such as Mg *Kα* and Al *Kα* are used. When the X-ray hit the sample surface, if the photon energy is higher than the binding energy it is absorbed by an atom in the solid and result the photoemission of the electrons from the core and valence levels. The emitted electrons are measured by spectrometer and produce the spectrum which represents the electron intensity. The binding energy of photoemitted electrons is a fingerprint parameter to find the element it belongs to and the level of energy which they are emitted.

The kinetic energy of the emitted electrons depends on the photon energy and the essential relationship can be given as follows;

$$h\nu = KE + BE + \phi \tag{5.6}$$

Here, hν and ϕ are the photon energy and spectrophotometer work function, respectively. When a photoelectron is emitted, it is necessary to be relax of the ionized atom. This occurs by ejection of secondary electron which is called an Auger electron and they are produced as a result of XPS process. Although Auger peaks have the ability to interfere with photoelectronic peaks, it can give worthy information about related atom. The penetration depth of X-ray beam into material depends on the kinetic energy of the electron being used. Its magnitude is determined by the given relation in the following,

$$\Lambda = \lambda * \cos\theta \tag{5. 7}$$

where Λ is electron attenuation length, θ is emission angle, λ is inelastic mean free path which bases on kinetic energy of electron and the density of solid. For the energy range of 200-2000 eV, the electron attenuation length is less than 10 nm, therefore XPS is called as a surface-sensitive technique.

In this work, X-ray photoelectron spectroscopy (XPS; SPECS Phoibos 150 3D-DLD) analysis was used to identify the electronic state and quantity of constituent elements. XPS measurements were performed with a monochromatic Mg K_α radiation source (hν=1254 eV) with a power of 200 W and take off angle of 45°. The spot size is 2 mm (medium area). The analyzer pass energy, the step size and dwell time were set to 40 eV, 0.4 eV and 0.3 sec for the survey spectrum and 30 eV, 0.05 eV and 2 sec for the high resolution spectra, respectively. After the survey spectrum measurement, high resolution measurements of interested elements were followed. Curve fitting was applied to high resolution spectra each element so as to understand the electronic state of the constituent elements and make the quantitative analysis of them. The electronic state of an element is determined with respect to chemical shift in the energy positions of related peak. This is caused by changing electrostatic potential of the core electrons. When an atom is bonded to another, its valence electron density is changed with respect to its elemental state and result the shift in binding energy position

While working with insulating samples, photoemission from these samples results the electrostatic charging which is observed in the positive direction. As a result of the charging, the peak position shifts to higher binding energy side. Therefore in this work, the spectra were corrected with respect to C *1s* peak at 284,6 eV (Yazici et al., 2015). After applying the Shirley background subtraction, the deconvolution process of the spectra was done with Gaussian–Lorentzian peak profile using CasaXPS software.

5.6.5. Spectrophotometric Analysis

Optical measurements are necessary for determining the transmission, absorption, and reflection. As an outcome of these measurements, absorption coefficient and bandgap value of examined material were calculated. In this work, transmission measurements were taken by A PerkinElmer Lambda 950 UV/VIS/NIR spectrometer and they were used to determine the band gap of CdS buffer layers.

5.6.6. Spectroscopic Ellipsometry (SE)

Spectroscopic ellipsometry is a non-destructive technique which determine the optical properties of the sample. A beam of polarized light illuminates the characterized sample and ellipsometer measures the change in polarization state of incoming light after reflection or transmitted through the sample. The change in this polarization state which is defined in equation 5.8 is represented by ellipsometric parameters of Psi (Ψ) and Delta (Δ) which measures the phase and amplitude changes of incident light, respectively.

$$\tan\psi\, e^{i\Delta} = \rho = \frac{r_p}{r_s} \tag{5.8}$$

Here, ρ is the ratio of reflectivity of p-polarized (r_p) to the s-polarized (r_s) light and Δ is the phase. Having high accuracy, sensitivity and also allowing determine the multiple layered sample's properties, SE is commonly used in thin film technology. However, to determine the thickness and optical constants of examined sample the suitable optical model should be created and the SE data should be fit according to this model (Cantaş, 2010).

In this thesis, the ellipsometric measurements (Ψ,Δ) of the deposited films were taken by spectroscopic ellipsometer (SE; AWoollam M-2000X) with the photon energy range from 1.24 to 5.05 eV in ambient conditions. A Xenon arc lamp was used as a light source and the angle of incidence was constant at 65.82° for all measurements. In order to determine the thickness, surface roughness and optical constants of CdS films, these SE parameters were modeled and fitted. Many different models were constructed but the best result was obtained from the two layers of CdS where one of them is on and the other is bottom of the SLG substrate. During the CdS deposition, the glass substrates horizontally immersed into the solution so both sides of the substrates covered. Figure 5.13. represents the constructed model.

SE measurements Ψ and Δ oscillate. The reason of this oscillations are caused by the interference between the reflected light from the sample surface and the light that transmitted through the sample and turns back from the bottom interface. As an optical model of the CdS layers the generalized oscillator (gen-osc) function was used. This model provides the Kramers-Kronig consistency of the evaluated optical constants and diminish the noise effects. CdS films were modeled using five oscillators. The surface roughness was modeled as a Bruggeman effective approximation (BEMA) layer. With this layer, it was assumed that the top layer of the film consists of 50% void and 50% CdS film. The fit parameter was only the thickness of this layer. According to model if the surface roughness is negative this means that the surface contains -50% void and the optical properties of this layer is increased (instead of decreasing). These optical models and parameters were provided by CompleteEASE software (Woollam, 2011).

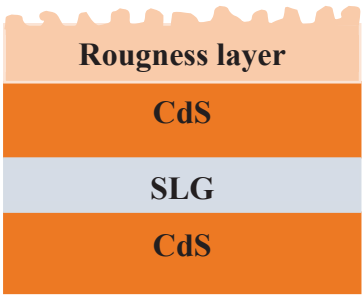

Figure 5.13. Optical model for fitting of SE data.

The quality of fit was determined using root mean squared error (RMSE) which is defined in equation 5.9. This quantifies the degree of matching the generated optical model and the measured data.

In the equation, N is the total number of data points taken, σ is experimental error and M is the number of fitted parameters. The value of RMSE represents the goodness of fit and the possible lowest value of it is desired in terms of accuracy between the data and the model (Cantas, Aygun, & Basa, 2014).

$$RMSE = \sqrt{\frac{1}{2N-M} \times \sum_{i=1}^{N} \left[\left(\frac{\psi_i^{\mathrm{mod}} - \psi_i^{\mathrm{exp}}}{\sigma_{\psi,i}^{\mathrm{exp}}} \right)^2 + \left(\frac{\Delta_i^{\mathrm{mod}} - \Delta_i^{\mathrm{exp}}}{\sigma_{\Delta,i}^{\mathrm{exp}}} \right)^2 \right]} \tag{5.9}$$

5.6.7. Electrical Characterization

I-V measurement of solar cell devices are taken so as to determine the efficiency. I-V experimental setup interfaced with a computer is shown in Figure 5.14. While obtaining the I-V curve of a CZTS cell, to generate the sweeping voltage a function generator was used. The amplitude and frequency of saw wave was set at 2Vp-p and 0.005 Hz, respectively. One probe from the function generator was placed on a resistor with 10 ohm resistance while the other probe was placed on the CZTS cell. Two Keithley nanovoltmeter are interfaced with a computer and controlled by Labview program that contains serial instrument control, data analysis and data storage. Probes of one of the nanovoltmeter were connected to the front contact and the back contact of the CZTS solar cell to measure the voltage across the device, while the probes of other nanovoltmeter were placed on the ends of the resistor to measure the current flowing out of the device.

Figure 5.14. I-V measurement system.

This four-probe arrangement helps to eliminate the contact resistance between the probe and contact interfaces. We used a halogen lamp as a light source, calibrated to provide the same short circuit current as that obtained from I-V measurements performed at METU.

The intensity of input light was 1 kW/m^2 and the devices were measured at room temperature, around 25 °C. Graphical programming tool of Labview program provides to see I-V curve, in which the current of the solar cell is plotted on y-axis against the applied voltage on x-axis.

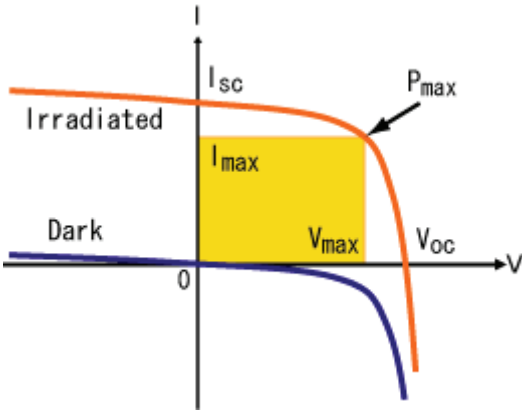

Figure 5.15. I-V curve of solar cell under dark and irradiated condition.

Light I-V measurements were used to determine the values of Voc, Isc, Vm, Im, FF and cell conversion efficiency, while dark I-V measurements are employed to determine loss parameters of solar cells such as R_S, R_{SH}, n, I_0. Figure 5.15. shows a dark IV curve, a light IV curve and the information about the device they reveal.

CHAPTER 6

RESULTS AND DISCUSSION

6.1. Absorber Layer Characterization

In this work the precursor of CZTS thin films were deposited sequentially stacked because stacked precursor has some beneficials when compared with simultaneous deposited precursors. Thanks to regulation of the thickness of each element, the compositional ratio can be easily checked. The 630 nm thick CZT metallic precursors were sputtered on Mo coated SLG substrates from bottom to top SLG/Mo/Cu/Sn/Zn/Cu. In terms of Cu layer thickness, two types of stacking order were used. Type I order is represented as SLG/Mo/Cu(55 nm)/Sn/Zn/Cu(120 nm) and Type II is represented as SLG/Mo/Cu(120 nm)/Sn/Zn/Cu(55 nm).

There are many reasons to select this stacking order such as; i) because of easily diffusion of Cu from bottom to top layer, the middle Zn layer can prevent to formation of vacancies which resulted the diffusion of Cu, ii) having low melting point (231.93 °C) Sn easily evaporate, so with this stacking order the Sn loss can be minimized, iii) due to the easily volatility of Zn, the middle Zn layer can prevent the ZnS phase formation at the surface.

To obtain CZTS p-type absorber layer, CZT precursors were annealed under S vapour and Ar atmosphere. The sulfurization procedure was performed inside a quartz glass tube in a furnace. Two graphite boxes with open cover were used. The 600 mg sulfur powder (99.98%) was added to the graphite box and placed to the edge of the furnace while the CZT precursor was placed into the center of the furnace inside with the other graphite box. As a carrier gas, 100 sccm Ar was sent into the quartz tube and the pressure was kept at atmospheric pressure during the sulfurization. The temperature of the furnace reached to 270 °C in 5 minutes and stayed at this temperature for 3 minutes. Then it was risen to 550 °C within 5 minutes.

For all CZTS films that used in this work were sulfurized at 550 °C for different time durations. The details of the sulfurization were mentioned in Chapter 5.1.2.

Table 6.1. Sulfurization parameters of CZTS samples. Here Type I and II represent SLG/Mo/Cu (55 nm)/Sn/Zn/Cu (120 nm) and SLG/Mo/Cu (120 nm)/Sn/Zn/Cu (55 nm) orders, respectively.

Sample	Order	Sulfurization Temperature (°C)	Sulfurization Time (min)
A	Type I	550	30
B	Type I	550	45
C	Type I	550	60
D	Type II	550	45
E	Type II	550	45
F	Type II	550	45
G	Type II	550	45

The length and the temperature of heat treatment are important because during the process a liquid phase might form and this might result the formation of de-wetting, accumulation of melted film to the edge of the substrate and phase segregation. In order to achieve grain growth, high temperature sulfurization (>500°C) is chosen. But it is possible to occur decomposition and volatilization of Zn and Sn elements at high temperature sulfurization (Olgar, Klaer, Mainz, Ozyuzer, & Unold, 2017). Although there were tried many sulfurization temperature, in this work we focused on the temperature of 550 °C. To understand how the CZTS growth process advances at 550 °C, three sulfurization durations, 30, 45 and 60 min, were tried. After the investigation of device characterization of CZTS films having Type I order, it was decided to continue sulfurize the CZTS films for 45 min. Therefore, it was followed 45 min sulfurization for the films having Type II order. Table 6.1. gives the order type and sulfurization condition of each sample.

6.1.1. X-Ray Diffraction (XRD) Analysis

X-Ray Diffraction technique allows a knowledge about the bulk of examined sample and its accuracy is 10%. CZTS structure grow from solid-state reaction between Cu_2SnS_3 and ZnS. Since, having similar crystal structure of ZnS, Cu_2SnS_3 and CZTS, it is very difficult to confirm their existence or co-existence in the sample, merely by XRD technique (Olgar et al., 2017). Due to the fact that the diffraction peaks of Cu_{2-x} is different from CZTS, this phase can be easily detected by XRD.

But, Cu related secondary phases can be eliminated by KCN treatment, the existence of this phase is not considered as a big problem for the CZTS absorber. It is also easy to detect SnS, SnS_2 and Sn_2S_3 phases by XRD. These phases form when the film is Sn rich in composition (Fernandes et al., 2011). Cu_xSnS_{x+1} (CTS) phases occur as a tetragonal-Cu_2SnS_3, cubic-Cu_2SnS_3 and orthorhombic-Cu_3SnS_4. Among them the solely orthorhombic-Cu_3SnS_4 can be easily defined by XRD, because cubic and tetragonal phases have similar unit cell sizes with CZTS as happening with ZnS (Fernandes et al., 2011). Figure 6.1. (a), (b) and (c) show the XRD patterns of CZTS films having Type I, Type II and both Type I and II order, respectively. As a comparison, Figure 6.1. (c) demonstrates the Type I and Type II CZTS films both sulfurized at 550 °C for 45 min. The results of peak assignments associated with CZTS were listed in Table 6.2. Although Type I samples sulfurized at different time duration, the XRD patterns of them are very similar. Since the Type II samples have the same growth parameters, as expected their XRD patterns are also the same which reflects the reproducibility of CZTS films.

Both Type I and II CZTS thin films show many characteristic peaks of kesterite CZTS (JCPDS 26-0575), Cu_2SnS_3 (JCPDS 027-0198) or ZnS (JCPDS 05-0566) at 28.50°, 32.99°, 47.33°, 56.17° and 58.97°. However the peaks at 37.0° (Alvarez Barragan, Malekpour, Exarhos, Balandin, & Mangolini, 2016) 29.67°, 37.96°, 44.99°, 58.97°, 69.23° and 76.44° (JCPDS 026-0575) link with only CZTS which supporting that the examined films contain CZTS structure (in Table 6.2.). Although the films consist of other characteristic peaks of kesterite CZTS, it cannot be ruled out the existence of ZnS or Cu_2SnS_3. It is possible to observe a mixture of CZTS, ZnS and Cu_2SnS_3 (Cheng et al., 2011). Cu_2S peak (45.8°) was not found in any sample.

Based on the XRD sensitivity, due to the fact that their most intense peaks are not exist, it can be ruled out the presence of Cu_2S (45.8°) (Cheng et al., 2011), CuS (31.8) (Cheng et al., 2011), SnS (31.53°) (JCPDS 039-0354), SnS_2 (15.02°) (JCPDS 023-0677), Sn_2S_3 (21.49°) (JCPDS 014-0619), Cu_3SnS_4 (27.31°) (Fernandes et al., 2010), Cu_4SnS_6 (29.58°) (JCPDS 036-0053). There is not any significant difference in the full-width-half-maximum (FWHM) values of the CZTS films. Type I films have 0.12° and Type II films have 0.16° FWHM values. The 15 min variation in sulfurization time does not influence the crystallinity but the change in stacking order results the little difference in the crystallinity of CZTS thin films. The XRD pattern of all films exhibit a diffraction peak at 40.5° which is the strongest peak of Mo (110) (JCPDS 042-1120) coming from the back contact. But this peak position also corresponds to MoS_2 at 40.99°, which has its

strongest peak at 14.4° (JCPDS 024-0515) and this region is outside where we focused on. The diffraction peak at around 73.60° might corresponds to (205) diffraction peak of MoS_2 at 73.66° (JCPDS 037-1492) and (211) diffraction peak of Mo at 73.68° (JCPDS 042-1120).

The XRD pattern of Type I CZTS films are consistent with a mixture of SnO_2 and the Cu_4SnS_4 phases because these phases contribute to the strongest diffraction at 26.61° (JCPDS 041-1445) and 26.70° (Cheng et al., 2011), respectively. However, the diffraction peaks at around 33.89 and 51.78° confirm the existence of SnO_2 (JCPDS 041-1445). For the CZTS films the segregation of SnO_2 is reported (Hazama, Tajima, Masuoka, & Asahi, 2016). Although any SnO_2 peaks were encountered in the XRD pattern of Type II CZTS films, they showed some different peaks which were not detected for the Type I CZTS films. The additional peaks were detected at 25.80°, 36.30°, 42.60° and 50.41°. These peak positions do not belong to CZTS, ZnS and Cu_2SnS_3. A detail investigations have revealed that MoO_2 has the strongest peak at 26.03° with (-111) plane (JCPDS 032-0671). Although the substrates were cleaned before the CZTS deposition, the existence of MoO_2 is the result of the Mo oxidation before uploading the substrate to deposition chamber. Another peak at 36.30° can be MoO_2 with (200) plane at 36.77° (JCPDS 032-0671) or ZnO with (101) plane at 36.25° which is the strongest peak of ZnO (JCPDS 036-1451). As a result of the detail investigation for the peaks detected at 42.60° and 50.41°, it was not found well matched peaks of any material. These peaks might belong to Cu-Sn-Zn related alloy formation. However, for a now, these peaks are unclear and under investigation.

The diffraction peak at around 76.44° can be related with (332) diffraction plane of CZTS (JCPDS 026-0575) or Cu_2SnS_3 (JCPDS 019-0412). Since we observed the strongest diffraction peaks of both phases, it cannot ruled out the existence of Cu_2SnS_3 phase. To calculate the average crystalline size for the strongest (112) CZTS peak, the Debye-Scherrer's formula as given with Equation 6.1 was used (Abd-Elkader & Shaltout, 2015).

$$D = \frac{0.9\lambda}{\beta \cos\theta} \tag{6.1}$$

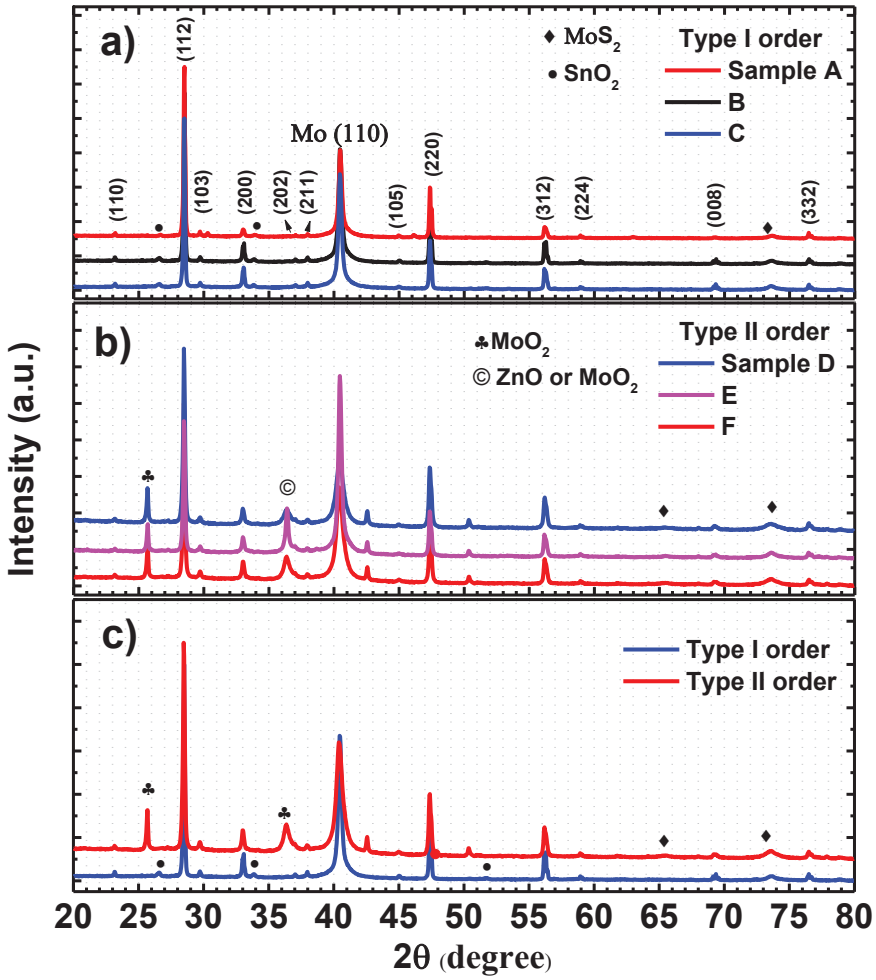

Figure 6.1. XRD spectra of CZTS films having stacking order a) Type I, b) Type II and c) Type I and Type II order CZTS films sulfurized for 45 min at 550 °C.

Here, the 0.9 is the particle shape factor which depends on the shape of the particles and this value is for spherical particles, β is the full width at half maximum (FWHM) of the selected diffraction peak, and θ is the Bragg's angle. The obtained crystalline size was 63.0 nm for the Type I films while for the Type II films this value was calculated as 50 nm. The size of the grains are not large. The large grains indicate the existence of $Cu_{2-x}S$ crystal (Fernandes, Salomé, & Da Cunha, 2009) but XRD analysis were not declared the formation of this phase.

Type I and Type II CZTS samples both showed the characteristic peaks of CZTS structure but both stacking orders showed some extra phases. SnO_2, MoO_2 and/or ZnO phases were detected for the Type I and Type II orders, respectively. According to XRD results, it was assumed that Type I order allows more Sn accumulation through the film surface and results the oxidation during the sulfurization.

For the Type II order, it was assumed that thick Cu layer on the Sn layer might increase the formation of Cu-Sn alloy in the vicinity of back contact and might reduce the Sn accumulation through the surface.

Table 6.2. The possible XRD peaks of CZTS films with Cu *Kα* radiation.

Structure (hkl)	2θ (°)	Source
CZTS (110)	23.10	JCPDS 026-0575
CZTS (112)	28.50	JCPDS 026-0575
CZTS (103)	29.68	JCPDS 026-0575
CZTS (200)	32.99	JCPDS 026-0575
CZTS (202)	37.02	JCPDS 026-0575
CZTS (211)	37.96	JCPDS 026-0575
CZTS (105)	44.99	JCPDS 026-0575
CZTS (220)	47.33	JCPDS 026-0575
CZTS (312)	56.17	JCPDS 026-0575
CZTS (224)	58.97	JCPDS 026-0575
CZTS (008)	69.23	JCPDS 026-0575
CZTS (332)	76.44	JCPDS 026-0575

The formation of Cu-Sn alloy may enhance CTS phase which contribute to CZTS formation. However, Type II order could not prevent the Zn accumulation through the surface of the films. Therefore, ZnO formation was detected for Type II CZTS films. In summary, due to the overlap of the strongest XRD peaks of CZTS, ZnS and Cu_2SnS_3, the existence of ZnS and Cu_2SnS_3 is still unclear. However, additional characterizations will differentiate these phases.

6.1.2. Surface Morphology and Composition

SEM images of the Type I CZTS films of A, B and C, Type II CZTS films of D, E and F are shown in Figure 6.2. and Figure 6.3. respectively. For the Type I films, it was not observed remarkable microstructure difference.

SEM image of sample A include different features at the edge of the image which might be the SnS_2 phase which was not detected by XRD because it might not densely form on film surface.

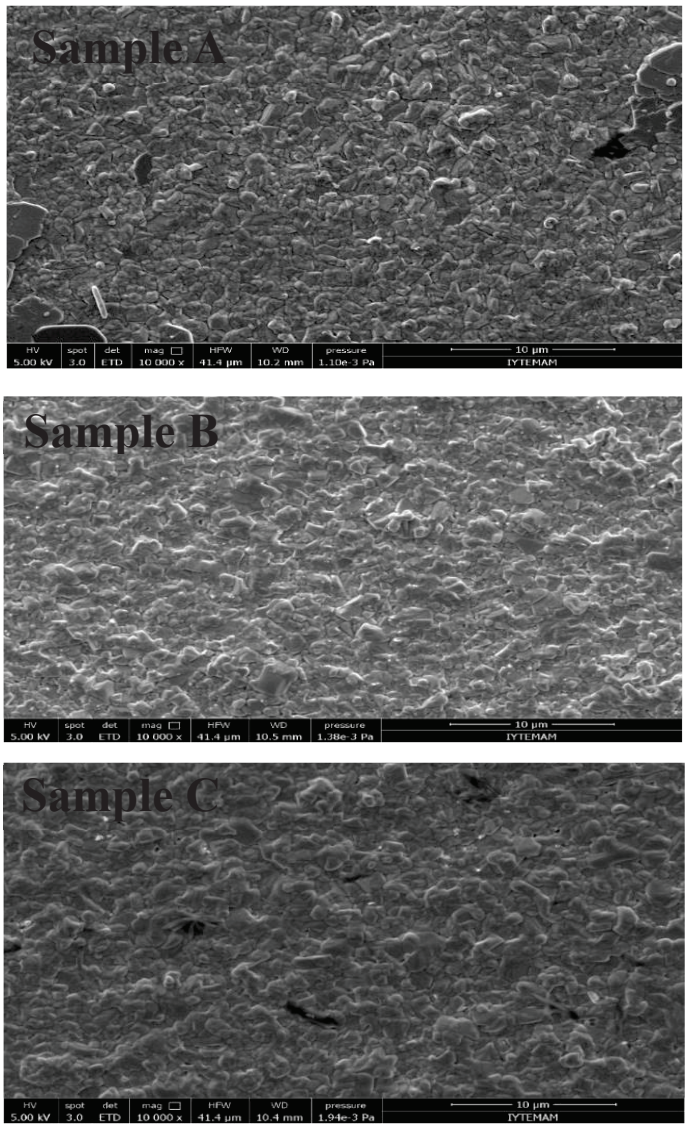

Figure 6.2. SEM images of CZTS samples (Type I order) of A, B and C.

Although different sulfurization time were used for the Type I CZTS films, remarkable difference of surface grain sizes were not detected. However, the surface morphology of the CZTS films of Type II are different. The change in the stacking order resulted the difference on surface morphology. As well as the grain size detected by XRD has difference of 10 nm, the difference in the surface grains is also seen from the SEM surface images of Type I and Type II samples. Although the grains of Type I CZTS films can be easily observed, they have inhomogeneous grain distribution.

However, the consisting of well-defined grain boundaries is important for CZTS absorber layer because they can behave as less recombination site for charge carriers (Khalkar et al., 2015). Type II CZTS films have similar surface structure with smaller grains than Type I samples. These similar structures show the reproducibility's of our films. In the literature the large grain size are detected for the films having Cu-rich composition (Scragg, 2010; Yeh, Lei, Lin, & Yang, 2016). The reason behind why Type I and II CZTS films have small grain size (based on the XRD analysis) is associated with that all CZTS films have Cu poor composition (except sample C) as given in the following EDS results.

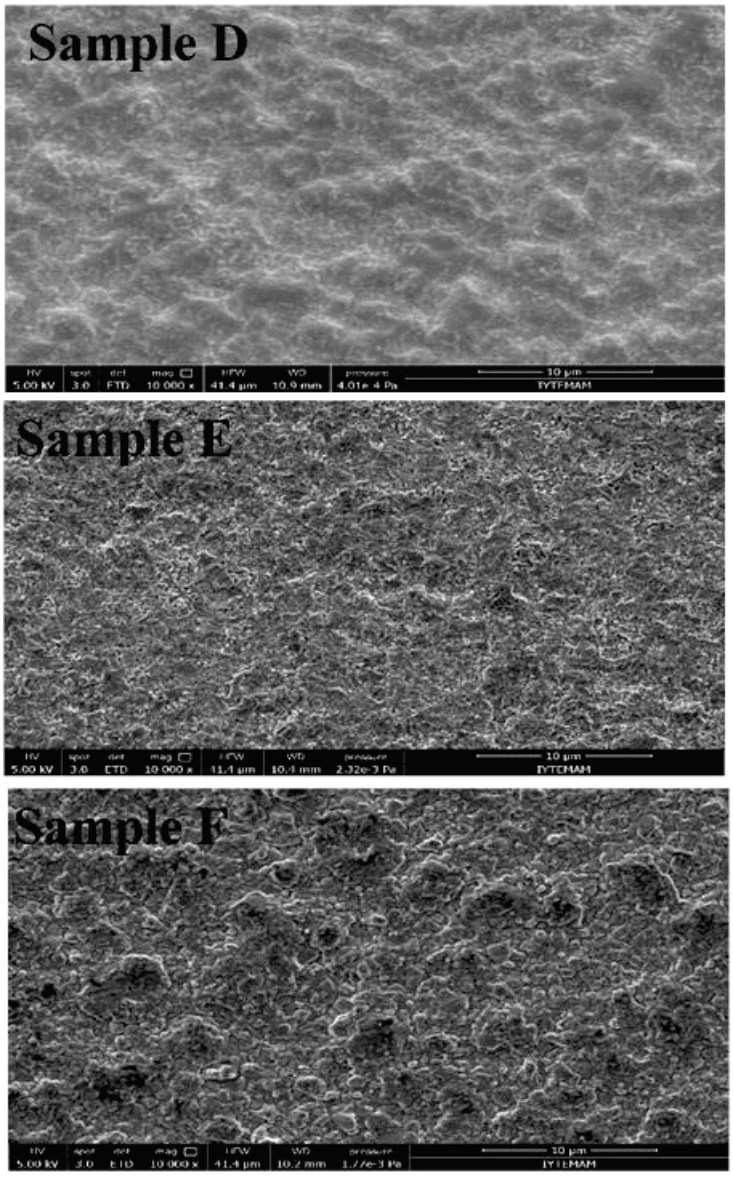

Figure 6.3. SEM images of CZTS samples (Type II order) of D, E and F.

But high Cu concentration might result Cu_2S secondary phase formation. Therefore, so as to obtain large grain size, it is important to well control of Cu atomic content. The elemental composition of the sulfurized CZTS films has been characterized by EDS whose sample penetration depth is 1μm and accuracy is 10%. The detected atomic concentrations of each element and atomic ratios of Cu/(Zn+Sn), Zn/Sn and S/Metal are shown in Table 6.3. Because each element independently changes in composition from the others, it is hard to tell for the films as 'Cu-poor', 'Zn-rich' etc. When the S element is reacted with metallic precursor, the amount entering the reaction bases on the quantity of the metal elements and the valence value of them such as Cu(I), Sn(IV) and Zn(II).

Since they are not independent each other, the atomic percent ratio of Cu/(Zn+Sn) and Zn/Sn are commonly used to describe the composition of CZTS films. Yet, these ratios cannot tell the deviations from the film stoichiometry.

Table 6.3. Having different sulfurization process, atomic percent of CZTS films determined by EDS.

Order	Sample	Atomic %				Cu/(Zn+Sn)	Zn/Sn	S/Metal
		Cu	Zn	Sn	S			
Type I	A	20.15	11.27	14.09	53.31	0.79	0.79	1.14
Type I	B	26.94	15.39	12.26	45.41	0.97	1.26	0.83
Type I	C	27. 50	14.90	11.93	45.67	1.02	1.25	0.84
Type II	D	20.96	13.48	11.09	54.47	0.85	1.22	1.20
Type II	E	20.33	13.41	11.36	54.90	0.82	1.18	1.22
Type II	F	20.72	13.57	11.33	54.37	0.83	1.20	1.19
Type II	G	20.78	13.58	11.20	54.40	0.84	1.21	1.19

The composition of Type I CZTS films showed that Cu-poor, Zn-poor, Sn-rich for the film A, slightly Cu-poor, Zn-rich for the film B and Zn-rich for the film C. Although there is little deviations from each other, the Type II films are generally Cu-poor and Zn-rich composition. As given in Table 6.3, while the sulfurization time is increasing the Sn concentration decreases due to the loss of Sn from the bulk. The Sn loss process is commonly encountered in the literature.

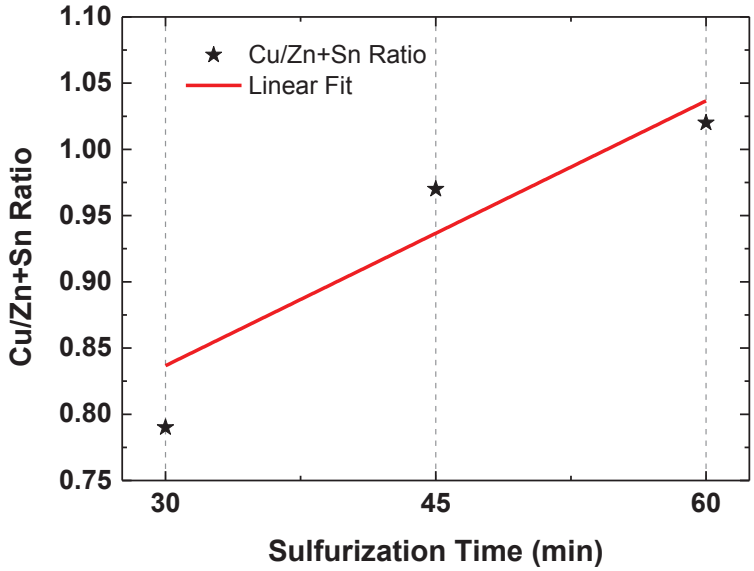

Figure 6.4. Sulfurization time dependence of Cu/Zn+Sn for the Type I samples.

Depending on the Sn concentration, in Figure 6.4. the Cu/Zn+Sn ratio increases with sulfurization time. Figure 6.5. shows the cross section of Type II CZTS D. According to thickness calibration CZTS film was grown 1.2µm but MoS_2 formation was detected. This result indicates that during the sulfurization, the diffusion of sulfur through the Mo coated substrate and resulted MoS_2 interface. For the Type I CZTS, because all CZTS films was used for fabrication of solar cell, we could not take the cross section of them.

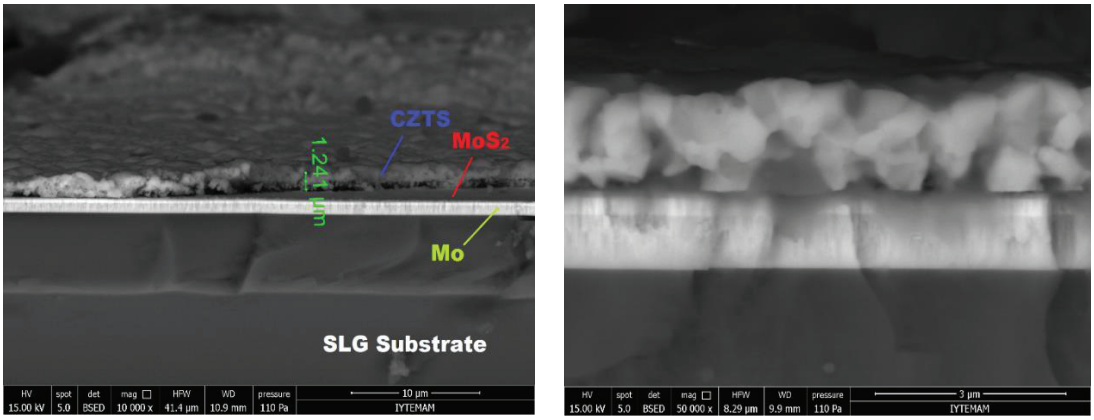

Figure 6.5. The SEM cross section of Type II CZTS sample D at different magnifications and regions.

In order to enhance the conductivity of CZTS films, it is necessary to increase the formation of Zn_{Sn} acceptors and to diminish the Sn_{Zn} donors. To achieve this, Zn/Sn ratio would be higher than 1 (Yeh et al., 2016).

But, high amount of Zn might have detrimental effects with lowering Cu/Zn ratio and decreasing the conductivity as well as changing the conduction type. Therefore, the Zn/Sn atomic ratio is important factor for determining the conduction type of CZTS (Yeh et al., 2016).

Furthermore, sulfur vacancy (V_S) which is a donor defect is another crucial parameter for the CZTS conductivity due to its low formation energy it is dominantly observed. The S-poor CZTS film results high concentration of V_S which might change the conduction type of CZTS from p-type to n-type as well as decrease the holes concentration (Yeh et al., 2016). Therefore, high content S is important to diminish V_S and obtain p-type conductivity of CZTS. Yeh *et al*, investigated the effect of sulfur content to the conductivity of CZTS films by changing thiourea concentration inside the solution, they recorded that S-rich CZTS films which have S/Cu+Zn+Sn ratios of 1.09 and 1.19 showed higher p-type conductivity than the S-poor CZTS films (Yeh et al., 2016).

When compared the Type I and Type II samples in terms of S content, there appears different opinions. Although the Type I samples have low sulfur content, the sample A has high amount of S. In Figure 6.2. SEM image of CZTS A thin film seem to have some particles on the surface that have more flat surface than surrounding. This structure was detected before for the different CZTS sample as given in Figure 6.6. and the EDS point analysis of those particles showed Sn rich composition which is strongly be SnS_2 formation.

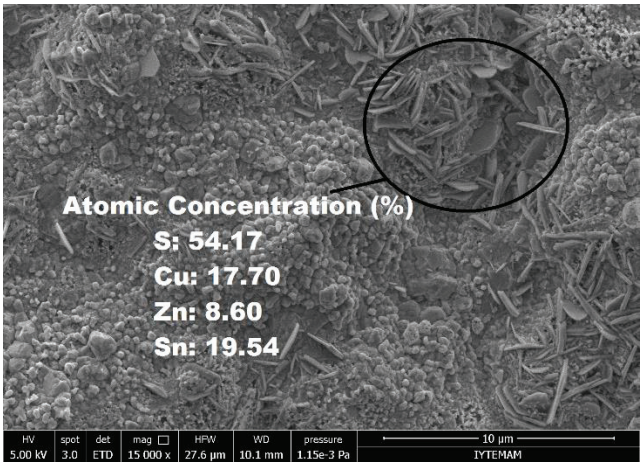

Figure 6.6. Demonstration of SnS_2 formation for different CZTS sample.

If the sulfur content is higher than 50% and at the same time the Sn content is higher than Zn, this results the formation of SnS_2. However, as seen in Figure 6.2. SnS_2 formation on CZTS A is not dense when compared with Figure 6.6. and also was not detected by XRD. The samples B and C has less S content than 50% which might decrease the p-type conductivity of CZTS. However, in terms of metal content the samples B and C in Type I and all Type II samples have the desired non-stoichiometric compositions to obtain efficiency. As given in the literature, it is reported that Cu-poor and Zn-rich compositions is necessary to achieve plausible efficiency.

6.1.3. Raman Analysis

The detected depth using Raman Spectroscopy is between 0.2 and 10 μm with the accuracy of 100%. Since the back scattering configuration is used in Raman scattering analysis, the penetration depth (d) of the incident light should be $d=1/2\alpha$ where α is the absorption coefficient of the examined sample.

If the absorption coefficient of CZTS is considered as higher than 10^4 cm^{-1}, the penetration depth of Raman laser with 514 and 633 nm wavelength are 150 and 170 nm, respectively (Fernandes et al., 2011). Due to the structural similarities of CZTS, ZnS and CTS in XRD analysis, Raman spectroscopy is widely used technique for structural characterization because the frequency and peak intensity are strongly sensible to the existence of defects in material (Skelton, Jackson, Dimitrievska, Wallace, & Walsh, 2015).The vibration of each anions and cations are observed in the specific frequency range. The phonon states between 250 and 300 cm^{-1} consist of the vibration of Zn cations, S anions and Cu cations. The vibrations of S anions make form the phonon states lying from 310 to 340 cm^{-1}. The phonon states from 340 to 370 contain the vibrations belonging to Sn cations and S anions (Khare, Himmetoglu, Johnson, et al., 2012). Raman measurements of A, B and C CZTS thin films were taken with 514 nm wavelength laser (depth is 150 nm) whereas for the film D and E, laser with 633 nm wavelength (depth is 170 nm) was used. The phonon modes below 200 cm^{-1} were not studied in this research. The variations in peaks shape and locations were observed. The peak enlargement was detected for the Raman spectrum of sample A, B and C. In the case of phonon confinement effect or the structural defects, the peak broadening and the shift to lower frequency side of the Raman peak can be observed for samples with crystal size lower

than 50 nm (Guc et al., 2016). The broadening of the band between 275 and 320 cm^{-1} could be assigned to the presence of ZnS (278 cm^{-1}), tetragonal CTS (297 cm^{-1}), SnS_2 (314 cm^{-1}) and cubic CTS (267, 303 cm^{-1}) secondary phases in addition to kesterite CZTS. A second broad band is also visible between 325 and 350 cm^{-1}. The broadening of this band could be imputed to a ZnS (352 cm^{-1}), tetragonal CTS (352 cm^{-1}), cubic CTS (356 cm^{-1}) and orthorhombic CTS (348 cm^{-1}) (Fernandes et al., 2011).

In this thesis, an intense and also broad Raman spectrum was observed for the films A, B and C. The bulk sample growth conditions effect this type of broadening such as high temperature thermal treatment and fast cooling of the sample. In order to obtain a more quantitative analysis, the fitting of the Raman spectra which include a very detailed analysis of the vibrational properties of CZTS were performed. During the deconvolution process of experimental Raman scattering of CZTS films, the Lorentzian line shape was used and the peak positions were let to change in order to get the best matching with the experimental spectra. At the end of the fitting process, ıt was observed that the sum of all synthetic peaks (red line) gave well matching with the experimental Raman spectra (solid black spheres).

The goodness of peak fitting were determined by the r-square value which is offered by the OriginPro 9 software. The better the quality of the peak fit, the closer the r-square value is to 1. The obtained r-square values are 0.97, 0.96, 0.98 and 0.99 for the CZTS films of A, B, C and D, respectively. The fitting of the spectra with Lorentzian curves revealed the existence of many contributions from different vibration modes. In Figure 6.7. the peak fitting results of Type I samples of A, B, C and Type II sample of D are given. The Table 6.4 the peak fit results of each CZTS sample were listed.

Deconvolution was developed markedly when we assumed that the intense and broad spectral region consists of two peaks, one at around 330-331 cm^{-1} and another at around 337 cm^{-1} (Figure 6.7.). Although the main Raman peak of CZTS is observed at 337-338 cm^{-1} which is assigned to the vibration of sulfur anions in kesterite CZTS, deconvolution results gave that the main peaks were at 331.7, 330.2, 330.9 and 330.7 cm^{-1}, for the films A, B, C and D respectively. In the literature, the peak observed between 330-331 cm^{-1} is called as a partial disordered kesterite (PD-KS) phase which is detected in the non-stoichiometric films (Kaushik, Rao, & Subrahmanyam, 2017). The existence of disorder in the Cu and Zn sublattices might result the change in crystal symmetry of CZTS films from kesterite to disorder kesterite.

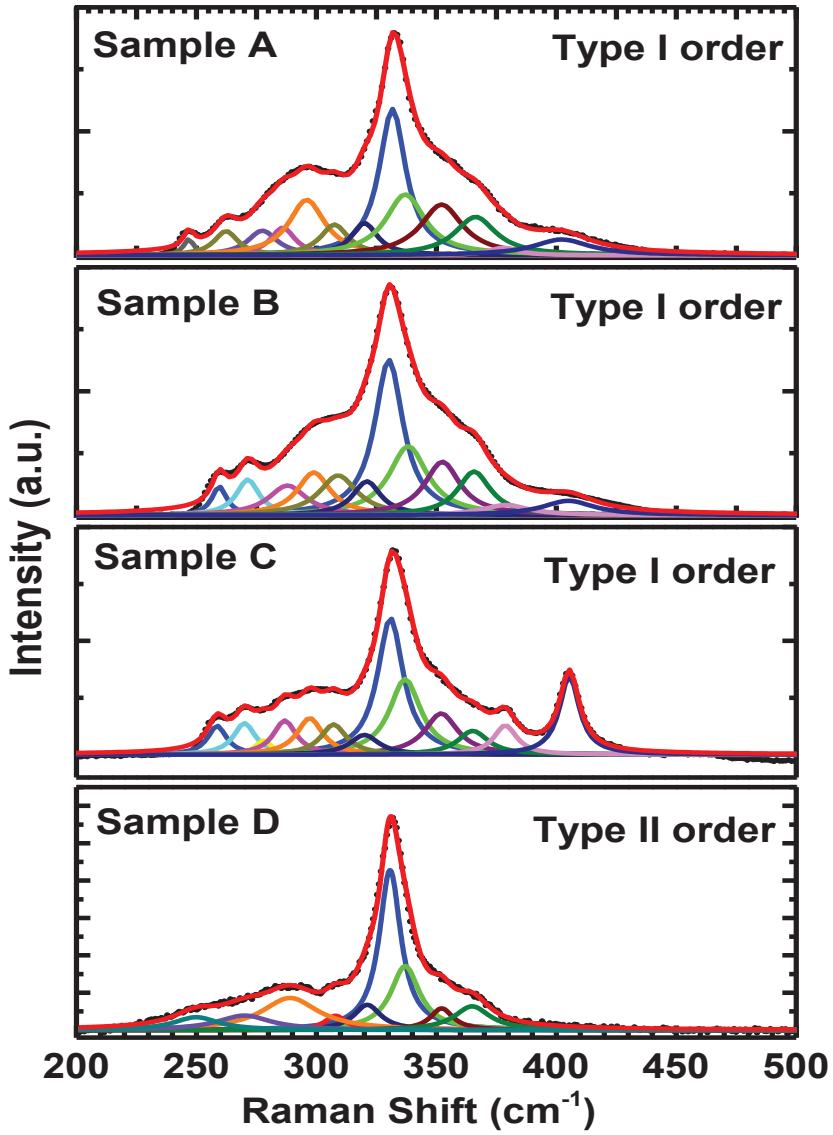

Figure 6.7. Fitting of Raman spectra of CZTS thin films having stacking order Type I (A, B and C) and Type II (D). The black spheres show the experimental data, Lorentzian curves in different color represent the synthetic peaks of the spectrum and the red line gives the envelope of the synthetic peaks.

Schorr *et al*, demonstrated the partially disorder kesterite (PD-KS) for the disorder of Cu and Zn atoms lying Cu+Zn (001) layer by using neutron diffraction technique (Schorr, Hoebler, & Tovar, 2007). The KS and ST structures have 3 meV/atom binding energy difference (Chen et al., 2009). The PD-KS peak observed between 330-331 cm^{-1} might be thought as a first step of this kind transformation. Consequently, it can be presumed that the binding energy difference between KS and PD-KS structures might be lesser than 3 meV/atom (Valakh et al., 2013).

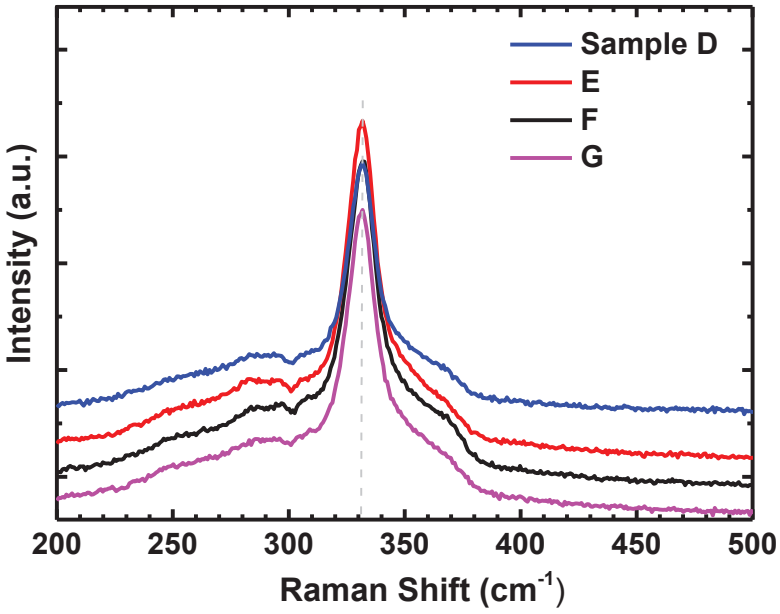

Figure 6.8. Raman measurements of CZTS films growing with Type II order.

Figure 6.8. shows Raman measurements of all Type II CZTS films which is not seen remarkable differences between each film so demonstrates the reproducibility Although the main A symmetry mode in CZTS is constituted the only vibration of S anions, the statistical disorder in the nearest Cu and Zn cations results the widening of this mode (Valakh et al., 2013). The atomic mass of Zn is 65.38 g/mol which is higher than the atomic mass of Cu 63.54 g/mol. In the case of Zn rich and Cu poor stoichiometry, the atomic distribution of Zn cations will be higher than the Cu cations near the S anions and will result the increase in effective masses. The increase in the effective masses causes the reduction in the frequency value. The existence of a PD-KS phase reflects the view of a widened A symmetry mode at lower frequency than the main kesterite A symmetry mode at 337-338 cm^{-1}. It is put forwarded that the peak observed nearly at 331 cm^{-1} has been assigned to Cu-poor CZTS films with a high concentration of instrinsic structural defects. These defects are the result of Zn antisite on Cu atom (Zn_{Cu}) and Cu vacancy (V_{Cu}). In addition to this, the peak seen at 331 cm^{-1} has been reported the presence of local structural inhomogeneity within the disordered cation sublattice (Hall, 1978). For the Cu-poor CZTS films, it has been reported that all Zn-atoms and half of the Cu-atoms are statistically distributed on both 2c (0,1/2,1/4) and 2d (0,1/4,3/4) sites (Schorr et al., 2007). Therefore the space symmetry changes from KS phase (*I*4 space group) to a PD-KS phase (*I*42m space group) which is very close to ST phase.

Chen *et al*, have theoretically calculated the physical properties of the PD-KS structure and they have shown that the disorder in Cu+Zn layer results an expansion in volume of 0.3%. Since PD-KS does not follow the octet rule it has higher energy than ST and PMCA crystal structures but its crystallographic symmetry equals to ST structure (Chen et al., 2009). Since the contribution of Cu and Zn elements to the band structure is not strong, the shape of total density of states (DOS) nearly similar for KS, ST and even PD-KS (Chen et al., 2009). There are some techniques to detect Cu-Zn disorder, but they have some limitations. Having been neighbor on the periodic table Cu and Zn have equal number of electrons and they have same atomic form factors so X-ray techniques cannot differentiate Cu^{+} and Zn^{+2} (Schorr et al., 2007). Due to having different neutron scattering length, neutron diffraction capable to differentiate Cu and Zn but they are not convenient for thin films. Nuclear Magnetic Resonance (NMR) is sensible to Cu-Zn disorder in CZTS powder (Scragg et al., 2014) thus, Raman spectroscopy is favorable to detect this disorder. In addition to PD-KS peak, all films have also two strong peaks at about 286-288 and 337-338 cm^{-1} which is assigned to main vibrational A symmetry modes of KS CZTS. The presence of these peaks declared the fact that, CZTS films in this work are the mixture of two CZTS mode of PD-KS and KS which is not unusual for the non-stoichiometric compositions.

Also, PD-KS and KS structures have very close formation energy, the observation both of them in the same film is possible. The Raman spectrum of sample A is more broaden than the other films. Peak fit result showed a peak at 246 cm^{-1} which was not detected for the film B, C and D. The presence of this peak accompanied by the E (TO) vibration mode of CZTS (Dumcenco & Huang, 2013). Meanwhile, because the E and B modes include both anion and cation vibrations, they show LO-TO splitting. The sample D also contain a peak at 250 cm^{-1} which attributed to B(LO) vibration of KS-CZTS (Dumcenco & Huang, 2013). The features observed in deconvolution of sample B and C at 258 cm^{-1} correspond to E(LO) mode of KS CZTS. This peak has been detected experimentally at 255 cm^{-1} whereas calculated at 257.85 cm^{-1} (Dumcenco & Huang, 2013). The peak which was observed directly and better resolved as a result of deconvolution at 270 cm^{-1} in the spectrum of sample B, C and D attributed to A vibration mode of KS CZTS. Even though this mode has not been observed experimentally, the theoretical calculations by Khare *et al*, already reported the existence of this vibration mode for KS CZTS (Khare, Himmetoglu, Cococcioni, & Aydil, 2012).

Deconvolution of sample A and C showed a contribution to the Raman spectra different from sample B and D. This additional peak observed at 278 cm^{-1} (Cheng et al., 2011) which can be assigned to either ZnS secondary phase or to E(TO) vibration mode of KS CZTS (Guc et al., 2016). However, this peak needs to be weak because it can be ZnS. The other common peak for all films, which was not experimentally resolved in the spectra but appeared as a result of deconvolution of the experimental spectra was between 296 and 297 cm^{-1} and can be attributed to tetragonal Cu_2SnS_3 (CTS) secondary phase (Fernandes et al., 2011). However, the sample D does not include a peak at that point. In Figure. 6.7. for the films A, B and C the intensity of this peak diminishes while the sulfurization time increasing. It can be thought that, forming at the early time of sulfurization tetragonal CTS phase turns to CZTS as sulfurization time increasing. The samples A, B, C and D has the Raman peak at 307.5, 308.0, 307.2 and 307.8 cm^{-1}, respectively.

Table 6.4. Frequency (cm^{-1}) of detected phases from fitting of Raman spectra and related symmetry.

Symmetry	**Detected phases (cm^{-1})**	**Detected Samples**
A, KS	337-338	A,B,C,D
Disordered KS	330-331	A,B,C,D
A, KS	286-288	A,B,C,D
E(TO), KS	246	A
B(LO), KS	250	D
E(LO), KS	258	B,C
A, KS	270	B,C,D
E(TO) KS/ ZnS	278	A,C
Tetragonal CTS	296-297	A,B,C
B(TO) KS	307.2-307.8	A-D
B(LO) KS	320	A,B,C,D
B(TO) KS/ ZnS	352	A,B,C,D
E(LO) KS	365-366	A,B,C,D
KS	378	A,B,C
MoS_2	402.3, 404.0, 405.4	A,B,C

The theoretical calculations of Khare e*t al*, and Guc *et al*, have been reported that this mode with a peak located at 307.6 cm^{-1} is identified as B(TO) vibration of KS CZTS (Guc et al., 2016; Khare, Himmetoglu, Cococcioni, et al., 2012). The shift between the calculated and the experimental peak positions might be based on LO-TO splitting (Khare, Himmetoglu, Cococcioni, et al., 2012). The other common peak which was not well resolved in Raman spectrum but detected by peak fitting of all samples was encountered at 320 cm^{-1}. This uncommon peak has been observed experimentally and assigned to B(LO) vibration mode of KS CZTS (Guc et al., 2016).

In the case of peak at 352 cm^{-1} observed a decrease in the intensity while the sulfurization time increasing. This peak might be attributed to either ZnS secondary phase or the B(TO) vibration mode of KS CZTS (Guc et al., 2016). Although we detected the main vibration mode of CZTS, the presence of ZnS secondary phase cannot be ruled out. The formation of ZnS secondary phase is possible because it is generally detected for the CZTS having Zn rich and Cu poor composition.

However, because of its high bandgap value (3.7 eV) (Alvarez Barragan et al., 2016) to detect the presence of ZnS exactly UV Raman excitation with 325 nm wavelength could be needed. On the other hand, fitting spectra gave also a contribution between 365 and 366 cm^{-1} for all samples which has been identified with E(LO) mode of KS CZTS (Dimitrievska et al., 2014). The peak fit results of all Type I CZTS films have a Raman peak at 378 cm^{-1} which might be attributed to KS CZTS structure which is seen at 375 cm^{-1} (Olgar et al., 2017).

The Raman measurements demonstrated the presence of additional vibration modes at about 402.3, 404.0 and 405.4 cm^{-1} for the films A, B and C, respectively which is the characteristic A_{1g} mode of the MoS_2 interfacial phase. Although any peak associates with MoS_2 was not detected for the Type II film of D, it does not mean that there is not this phase because from the XRD measurement the existence of MoS_2 layer was detected. Maybe this layer is too thin to be determined by Raman measurement. The position of this peak links with the thickness of MoS_2 layer. While the thickness increases the peak position of this vibration mode shifts through the higher frequency side where the bulk position at 408 cm^{-1} (Li et al., 2013). Li *et al* has also reported that for the 514 nm wavelength laser the peak positions 403, 404.8 and 405.8 cm^{-1} contributes to the monolayer, bilayer and trilayer of MoS_2, respectively. In this thesis, for the sulfurization time 30 and 45 min there were slightly appeared MoS_2 peak whereas for the sulfurization time of 60 min the sharp MoS_2 peak was detected.

This means that whilst the sulfurization time increasing the penetration of sulfur increases also and results the MoS_2 interface layer. In summary, the CZTS film A represents SnS features on surface images but this formation was not detected neither XRD nor Raman analysis. From the Raman measurements of all CZTS films, any formation of Cu_2S was detected at 475 cm^{-1} which supports the XRD analysis. Since both XRD and Raman peaks of CZTS and ZnS overlap, the existence of ZnS is still not clear. UV excitation is needed to differentiate ZnS formation. Since the XRD peaks of CZTS and Cu_2SnS_3 overlap, with the help of Raman analysis the presence of Cu_2SnS_3 secondary phase for the Type I CZTS films was shown but Type II CZTS film did not contain any characteristic Raman peak of Cu_2SnS_3 phase. The sulfurization time enhanced the penetration of sulfur through the Mo back contact and caused the thicker MoS_2 layer.

Since both Type I and Type II CZTS films were prepared for non-stoichiometric composition, this revealed point defects and secondary phases with respect to growth conditions; due to the presence of these defects the disorder in the lattice were detected.

6.1.4. X-Ray Photoelectron Spectroscopy (XPS) Analysis

The XPS spectra of CZTS films were analyzed so as to identify the surface composition distribution and chemical bonding states of the constituent elements. The high resolution spectra of C*1s*, S*2p* Cu*2p*, Sn*3d* and Zn*2p* valence regions were measured in detail and calibrated with respect to C*1s* peak at 284.6 eV (Yazici et al., 2015). In order to identify the atomic multivalency of each element in CZTS, high resolution spectra were de-convoluted. In addition, to calculation the atomic concentration of constituent elements, the area of peaks and sensitivity factors of each elements provided by the CASAXPS software were used. Before the de-convolution, the Shirley type background was subtracted to the high resolution spectra of each elements and Gaussian-Lorentzian product GL(p) function was used by considering the theoretical assumptions. The Zn, Cu, S *2p* and Sn *3d* peaks occur as doublets of $2p_{3/2}$, $2p_{1/2}$ and $3d_{5/2}$, $3d_{3/2}$.

The *2p* spectra was fitted using I($2p_{3/2}$):I($2p_{1/2}$) intensity ratio of 2:1 whereas *3d* spectra was fitted using I($3d_{5/2}$):I($3d_{3/2}$) intensity ratio of 3:2 (Yazici et al., 2015). During the fitting process, spin-orbital splitting values and FWHM value of each couple elements were constrained. Constrains on the peak positions were not applied.

Because of the electron transpose while the bonding process which results the change in net charge, little deviations are observed in the binding energies of the same element of different CZTS films (Moholkar, Shinde, Babar, Sim, Kwon, et al., 2011). Figure 6.9. (a) and (b) demonstrates the peak fitting results of Cu and Zn *2p* valence regions, respectively of Type I (sample A, B and C) and Type II (sample D) samples.

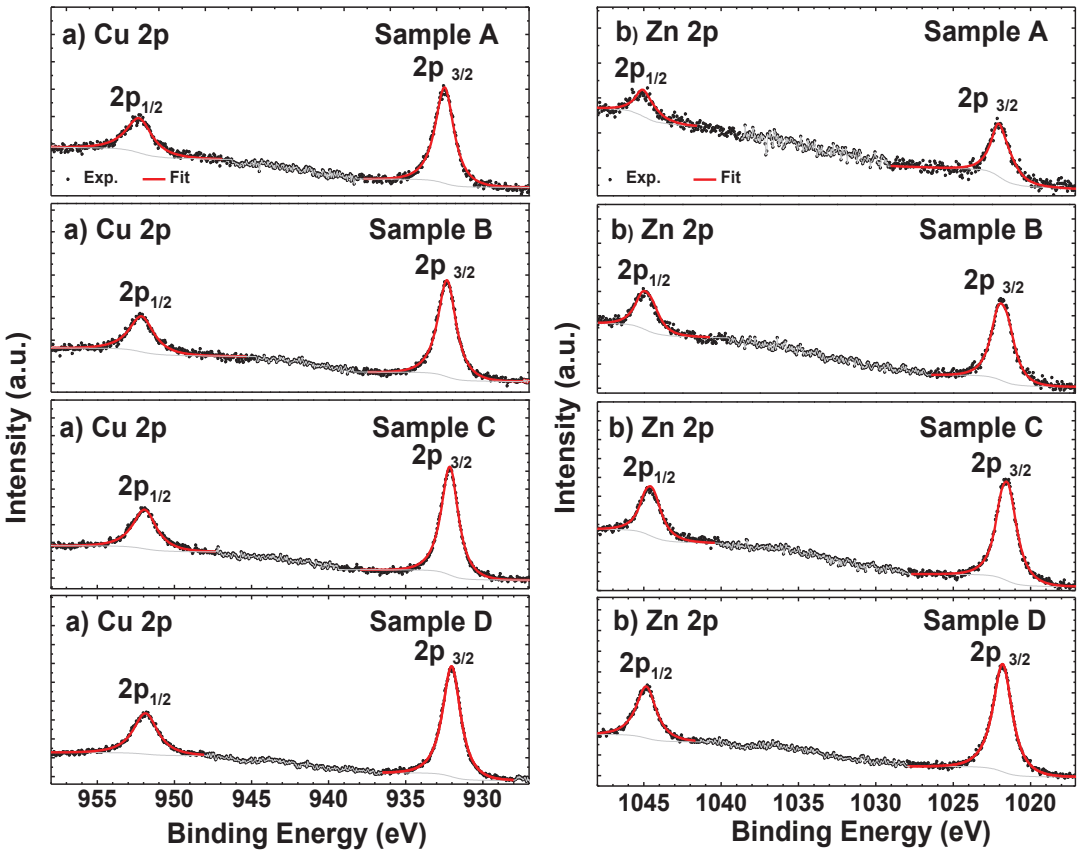

Figure 6.9. XPS peak fitting results of Type I (Sample A, B and C) and Type II (Sample D) CZTS films a) Cu, b) Zn *2p* valence regions.

In Figure 6.9. (a) The Cu *2p* core levels are seen as Cu $2p_{1/2}$ and $2p_{3/2}$ coupled doublets with peak splitting of 19.8 eV which is indicative of monovalent copper, Cu (I), and it is consistent with the reported literature values (Mali et al., 2012; Ricardo, Su'ait, Müller, & Scardi, 2013; Yin et al., 2013). During the peak fitting of Cu *2p* regions, GL(90) line shape was used and the results were listed in Table 6.5. $2p_{3/2}$ peak positions are detected at 932.5, 932.3, 932.2 and 932.0 eV.

Cu $2p_{3/2}$ peak is given between 932.0 (Moholkar, Shinde, Babar, Sim, Kwon, et al., 2011) and 932.5 eV (Hurtado et al., 2014) that allows to conclude that copper is in the +1 oxidation state Cu(I).

The well-known shake up satellite shoulder between 940-945 eV (Ruan et al., 2014) which is a clue about the presence of CuO was not detected, therefore, the Cu^{2+} (Cu(II)) state is absent. In the Cu $2p_{3/2}$ peak region it was not detected a shoulder between 935.0 and 935.5 eV which represents the $CuSO_4$ formation (Krylova & Andrulevičius, 2009). It can be came to conclusion that neither copper oxide nor copper sulfate phases formed on the film surface.

Zn *2p* spectra were fitted using GL(90) line shape and consist of $2p_{1/2}$ and $2p_{3/2}$ with a doublet separation of 23.0 eV which can be attributed to bivalent zinc Zn (II) (Deepu et al., 2014). Figure 6.9. (b) shows peak fitting of Zn *2p* valence regions of Type I (A, B and C) and Type II (D) samples. The $2p_{3/2}$ peaks were appeared at 1021.9, 1021.8, 1021.6 and 1021.8 eV for the films A, B, C and D, respectively. These peaks could be attributed to the existence of Zn^{2+} (Ruan et al., 2014). The peak position of Zn $2p_{3/2}$ attributes to Zn in CZTS or Zn in ZnO.

The peak fitting analysis of Sn *3d* core level (Figure 6.10. (a)) was done according to GL(55) line shape and the spectra were observed as $3d_{3/2}$ and $3d_{5/2}$ doublets with peak separation of 8.4 eV. As a result of de-convolution of film A, B and C, one of Sn $3d_{5/2}$ peak observed at 486.6, 486.7 and 486.6 eV, respectively. These peak positions match with Sn $3d_{5/2}$ peak of SnO (Kwoka & Krzywiecki, 2017) phases. The other Sn $3d_{5/2}$ peaks were observed at 486.3 for the Type I films and at 486.4 eV for the Type II film. In the literature Sn $3d_{5/2}$ peak is given at 485.3 (Deepu et al., 2014), 486.2 (Shin et al., 2011) and 486.4 (Hurtado et al., 2014) eV which confirms the Sn(IV) electronic state as expected for CZTS formation.

The S *2p* spectra was observed (Figure 6.10. (b)) in the range of 160 to 164 eV which assign to the S in metal sulfides (Das, Frye, Muzykov, & Mandal, 2012). All S *2p* valence regions were fitted using GL(75) line shapes. The peak fitting result of all S *2p* spectra show more than one $2p_{3/2}$ and $2p_{1/2}$ doublets each of which is constrained to have a binding energy difference of 1.2 eV. The S *2p* region of sample A is wider than the other films. This represents the existence of additional S peaks. Therefore, the peak fitting results of sample A contained three and the other films contain two couples of S *2p* peaks. The detected peak at 161.6 and 161.7 eV attributed to monosulfide S^{-2} (Das et al., 2012; Ruan et al., 2014) as expected for CZTS structure. An additional peak was observed for the films A, B and C at 162.2, 162.0 and 162.2, respectively. The position of these peaks were assigned to disulfide (S_2^{-2}) (Yazici et al., 2015).

At the higher binding energy side, the peak at 163.9 eV for the film A was detected which corresponding to S-S bonds (Krylova & Andrulevičius, 2009).

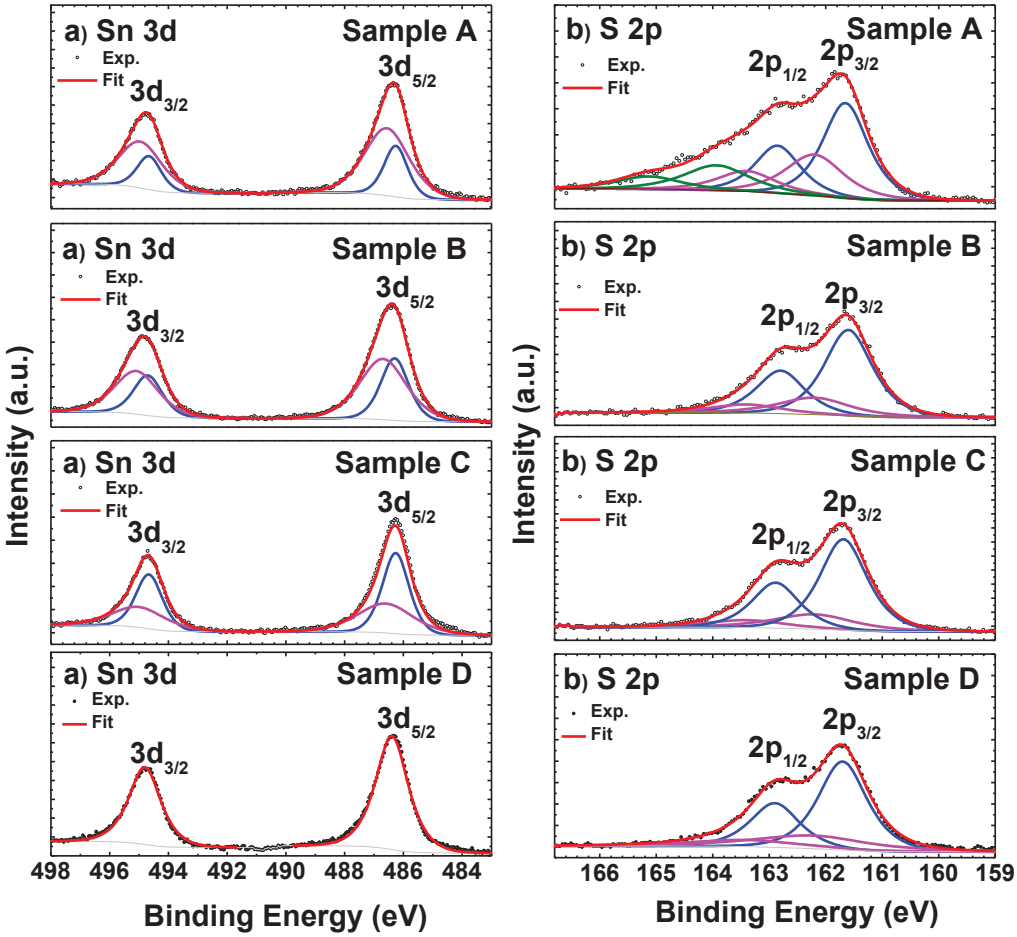

Figure 6.10. XPS peak fitting results of CZTS films a) Sn *3d*, b) S *2p* valence regions.

S *2p* spectra of sample D, the second S *2p* peak was detected at 163.4 eV which represents the polysulfide (S^{-2}_n where $2 \leq n \leq 8$) phase (Yazici et al., 2015) on the surface of films.

Table 6.5. Peak fitting results of main XPS core levels of Type I and Type II CZTS films.

Sample	Zn $2p_{3/2}$ (eV)	Cu $2p_{3/2}$ (eV)	1st Sn $3d_{5/2}$ (eV)	2nd Sn $3d_{5/2}$ (eV)	1st S $2p_{3/2}$ (eV)	2nd S $2p_{3/2}$ (eV)	3rd S $2p_{3/2}$ (eV)
A	1021.9	932.5	486.3	486.6	161.7	162.2	163.9
B	1021.8	932.3	486.3	486.7	161.6	162.0	-
C	1021.6	932.2	486.3	486.6	161.7	162.2	-
D	1021.8	932.0	486.4	-	161.7	-	163.4

After the deconvolution process, the surface quantification of CZTS films were calculated by following the equation 6.2.

$$C_x = \frac{(I_x/S_x)}{\Sigma I_i/S_i} * 100 \quad (6.2)$$

Here, C_x, I_x and S_x are the atomic %, area and the atomic sensitivity factor of element x which constitutes the sample. The I_i and the S_i are the area and the atomic sensitivity factor of i-th element inside the sample. The quantification of CZTS surface structures were listed in Table 6.6. Although there are some correlations with the compositions determined from EDS, the results of XPS showed that the surface composition of each film is different from the deeper layer composition which determined by EDS analysis. This results claimed that CZTS films are not homogeneous towards the depths of the films and they have different atomic compositions.

In Table 6.6, it is seen that all CZTS films are sulfur deficient at the surface except the CZTS A. SEM images of this film showed some different features at the edge of the graph which was considered SnS_2 secondary phase formation.

Since both EDS and XPS composition results demonstrated that the CZTS A has the sulfur concentration above 50% and the Sn concentration higher than the Zn, supporting the formation of SnS_2 on the surface.

Table 6.6. The surface quantification of Type I and Type II CZTS films.

Order	Sample	Atomic %				Cu/(Zn+Sn)	Zn/Sn	S/Metal
		Cu	**Zn**	**Sn**	**S**			
Type I	**A**	17.8	8.3	19.4	54.5	0.6	0.4	1.2
Type I	**B**	18.1	14.3	27.0	40.6	0.4	0.5	0.7
Type I	**C**	19.0	19.3	18.3	43.4	0.5	1.1	0.8
Type II	**D**	25.8	19.2	14.9	40.1	0.8	1.3	0.7

The Sn concentration at the surface of Type I samples were higher than the EDX results of the same samples. This is because that during the evaporation of Sn from the CZTS films might form SnO_2 which was detected by XRD analysis and increased the Sn concentration at the surface. Sn concentration of Type II sample D is lower than the Type I CZTS films. Since we thought that the change in the stacking order from Type I to Type II might diminish the Sn loss during the CZTS growth process. Therefore, to decrease the Sn loss from the CZTS during the sulfurization and to form Cu-Sn alloy formation, the stacking order was changed and in Type II order instead of thin Cu layer, the thick Cu layer was deposited adjacent to Sn layer. According to XPS quantification results, Type II CZTS D contains 14.9 % Sn element on the surface which was diminished by the changing the stacking order. The decrease in Sn composition may be caused by allowing Cu-Sn alloy formation and reducing Sn accumulation through the film surface.

Su *et al*, investigated the formation of phases during the growing of CZTS structure (Su, Chiu, & Ting, 2015). They firstly deposited Cu and Sn layer in sequence, respectively on Mo coated SLG substrate and detected Cu_6Sn_5 alloy formation. After depositing Zn layer on the previous layers, they detected the transformation of Cu_6Sn_5 to Cu_3Sn and also the formation of Cu_5Zn_8 alloy.

Olgar *et al.* used two different stacking orders so as to understand which order is more suitable to increase the homogeneity of CZTS structure. They came to decision that instead of SLG/Mo/Zn/Sn/Cu, the SLG/Mo/Cu/Sn/Zn/Cu stacking order, which the 30% of Cu was at top and 70% of Cu was on Mo layer, is more suitable in terms of compactness of CZTS absorber for thin film solar cell (Olgar et al., 2016).

Since there are works that reported the advantages of SLG/Mo/Cu/Sn/Zn/Cu stacking order and the Cu-Sn alloy formation on the conversion efficiency of solar cell, in this work we assumed that Type II order is better than Type I order in terms of Cu-Sn alloy formation which results better film compactness. In Type I CZTS films, the thin Cu layer near the Sn layer might diminish the formation of these alloys and might results the Sn loss from the bulk of the film during the sulfurization.

Clearly, for the Type I samples, the Cu and Zn $2p_{3/2}$ peak positions shifted to lower binding energy side with increasing the Cu and Zn concentrations. The reason of this shifting is not clear. This shift might be explained by the formation of different phases on the film surface. When Cu/Zn+Sn ratio is considered, Type I CZTS films are highly Cu poor and this ratio is in the desired range for Type II CZTS.

In terms of Zn/Sn ratio, Type I CZTS films of A and B are Zn deficient whereas sample C is slightly Zn rich. However, the Type II sample D has Zn/Sn ratio in the desired Zn-rich range. In summary, the characterizations of physical properties of Type I and Type II CZTS samples have been occurred. Type I samples revealed that the sulfurization time did not showed remarkable difference in the crystal structure and surface morphology of films but they have different compositions due to the increment in Sn loss with sulfurization time. They have also MoS_2 interface layer formation with different thickness depending on the amount of penetrated S. Raman analysis showed the increase in the intensity of peak related with MoS_2 with sulfurization time which can be attributed that the higher sulfurization time thicker MoS_2 interface layer. Surface composition by XPS showed that all Type I CZTS films are in sulfur deficient except sample A. The reason of high sulfur content of sample A was confirmed as a formation SnS_2 secondary phase on the surface.

The crystal structure and the surface morphology of Type II CZTS film is different from the Type I samples. Also the composition of these samples are Zn-rich and Cu-poor which are desired for efficient solar cells. The different stacking order results difference in the surface morphology, crystal structure as well as composition of grown CZTS films. By considering all analysis of Type I and Type II samples, Type II CZTS films are more promising absorber layer for efficient soar cells.

6.2. Buffer Layer Characterization

The optical properties of buffer layer is highly crucial to increase the solar cell efficiency. Therefore, the bandgap of buffer layer should be high to diminish the light absorption and increase the transmission of this layer. CdS is an n-type semiconductor with high bandgap energy is 2.42 eV. CdS is one of the most promising candidate among the other buffer layers and it is commonly used in high efficient solar cells. So far, the highest efficient CIGS (22.8%) (Salome et al., 2017) and CZTS (9.4%) (Tajima et al., 2017) solar cells have been achieved with CdS buffer layer.

6.2.1. Growth Mechanism of CdS Thin Films

In this study, the CdS thin films were deposited by chemical bath deposition (CBD) technique which has three different growth stages such as induction time, compact and porous layers deposition time, respectively (Sandoval-Paz & Ramírez-Bon, 2009). During the induction time, due to the forming of nucleation the growth rate is very low. The second growth stage is the ion-by-ion process which has high and linear growth rate. This process depends on the ion exchange between the Cd^{2+} and S^{2-}. The quality of CdS formed during this process is compact, adherent and extremely reflecting (W.-D. Park, 2012). And lastly, during the final stage of growth process which is called cluster-by-cluster, the growth rate is extremely low. The quality of grown CdS film is low and porous. Thus, the determination of the growth stages of CdS films with CBD technique is important to take control of optical properties for solar cell application. In this study, CdS thin films were grown on SLG substrates with deposition times changing from 30 min to 90 min. The optical and structural properties were examined in detail.

6.2.2. X-Ray Diffraction Analysis

CdS films have two types of crystal structures cubic (zincblend) and hexagonal (wurtzite) and the formation of them depends the growth process and the substrate temperature. The growing ion-by ion results the crystal structure pure hexagonal or cubic phase or mixed of them (M. A. Kumar & Muthukumaran, 2013). In addition, because hexagonal and cubic crystal structures have low formation energy difference, the coexistence of them have been reported previously (Slonopas et al., 2016). The low and high temperature depositions result cubic and hexagonal phases, respectively. An also it can be observed phase transition from cubic to hexagonal by applying annealing treatment.

The crystallinity of CdS thin films having different thickness were confirmed by XRD. All films have three peaks of CdS. Figure 6.11. shows the X-ray diffraction patterns for the samples at various deposition time. The main peak was observed at 26.7°, 26.7°, 26.7°, 26.6° and 26.6° for the 30, 45, 60, 75 and 90 min deposition times, respectively. There observed a slight shift at the position of mean peak.

Since the most intense diffraction angle position of wurtzite and zincblende structures match within 1%, determination of exact crystal structure by XRD became a difficult work. The peaks observed at 26.7° is given (002) phase of hexagonal structure (Ezekoye et al., 2015) whereas the peaks at 26.6° and 26.6° represent the cubic structure of (111) plane (Kariper et al., 2011; P. Kumar et al., 2012; Slonopas et al., 2016). Therefore, it is hard to tell the exact crystal structure by considering the main peak.

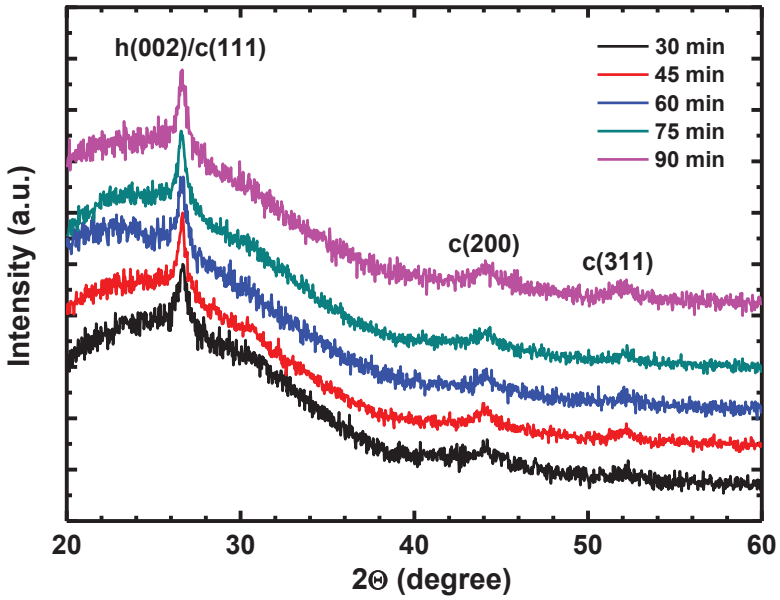

Figure 6.11. XRD spectra of CdS films grown at different deposition time.

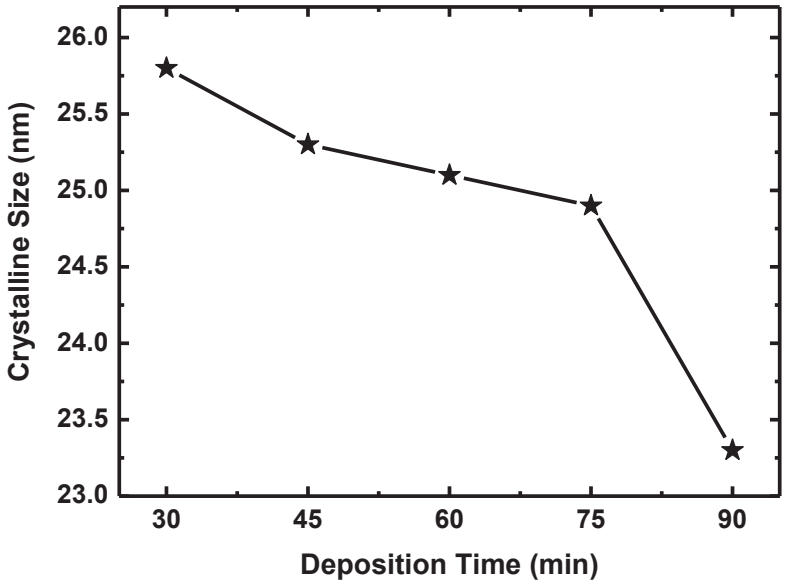

Figure 6.12. Crytallite size of c(111)/h(200) peak of CdS films grown at different deposition time.

Crystallite size (*D*) was calculated by Debye-Scherrer's formula given with equation 6.1. The full width at half maximum (FWHM) of the h(002) or c(111) diffraction peak decreased with deposition time (in Figure 6.12.) which can be attributed to the decrease crystallite size and worsen of crystallinity. The reason of the diminishing the crystallite size is changing the deposition process from the ion-by-ion to mixed of ion-by-ion and cluster-by-cluster which results porous layer on the inner compact layer. It is observed that the crystallite size changes from 23.3 to 25.8 nm and it is decreasing with deposition time. This is usually detected result that crystal size of grown CdS film in cluster-by-cluster process is smaller than in ion-by-ion process (Sandoval-Paz & Ramírez-Bon, 2009). The second diffraction peak was detected at approximately 44.10° for all films corresponds to (220) reflection of cubic phase (Fernando et al., 2015). The third peak was encountered from 52.09 to 52.20° range which assign to (311) plane of the cubic CdS (Fernando et al., 2015; Manikandan, Dilip, Mani, & Prince, 2015). The intensity of c(311) peak increased with deposition time which can be said that decrease in Cd/S atomic ratio resulted the increase in crystallinity of CdS films (Husham, Hassan, Mahdi, Selman, & Ahmed, 2014). XRD results indicate that, for the CdS films deposited at low deposition time consist of mixed hexagonal and cubic phase. However, as the deposition time increases, the cubic structure is being a dominant phase into the CdS lattice.

6.2.3. Surface Morphology and Composition

The surface morphology of grown CdS thin films with different time duration was monitored by SEM image analysis. Figure 6.13. shows that morphology of the deposited CdS thin films was highly affected by the deposition time. As seen from Figure 6.13. when the deposition time increased, the film surface became more compact. In the first 30 min, there were many voids and pinholes at the film surface. They reduced with the deposition time. According to Figure 6.13. in the 60 min CdS thin film covers much of the substrate surface and the subsequent deposition simply fills in the free space between the crystals. At the early time of CBD of CdS films, the inner compact layer with higher crystallinity is deposited by ion-by-ion mechanism and after time passed the lower quality of CdS layer is deposited on the inner compact layer.

After time passing, the deposition process turns to cluster by cluster mechanism which deposit the larger particles, clusters, on the inner compact layer and forms lower quality porous layer. As the deposition time was increased, the deposited CdS thin films became pinhole and void free because of the clusters deposition.

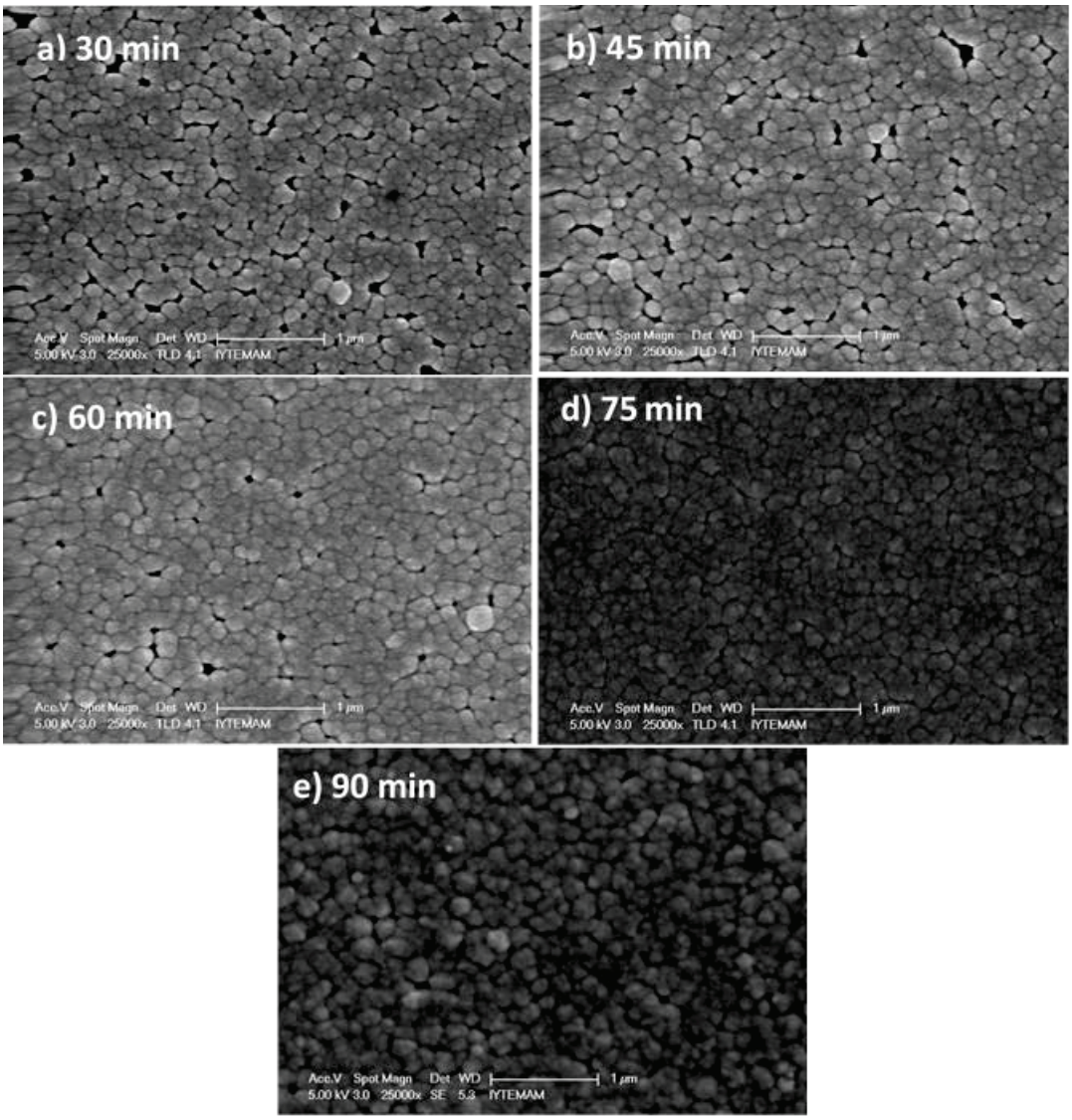

Figure 6.13. SEM images of thin CdS films grown on SLG susbstrates by CBD technique a) 30 min, b) 45 min, c) 60 min, d) 75 min, e) 90 min deposition times.

The atomic concentrations of grown CdS films were determined by EDX analyses. Table 6.7 summarized the atomic concentration and ratio of Cd and S elements. EDS results showed that the all thin CDS films contain higher amount of Cd than S. This might be the result of having higher reactivity of Cd with respect to S (Husham et al., 2014).

SEM and EDS results suggest that CdS films cover much of the substrate surface within the initial 60 min of the deposition. At the deposition time higher than 60 min, the decrement in the Cd/S ratio in the solution was observed. This might be explained by the sedimentation of agglomerated clusters. Since the excess Cd ion or S vacancy increase the n-type conductivity, low deposition time is desired in terms of solar cell application.

Table 6.7. EDX analyses of CdS thin films prepared using different deposition time.

Sample	Atomic % Cd	Atomic % S	Cd/S Ratio	Thickness (nm)
30 min	58.03	41.97	1.38	70.0
45 min	57.15	42.85	1.33	85.0
60 min	57.05	42.95	1.33	120.0
75 min	53.68	46.32	1.16	133.0
90 min	52.63	47.37	1.11	148.0

6.2.4. Spectroscopic Ellipsometer (SE) Characterization

The spectroscopic ellipsometer (SE) is an optical technique that supply detailed information on the interband transition energy, electronic properties and the thickness of materials. Psi (Ψ) and Delta (Δ) are the ellipsometric parameters which measures the phase and amplitude changes of incident light, respectively. In order to define the wavelength dependence of optical constants, the appropriate optical model was constructed. In Figure 6.14. (a) and (b) the solid lines represent the best fit results of the ellipsometric parameters Ψ and Δ. There observed small deviations between the experimental data and the model. This is because of the effect of depolarization which caused by the roughness and grain boundaries. The quality of fits determined from the root mean squared error (RMSE) analysis as given in equation 5.9. The details of measurement, constructed model and fitting procedure were mentioned in Chapter 5.6.6.The fitting results were also listed in Table 6.8.

Figure 6.15. shows the thickness measurement results of CdS films. As expected, the thickness of grown films increased with deposition time but the growth rate was different for each 15 min time periods. At the first time of deposition because the source materials are sufficiently exist, the ion-by-ion processes play more crucial role than the cluster-by-cluster process.

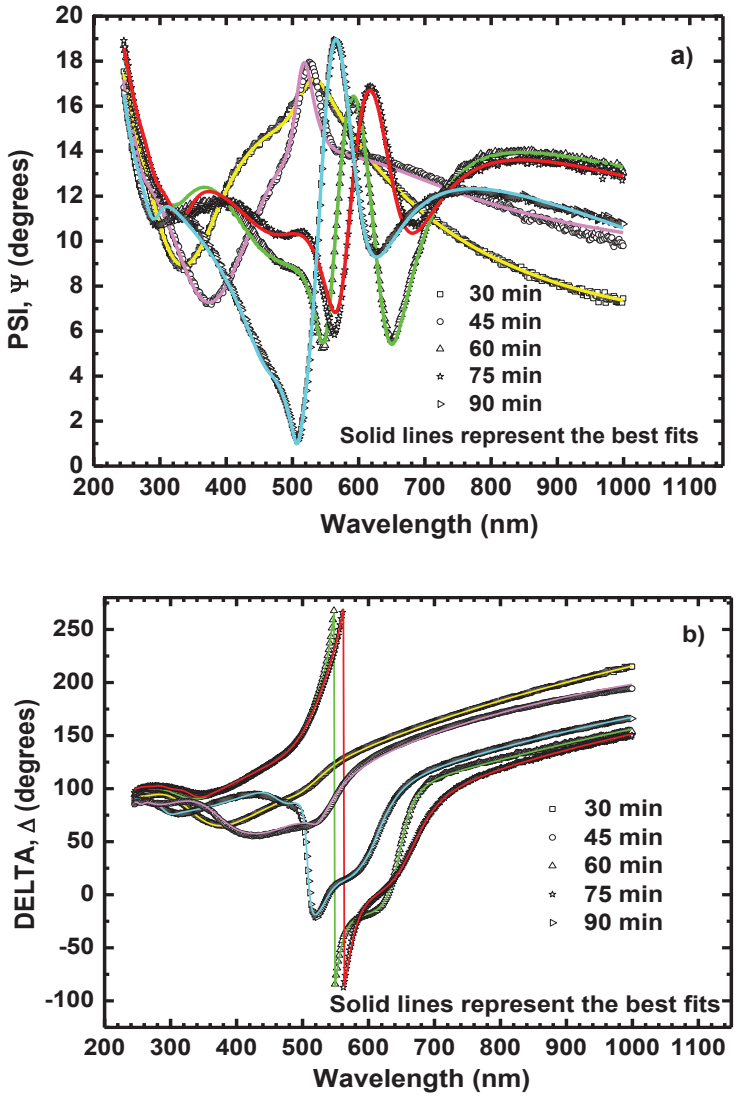

Figure 6.14. Ellipsometric data and optical model fit of CdS films a) PSI (Ψ), b) DELTA (Δ). The scatter plots represent the measured data whereas the solid line represent the fit result.

After some time, due to the amount of source materials diminishes the cluster-by-cluster process becomes more dominant than ion-by-ion processes and decreases the deposition rate.

According to Figure 6.15., due to the high deposition rate it is assumed that in the first 60 min growth the ion-by-ion processes was dominant and then it turned to mixed of ion-by-ion and cluster-by-cluster process with decreasing deposition rate. For the thickness calculation, the model was constructed by two CdS layer due to being covered both sides of SLG substrate. The thickness of top CdS layer was chosen as a real thickness, because the thickness of bottom CdS layers were calculated 8-10 nm less than

top layer. Although the thickness of both CdS layer has nearly the same, they was determined with a little difference.

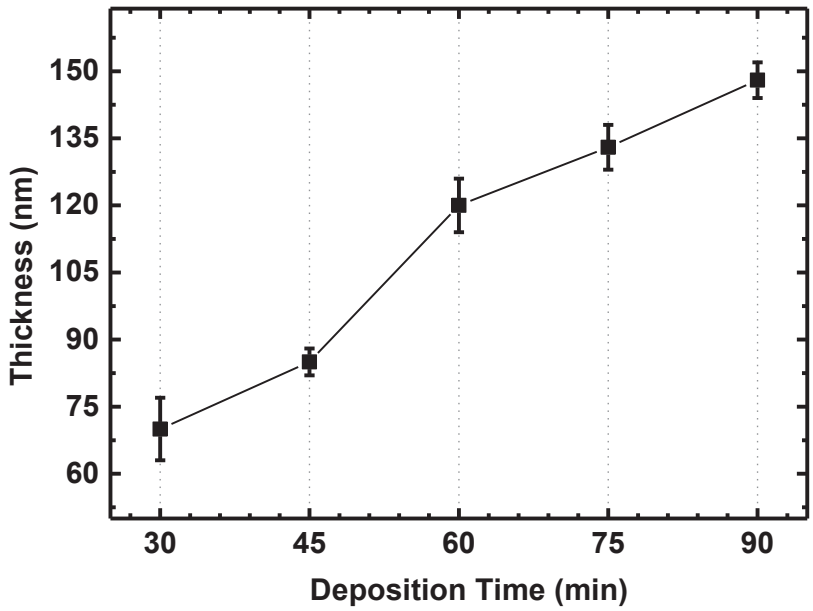

Figure 6.15. CdS thickness variation with respect to deposition time.

The optical constants *ie*. refractive index *n*, extinction coefficient *k*, and dielectric function ε, are given by the following equation where ϕ is the incident angle, ρ is the amplitude ratio of the reflectance coefficients of the polarized light.

$$\varepsilon = \varepsilon_1 + i\varepsilon_2 = (n+ik)^2 = \sin^2\phi\left[1+\tan^2\phi\left(\frac{1-\rho}{1+\rho}\right)^2\right] \tag{6.3}$$

Table 6.8. Spectroscopic Ellipsometric fitting results of CdS thin films.

Deposition Time (min)	Sample Thickness (nm)	RMSE	Roughness (nm)	Refractive Index at 2.06 eV	Optical Bandgap, E_g, (eV)
30	70.0	1.6	7.3	2.39	2.30
45	85.0	3.2	10.0	2.53	2.32
60	120.0	2.5	10.2	2.51	2.25
75	133.0	2.7	10.4	2.46	2.22
90	148.0	2.2	12.1	2.43	2.22

The fitting of SE measurements of CdS films also provided the refractive index (n) and extinction coefficient (k). Figures 6.16. (a) and (b) show the n and k of CdS thin films with respect to photon energy, respectively.

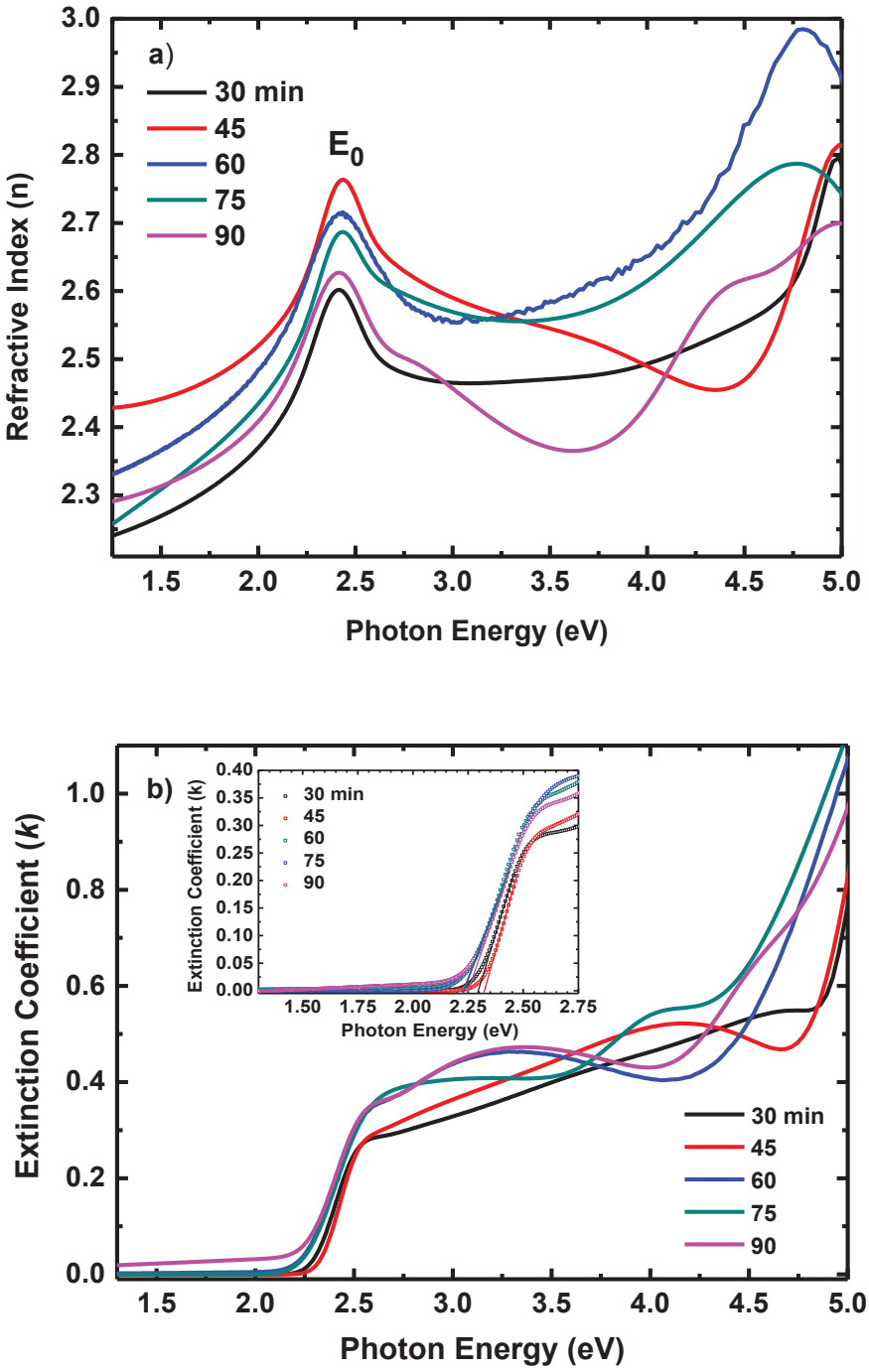

Figure 6.16. Distribution of a) refractive index and b) extinction coefficient of CdS films with different thickness. The inset figure gives the band gap determination of CdS films.

The bulk CdS has refractive index 2.52 at 2.06 eV photon energy (600 nm wavelength) (Lisco, Kaminski, Abbas, Bowers, et al., 2015). However, depending on the deposition technique refractive index value of CdS has different value. CdS films deposited by radio frequency (rf) sputtering, vacuum evaporation and spray pyrolysis have refractive index in the range of 2.25-2.51 (El Assali et al., 2000; Khan et al., 2010), 2.12 (Senthil, Mangalaraj, Narayandass, & Adachi, 2000) and 2.19-2.32 (Pal et al., 1997; Senthil et al., 2000), respectively.

The CdS film deposited for 30 min showed irrelevant refractive index value. This might be the result of containing more pinholes and voids as seen SEM image. Except this sample, the refractive index showed inverse proportion with the CdS film thickness. This has the direct relation with including porous layer. The decrease in ion-by-ion and increase in the cluster-by-cluster process causes porous layer deposition and results a prominent reduction in the refractive index. The CdS films grown at 45 and 60 min showed the refractive index value close to bulk form of CdS.

Furthermore, the refractive index versus photon energy graph of CdS films show two maxima. The first maxima was observed between 2.40 and 2.43 eV whereas the second one was between 4.77 and 4.98 eV. These maxima signify the transition along the Γ→A direction of the Brillouin zone and the fundamental absorption peak, respectively (Sandoval-Paz & Ramírez-Bon, 2009; Slonopas et al., 2016). The visible change in the position of transition energy (E_0) was detected. Except the 30 min grown CdS, the transition energy was decreases with deposition time. This is explained by the difference in the layer microstructure which contains CdS porous layer grown by the mixed of ion-by-ion and cluster-by-cluster deposition process.

The extinction coefficient of a material depends on its absorption. The optical bandgap ($E_{g,\,SE}$) of CdS films were determined from extrapolating the straight portion of the *k* vs. *hv* graph, on *hv* axis at absolute minimum of *k*. Figure 6.16 (b) shows the distribution of extinction coefficient with respect to photon energy and the inset figure demonstrates the bandgap determination. Depending on the CdS film quality, the absorption edge shifted in lower photon energy side which also represents decreasing the band gap energy. CdS film grown 45 min has the highest absorption edge and band gap energy. And then the CdS film grown 30 min follows this order. Figure 6.17 shows the refractive index variation with respect to deposition time. From the Figure 6.18., the variation of E_g with deposition time can be seen.

Except the CdS film deposited at 30 min, band gap decreases with deposition time which can be explained by the reduction in the crystallite size as determined from XRD and the reduction in the quality of surface layer. The $E_{g, SE}$ values are given in Table 6.8.

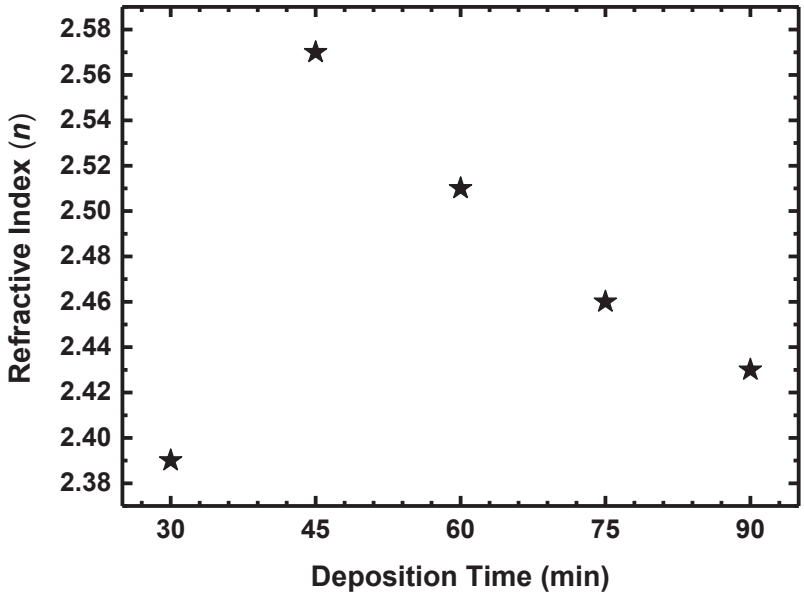

Figure 6.17. Refractive index variation with respect to deposition time of CdS films at 600 nm wavelength.

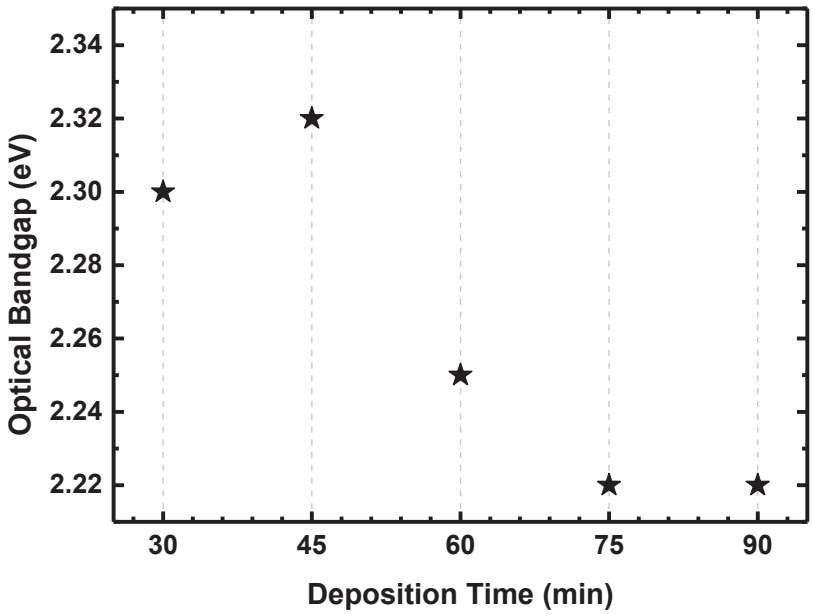

Figure 6.18. The optical bandgap distribution of CdS thin films with respect to deposition time.

Figures 6.19. (a) and (b) show the dielectric functions (ε_1, ε_2) of CdS thin films with respect to photon energies. The real part of dielectric function (ε_1) deals with the index of refraction (Ortuño-López et al., 2013) whereas the imaginary part of the dielectric function (ε_2) connects with the transitions at the critical points of the Brillouin zone (Hofmann et al., 1993).

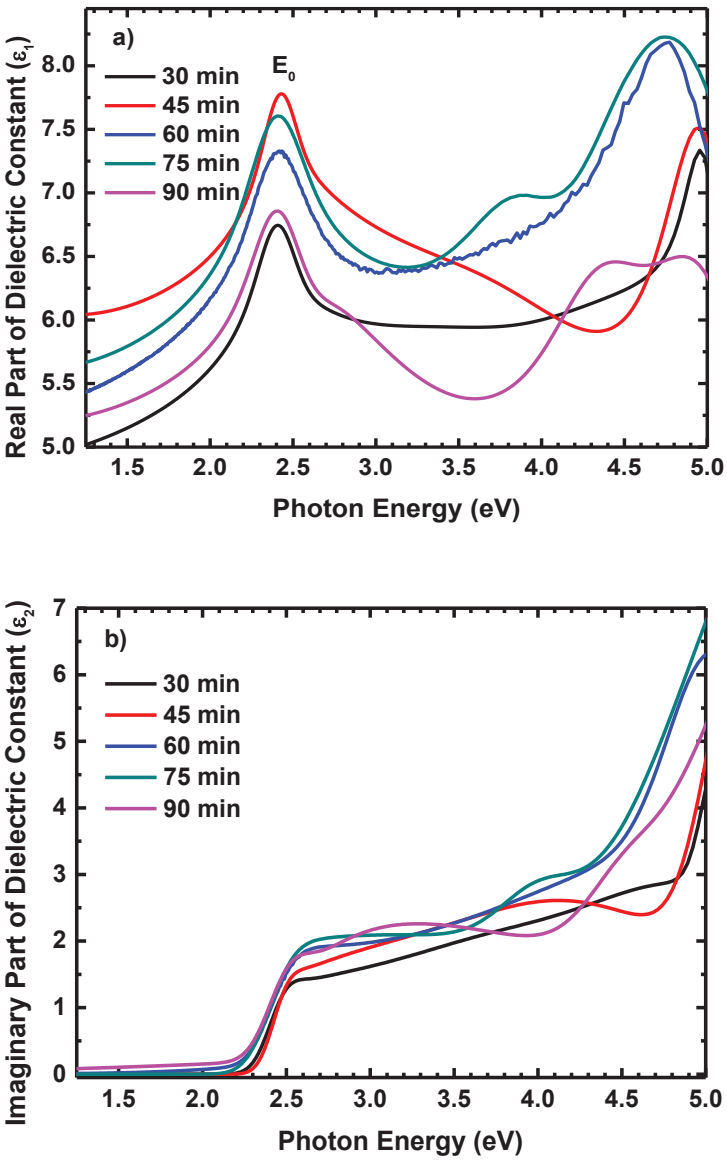

Figure 6.19. Dielectric constant of CdS films a) real part (ε_1), b) imaginary part (ε_2).

The optical transitions between Cd *4d* and S *3s* states and the conduction band determine the structure of ε_2 function. The change in dielectric constant with photon energy represents the interaction between photons and electrons in the film. The CdS films with hexagonal and cubic crystal structure have different shape of ε_2 function.

It was reported that the cubic CdS has E_0, E_{1B} and E_2 peaks whereas the hexagonal CdS has an additional two peaks E_{1A} and F_1 for the imaginary part of dielectric constants (Cardona, Weinstein, & Wolff, 1965). In Figure 6.19 (a), the peak E_0 observed at 2.40-2.43 eV range relates the transition energy from the valence band to conduction band along the Γ point in the Brillouin zone (Hofmann et al., 1993; W.-D. Park, 2012).

As a conclusion, it was observed that the enhancement of the deposition time results the shift in the position of transition through the Γ→A direction of the Brillouin zone, diminishes the refractive index, intersect value of k-hν graph which gives the band gap energy. The reason of observed results is the change in the deposition mechanism from ion-by-ion to mixed of ion-by-ion and cluster-by-cluster (Slonopas et al., 2016) and increase in the porous film formation.

6.2.5. Raman Analysis

Figure 6.20. shows the Raman spectra of CdS films deposited at different time period. Each sample has three peaks which are the multi-overtones of longitudinal optical phonons (LO). It is seen clearly from the Figure 6.20. that 1LO is the dominant mode of each CBD-grown CdS films. The position of main peak 1LO mode was listed in Table 6.9. As seen from the Table 6.9, the positions change from 299.8 to 301.3 cm^{-1} and they slightly shift towards the lower wavenumber side. These positions of 1LO peak is commonly detected in the literature (Oladeji et al., 2000). The position of 1LO mode of all CdS samples shifted from the bulk CdS peak which is detected at 305 cm^{-1} (Maticiuc et al., 2014; Oladeji et al., 2000). The peak positions of LO modes does not depend on particle size (Shiang, Risbud, & Alivisatos, 1993). However, some authors believe the lattice stress links with this shift (Maticiuc et al., 2014). In our study, the shift in 1LO position is not seemed related with grain size variation. The change in the shift of the peak positions is inversely proportional with the change in Cd/S ratio. When the Cd/S ratio increases, the position of 1LO peak shifted through the lower wavenumber side. There is not clear explanation related with this issue in the literature. The atomic weight of Cd and S ions are 112.4 and 32.06 g/mol, respectively. If the Cd concentration is higher than the S, due to effective mass will increase the peak position of 1LO could shift through the lower frequency side. It might also be considered that the excess of Cd or deficiency in S atoms cause a disorder in the lattice and results the shift.

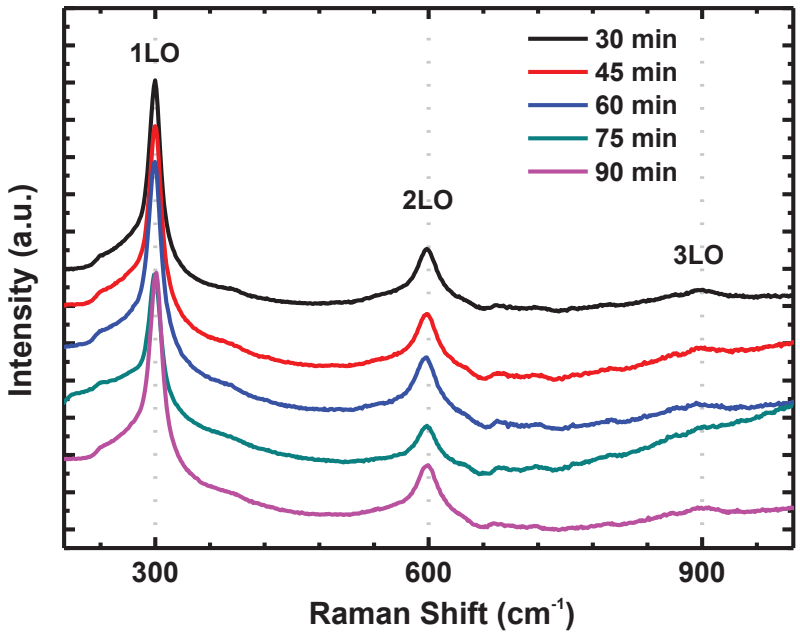

Figure 6.20. Raman spectra of CdS thin films deposited at various time.

Table 6.9. Position of 1LO peak for CdS films.

Sample Deposition Time (min)	Main Peak (cm^{-1})
30	299.8
45	300.0
60	300.0
75	300.1
90	301.3

It was reported that, by using the Raman analysis, it is hard to tell the difference between cubic and hexagonal crystal structures and also the phase transition between these structures (Sivasubramanian et al., 2006). Since in cubic phase, the frequency of LO phonon mode is nearly match with the A1 (LO) phonon mode in the hexagonal phase (Zelaya-Angel et al., 1997). However, there is report that if the FWHM value of 1LO peak is in the range of 20-30 cm^{-1}, it might be cubic CdS (Oladeji et al., 2000). The first over tone mode (2LO) is observed between 599-601 cm^{-1} wavenumber ranges which are also observed in different research (Oladeji et al., 2000). There is also hardly visible second over tone mode (3LO) at approximately 900 cm^{-1}.

6.2.6. X-Ray Photoelectron Spectroscopy (XPS) Analysis

The chemical state of compound elements and atomic concentration of CdS thin films were investigated from the high resolution XPS photoelectron peaks. At the surface spectrum, the C *1s* peak was observed and it was used to calibrate the high resolution spectrum with respect to C *1s* peak at 284.6 eV which is the characteristic of aromatic/aliphatic carbons (Yazici et al., 2015). The survey measurement showed the presence of Cd, S, as well as C, O and N core levels. The core level spectra of Cd *3d* and S *2p* were recorded by using high resolution scan spectra. Figures 6.21. and 6.22. show high resolution of Cd *3d* and S *2p* valence regions, respectively. Cd *3d* and S *2p* spectra did not show great change among the investigated samples. The detailed curve-fit results for CdS films are summarized in Table 6.10 and 6.11,. The curve-fit results give the binding energies, spin-orbit splitting and fwhm values of Cd *3d* and S *2p* valence regions. The S *2p* and Cd *3d* peaks occur as doublets of $2p_{3/2}$, $2p_{1/2}$ and $3d_{5/2}$, $3d_{3/2}$. The *2p* spectra was fitted using a 2:1 peak area ratio for $2p_{3/2}$ to $2p_{1/2}$ whereas *3d* spectra was fitted using a 3:2 peak area ratio for $3d_{5/2}$ to $3d_{3/2}$. During the fitting process, spin-orbital splitting values of each couple of elements were constrained. Because of the electron transpose while the bonding process which results the change in net charge, little deviations are observed in the binding energies of the same element of different CdS films (Moholkar, Shinde, Babar, Sim, Kwon, et al., 2011). It can be found in the literature that the peak position of Cd $3d_{5/2}$ component is observed in the range of 404.4 to 406.6 eV which is the result of different surface composition of CdS films.

Similarly, the position of Cd $3d_{5/2}$ component was observed between 404.7 and 405.1 eV in this study which indicate the bivalent character of Cd (Cd^{2+}). There is a shoulder at low binding energy side of Cd *3d* region which indicates N *1s* coming from N-O and N-C and have binding energy between 403.0-403.3 eV and 401.5-401.9 eV, respectively.

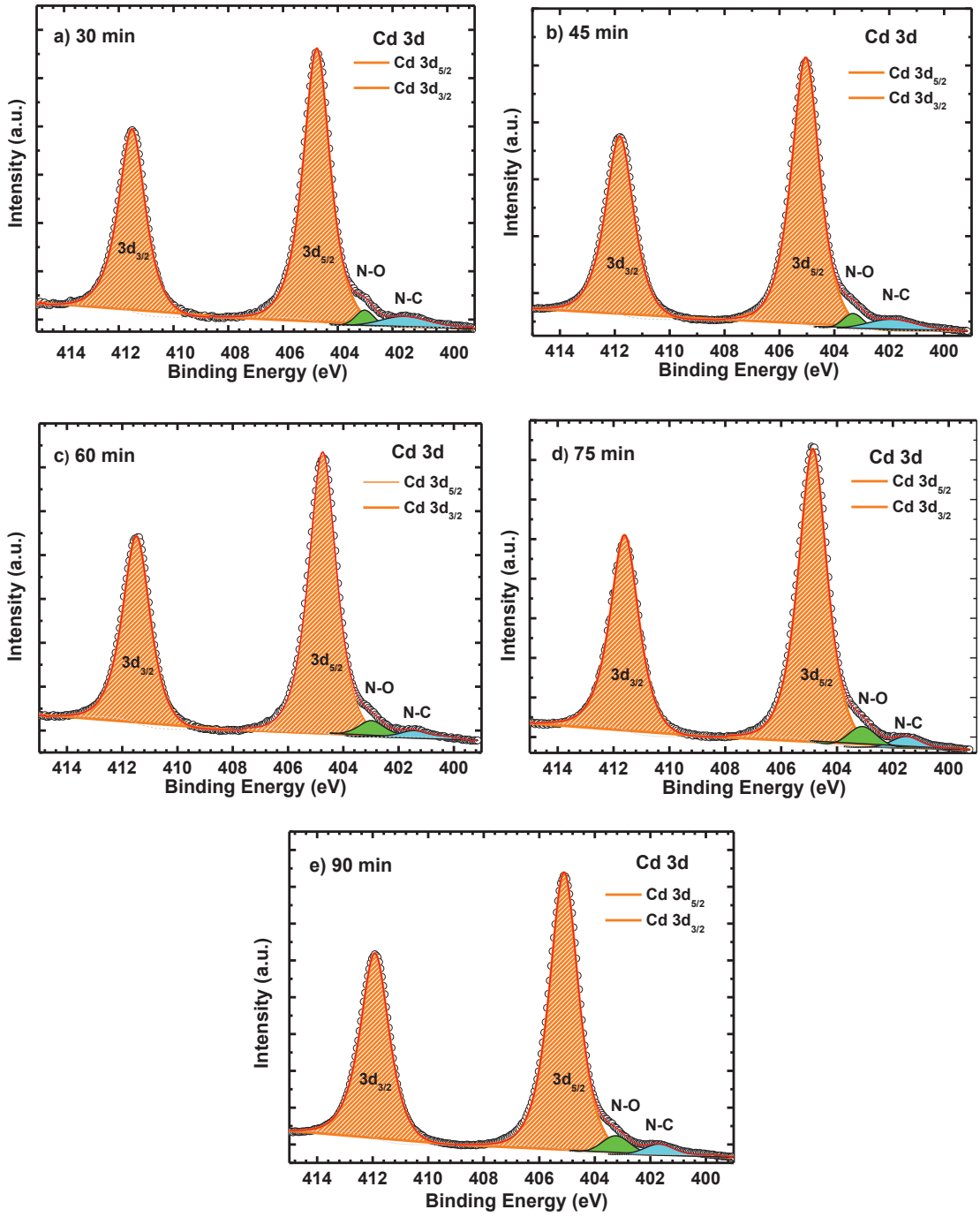

Figure 6.21. High resolution spectra of Cd 3d region of CdS films deposited at a) 30 min, b) 45 min, c) 60 min, d) 75 min, e) 90 min.

The S *2p* core level spectrum varies from 160.0 to 164.0 eV in Figure 6.22. In this work, S *2p3/2* peaks were observed between 161.1 to 161.4 eV binding energy region interpreting the monosulfide structure (S^{2-}) which corresponds to the CdS (Yazici et al., 2015). It is also important to notice that there is no elemental sulfur on the surface which means all chemicals made a reaction.

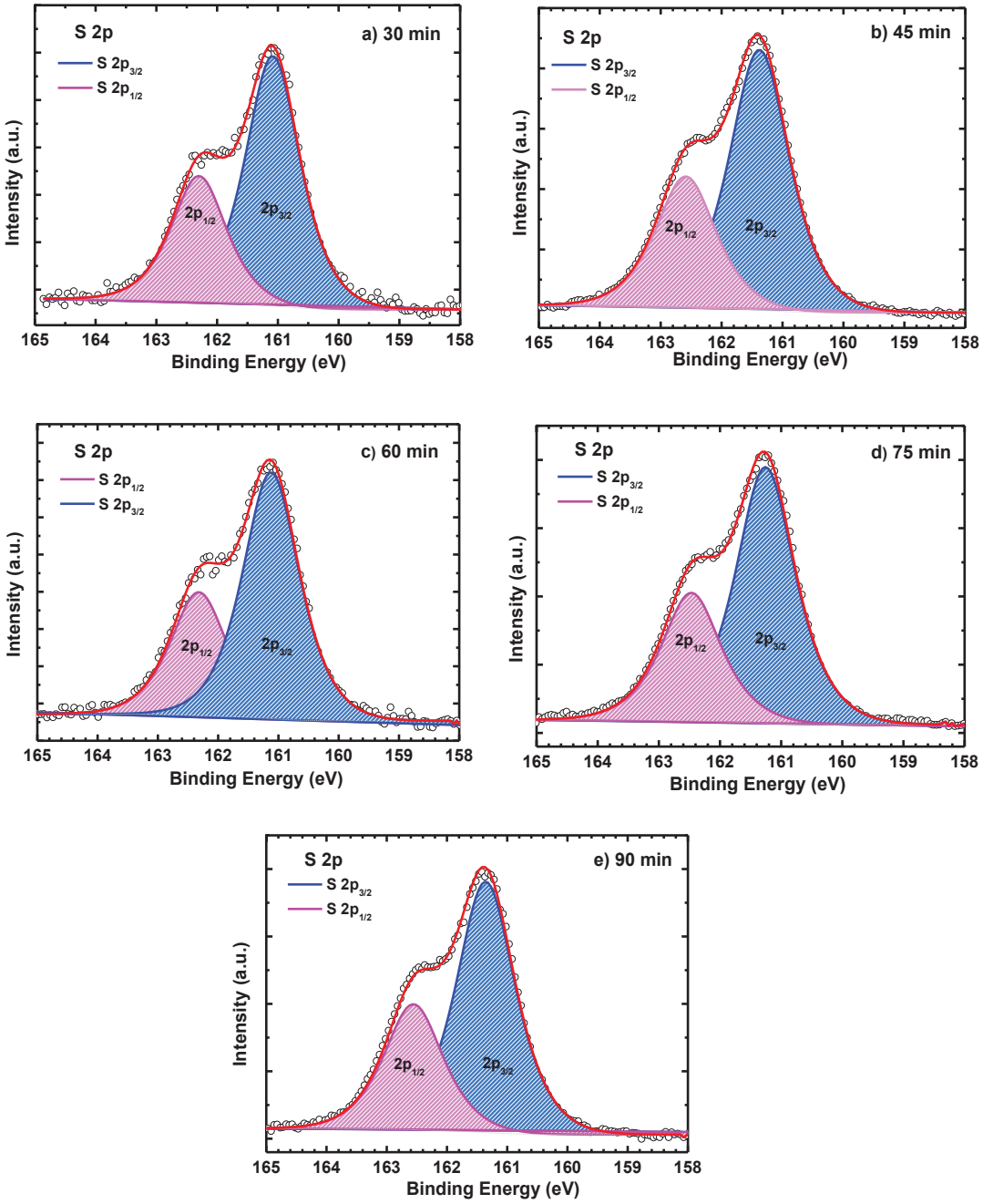

Figure 6.22. High resolution spectra of S 2p region of CdS films deposited at a) 30 min, b) 45 min, c) 60 min, d) 75 min, e) 90 min.

By increasing time, except the CdS film deposited at 45 min, the S *2p* and Cd *3d* peaks showed small shift through the higher binding energy side. This might be explained with the decrease in the crystallite size where the similar result has been declared by Thakur et al., (Thakur, Joshi, & Patil, 2010). The binding energy values for Cd and S are agree very well with the published binding energy values for CdS films.

Table 6.10. Cd *3d* region fit parameters.

Sample	Cd $3d_{3/2}$	Splitting (eV)	FWHM (eV)	Line Shape	N-O	N-C
30 min	411.5	6.8	1.15	GL(75)	403.0	401.6
45 min	411.8	6.8	1.20	GL(75)	403.3	401.9
60 min	411.5	6.9	1.16	GL(75)	403.0	401.5
75 min	411.6	6.9	1.20	GL(75)	403.0	401.5
90 min	411.9	6.8	1.21	GL(75)	403.2	401.7

Table 6.11. S *2p* region fit parameters.

Sample	S $2p_{1/2}$	S $2p_{3/2}$	Splitting (eV)	FWHM	Line Shape
30 min	162.3	161.1	1.2	1.10	GL(70)
45 min	162.6	161.4	1.2	1.16	GL(70)
60 min	162.3	161.1	1.2	1.11	GL(70)
75 min	162.5	161.3	1.2	1.15	GL(70)
90 min	162.6	161.4	1.2	1.15	GL(70)

The quantification analysis was obtained from peaks area and private sensitivity factor of each element and its components. The obtained atomic concentration of Cd and S were given in Table 6.12, respectively. The XPS spectra exhibit Cd rich CdS film at low deposition time. It was obtained that the concentration of Cd was decreasing whereas the concentration of S was increasing with deposition time. This is the result of the replacement of ion-by-ion mechanism with the mixed of ion-by-ion and cluster-by-cluster mechanism at higher deposition times. Quantification result is very close to EDS analysis. The XPS is a surface sensitive technique and takes measurement from 5-10 nm deep.

Quantification result demonstrated that the atomic composition of surface layer changed and became distant from the desired composition with deposition time. The CdS film grown 90 min, has composition lower than the stoichiometry. These are the result of change in the deposition mechanism and the decrement in the amount of chemicals. These results supported to the SE and EDS analyses.

Table 6.12. Quantification analysis of CdS thin films by XPS peak fit.

Sample	Atomic % Cd	Atomic % S	Cd/S Ratio
30 min	54.88	45.12	1.22
45 min	54.00	46.00	1.17
60 min	51.24	48.76	1.05
75 min	51.34	48.66	1.05
90 min	47.68	52.32	0.91

Figure 6.23. shows the O *1s* spectrum. In this figures, different oxidation states of C and N are noticeable. It must be remembered that any CdO and Cd(OH) formation were encountered in Cd *3d* valence regions. The peak-fit result of O *1s* region support this outcome. O *1s* decomposed in three or four elementary peaks which are O=N (BE=530.5-530.8 eV), O=C (BE= 531.4-531.8 eV), O-C (532.5-532.7 eV) (Nalwa, 2001), O_2 molecule (BE=533.5-533.9 eV (which is probably chemisorbed from water)) (Gubbala et al., 2009; N. Kumar et al., 2013).

Figure 6.24. shows deconvolution of the C *1s* signal of CdS films which consists of three or four different components which are C-C (BE=284.6 eV) (Mattevi et al., 2009), C-N (BE=285.6-285.9 eV) (Shimizu, Phanopoulos, Loenders, Abel, & Watts, 2010), C-O (BE=286.3-286.5 eV) (Shimizu et al., 2010), C=O (BE=287.9 eV) (Sette et al., 2013) and C=O-N (BE=288.3 eV) (Heinz et al., 2008).

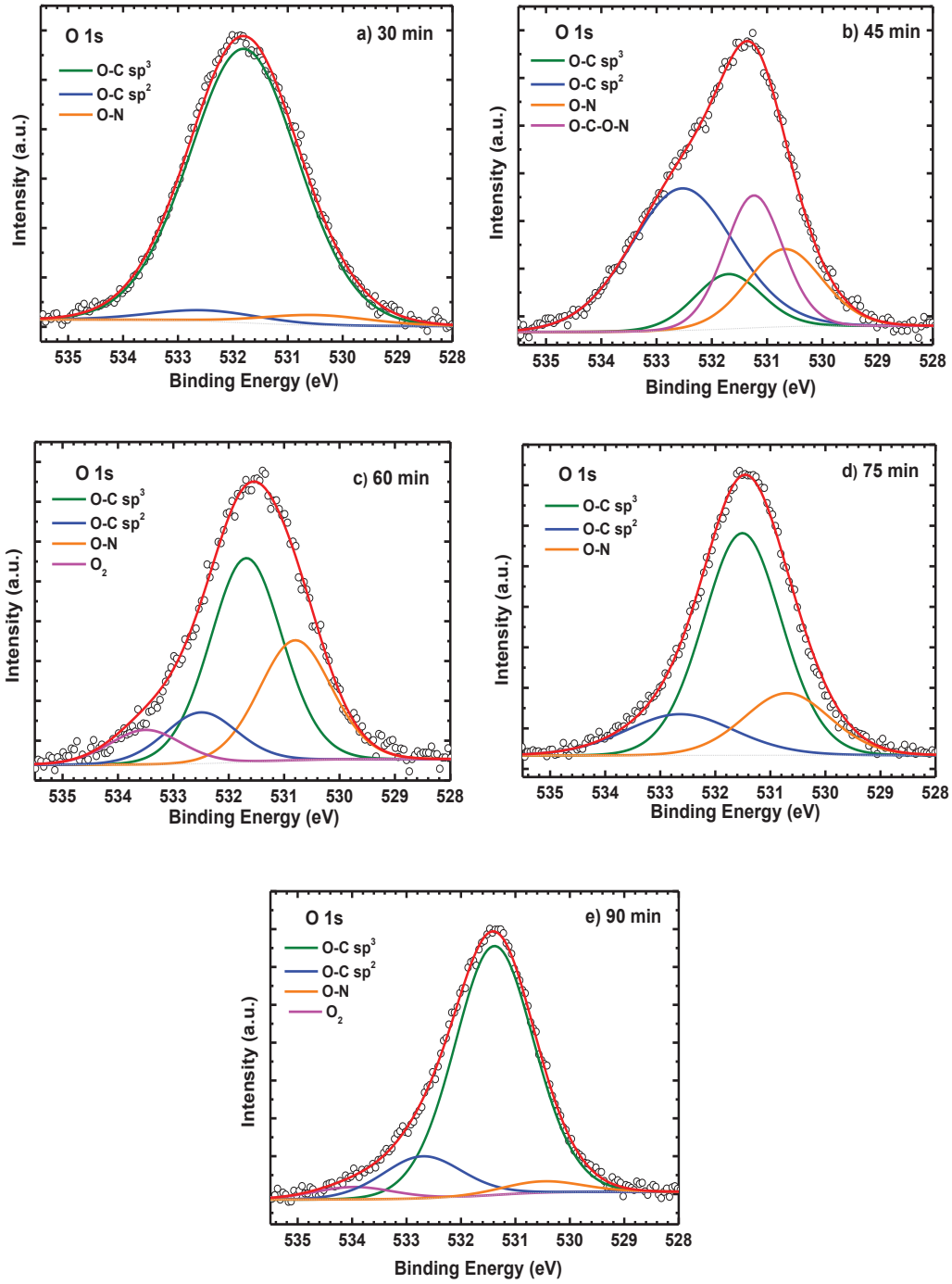

Figure 6.23. High resolution spectra of O 1s region of CdS films deposited at a) 30 min, b) 45 min, c) 60 min, d) 75 min, e) 90 min.

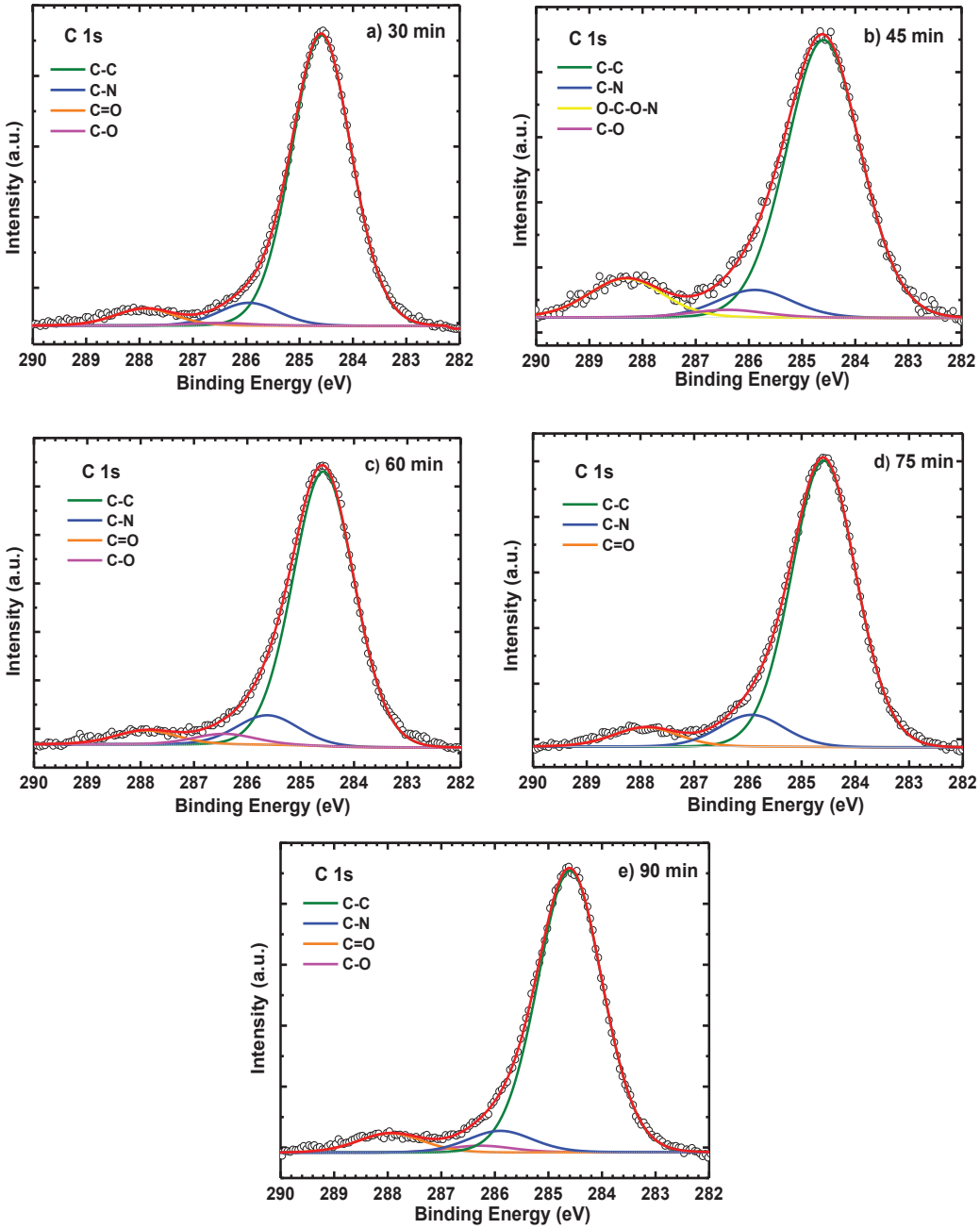

Figure 6.24. High resolution spectra of C *1s* region of CdS films deposited at a) 30 min, b) 45 min, c) 60 min, d) 75 min, e) 90 min.

6.2.7. Optical Properties

The transmission measurement of CdS films grown different deposition times were taken in the range of 200-2500 nm at room temperature. In Figure 6.25. (a) and (b), the transmission spectra and the bandgap determination of the films, respectively are given.

Because of the interference of the films, fluctuations and wave-like pattern are observed in transmission curves. In the visible wavelength range (400-700 nm), the optical transmission is observed in the range of 70-80% which is smaller than that of the substrate's transmission of about 90%. With the help of the Tauc relation in equation 6.4, the optical band gap energy (E_g) for the allowed direct transition was determined.

$$(\alpha h\upsilon)^2 = K(h\upsilon - E_g) \tag{6.4}$$

The absorption coefficient of CdS films were determined using the equation 6.5

$$\alpha = -\frac{\ln(T-R)}{d} \tag{6.5}$$

where α, d , T and R are absorption coefficient, thickness, transmission and reflection of film, respectively. The optical bandgap of the films were obtained from the plot of $(\alpha h\upsilon)^2$ versus ($h\upsilon$). In order to define bandgap energy, the straight-line portion was extrapolated to the energy axis at $(\alpha h\upsilon)^2=0$.

Since the CdS film grown 30 min has many voids, its transmission closes to SLG substrate. Generally the transmission decreases with the film thickness. However, the transmission in the visible region is found to be almost independent of film thicknesses and in the NIR region it shows opposite order of visible region. The increase in the absorption of light at higher wavelength region is generally created by crystalline defects as grain boundaries and dislocations.

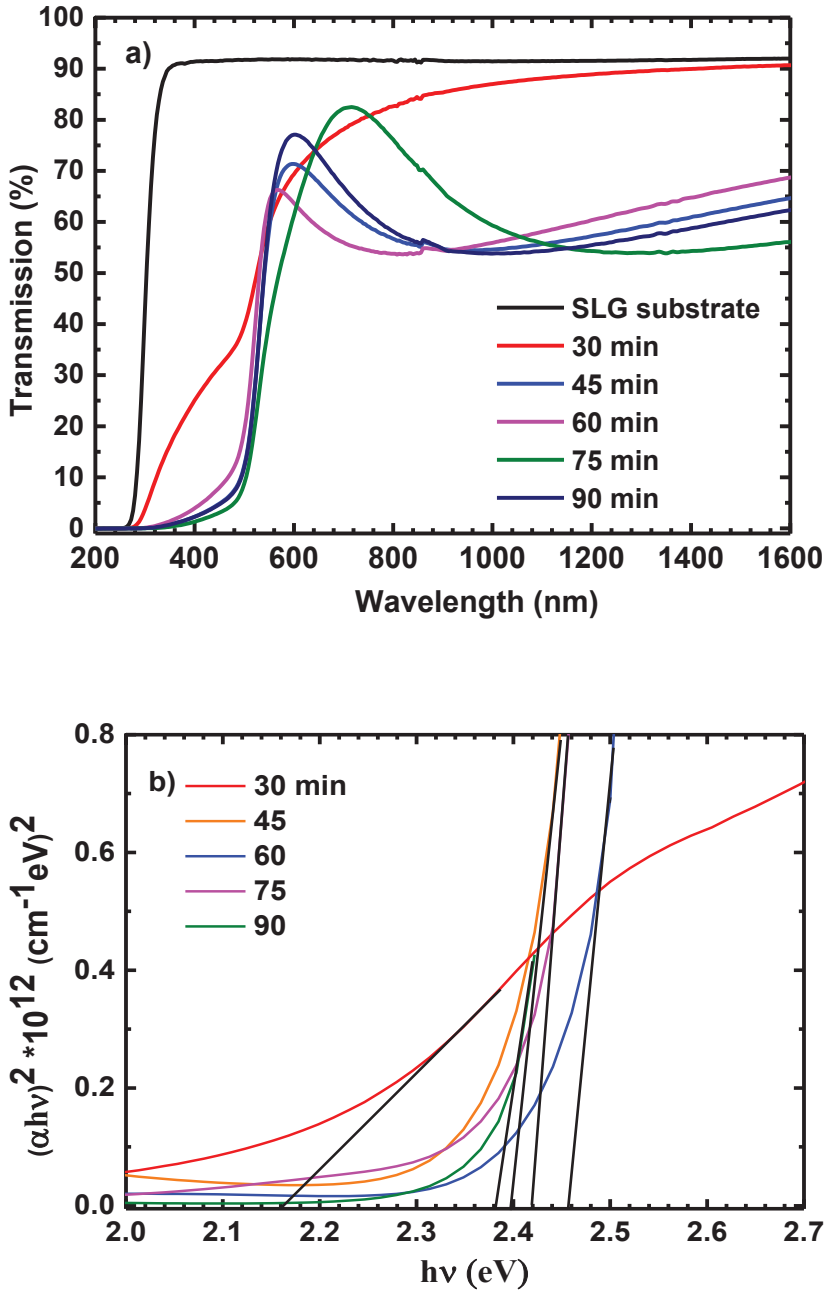

Figure 6.25. a) Transmission, b) bandgap determination of CdS films.

The higher transmission of CdS films grown 75 and 90 min which are the thick films is indication of high degree of stoichiometry. EDS analysis showed that the CdS films grown 30, 45 and 60 min have high amount of Cd with Cd/S ratio is 1.38, 1.33 and 1.33, respectively. The CdS films grown 75 and 90 min have Cd/S ratio of 1.16 and 1.11, respectively which are closer to the stoichiometry. The similar results have been detected in the literature that the high amount of Cd reduces the transmission (Maticiuc et al., 2014).

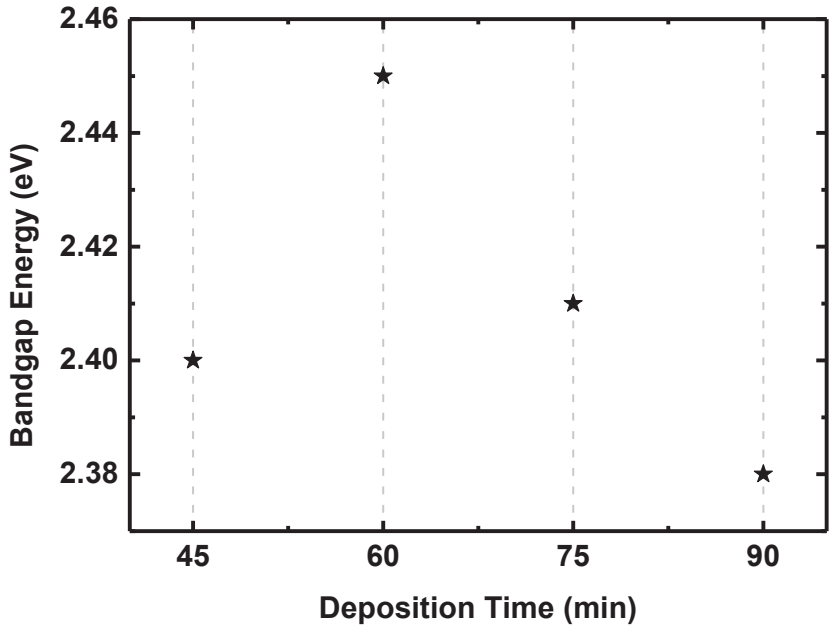

Figure 6.26. The change in the bandgap of CdS films with respect to deposition time.

Figure 6.26. shows the change in bandgap energy obtained from transmission measurement with respect to deposition time. The CdS film grown 30 min has very low bandgap energy of 2.16 eV which is not suitable as a buffer layer for solar cell application therefore it was not shown in Figure 6.26. The band gap energies of other CdS films were found to be between 2.38 and 2.45 eV depending on deposition time. The CdS film grown 90 min has the lowest whereas the sample grown 60 min has the highest bandgap energy. After the 60 min deposition, the bandgap showed decrement which might be the result of change in the growth mechanism.

Except the CdS film grown 45 min, the variation of bandgaps with depositions times showed similar trend that obtained from the SE analysis. But depending on the difference of analysis technique, there are difference in bandgap value.

6.3. Device Characterization

In this work SLG/Mo/CZTS/CdS/ZnO/AZO solar cell structure was used. The growth details of each layers were mentioned in Chapter 5. The devices fabricated using Type I CZTS were studied with thick (~108.2 nm) CdS layer. According to name of Type I CZTS absorber layers, these devices were called with cell A, B and C, respectively. The devices fabricated using Type II CZTS were studied for the different thickness of CdS layer and they were named with cell D, E, F and G.

Figure 6.27. demonstrates the fabricated solar cells and designed cell areas with top contacts. In this study, the investigated devices showed electrically inhomogeneity. The photovoltaic characteristic of each designed cell showed different results for the same device. Therefore, in this work, only the highest efficiency values were given.

Figure 6.27. Representation of constructed CZTS solar cell.

The devices A, B and C were constructed using device structure of SLG/Mo/CZTS/CdS/ZnO/AZO for the CZTS A, B and C. Figure..(a-c) demonstrate J-V curve of cell A, B and C, respectively. For the cell A and C, the J-V curve under dark and light showed the same results. The shape of the J-V curve looks like ohmic instead of p-n junction. On the contrary, the J-V curve of cell B looks like the p-n junction. For the cell B, the shift of J-V curve under illumination was also observed. There might be many reasons for observing these results. The absorber layer characterizations for Type I CZTS films revealed that, the sulfurization time create some differences between the Type I CZTS absorber layers A, B and C. According to XRD and Raman analyses, SnO_2 and tetragonal CTS formations were detected for all Type I CZTS films. The bandgap of tetragonal CTS and SnO_2 are 1.35 eV (Fernandes et al., 2010) and 3.6 eV, respectively.

For the film A the formation of SnS_2 was also detected at some places on the film surface. All of these impurity phases have detrimental effect for photovoltaic characteristic of CZTS solar cell. If the bandgap of secondary phase is higher than the bandgap of CZTS (Eg=1.45 eV), the positive conduction band offset (CBO) with respect to conduction band minimum (CBM) of CZTS forms and the band offset will be a barrier for both the majority and minority carriers. In this case the secondary phase decreases the conductivity but it does not increase the recombination of charge carriers at the interface because it behaves as a sink for only one type of carrier and decreases the current density

(Bao, 2014). In the case the wider band gap secondary phase forms in the bulk of CZTS, since it reduces the photoactive volume which absorbs the incoming light and generates the photocarriers. And also in the interface, it can enhance series resistance, decrease FF and J_{SC} (M. Kumar et al., 2015). If the bandgap of secondary phase at Mo/CZTS or CdS/CZTS interface is lower than the bandgap of CZTS, it causes the negative CBO with respect to conduction band minimum of CZTS. In this case these impurity phase behaves as a recombination centers for both minority and majority carriers and limit the V_{OC}. Since the charge carrier separation is prevented, the carrier collection diminishes the cell efficiency. For the Type I CZTS films A, B and C, due to the SnO_2 has higher E_g than CZTS, the positive CBO might be formed. For the CZTS(e) solar cells, it has been reported that the SnO_2 phase occurs at the grain boundaries and the CBO with CZTS(e) absorber layer was calculated between 0.6 and 0.8 eV (Sardashti et al., 2015). Due to the positive CBO value, the barrier is formed and neither electrons nor holes trapping is detected. The XPS surface composition analyses in this study showed that the Type I CZTS films are Sn rich at the film surface which declares the SnO_2 at the surface. Therefore, the similar effect might have been occurred in our study.

Furthermore, for all Type I CZTS films the existence of CTS phases which has lower E_g than that of CZTS. The CBO value of CTS/CZTS interface has been reported as 0.2 and 0.5 eV (Bao, 2014) indicates that there occurs recombination process at the CTS/CZTS interface layers due to the flowing of both majority and minority charge carriers to CTS. This process decreases both the J_{SC} and V_{OC}.

For the CZTS A, SnS_2 is another detected secondary phase which is an n-type semiconductor with having indirect bandgap of 2.24 eV. This secondary phase may form a secondary diode inside the CZTS absorber layer or by behaving like an insulator in nature, it can result high photocarrier recombination (M. Kumar et al., 2015).

The composition of CZTS absorber layers has also effect on the photovoltaic performance of Type I CZTS solar cells. According to EDS analysis, CZTS A is Cu and Zn poor, CZTS B is Cu poor and Zn rich, CZTS C is only Zn rich. In the literature, the efficient CZTS solar cells have commonly Cu-poor and Zn-rich composition. Among them, the only CZTS B has the desired composition which has photo-conversion efficiency. EDX results were also declared that CZTS B and C are sulfur deficient. The S concentration is lower than 50% which means that the CZTS formation reaction was not completed well.

Since the sulfur vacancies behaves as a donor type defects which are not favorable for CZTS solar cell performance due to decreasing p-type conductivity (M. Kumar et al., 2015). MoS_2 layer is a factor for photo-conversion efficiency of solar cell. For the CZTS films A and B, Raman peak of MoS_2 was resolved as a result of peak fitting. However, for the CZTS C which was grown by the highest sulfurization time, this peak was appeared with highest intensity. The existence of this interface layer was also supported by XRD analysis. The increase in the sulfurization time resulted thick MoS_2 interface layer. The control of the CZTS/Mo interface is an important point because the thickness and intrinsic conductivity of MoS_2 layer strongly affect the electrical property of the back contact and the adhesion of the CZTS absorber layer. The increase in the thickness of MoS_2 interlayer acts as a back-contact blocking barrier which restricts hole transport across the Mo/CZTS interface to Mo and results poor device performance (K. J. Yang et al., 2015).

Even though the bulk conductivity of MoS_2 layer is an n-type, it has been reported both an n-type and p-type ultrathin MoS_2 layer (Dolui, Rungger, & Sanvito, 2013). The thick (~300 nm) MoS_2 layer generate a Schottky-type barrier with Mo back contact, enhances the series resistance and reduces the V_{OC} (K. Wang et al., 2010). In order to obtain good electrical contact with CZTS, the p-type MoS_2 interfacial layer is desired. Since n-type MoS_2 interface layer causes the barrier and blocks the transition of charge carriers. If the n-type MoS_2 layer formed at the interface between the Type I CZTS and Mo back contact, it causes a barrier for hole transport between Mo/MoS_2 interface. In this work, the thickness of MoS_2 layers were detected from the cross section image of the devices but the semiconductor types were not detected.

Another detrimental effect for Type I CZTS films is the thick CdS buffer layer. For the Type I solar cells approximately 108.2 nm thick CdS layer was used. Thick CdS causes the optical loss and decreases the solar cell characteristics of the related device. These are the possible reasons for the poor photovoltaic characteristics of Type I CZTS cells.

A straight-forward method was used for estimating the series and the shunt resistance of solar cell. In this method, the slope of J-V curve at the open-circuit voltage and short-circuit current density point gives the series and the shunt resistance, respectively. For the ideal solar cell R_{SH} and R_S are infinite and zero, respectively. The shunt resistance (R_{SH}) and series resistance (R_S) effect the photovoltaic performance of solar cell.

Since the magnitude and the effect of both series and shunt resistances link with the geometry and area of the solar cell, the resistive losses become larger while solar cell size increases. Shunt resistance results from the imperfections in bulk and cell surface. Shunt resistance stands for a parallel high-conductivity path across the p-n junction and the low value of it enhances the leakage current which diminishes the efficiency, maximum output power and the open circuit voltage (Singh & Ravindra, 2012).

The series resistance forms due to the back contact resistance between Mo and CZTS interface, front contact (Al:ZnO) resistance and the bulk resistance of the photoactive material (Kavitha et al., 2016). And also the absence or reduced amount of photon absorption in the buffer layer reduces the fill factor (FF) because of the enhancement of series resistance (Buffiere et al., 2014). The high value of series resistance decreases the short circuit current density and FF.

There are different factors that affect the short-circuit current density and lower it i) having a high positive conduction-band offset (CBO) between CZTS and CdS interface, ii) enhanced interface recombination at the interface between CZTS and CdS layers, iii) for short wavelength light the absorption losses induced by CdS layer, iv) for long wavelength light the low diffusion length of minority carriers (low mobility and/or life time of excited electrons) (Tajima et al., 2017). The other very important point is the optimization of band structure between CZTS/CdS heterojunction. The interface is strongly depend on the electron affinities of the constituted elements in the junction. The electron affinities can be changed with different deposition conditions such as using different growth method, pre and post-treatments.

The growth methods, pre- and post-deposition conditions have crucial effects on the nature of CZTS/CdS heterojunction as well as the band alignment. The photogenerated electrons have to pass CZTS/CdS interface, thus the conduction band offset (CBO) at this interface is very important. Depending on the difference in the electron affinities of the absorber and buffer layer, there exist two types of heterojunction interface which are ‘spike’ (type-I) or ‘cliff’ (type-II) like CBO. The cliff type is the negative CBO where the conduction band minimum of the buffer layer lies below that of the absorber layer and large cliff decreases the V_{OC} by increasing the probability of charge carrier recombination at the interface.

The spike type is the positive CBO where the conduction band minimum is of the buffer layer lies above that of the absorber layer and results the energy barrier for electrons.

The electrons at the conduction band of absorber should be overcome the barrier to be injected into the buffer layer. Although the carrier recombination (from the conduction band of buffer layer to valence band of absorber layer) at heterojunction interface diminishes by the positive CBO, the large spike limits the flow of minority carriers when they are transferred from the absorber to buffer layer and decreases the J_{SC} and the efficiency of the solar cell.

The band alignment of CZTS/CdS heterojunction is highly debatable in the literature. There are many reports that have different results on CZTS/CdS band structure. A spike-like CBO of 0.41 eV with pump/probe photovoltage shifts of the photoelectron spectra have been reported by Haight *et al.* (Haight et al., 2011). The another spike-like CBO of 0.1 eV between CZTS/ CdS interface has been reported using ultraviolet photoelectron spectroscopy by Kato *et al*. (Kato, Hiroi, Sakai, & Sugimoto, 2013). The first principle calculations by Nagoya *et al.* have reported a spike like CBO of 0.2 eV (Nagoya, Asahi, & Kresse, 2011). On the contrary, there are also some reports which support the cliff-like CBO of CZTS/CdS heterojunction. Santoni *et al.* have reported a cliff like CBO by calculating direct (-0.30 eV) and indirect (-0.34 eV) methods (Santoni et al., 2013). Li *et al*. used synchrotron radiation photoemission spectroscopy for determine the CBO at the CZTS/CdS junction and it was obtained -0.06 eV cliff like CBO (J. Li et al., 2012). Tajima *et al.* using hard X-ray photoelectron spectroscopy have measured a flat CBO for CZTS/CdS interface (Tajima et al., 2013). Therefore, in the literature the optimal CBO value should be in the range from +0.4 to -0.2 eV for the CZTS/CdS interface (Tajima, Itoh, Hazama, Ohishi, & Asahi, 2015).

From the J-V curve of cell B in Figure 6.28 (b), the J_{SC}, V_{OC}, FF and η were calculated as 1.75 mA/cm^2, 140.8 mV, 27.3% and 0.07%, respectively. The activated cell area is 0.057 cm^2. For the solar cell B, the R_{SH} and R_S were determined as 87.55 Ω cm^2 and 73.7 Ω cm^2, respectively. R_S value is very high whereas R_{SH} is very low when compared with the ideal solar cell. Due to the high R_S, the magnitude of J_{SC} and the FF are very low. The detailed parameters of the solar cells extracted from the J-V curve characteristics are listed in Table 6.13.

The dark and illuminated J-V curves of cell B are cross over. There are different reasons for observing this crossover. Wang *et al.*, has reported that between Mo and CZTS interface the back contact blocking barrier (Schottky barrier) which restricts the hole transform across the Mo to CZTS layer interface is formed.

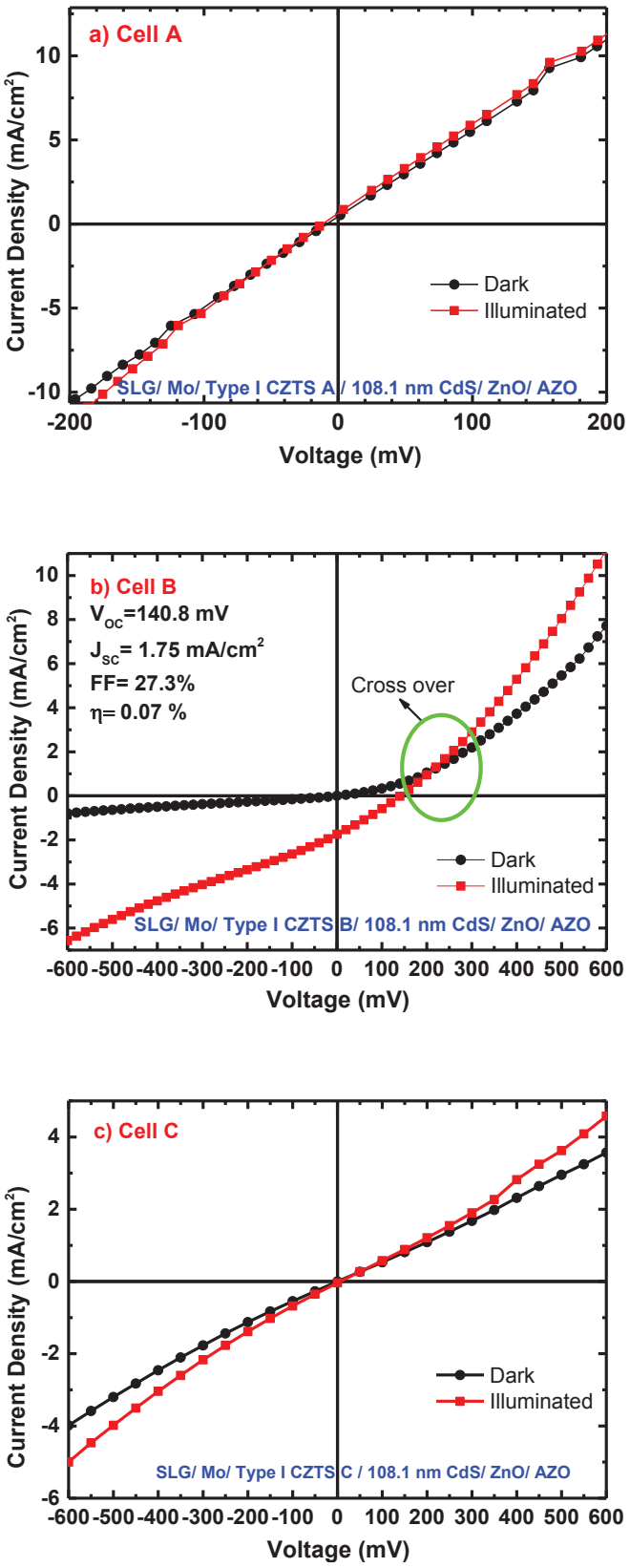

Figure 6.28. J-V curve of Type I solar cells a) A, b) B and c) C.

They calculated the barrier height as 0.32 eV which causes the high series resistance and cross-over of dark and light J-V curves (K. Wang et al., 2010).

The crossover of dark and illuminated J-V curve in CIGS/CdS and CZTSSe/CdS solar cells is reported due to the result of photoexcitation in the CdS buffer layer (Meher, Balakrishnan, & Alex, 2016). Based on this, it is assumed that the origin of the crossover phenomena in CZTS solar cells is most probably link with the photo-doping of the CdS buffer layer. The presence of Cd vacancies (V_{Cd}^{-}) in the CdS buffer layer causes the illumination dependent deep acceptor-like trap states (Neuschitzer et al., 2015). In dark condition of the solar cell, these acceptor like traps are negatively charged by capturing electrons and they partially compensate n-type doping of CdS because there are no available photo-generated holes in CdS layer to neutralize these acceptor states (Chung, Bob, Song, & Yang, 2014). As a result inside the CdS buffer layer, more negative space charge is generated under equilibrium conditions which reduces the conduction band bending which means the increment in the spike (Buffiere et al., 2014).

Under illumination, the behavior of these deep acceptor-like trap states are different. When the solar cell is lighted, electron-hole pairs are created due to the absorption of photons by CdS buffer layer. These photo-generated holes from the CdS valence band are captured by these deep acceptor-like trap states and neutralize them. Since the carrier of CdS is trapped by the acceptor defects, CdS is named with photo-dopped CdS. After this process, the barrier height is reduced at both CZTS/CdS and CdS/ZnO interface. The height of spike is important because they can act as a barrier for photo-generated electrons. Having light sensitive defects inside the buffer layer causes the cross over in dark and light J-V curves due to the change in the barrier height of spike under dark and illumination of solar cell. Figure 6.29. demonstrates the band diagram of CZTSe/CdS heterojunction with light sensitive defects in CdS buffer layer.

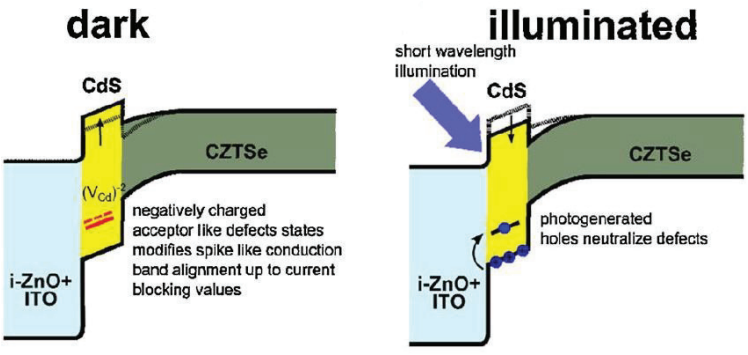

Figure 6.29. Demonstration of band alignment of CZTSe/CdS heterojunction under dark and illuminated conditions, with light-sensitive trap states inside CdS buffer layer (Source: Neuschitzer et al., 2015).

Figure 6.30. demonstrates the cross section of solar cell B. From this image, it is clear that CZTS absorber and CdS buffer layers were grown 1.2 µm and 108.1 nm, respectively. The total thickness of ZnO and AZO layers was detected as 345.4 nm. It seems that CZTS film grown very well without any void. However, 59.5 nm thick MoS_2 interface layer was detected which might form during the sulfurization process of CZTS.

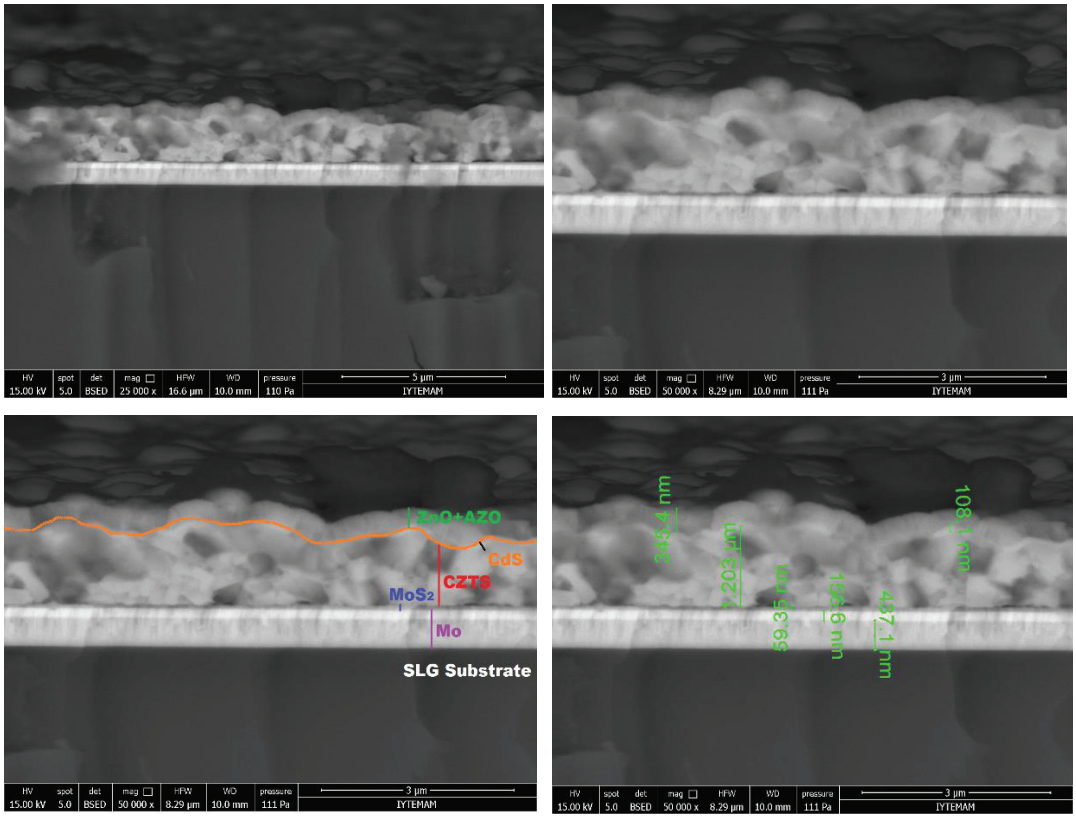

Figure 6.30. SEM cross view of cell B.

Similarly, the devices constructed using Type II CZTS absorber layers were called according to name of CZTS absorber layers. For these device structures, the CZTS absorber layers were grown with the same parameters but there observed little deviations in the film composition and the structure of CZTS films. As mentioned in the section 6.1., Type II CZTS films were deposited with changing the order of Cu layers which have different thickness. For the order of Type II CZTS, thick Cu layer were sequentially deposited with Sn layer. The thin Cu layer was deposited as a capping layer to top of the precursor. In this way it was investigated the effect of Cu thickness near the Sn layer. And also for the Type II solar cells the change in the thickness of CdS was investigated. The morphology and the electrical performance of CdS buffer layer strongly depend on the deposition parameter as well as the post and pre-deposition treatments.

Therefore for the Type II CZTS solar cells the only thickness effect of CdS on the electrical performance of the devices was investigated. Thickness of CdS was changed using different deposition time. For selecting the thickness of CdS, the thickness calibration of CdS as mentioned in section 6.2. was used. However, there observed little deviations in the CdS thickness from the calibration results. This difference may be originated from the different surface roughness of SLG substrate and CZTS film or from the experimental factors during the CBD deposition.

For the Type II CZTS absorbers, the device structures were fabricated as SLG/ Mo/CZTS (D)/140.3 nm CdS/ZnO/AZO, SLG/Mo/CZTS (E)/134.9 nm CdS/ZnO/AZO, SLG/Mo/CZTS (F)/102.5 nm CdS/ZnO/AZO and SLG/Mo/CZTS (G)/75.54 nm CdS/ ZnO/AZO. For Type II CZTS solar cells, the improvement in the photovoltaic characteristics were detected. However, the efficiency value is lower than the literature. There are some critical points about the poor photovoltaic performance of Type II CZTS solar cells. The XRD analysis of Type II CZTS absorber films have showed that these films contain MoS_2, MoO_2 and ZnO phases as well as CZTS structure.

The cross section of all devices revealed the existence of MoS_2 layers with the thickness between 48 and 118 nm. This layer forms as a result of partial sulfurization of Mo back contact during the sulfurization of CZT metallic precursors. The thickness of this layer is low when compared with the literature (K. J. Yang et al., 2015). The existence of MoO_2 interlayer between Mo/CZTS interface was detected. The beneficial effect of MoO_2 interlayer on the photovoltaic performance of CIGS and CZTSe solar cells have been reported (Lopez-Marino et al., 2016). The formation of MoO_2 interlayer increased the V_{OC} and FF when exists at a certain amount. For the CZTS it has been reported that the increase in the oxygen content at the Mo back contact lowers the Mo-S interaction and decreases the MoS_2 layer formation and improves the photovoltaic characteristic of CZTS by reducing R_S. Therefore, 20-30 nm thick MoO_2 interlayer may improve the back contact interface by reducing the MoS_2 formation (Lopez-Marino et al., 2016). However, the MoO_2 formation was detected by the only XRD analysis and from the cross section of these devices the existence of this layers are not apparent.

The other detected phase by XRD of Type II CZTS films is the ZnO. ZnO is an n-type semiconductor with bandgap of 3.3. eV. The CBO value for the ZnO/CZTS interface was determined as 0.09 eV by experimentally and 0.07 eV from the first principle calculation which implying Type I band alignment (G. Yang et al., 2015).

The low CBO value represents that there occur ideal band structure between CZTS/ZnO where there is not high barrier for the electron transfer from CZTS to ZnO. J-V curve of cell D is given in Figure 6.31. For this device structure 140.0 nm thick CdS layer was used. The determined J_{SC}, V_{OC}, FF and η from the J-V curve are 1.62 mA/cm^2, 255.3 mV, 32.9% and 0.14%, respectively. The active cell area is 0.070 cm^2 for this measurement. The R_{SH} and R_S values are 282.2 and 97.3 Ω cm^2, respectively.

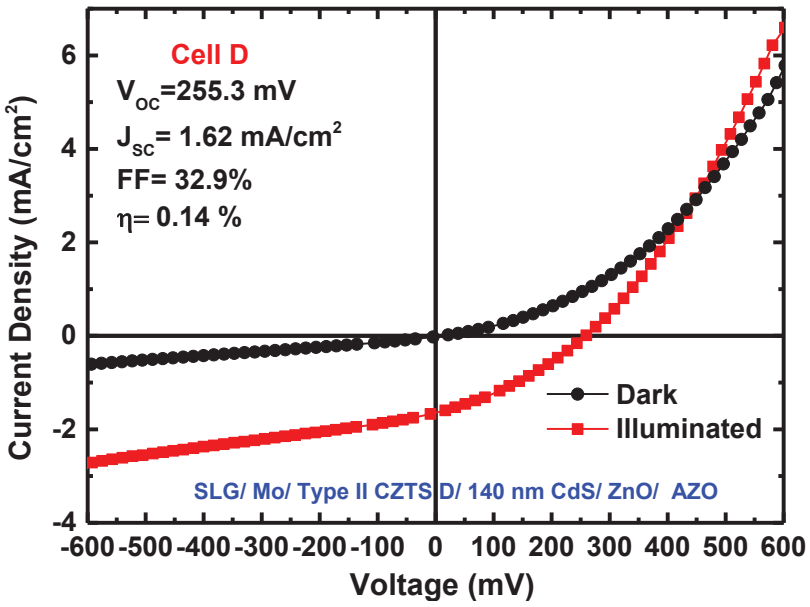

Figure 6.31. J-V curve of Type II CZTS cell D.

When the device D is compared with the cell B the improvement in V_{OC}, FF and η were detected. Although the thicker CdS was deposited than that of cell B, the development in photovoltaic characteristics were observed. This might be the result of improvement in the Type II CZTS structure in terms of composition which is in the desired range for the Type II CZTS. However, the J_{SC} of cell D is lower than that of the cell B due to the higher value of R_S for the cell D. The reason of high R_S might be the existing of thicker MoS_2 layer which can enhance contact resistance. Figure 6.32. shows the cross section of the device D. The CZTS D layer in this cell has some porous and due to the porous structure the thickness of CZTS film was determined 1.495 μm which is higher than the expected thickness. The CdS thickness is 140.0 nm which is the thickest that was used in this study. The total thickness of ZnO and AZO layers are 345.3 nm. The 118.8 nm thick MoS_2 interface layer which is the thickest one that observed in this study was detected due to the sulfurization of Mo back contact during the CZTS growing.

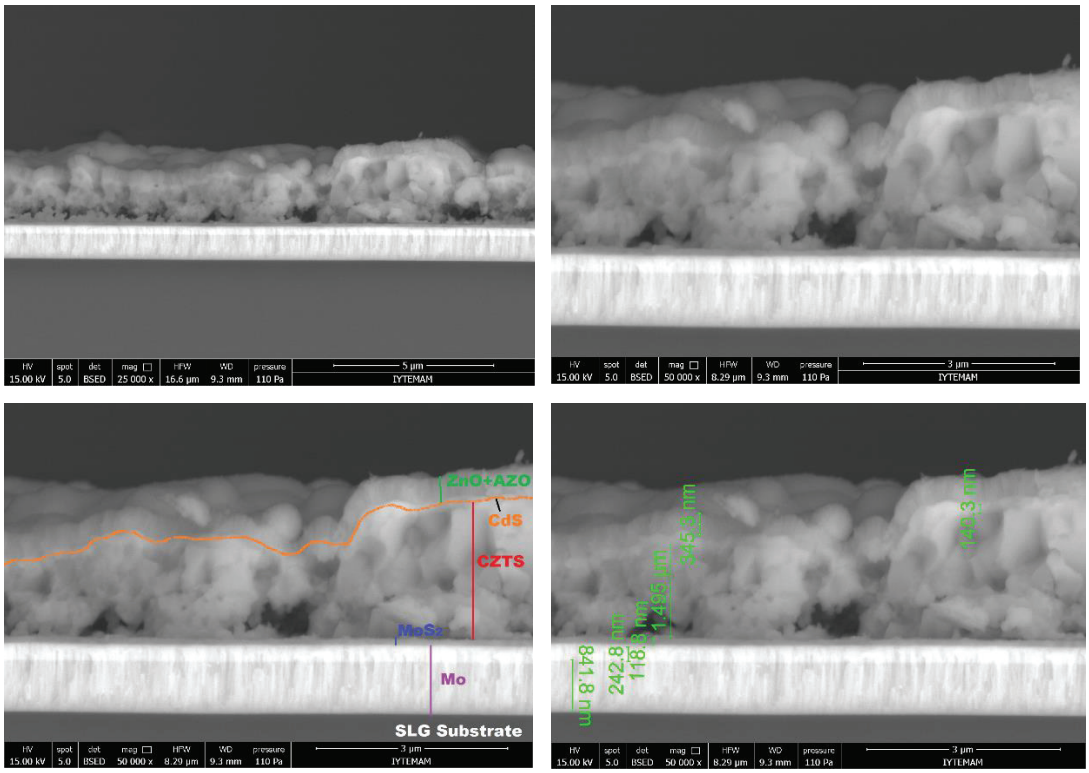

Figure 6.32. SEM cross view of cell D.

Cross section of some solar cells showed that CZTS layers used for device fabrications are porous. In the CZTS literature, it is often reported the voids at the Mo-CZTS interface (in Figure 6.33.) which decreases the electrical conductivity (Khalkar et al., 2015; Tajima et al., 2015). These voids called Kirkendall voids form due to the Kirkendall effect because of the different interdiffusion velocity of Cu, Zn and Sn element. These voids most probably formed at the Cu-Sn interface as demonstrated in Figure 6.34. For example, during the film growth process Cu tend to migrate towards the film surface. Since the Cu has higher diffusivity than Sn, the migration of Cu through the Sn results the Cu-Sn alloy formation at the Cu-Sn interface and results the voids behind. During the sulfurization of the metallic precursor, Cu continue to migrate through the surface to form Cu_2S and the flux of voids move towards the substrate.

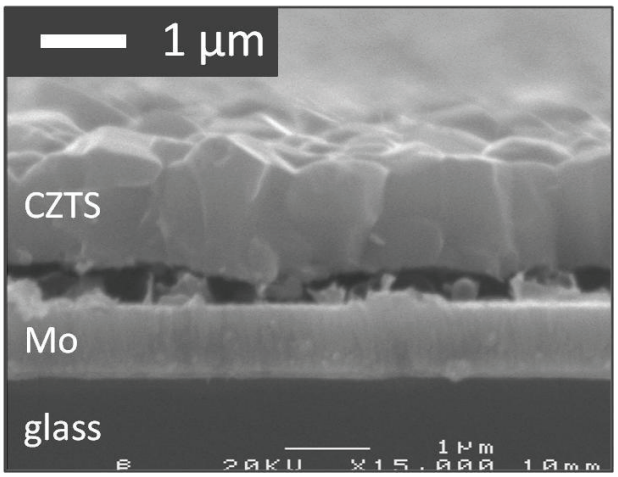

Figure 6.33. Kirkendall voids in CZTS Source: (Scragg, 2010).

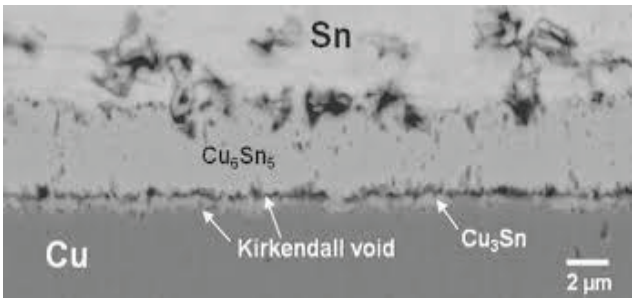

Figure 6.34. The formation of Kirkendall voids between Cu-Sn metallic stack interfaces (Source: J.-M. Park, Kim, Jeong, & Park, 2014).

In that the void formation by Kirkendall effect bases on the diffusion process and it is activated by thermally, thus it is expected for this study that it might occur at high rate. Since it decreases the electrical conductivity as well as J_{SC} (Tajima et al., 2015), the Kirkendall voids are one of the main parameters that effect the photovoltaic characteristics of the CTZS solar cells.

J-V curve of cell E is given in Figure 6.35. For this device structure 134.9 nm thick CdS layer was used. The determined J_{SC}, V_{OC}, FF and η from the J-V curve are 3.73 mA/cm^2, 317.0 mV, 33.8% and 0.4%, respectively. The active cell area is 0.215 cm^2 for this measurement. When the device E is compared with the cell D the improvement in V_{OC}, FF and η were detected. The R_{SH} and R_S are 157.2 and 55.7 Ω cm^2, respectively.

The reduction in the R_S is the result of the existence of thinner MoS_2 layer with respect to the cell D. However the decrement in R_{SH} was observed. Since the CZTS absorbers are not homogeneous, the reduction of R_{SH} might be from the localized imperfections in absorber layer of the measured cell. From the dark and illuminated J-V curves of cell E, it was not observed cross over.

For this cell, the deep acceptor-like trap states in CdS buffer layer which depends on buffer layer growth process might be reduced. The decrement in thickness of CdS buffer layer improved the photovoltaic response of the CZTS cell E.

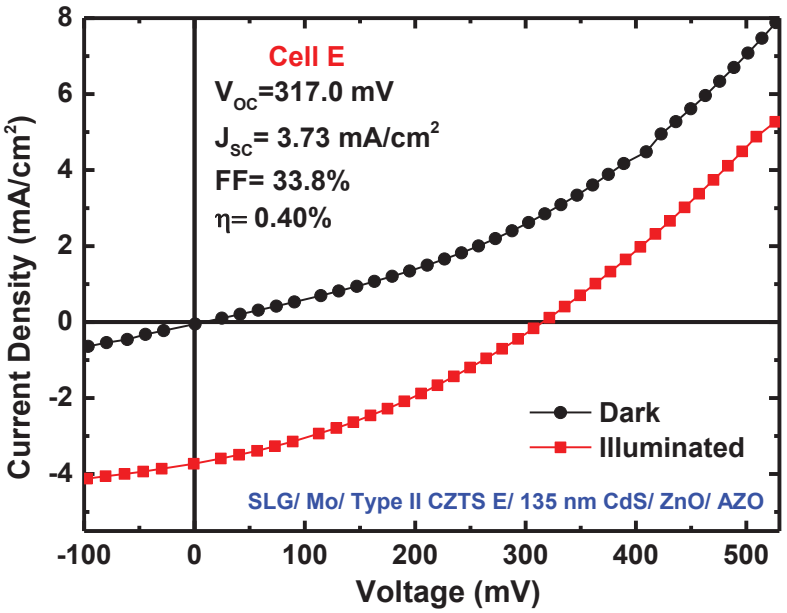

Figure 6.35. J-V curve of Type II CZTS cell E.

Figure 6.36. demonstrates the cross section of cell E. The thickness of CZTS film was determined 1.2 µm which is the expected thickness. The CdS thickness is 134.9 nm. The total thickness of ZnO and AZO layers are 356.2 nm. The 70.35 nm thick MoS_2 interface layer which was detected due to the sulfurization of Mo back contact during the CZTS growing.

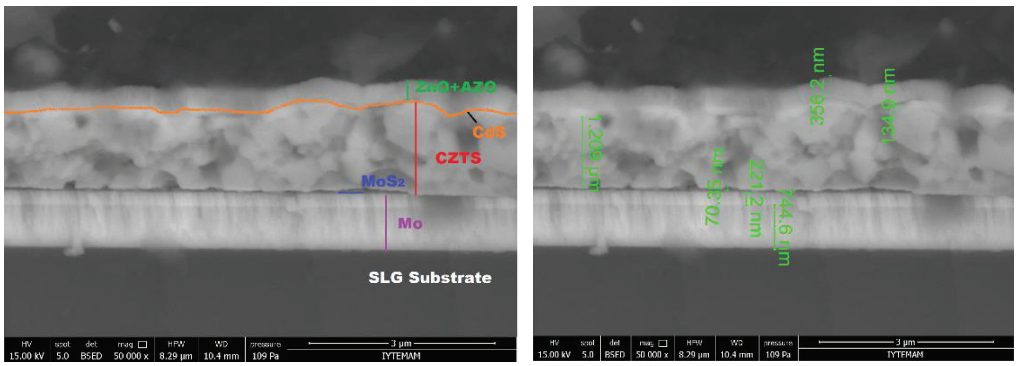

Figure 6.36. SEM cross view of cell E.

The J-V characteristic of CZTS cell F is given in Figure 6.37. This device was fabricated using 102.5 nm CdS layer. The determined J_{SC}, V_{OC}, FF and η from the J-V curve are 2.76 mA/cm^2, 402.0 mV, 53.8% and 0.6%, respectively. The active cell area is 0.123 cm^2 for this measurement. The R_{SH} and R_S values are 692.0 and 37.3 Ω cm^2, respectively. For this film R_{SH} and FF have the highest values that obtained in this study. The reason of the highest R_{SH} might be improvement in the CZTS absorber layer by reducing void formation which is seen from the cross section in Figure 6.38. and the improvement in CdS/CZTS heterojunction.

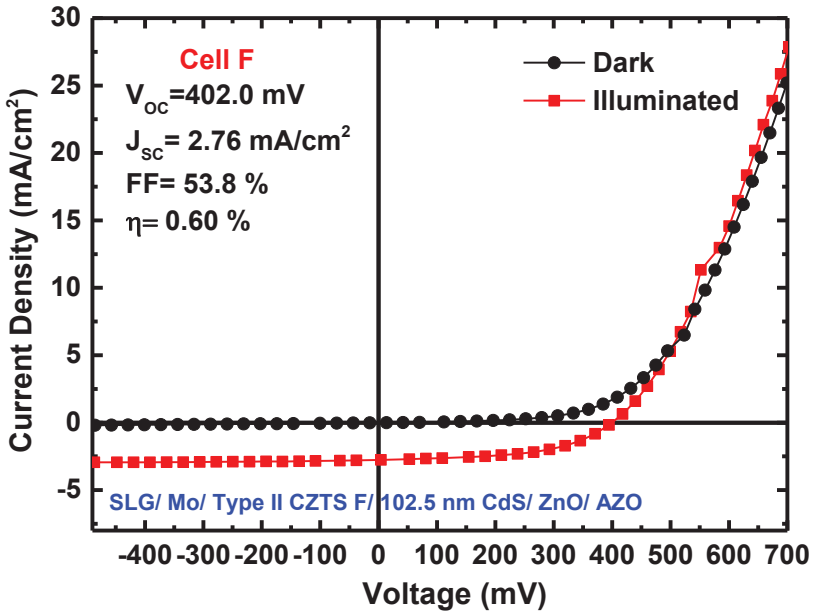

Figure 6.37. J-V curve of Type II CZTS cell F

The CdS thickness of the cell F is nearly the same for the cell B where the CdS thickness is 108.1 nm. Although the CdS buffer layers have the same deposition time for both the cells B and F, there observed a few nanometer difference in the CdS thickness. Therefore these cells are the examples that showing the difference in Type I and II CZTS absorber layers in best. When the cell F is compared with the cell B, J_{SC}, V_{OC}, FF and η values are improved. The XRD pattern of CZTS B showed the existence of SnO_2 whereas the CZTS F showed ZnO. The higher CBO for SnO_2/CZTS interface than ZnO/CZTS interface has been reported which means that the existence of SnO_2 causes higher barrier for the electrons than the ZnO and reduces the cell efficiency. And also Type I CZTS B includes tetragonal CTS phase whereas the Type II CZTS F is not.

The existence of this phase might increase the recombination for the cell B and reduces the photovoltaic characteristic. From the EDS results, due to the S content in

Type II CZTS F is higher than 50% which means that the film is not sulfur deficient and the CZTS formation process completed. And also using Type II order, the Sn loss decreased by alloy formation and the XPS surface analysis indicated that for Type II CZTS film Sn concentration at the surface was reduced. Therefore the improvement in Type II CZTS enhanced the efficiency of cell F.

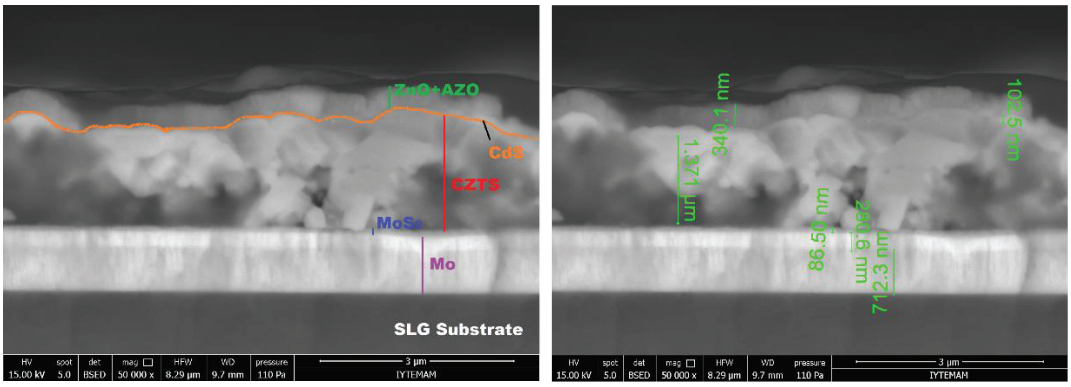

Figure 6.38. SEM cross view of cell.

When the cell F is compared with the cell E, the open-circuit voltage, FF and the efficiency values were improved but the short-circuit current density decreased. The R_{SH} is boosted from 156 to 692 Ω cm^2 with decreasing the CdS thickness that used for the cell E. Since the R_{SH} is high, there might be different reason for the reduction in the J_{SC}.

The J-V characteristic of CZTS cell G is given in Figure 6.39. This device was fabricated using 75.54 nm CdS layer. The determined J_{SC}, V_{OC}, FF and η from the J-V curve are 5.77 mA/cm^2, 390.0 mV, 42.9% and 0.96%, respectively. The active cell area is 0.105 cm^2 for this measurement. The R_{SH} and R_S values are 244.4 and 25.9 Ω cm^2, respectively. Cell G has the highest J_{SC} and η the lowest R_S values in this work. The reason of the lowest R_S is having the thinner MoS_2 interface layer than the other CZTS films used in this study. Thin MoS_2 layer might decrease the back contact barrier and resulted the lower R_S than the other CZTS used in this work. By decreasing CdS thickness, J_{SC} grows up from 2.76 to 5.77 mA/cm^2 and therefore the efficiency jumps from 0.6 to 0.96%. However, the reduction in R_{SH} resulted the similar effect on the FF and V_{OC} when compared with the cell D which may be accounted for by the localized shunting path (Kirkendall voids) (Sugimoto, Liao, Hiroi, Sakai, & Kato, 2013) as shown the cross section of cell G in Figure 6.40.

The cross section images show that CZTS G has a lot of voids in some regions. From the different magnified images, there observed nonuniform film across the back contact.

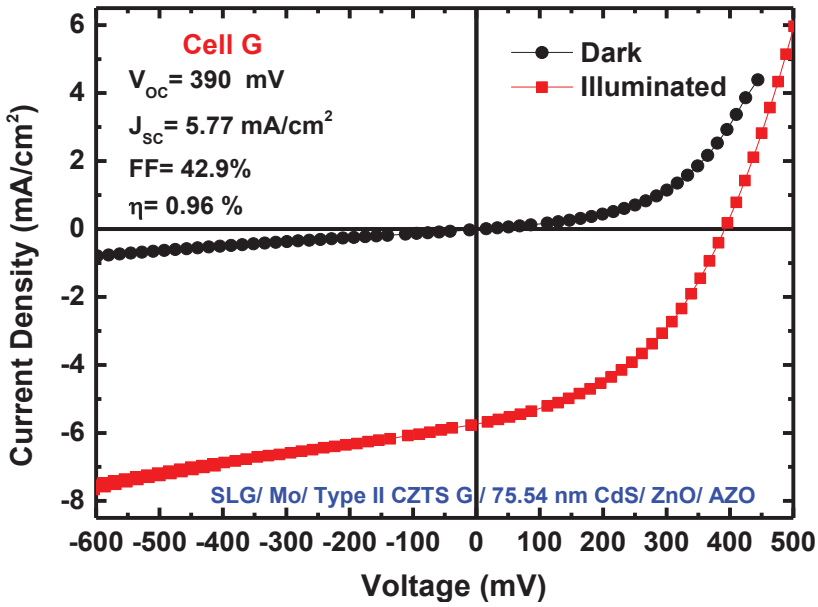

Figure 6.39. J-V curve of Type II CZTS cell G.

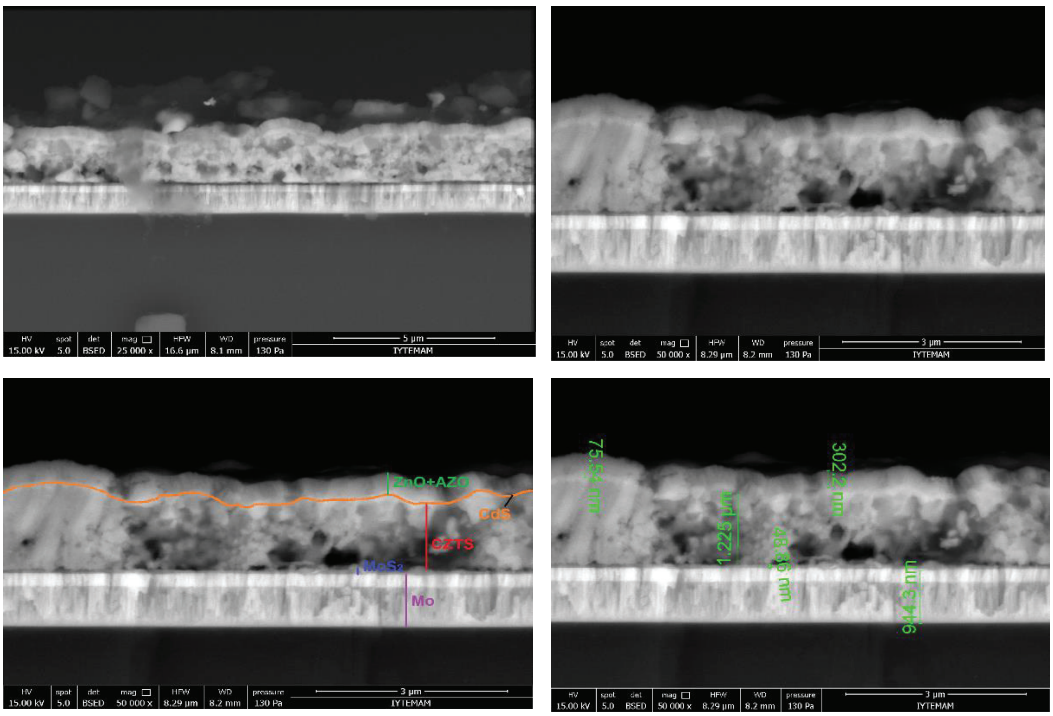

Figure 6.40. SEM cross view of cell G.

Table 6.13. Comparison of light device characteristics of SLG/Mo/CZTS/CdS/ZnO/AZO heterojunction solar cells using different type of CZTS and CdS buffer thickness.

Cell	Absorber Type	CdS Thickness (nm)	V_{OC} (mV)	J_{SC} (mA/cm^2)	FF (%)	η (%)	R_{SH} (Ωcm^2)	R_S (Ωcm^2)
B	I	108.1	140.8	1.75	27.3	0.07	87.6	73.7
D	II	140.0	255.3	1.62	32.9	0.14	282.2	97.3
E	II	134.9	317.0	3.73	33.8	0.40	157.2	55.7
F	II	102.5	402.0	2.76	53.8	0.60	692.0	37.3
G	II	75.54	390.0	5.77	42.9	0.96	244.4	25.9

The photovoltaic characteristics of Type I and Type II CZTS solar cells have discussed in terms of the stacking and composition difference of absorber layers, the effect of formed secondary phase in the absorber layer, MoS_2 interface layer, void formation inside the absorber layer and the thickness of CdS buffer layer. Table 6.13. summarize the photovoltaic properties of the examined CZTS solar cells in this study.

For the Type II CZTS solar cells, the effect of especially CdS thickness was investigated from the J-V curves. In order to realize this effect on the photovoltaic response of solar cell, the J-V curve of Type II D, E, F and G solar cells are given in Figure 6.41. Although the growth process of these absorbers are the same, there is little deviations in their composition and the bulk structure. By considering these films are nearly the same, the different thick CdS buffer layers are used for the device structure. For the Type II CZTS solar cells, the significant improvements in the photovoltaic properties were observed. The CZTS samples with Type II order where the thick Cu was deposited sequentially with Sn layer have Cu poor and Zn rich composition which leads to decrease of the Sn_{Zn}, Cu_{Sn}, Cu_{Zn} + Sn_{Zn} and $2Cu_{Zn}$ + Sn_{Zn} defects. These defects are highly effective recombination centers for electron-hole pairs (Sagna et al., 2015). The Zn_{Cu} +V_{Cu} defect clusters may formed which provide an increase of the optical and electrical properties. In the literature, it is put forwarded that higher efficiency from the solar cells can be obtained when the Cu and Sn layers are sequentially deposited and the Cu plays a crucial role in the solar cell performance. With the deposition of thick Cu layer below the Sn layer in the stacking order may improve the CZTS as well as develop the band alignment of CdS/CZTS heterojunction with resulting the increment in V_{OC} (Tajima et al., 2015).

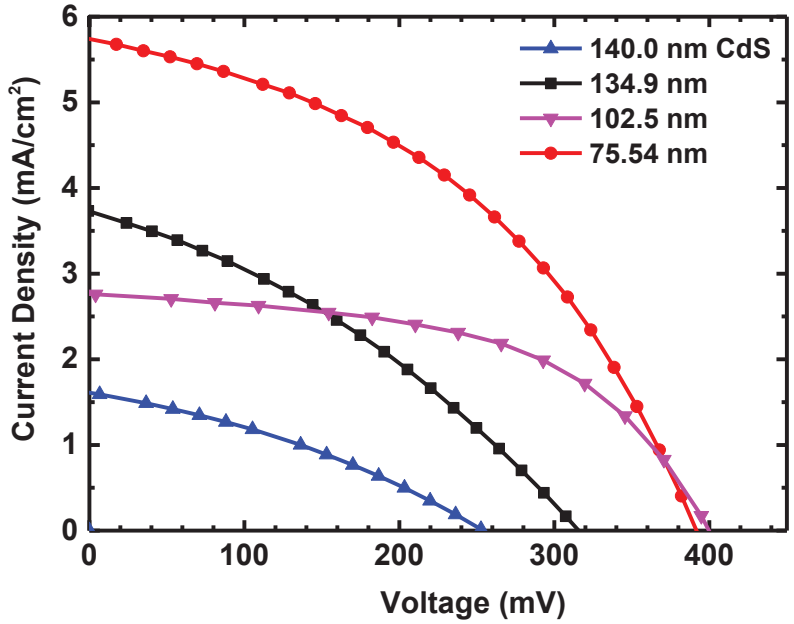

Figure 6.41. J-V curve of Type II CZTS solar cells under illuminated condition.

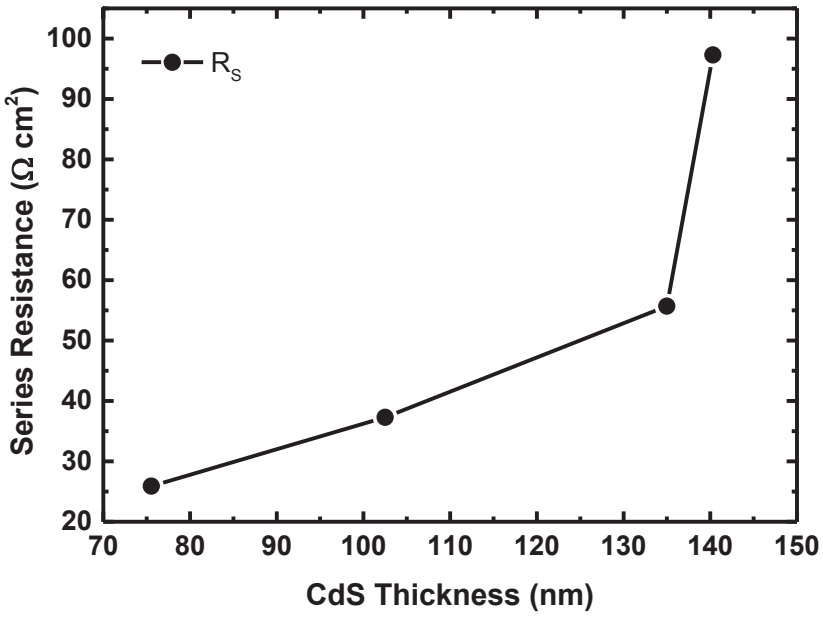

Figure 6.42. Variation of Series Resistance (R_S) with respect to CdS buffer layer thickness.

Figure 6.42. demonstrates the variation in R_S with respect to CdS thickness. In order to decrease series resistance, the thickness of CdS should be as small as possible. The thickness of MoS_2 interlayer is also important for low series resistance where the lowest R_S is obtained for the cell G having thinnest CdS buffer and MoS_2 interface layer. Figure 6.43. gives the change in solar cell parameters under illumination with respect to thickness of CdS buffer layer.

The variation of V_{OC} is given in Figure 6.43. (a). V_{OC} enhances with diminishing CdS thickness but slight reduction was detected for the cell G with thinnest CdS buffer layer. The reason of this slight decrement is the reduction in R_{SH} with respect to cell F. In Figure 6.43. (a) and (c), the variation of V_{OC} and FF have similar trend with CdS thickness. Figure 6.43. (b) shows that J_{SC} improved with reduced CdS layer due to the decrement in the absorption loss in the blue region (the wavelength between 492 and 455 nm) inside buffer layer.

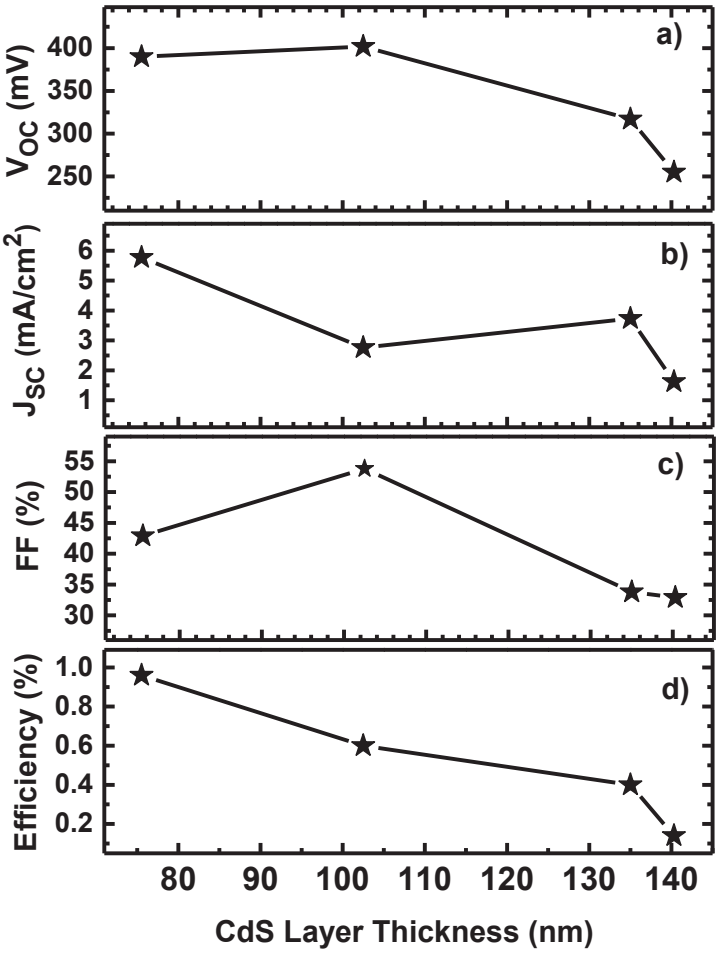

Figure 6.43. Effect of CdS buffer layer thickness on solar cell parameters a) V_{OC}, b) J_{SC}, c) FF and d) η.

However, for the cell E a little increment was detected which might be caused reduction in interface recombination or decreasing in the positive CBO at CdS/CZTS interface which depends on deposition process. In the case of very thin buffer layer, it decreases the space charge width and results in a poor collection of the photo-generated carriers.

Very thin buffer layer may enhance the leakage current due to the increasing in pinholes or voids. Otherwise, pinholes can cause direct contacts between the window layer and the CZTS, which results to weak photovoltaic performance by reducing the efficiency. Therefore, the determination of the optimum thickness for buffer layer is very crucial. Conversely, more number of photons will absorbed by the thick buffer layer and therefore, they cannot reach the CZTS absorber layer. In addition, if the thickness of CdS buffer layer is high, the carrier collection will be more difficult because the carrier collection path becomes longer. In this case the generated electron-hole pairs do not contribute to the photocurrent and causes the optical loss. Therefore, solar cell efficiency reduces with the enhancement of CdS thickness as seen in Figure 6.43.(d).

The results obtained from this thesis showed that there are many different parameters such as CZTS stoichiometry, secondary phase formation, thickness of CdS, existence of light-sensitive deep trap states which affect the photovoltaic performance of solar devices.

CHAPTER 7

CONCLUSION

In this thesis, the optimization of CZTS absorber and CdS buffer layers with convenient properties to fabricate efficient solar cells have been studied. The main targets of this project were determine the influence of sequentially grown Cu and Sn layers on CZTS absorber layer properties and the thickness effect of CdS buffer layer on the photovoltaic response of fabricated solar cells. As described in Chapter 5, two step process were followed to grown CZTS absorber layers on Mo coated SLG substrates. The first step is based on vacuum deposition of precursors by magnetron sputtering technique. The second process was followed by a heat treatment in sulfur atmosphere. The CZT metallic precursors were deposited by trying two different Cu thickness sequentially grown with Sn layer. In terms of Cu thickness, two different orders Type I (Mo/SLG/Cu (55 nm)/Sn/Zn/Cu (120 nm)) and Type II (Mo/SLG/Cu (120 nm)/Sn/Zn/Cu (55 nm)) have been developed for the metallic precursor growth, with the aim of achieving a good homogeneity, control of the film composition and phase stability. The reason of sequentially grown Cu and Sn layers was to reduce the Sn loss during the sulfurization by forming the Cu-Sn related alloy formation which can be formed at room temperature. All CZTS films in this work was sulfurized at 550 °C under sulfur atmosphere. The details of CZTS growth mechanism has been given in Chapter 5.1.

The influence of sulfurization time was investigated for Type I CZTS films. The sulfurization time tested had little influence on the film surface morphology and crystal structure properties but the film composition, secondary phase and MoS_2 interface layer formations affected by sulfurization times. The increase in MoS_2 interface formation for Type I CZTS films was also detected with sulfurization time. XRD analyses of Type I CZTS films consist of the main peaks of CZTS structure and SnO_2 phase. Mo peaks from substrate and the peak belongs to MoS_2 interface layer were also detected. Raman analysis of Type I CZTS showed spectrum broadening which is the result of existence of secondary phases. Therefore, the peak fitting was applied for Raman spectrum to resolve the existence phases. The peak fitting of Raman analysis of Type I CZTS demonstrated

that the disorder kesterite CZTS phase which is detected between 329 and 331 cm^{-1} was the dominant phase for these films.

Other detected phase was CTS which cannot be identified by XRD due to the match of XRD peaks with CZTS and ZnS. SEM surface images of Type I CZTS films were nearly the same but the film A which was sulfurized for 30 min contained a flat shape structures localized film surface. The point analysis of this structures by EDX confirmed the formation of SnS_2 phase which is one of the binary phases accompanying CZTS formation. The bulk composition of Type I CZTS films by EDX analysis showed different compositions depending on sulfurization times. Sn loss increased with sulfurization time which is commonly observed for CZTS films due to having low melting point of Sn. Sn loss from the bulk CZTS accumulated on the films surface and formed SnO_2 phase. In Type I order where the thin Cu layer was sequentially deposited with Sn, there might not reduce Sn loss during the sulfurization and resulted SnO_2 phase on the film surfaces. Depending on Sn loss, Cu/Zn+Sn ratio increased with sulfurization time where this ratio should be in the range of 0.8-0.9 for solar cell applications. For efficient solar cells, CZTS absorber layer should be Cu-poor and Zn-rich composition. Type I CZTS absorbers did not have this desired composition except CZTS B which was sulfurized for 45 min. Type I CZTS absorbers were also S deficient where the CZTS formation process was not completed. The S concentration was lower than 50% except CZTS A where SnS_2 formation on the film surface increased S concentration. Sulfur vacancy plays a donor type defects which reduce the p-type conductivity. Surface quantification of Type I CZTS films was determined by XPS analysis. Type I CZTS films had Sn rich surface composition which confirmed the Sn loss from the bulk and accumulation on the CZTS surface. XPS surface characterization was also showed that Cu and Zn composition on the films surface increased with sulfurization time. XPS surface analysis of Type I CZTS films demonstrated that Cu, Zn, Sn and S elements had chemical states of +1, +2, +4 and -2, respectively that expected in CZTS structure. For Type I films, SnO_2 formation at the surface of films was also detected by XPS surface analysis.

Type II CZTS films were grown by using Mo/SLG/Cu (120 nm)/Sn/Zn/Cu (55 nm) order. The depositing of thick Cu near the Sn layer changed the CZTS properties. Four Type II CZTS films were grown by using sulfurization process at 550 °C for 45 min. All Type II CZTS films showed similar properties.

XRD analysis confirmed the formation of CZTS but ZnO and MoO_2 phases were also detected. Similar to Type I CZTS films, Mo and MoS_2 peaks were also observed. By changing the Cu order, the broadening in Raman spectrum was reduced. Similarly Type I CZTS films, the disorder kesterite phase was dominant for all Type II CZTS but CTS phase formation was not detected for these samples from Raman analysis. According to SEM images, changing the Cu thickness near the Sn layer did not result the change in surface morphology of Type II CZTS from Type I films but apparent change in bulk composition was encountered from EDS analysis. Sn loss was reduced and S deficiency was eliminated for Type II CZTS samples. All Type II CZTS films were in the desired composition of Cu-poor and Zn- rich. Although Type II order did not prevent the Zn accumulation on the films surface which caused the formation of ZnO phase, the absence of neither CTS nor other secondary phases confirmed the role of Cu-Sn alloy formation in the reduction of Sn loss. Depositing thick Cu near Sn layer might enhance the CTS phase which involves in the reactions for CZTS formation. XPS analysis revealed that Cu, Zn, Sn and S elements had chemical states of +1, +2, +4 and -2, respectively that expected in CZTS structure. According to quantification analysis by XPS, Type II CZTS film had less Sn concentration than Type I CZTS on the film surface but Zn concentration was higher due to the ZnO formation on the surface. Quantification analysis showed that bulk and surface compositions of CZTS films were different which means that grown CZTS films were not homogeny. Analysis of CZTS absorbers demonstrated that Type II order CZTS films had the higher degree of phase purity than Type I order films and desired composition for solar cell applications. Consecutively grown thick Cu and Sn layers enhance the quality of CZTS absorbing films used for solar cell applications.

CdS buffer layers were deposited by chemical bath deposition technique. Different deposition time durations were used and thickness of grown CdS films were determined using spectroscopic ellipsometer. Thickness of CdS showed direct proportion with deposition time. In the first 60 min deposition, high deposition rate was detected which was occured due to the dominance of ion-by-ion processes. XRD analysis of CdS films showed mixed hexagonal and cubic phase for the low deposition time but cubic phase was dominant phase for the high deposition time. Surface morphology of the deposited CdS thin films was highly affected by the deposition time. The CdS films deposited at low deposition time had many voids and pinholes at the film surface and they reduced with the deposition time. According to EDS analysis, the Cd/S ratio decreased with deposition time which was supported with XPS surface quantification analysis.

Since the sulfur vacancy plays a role in donor type defect which increase n-type conductivity, excess Cd concentration is desired. CdS films showed higher than 70% transmission and optical bandgap values between 2.38 and 2.45 eV depending on deposition time. Except the CdS film deposited 30 min, all CdS films showed the desired properties for photovoltaic applications.

The grown CZTS films were used for the construction of device structure of SLG/Mo/CZTS/CdS/ZnO/Al:ZnO. For the cell fabricated using Type I CZTS, CdS buffer layer, ZnO and AZO layers were deposited 108.1, 40 and 300 nm, respectively and the effect of sulfurization time of CZTS absorber layer on the photovoltaic response of solar cell has been investigated. For the cell A and C where the CZTS films were sulfurized for 30 and 60 min, respectively, the ohmic J-V curves were detected and there was not observed any shift under illumination. On the contrary, the J-V curve of cell B was as expected and the shift of J-V curve under illumination was also observed.

For the solar cell B, J_{SC}, V_{OC}, FF and η were calculated as 1.75 mA/cm^2, 140.8 mV, 27.3% and 0.07%, respectively. The R_{SH} and R_S were determined as 87.55 Ω cm^2 and 73.7 Ω cm^2, respectively for the cell B. The reasons of poor photovoltaic characteristics of Type I solar cells might be the existence of secondary phases, formation of MoS_2 interface layer and thick coated CdS layer. For the solar cell B, R_S value is very high whereas R_{SH} is very low when compared with the ideal solar cell. Due to the high R_S, the magnitude of J_{SC} and the FF are very low.

The junction between the absorber and CdS layers is important in terms of CBO which plays a major role in minority carrier transport in the junction region. For high performance CdS/CZTS solar cells, a spike-like conduction band offset is one of the crucial factors. Because too high of a spike in the band alignment results a drastic decrement in short circuit current (J_{sc}) and efficiency, because it acts as a barrier for electrons. However, it can also be the origin of efficiency, fill factor and current-reducing distortion in current–voltage curves such as light/dark curve crossover if light-dependent defect states are exist in the buffer layer. Since the interface between CdS/CZTS was not studied by UPS or XPS in this thesis, it cannot be said that the high barrier or very low barrier CBO are the exact reason of observing poor photovoltaic response from the Type I solar cells. The detected phases of SnO_2, SnS_2 and CTS are highly detrimental for PV characteristics of solar cells. Since SnO_2 has higher E_g (3.6 eV) than CZTS, the high positive CBO might be formed where for the CZTS(e)/SnO_2 interface this value was reported between 0.6 and 0.8 eV.

The other detected phase CTS has lower E_g than that of CZTS which results CBO value between 0.2 and 0.5 eV below the CBM of CZTS. Therefore this phase acts as a recombination center for minority charge carriers and causes the reduction in both J_{SC} and V_{OC}. SnS_2 is another detected secondary phase for the cell A. Since this phase may form a secondary diode inside the CZTS absorber layer or by behaving like an insulator in nature, it can result high photocarrier recombination and causes the reduction in PV characteristics of solar cells. These are the reasons that caused poor photovoltaic response of Type I solar cells.

The effects of CdS buffer layer thickness on the photovoltaic characteristics were studied for Type II solar cells. The CZTS that used for construction of Type II solar cells have desired composition of Cu-poor and Zn-rich. Since these Type II CZTS films have less detrimental superior phases than Type I CZTS absorbers. Thus, the photovoltaic performance of Type II solar cell are improved. The CdS thickness that used for construction of Type II solar cells are varied from 75.54 to 140.0 nm. Using thin CdS layer, the open-circuit voltage and short-circuit current density were improved from 255.3 to 402.0 V and from 1.62 to 5.77 mA/cm^2, respectively. The thinnest CdS coated solar cell showed the highest photovoltaic characteristic but this thickness is not the optimum thickness for CdS layer. Therefore, in the future works, thinner CdS buffer layer can be used for increase the efficiency of CZTS solar cells.

For the same thickness of CdS in the solar cells B (Type I CZTS) and F (Type II CZTS), open-circuit voltage developed from 140.8 to 402.0 V and short-circuit current density was boosted from 1.75 to 2.76 mA/cm^2 which is the result of improvement of CZTS. Although higher photovoltaic characteristics were detected for Type II CZTS solar cells, they are lower than the in theory. The reason of obtaining low efficiency of these devices is due to the existence of ZnO phase which has higher bandgap (3.3 eV.) than CZTS. The CBO value for the ZnO/CZTS interface was determined as 0.09 eV by experimentally and 0.07 eV from the first principle calculation which implying less detrimental than the interface between SnO_2/CZTS.

In summary, in this thesis both Type I and Type II solar cells suffer from low open-circuit voltages and low short circuit currents. These results indicates that diffusion lengths and lifetime of minority carriers are quite low because of excess recombination.

REFERENCES

Abd-Elkader, O. H., & Shaltout, A. A. (2015). Characterization and antibacterial capabilities of nanocrystalline CdS thin films prepared by chemical bath deposition. *Materials Science in Semiconductor Processing, 35*, 132-138.

Ahmed, S., Deligianni, H., & Romankiw, L. T. (2012). Ohmic contact of thin film solar cell: Google Patents.

Alexander, J. N., Higashiya, S., Caskey, D., Efstathiadis, H., & Haldar, P. (2014). Deposition and characterization of cadmium sulfide (CdS) by chemical bath deposition using an alternative chemistry cadmium precursor. *Solar Energy Materials and Solar Cells, 125*, 47-53.

Ali, N., Hussain, A., Ahmed, R., Wang, M., Zhao, C., Haq, B. U., & Fu, Y. Q. (2016). Advances in nanostructured thin film materials for solar cell applications. *Renewable and Sustainable Energy Reviews, 59*, 726-737.

Alvarez Barragan, A., Malekpour, H., Exarhos, S., Balandin, A. A., & Mangolini, L. (2016). Grain-to-Grain Compositional Variations and Phase Segregation in Copper–Zinc–Tin–Sulfide Films. *ACS Applied Materials & Interfaces, 8*(35), 22971-22976.

Anbarasi, M., Nagarethinam, V., & Balu, A. (2015). Studies on the physical properties of undoped and Zn-doped CdS thin films prepared by spray pyrolysis technique using perfume atomizer. *History, 13*(38), 48-52.

Bao, W. (2014). *First Principles Study on Band Offsets at the Cu_2ZnSnS_4-Based Heterointerfaces* (Doctoral dissertation), Nagoya Institute of Technology.

Bao, W., & Ichimura, M. (2015). Influence of Secondary Phases in Kesterite-Cu_2ZnSnS_4 Absorber Material Based on the First Principles Calculation. *International Journal of Photoenergy, 2015,* 592079.

Bär, M., Nishiwaki, S., Weinhardt, L., Pookpanratana, S., Shafarman, W., & Heske, C. (2008). Electronic level alignment at the deeply buried absorber/Mo interface in chalcopyrite-based thin film solar cells. *Applied Physics Letters, 93*(4), 042110.

Baranowski, L. L., Zawadzki, P., Lany, S., Toberer, E. S., & Zakutayev, A. (2016). A review of defects and disorder in multinary tetrahedrally bonded semiconductors. *Semiconductor Science and Technology, 31*(12), 123004.

Biccari, F., Chierchia, R., Valentini, M., Mangiapane, P., Salza, E., Malerba, C., . . . Mittiga, A. (2011). Fabrication of Cu2ZnSnS4 solar cells by sulfurization of evaporated precursors. *Energy Procedia, 10*, 187-191.

Buffiere, M., Brammertz, G., Oueslati, S., El Anzeery, H., Bekaert, J., Messaoud, K. B., . . . Poortmans, J. (2014). Spectral current–voltage analysis of kesterite solar cells. *Journal of Physics D: Applied Physics, 47*(17), 175101.

Cantas, A., Aygun, G., & Basa, D. K. (2014). In-situ spectroscopic ellipsometry and structural study of HfO_2 thin films deposited by radio frequency magnetron sputtering. *Journal of Applied Physics, 116*(8), 083517.

Cantaş, A. (2010). *Production and characterization of HfO_2 high-k dielectric layers by sputtering technique* (Master's thesis), İzmir Institute of Technology.

Cardona, M., Weinstein, M., & Wolff, G. (1965). Ultraviolet reflection spectrum of cubic CdS. *Physical Review, 140*(2A), A633.

Chen, S., Gong, X., Walsh, A., & Wei, S.-H. (2009). Crystal and electronic band structure of Cu_2ZnSnX_4 (X= S and Se) photovoltaic absorbers: First-principles insights. *Applied Physics Letters, 94*(4), 041903.

Chen, S., Gong, X., Walsh, A., & Wei, S.-H. (2010). Defect physics of the kesterite thin-film solar cell absorber Cu_2ZnSnS_4. *Applied Physics Letters, 96*(2), 021902.

Chen, S., Yang, J.-H., Gong, X.-G., Walsh, A., & Wei, S.-H. (2010). Intrinsic point defects and complexes in the quaternary kesterite semiconductor Cu_2ZnSnS_4. *Physical Review B, 81*(24), 245204.

Cheng, A.-J., Manno, M., Khare, A., Leighton, C., Campbell, S., & Aydil, E. (2011). Imaging and phase identification of Cu_2ZnSnS_4 thin films using confocal Raman spectroscopy. *Journal of Vacuum Science & Technology A: Vacuum, Surfaces, and Films, 29*(5), 051203.

Chung, C.-H., Bob, B., Song, T.-B., & Yang, Y. (2014). Current–voltage characteristics of fully solution processed high performance $CuIn(S, Se)_2$ solar cells: crossover and red kink. *Solar Energy Materials and Solar Cells, 120*, 642-646.

Das, S., Frye, C., Muzykov, P. G., & Mandal, K. C. (2012). Deposition and characterization of low-cost spray pyrolyzed Cu_2ZnSnS_4 (CZTS) thin-films for large-area high-efficiency heterojunction solar cells. *ECS Transactions, 45*(7), 153-161.

Deepu, D. R., Rajeshmon, V. G., Kartha, C. S., Vijayakumar, K. P., Murli, C., Bhattacharyya, D., & Gadkari, S. (2014, April). *XPS depth profile study of sprayed CZTS thin films.* Paper presented at the AIP Conference Proceedings, (pp. 1666-1668). AIP.

Delbos, S. (2012). Këwhile thin films for photovoltaics: a review. *EPJ Photovoltaics, 3*, 35004.

Dimitrievska, M., Fairbrother, A., Fontané, X., Jawhari, T., Izquierdo-Roca, V., Saucedo, E., & Pérez-Rodríguez, A. (2014). Multiwavelength excitation Raman scattering study of polycrystalline kesterite Cu_2ZnSnS_4 thin films. *Applied Physics Letters, 104*(2), 021901.

Dolui, K., Rungger, I., & Sanvito, S. (2013). Origin of the n-type and p-type conductivity of MoS_2 monolayers on a SiO_2 substrate. *Physical Review B, 87*(16), 165402.

Dumcenco, D., & Huang, Y.-S. (2013). The vibrational properties study of kesterite Cu_2ZnSnS_4 single crystals by using polarization dependent Raman spectroscopy. *Optical Materials, 35*(3), 419-425.

Edoff, M., Schleussner, S., Wallin, E., & Lundberg, O. (2011). Technological and economical aspects on the influence of reduced $Cu(In,Ga)Se_2$ thickness and Ga grading for co-evaporated $Cu(In,Ga)Se_2$ modules. *Thin Solid Films, 519*(21), 7530-7533.

El Assali, K., Boustani, M., Khiara, A., Bekkay, T., Outzourhit, A., Ameziane, E., . . . Pouzet, J. (2000). Some structural and optical properties of CdS thin films prepared by RF sputtering. *Physica Status Solidi(A), 178*(2), 701-708.

Espitia, P. J. P., Soares, N. d. F. F., dos Reis Coimbra, J. S., de Andrade, N. J., Cruz, R. S., & Medeiros, E. A. A. (2012). Zinc oxide nanoparticles: synthesis, antimicrobial activity and food packaging applications. *Food and Bioprocess Technology, 5*(5), 1447-1464.

Ezekoye, B., Ighodalo, K., Ezekoye, V., Emeakaroha, T., Ezema, J., & Offor, P. (2015). Nanocrystalline Cadmium sulfide (CdS) thin film synthesized at different dip times by chemical bath deposition technique. *International Journal of Physical Sciences, 10*(13), 403-412.

Fairbrother, A., Izquierdo-Roca, V., Fontané, X., Ibáñez, M., Cabot, A., Saucedo, E., & Pérez-Rodríguez, A. (2014). ZnS grain size effects on near-resonant Raman scattering: optical non-destructive grain size estimation. *CrystEngComm, 16*(20), 4120-4125.

Fernandes, P., Salomé, P., & Da Cunha, A. (2009). Growth and Raman scattering characterization of Cu_2ZnSnS_4 thin films. *Thin Solid Films, 517*(7), 2519-2523.

Fernandes, P., Salomé, P., & Da Cunha, A. (2010). A study of ternary Cu_2SnS_3 and Cu_3SnS_4 thin films prepared by sulfurizing stacked metal precursors. *Journal of Physics D: Applied Physics, 43*(21), 215403.

Fernandes, P., Salomé, P., & Da Cunha, A. (2011). Study of polycrystalline Cu_2ZnSnS_4 films by Raman scattering. *Journal of Alloys and Compounds, 509*(28), 7600-7606.

Fernando, D., Khan, M., & Vasquez, Y. (2015). Control of the crystalline phase and morphology of CdS deposited on microstructured surfaces by chemical bath deposition. *Materials Science in Semiconductor Processing, 30*, 174-180.

Fontané, X., Izquierdo-Roca, V., Saucedo, E., Schorr, S., Yukhymchuk, V., Valakh, M. Y., . . . Morante, J. (2012). Vibrational properties of stannite and kesterite type compounds: Raman scattering analysis of $Cu_2(Fe, Zn)SnS_4$. *Journal of Alloys and Compounds, 539*, 190-194.

Gubbala, S., Russell, H. B., Shah, H., Deb, B., Jasinski, J., Rypkema, H., & Sunkara, M. K. (2009). Surface properties of SnO_2 nanowires for enhanced performance with dye-sensitized solar cells. *Energy & Environmental Science, 2*(12), 1302-1309.

Guc, M., Levcenko, S., Bodnar, I. V., Izquierdo-Roca, V., Fontane, X., Volkova, L. V., . . . Pérez-Rodríguez, A. (2016). Polarized Raman scattering study of kesterite type Cu_2ZnSnS_4 single crystals. *Scientific reports, 6,* 19414.

Guneri, E., Gode, F., Ulutas, C., Kirmizigul, F., Altindemir, G., & Gumus, C. (2010). Properties of p-type SnS thin films prepared by chemical bath deposition. *Chalcogenide Lett, 7*(12), 685.

Gürel, T., Sevik, C., & Çağın, T. (2011). Characterization of vibrational and mechanical properties of quaternary compounds Cu_2ZnSnS_4 and $Cu_2ZnSnSe_4$ in kesterite and stannite structures. *Physical Review B, 84*(20), 205201.

Haight, R., Barkhouse, A., Gunawan, O., Shin, B., Copel, M., Hopstaken, M., & Mitzi, D. B. (2011). Band alignment at the $Cu_2ZnSn(S_xSe_{1-x})_4$/CdS interface. *Applied Physics Letters, 98*(25), 253502.

Hall, S. S., JT; Stewart, JM. (1978). Kesterite, $Cu_2(Zn,Fe)SnS_4$, and stannite, $Cu_2(Fe,Zn)SnS_4$, structurally similar but distinct minerals. *Canadian Mineralogist, 16*(2), 131-137.

Hazama, H., Tajima, S., Masuoka, Y., & Asahi, R. (2016). Transport properties of the Cu_2ZnSnS_4 bulk systems: Effects of nonstoichiometry and defect formation. *Journal of Alloys and Compounds, 657*, 179-183.

Heinz, P., Bretagnol, F., Mannelli, I., Sirghi, L., Valsesia, A., Ceccone, G., . . . Rossi, F. (2008). Poly (N-isopropylacrylamide) grafted on plasma-activated poly (ethylene oxide): Thermal response and interaction with proteins. *Langmuir, 24*(12), 6166-6175.

Himmrich, M., & Haeuseler, H. (1991). Far infrared studies on stannite and wurtzstannite type compounds. *Spectrochimica Acta Part A: Molecular Spectroscopy, 47*(7), 933-942.

Hoffman, D., & Thornton, J. A. (1982). Internal stresses in Cr, Mo, Ta, and Pt films deposited by sputtering from a planar magnetron source. *Journal of Vacuum Science and Technology, 20*(3), 355-358.

Hofmann, P., Horn, K., Bradshaw, A., Johnson, R., Fuchs, D., & Cardona, M. (1993). Dielectric function of cubic and hexagonal CdS in the vacuum ultraviolet region. *Physical Review B, 47*(3), 1639.

Htay, M. T., Hashimoto, Y., Momose, N., Sasaki, K., Ishiguchi, H., Igarashi, S., . . . Ito, K. (2011). A cadmium-free Cu_2ZnSnS_4/ZnO hetrojunction solar cell prepared by practicable processes. *Japanese Journal of Applied Physics, 50*(3R), 032301.

Hurtado, M., Cruz, S., Becerra, R., Calderón, C., Bartolo-Pérez, P., & Gordillo, G. (2014, June). *XPS analysis and structural characterization of CZTS thin films prepared using solution and vacuum based deposition techniques.* Paper presented at the Photovoltaic Specialist Conference (PVSC), 2014 IEEE 40th (pp. 0368-0370) IEEE.

Husham, M., Hassan, Z., Mahdi, M., Selman, A. M., & Ahmed, N. M. (2014). Fabrication and characterization of nanocrystalline CdS thin film-based optical sensor grown via microwave-assisted chemical bath deposition. *Superlattices and Microstructures, 67*, 8-16.

Ilyas, U., Rawat, R. S., Tan, T., Lee, P., Chen, R., Sun, H., . . . Zhang, S. (2011). Oxygen rich p-type ZnO thin films using wet chemical route with enhanced carrier concentration by temperature-dependent tuning of acceptor defects. *Journal of Applied Physics, 110*(9), 093522.

International Energy Outlook 2016 With Projections to 2040. (2016, May). Retrieved from https://www.eia.gov/outlooks/ieo/pdf/0484(2016).pdf

Ito, K. (2014). *Copper zinc tin sulfide-based thin film solar cells*: John Wiley & Sons.

Ito, K., & Nakazawa, T. (1988). Electrical and optical properties of stannite-type quaternary semiconductor thin films. *Japanese Journal of Applied Physics, 27*(11R), 2094.

Ji, S., Shi, T., Qiu, X., Zhang, J., Xu, G., Chen, C., . . . Ye, C. (2013). A Route to Phase Controllable $Cu_2ZnSn(S_{1-x}Se_x)_4$ Nanocrystals with Tunable Energy Bands. *Scientific reports*, *3,* 2733.

Jiang, F., Ikeda, S., Tang, Z., Minemoto, T., Septina, W., Harada, T., & Matsumura, M. (2015). Impact of alloying duration of an electrodeposited Cu/Sn/Zn metallic stack on properties of Cu_2ZnSnS_4 absorbers for thin-film solar cells. *Progress in Photovoltaics: Research and Applications, 23*(12), 1884-1895.

Jimbo, K., Kimura, R., Kamimura, T., Yamada, S., Maw, W. S., Araki, H., . . . Katagiri, H. (2007). Cu_2ZnSnS_4-type thin film solar cells using abundant materials. *Thin Solid Films, 515*(15), 5997-5999.

Kamoun, N., Bouzouita, H., & Rezig, B. (2007). Fabrication and characterization of Cu_2ZnSnS_4 thin films deposited by spray pyrolysis technique. *Thin Solid Films, 515*(15), 5949-5952.

Kariper, A., Güneri, E., Göde, F., Gümüş, C., & Özpozan, T. (2011). The structural, electrical and optical properties of CdS thin films as a function of pH. *Materials Chemistry and Physics, 129*(1), 183-188.

Karthikeyan, S., Zhang, L., & Campbell, S. A. (2014, June). *In-situ stress and thermal stability studies of molybdenum bilayer back contacts for photovoltaic applications.* Paper presented at the Photovoltaic Specialist Conference (PVSC), 2014 IEEE 40th (pp. 0387-0389). IEEE.

Katagiri, H., Jimbo, K., Moriya, K., & Tsuchida, K. (2003). *Solar cell without environmental pollution by using CZTS thin film.* Paper presented at the Photovoltaic Energy Conversion, 2003. Proceedings of 3rd World Conference on (pp. 2874-2879). IEEE.

Katagiri, H., Jimbo, K., Yamada, S., Kamimura, T., Maw, W. S., Fukano, T., . . . Motohiro, T. (2008). Enhanced conversion efficiencies of Cu_2ZnSnS_4-based thin film solar cells by using preferential etching technique. *Applied Physics Express, 1*(4), 041201.

Katagiri, H., Saitoh, K., Washio, T., Shinohara, H., Kurumadani, T., & Miyajima, S. (2001). Development of thin film solar cell based on Cu_2ZnSnS_4 thin films. *Solar Energy Materials and Solar Cells, 65*(1), 141-148.

Katagiri, H., Sasaguchi, N., Hando, S., Hoshino, S., Ohashi, J., & Yokota, T. (1997). Preparation and evaluation of Cu_2ZnSnS_4 thin films by sulfurization of E-B evaporated precursors. *Solar Energy Materials and Solar Cells, 49*(1-4), 407-414.

Kato, T., Hiroi, H., Sakai, N., & Sugimoto, H. (2013). *Buffer/absorber interface study on Cu_2ZnSnS_4 and $Cu_2ZnSnSe_4$ based solar cells: band alignment and its impact on the solar cell performance.* Paper presented at the 28th European Photovoltaic Solar Energy Conference and Exhibition (pp. 2125-2127).

Kaur, K., Kumar, N., & Kumar, M. (2017). Strategic review of interface carrier recombination in earth abundant Cu-Zn-Sn-S-Se solar cells: Current challenges and future prospective. *Journal of Materials Chemistry A, 5*(7), 3069-3090.

Kaushik, D. K., Rao, T. N., & Subrahmanyam, A. (2017). Studies on the disorder in DC magnetron sputtered Cu_2ZnSnS_4 (CZTS) thin films grown in sulfide plasma. *Surface and Coatings Technology, 314*, 85-91.

Kavitha, N., Chandramohan, R., Valanarasu, S., Vijayan, T., Rosario, S. R., & Kathalingam, A. (2016). Effect of film thickness on the solar cell performance of CBD grown CdS/PbS heterostructure. *Journal of Materials Science: Materials in Electronics, 27*(3), 2574-2580.

Khalkar, A., Lim, K.-S., Yu, S.-M., Shin, D.-W., Oh, T.-S., & Yoo, J.-B. (2015). Effects of Sulfurization Pressure on the Conversion Efficiency of Cosputtered Cu_2ZnSnS_4 Thin Film Solar Cells. *International Journal of Photoenergy, 2015,* 750846.

Khan, Z. R., Zulfequar, M., & Khan, M. S. (2010). Optical and structural properties of thermally evaporated cadmium sulphide thin films on silicon (100) wafers. *Materials Science and Engineering: B, 174*(1), 145-149.

Khare, A. (2012). *Synthesis And Characterization of Copper Zinc Tin Sulfide Nanoparticles And Thin Films* (Doctoral dissertation),University of Minnesota.

Khare, A., Himmetoglu, B., Cococcioni, M., & Aydil, E. S. (2012). First principles calculation of the electronic properties and lattice dynamics of $Cu_2ZnSn(S_{1-x}Se_x)_4$. *Journal of Applied Physics, 111*(12), 123704.

Khare, A., Himmetoglu, B., Johnson, M., Norris, D. J., Cococcioni, M., & Aydil, E. S. (2012). Calculation of the lattice dynamics and Raman spectra of copper zinc tin chalcogenides and comparison to experiments. *Journal of Applied Physics, 111*(8), 083707.

Krebs, F. C., Hösel, M., Corazza, M., Roth, B., Madsen, M. V., Gevorgyan, S. A., . . . Jørgensen, M. (2013). Freely available OPV—the fast way to progress. *Energy Technology, 1*(7), 378-381.

Krylova, V., & Andrulevičius, M. (2009). Optical, XPS and XRD studies of semiconducting copper sulfide layers on a polyamide film. *International Journal of Photoenergy, 2009,* 304308.

Kumar, M., Dubey, A., Adhikari, N., Venkatesan, S., & Qiao, Q. (2015). Strategic review of secondary phases, defects and defect-complexes in kesterite CZTS–Se solar cells. *Energy & Environmental Science, 8*(11), 3134-3159.

Kumar, M. A., & Muthukumaran, S. (2013). Effect of deposition time on structural, optical and photoluminescence properties of $Cd_{0.9}Zn_{0.1}S$ thin films by chemical bath deposition method. *Journal of Materials Science: Materials in Electronics, 24*(8), 2858-2865.

Kumar, N., Ramadoss, R., Kozakov, A., Sankaran, K., Dash, S., Tyagi, A., . . . Lin, I.-N. (2013). Humidity-dependent friction mechanism in an ultrananocrystalline diamond film. *Journal of Physics D: Applied Physics, 46*(27), 275501.

Kumar, P., Saxena, N., Chandra, R., Gupta, V., Agarwal, A., & Kanjilal, D. (2012). Nanotwinning and structural phase transition in CdS quantum dots. *Nanoscale Research Letters, 7*(1), 584.

Kumar, Y. K., Babu, G. S., Bhaskar, P. U., & Raja, V. S. (2009). Preparation and characterization of spray-deposited Cu_2ZnSnS_4 thin films. *Solar Energy Materials and Solar Cells, 93*(8), 1230-1237.

Kwoka, M., & Krzywiecki, M. (2017). Impact of air exposure and annealing on the chemical and electronic properties of the surface of SnO_2 nanolayers deposited by rheotaxial growth and vacuum oxidation. *Beilstein Journal of Nanotechnology, 8*, 514.

Li, J., Du, Q., Liu, W., Jiang, G., Feng, X., Zhang, W., . . . Zhu, C. (2012). The band offset at CdS/Cu_2ZnSnS_4 heterojunction interface. *Electronic Materials Letters, 8*(4), 365-367.

Li, J. V., Kuciauskas, D., Young, M. R., & Repins, I. L. (2013). Effects of sodium incorporation in Co-evaporated $Cu_2ZnSnSe_4$ thin-film solar cells. *Applied Physics Letters, 102*(16), 163905.

Lisco, F., Kaminski, P. M., Abbas, A., Bass, K., Bowers, J. W., Claudio, G., . . . Walls, J. (2015). The structural properties of CdS deposited by chemical bath deposition and pulsed direct current magnetron sputtering. *Thin Solid Films, 582*, 323-327.

Lisco, F., Kaminski, P. M., Abbas, A., Bowers, J. W., Claudio, G., Losurdo, M., & Walls, J. (2015). High rate deposition of thin film cadmium sulphide by pulsed direct current magnetron sputtering. *Thin Solid Films, 574*, 43-51.

Lopez-Marino, S., Espíndola-Rodríguez, M., Sánchez, Y., Alcobé, X., Oliva, F., Xie, H., . . . Caballero, R. (2016). The importance of back contact modification in $Cu_2ZnSnSe_4$ solar cells: The role of a thin MoO_2 layer. *Nano Energy, 26*, 708-721.

Maeda, T., Nakamura, S., & Wada, T. (2011). First principles calculations of defect formation in in-free photovoltaic semiconductors Cu_2ZnSnS_4 and $Cu_2ZnSnSe_4$. *Japanese Journal of Applied Physics, 50*(4S), 04DP07.

Malerba, C. (2014). *Cu_2ZnSnS_4 thin films solar cells: material and device characterization* (Doctoral dissertation), University of Trento.

Mali, S. S., Patil, B. M., Betty, C. A., Bhosale, P. N., Oh, Y. W., Jadkar, S. R., . . . Patil, P. S. (2012). Novel synthesis of kesterite Cu_2ZnSnS_4 nanoflakes by successive ionic layer adsorption and reaction technique: characterization and application. *Electrochimica Acta, 66*, 216-221.

Manikandan, K., Dilip, C. S., Mani, P., & Prince, J. J. (2015). Deposition and characterization of CdS nano thin film with complexing agent triethanolamine. *American Journal of Engineering and Applied Sciences, 8*(3), 318.

Marchionna, S., Garattini, P., Le Donne, A., Acciarri, M., Tombolato, S., & Binetti, S. (2013). Cu_2ZnSnS_4 solar cells grown by sulphurisation of sputtered metal precursors. *Thin Solid Films, 542*, 114-118.

Mathew, X., Enriquez, J. P., Romeo, A., & Tiwari, A. N. (2004). CdTe/CdS solar cells on flexible substrates. *Solar energy, 77*(6), 831-838.

Maticiuc, N., Kukk, M., Spalatu, N., Potlog, T., Krunks, M., Valdna, V., & Hiie, J. (2014). Comparative study of CdS films annealed in neutral, oxidizing and reducing atmospheres. *Energy Procedia, 44*, 77-84.

Mattevi, C., Eda, G., Agnoli, S., Miller, S., Mkhoyan, K. A., Celik, O., . . . Chhowalla, M. (2009). Evolution of electrical, chemical, and structural properties of transparent and conducting chemically derived graphene thin films. *Advanced Functional Materials, 19*(16), 2577-2583.

Mazón-Montijo, D., Sotelo-Lerma, M., Rodríguez-Fernández, L., & Huerta, L. (2010). AFM, XPS and RBS studies of the growth process of CdS thin films on ITO/glass substrates deposited using an ammonia-free chemical process. *Applied Surface Science, 256*(13), 4280-4287.

McEvoy, A. J., Castaner, L., & Markvart, T. (2012). *Solar cells: materials, manufacture and operation*: Academic Press.

Meher, S., Balakrishnan, L., & Alex, Z. (2016). Analysis of Cu_2ZnSnS_4/CdS based photovoltaic cell: a numerical simulation approach. *Superlattices and Microstructures, 100*, 703-722.

Mendis, B. G., Goodman, M. C., Major, J. D., Taylor, A. A., Durose, K., & Halliday, D. P. (2012). The role of secondary phase precipitation on grain boundary electrical activity in Cu_2ZnSnS_4 (CZTS) photovoltaic absorber layer material. *Journal of Applied Physics, 112*(12), 124508.

Moholkar, A., Shinde, S., Babar, A., Sim, K.-U., Kwon, Y.-b., Rajpure, K., . . . Kim, J. (2011). Development of CZTS thin films solar cells by pulsed laser deposition: influence of pulse repetition rate. *Solar Energy, 85*(7), 1354-1363.

Moholkar, A., Shinde, S., Babar, A., Sim, K.-U., Lee, H. K., Rajpure, K., . . . Kim, J. (2011). Synthesis and characterization of Cu_2ZnSnS_4 thin films grown by PLD: solar cells. *Journal of Alloys and Compounds, 509*(27), 7439-7446.

Moriya, K., Tanaka, K., & Uchiki, H. (2007). Fabrication of Cu_2ZnSnS_4 thin-film solar cell prepared by pulsed laser deposition. *Japanese Journal of Applied Physics, 46*(9R), 5780.

Moriya, K., Tanaka, K., & Uchiki, H. (2008). Cu_2ZnSnS_4 thin films annealed in H_2S atmosphere for solar cell absorber prepared by pulsed laser deposition. *Japanese Journal of Applied Physics, 47*(1S), 602.

Nagaoka, A., Miyake, H., Taniyama, T., Kakimoto, K., Nose, Y., Scarpulla, M. A., & Yoshino, K. (2014). Effects of sodium on electrical properties in Cu_2ZnSnS_4 single crystal. *Applied Physics Letters, 104*(15), 152101.

Nagoya, A., Asahi, R., & Kresse, G. (2011). First-principles study of Cu_2ZnSnS_4 and the related band offsets for photovoltaic applications. *Journal of Physics: Condensed Matter, 23*(40), 404203.

Nagoya, A., Asahi, R., Wahl, R., & Kresse, G. (2010). Defect formation and phase stability of Cu_2ZnSnS_4 photovoltaic material. *Physical Review B, 81*(11), 113202.

Nakada, T., Iga, D., Ohbo, H., & Kunioka, A. (1997). Effects of sodium on Cu(In, Ga) Se_2-based thin films and solar cells. *Japanese Journal of Applied Physics, 36*(2R), 732.

Nakayama, N., & Ito, K. (1996). Sprayed films of stannite Cu_2ZnSnS_4. *Applied Surface Science, 92*, 171-175.

Nalwa, H. S. (2001). *Advances in surface science* (Vol. 38): Academic Press.

Nandur, A., & White, B. (2014, March). *Growth of Cu_2ZnSnS_4 (CZTS) by Pulsed Laser Deposition for Thin film Photovoltaic Absorber Material.* Paper presented at the APS Meeting Abstracts.

Neuschitzer, M., Sanchez, Y., López-Marino, S., Xie, H., Fairbrother, A., Placidi, M., . . . Saucedo, E. (2015). Optimization of CdS buffer layer for high-performance $Cu_2ZnSnSe_4$ solar cells and the effects of light soaking: elimination of crossover and red kink. *Progress in Photovoltaics: Research and Applications, 23*(11), 1660-1667.

Oladeji, I., Chow, L., Liu, J., Chu, W., Bustamante, A., Fredricksen, C., & Schulte, A. (2000). Comparative study of CdS thin films deposited by single, continuous, and multiple dip chemical processes. *Thin Solid Films, 359*(2), 154-159.

Olekseyuk, I., Dudchak, I., & Piskach, L. (2004). Phase equilibria in the Cu_2S–ZnS–SnS_2 system. *Journal of Alloys and Compounds, 368*(1), 135-143.

Olgar, M., Klaer, J., Mainz, R., Levcenco, S., Just, J., Bacaksiz, E., & Unold, T. (2016). Effect of precursor stacking order and sulfurization temperature on compositional homogeneity of CZTS thin films. *Thin Solid Films, 615*, 402-408.

Olgar, M., Klaer, J., Mainz, R., Ozyuzer, L., & Unold, T. (2017). Cu_2ZnSnS_4-based thin films and solar cells by rapid thermal annealing processing. *Thin Solid Films, 628*, 1-6.

Ortuño-López, M., Ochoa-Landín, R., Sandoval-Paz, M., Sotelo-Lerma, M., Flores-Acosta, M., & Ramírez-Bon, R. (2013). Studies on the properties of CdS films deposited from pH-controlled growth solutions. *Materials Research, 16*(4), 937-943.

Ouachtari, F., Rmili, A., Elidrissi, B., Bouaoud, A., Erguig, H., & Elies, P. (2011). Influence of bath temperature, deposition time and S/Cd ratio on the structure, surface morphology, chemical composition and optical properties of CdS thin films elaborated by chemical bath deposition. *Journal of Modern Physics, 2*(09), 1073.

Özgür, Ü., Alivov, Y. I., Liu, C., Teke, A., Reshchikov, M., Doğan, S., . . . Morkoc, H. (2005). A comprehensive review of ZnO materials and devices. *Journal of Applied Physics, 98*(4), 11.

Pal, U., Silva-Gonzalez, R., Martinez-Montes, G., Gracia-Jimenez, M., Vidal, M., & Torres, S. (1997). Optical characterization of vacuum evaporated cadmium sulfide films. *Thin Solid Films, 305*(1-2), 345-350.

Park, J.-M., Kim, S.-H., Jeong, M.-H., & Park, Y.-B. (2014). Effect of Cu–Sn intermetallic compound reactions on the Kirkendall void growth characteristics in Cu/Sn/Cu microbumps. *Japanese Journal of Applied Physics, 53*(5S3), 05HA06.

Park, S.-N., Sung, S.-J., Son, D.-H., Kim, D.-H., Gansukh, M., Cheong, H., & Kang, J.-K. (2014). Solution-processed Cu_2ZnSnS_4 absorbers prepared by appropriate inclusion and removal of thiourea for thin film solar cells. *RSC Advances, 4*(18), 9118-9125.

Park, W.-D. (2012). Optical constants and dispersion parameters of CdS thin film prepared by chemical bath deposition. *Transactions on Electrical and Electronic Materials, 13*(4), 196-199.

Polman, A., Knight, M., Garnett, E. C., Ehrler, B., & Sinke, W. C. (2016). Photovoltaic materials: Present efficiencies and future challenges. *Science, 352*(6283), aad4424.

Prabhakar, T., & Jampana, N. (2011). Effect of sodium diffusion on the structural and electrical properties of Cu_2ZnSnS_4 thin films. *Solar Energy Materials and Solar Cells, 95*(3), 1001-1004.

Ravichandran, K., & Philominathan, P. (2009). Comparative study on structural and optical properties of CdS films fabricated by three different low-cost techniques. *Applied Surface Science, 255*(11), 5736-5741.

Ricardo, C. A., Su'ait, M. S., Müller, M., & Scardi, P. (2013). Production of Cu_2(Zn, Fe)SnS_4 powders for thin film solar cell by high energy ball milling. *Journal of Power Sources, 230*, 70-75.

Riha, S. C., Jin, S., Baryshev, S. V., Thimsen, E., Wiederrecht, G. P., & Martinson, A. B. (2013). Stabilizing Cu_2S for photovoltaics one atomic layer at a time. *ACS Applied Materials & Interfaces, 5*(20), 10302-10309.

Rios, L. E. V., Neldner, K., Gurieva, G., & Schorr, S. (2016). Existence of off-stoichiometric single phase kesterite. *Journal of Alloys and Compounds, 657*, 408-413.

Ruan, C.-H., Huang, C.-C., Lin, Y.-J., He, G.-R., Chang, H.-C., & Chen, Y.-H. (2014). Electrical properties of $Cu_xZn_ySnS_4$ films with different Cu/Zn ratios. *Thin Solid Films, 550*, 525-529.

Sagna, A., Djessas, K., Sene, C., Belaqziz, M., Chehouani, H., Briot, O., & Moret, M. (2015). Growth, structure and optoelectronic characterizations of high quality Cu_2ZnSnS_4 thin films obtained by close spaced vapor transport. *Superlattices and Microstructures, 85*, 918-924.

Salome, P., Keller, J., Törndahl, T., Teixeira, J., Nicoara, N., Andrade, R.-R., . . . Leitão, J. (2017). CdS and $Zn_{1-x}Sn_xO_y$ buffer layers for CIGS solar cells. *Solar Energy Materials and Solar Cells, 159*, 272-281.

Salomé, P., Rodriguez-Alvarez, H., & Sadewasser, S. (2015). Incorporation of alkali metals in chalcogenide solar cells. *Solar Energy Materials and Solar Cells, 143*, 9-20.

Sandoval-Paz, M., & Ramírez-Bon, R. (2009). Analysis of the early growth mechanisms during the chemical deposition of CdS thin films by spectroscopic ellipsometry. *Thin Solid Films, 517*(24), 6747-6752.

Santoni, A., Biccari, F., Malerba, C., Valentini, M., Chierchia, R., & Mittiga, A. (2013). Valence band offset at the CdS/Cu_2ZnSnS_4 interface probed by x-ray photoelectron spectroscopy. *Journal of Physics D: Applied Physics, 46*(17), 175101.

Sardashti, K., Haight, R., Gokmen, T., Wang, W., Chang, L. Y., Mitzi, D. B., & Kummel, A. C. (2015). Impact of Nanoscale Elemental Distribution in High-Performance Kesterite Solar Cells. *Advanced Energy Materials, 5*(10), 1402180.

Schorr, S., Hoebler, H.-J., & Tovar, M. (2007). A neutron diffraction study of the stannite-kesterite solid solution series. *European Journal of Mineralogy, 19*(1), 65-73.

Schubert, B. A., Marsen, B., Cinque, S., Unold, T., Klenk, R., Schorr, S., & Schock, H. W. (2011). Cu_2ZnSnS_4 thin film solar cells by fast coevaporation. *Progress in Photovoltaics: Research and Applications, 19*(1), 93-96.

Scofield, J. H., Duda, A., Albin, D., Ballard, B., & Predecki, P. (1995). Sputtered molybdenum bilayer back contact for copper indium diselenide-based polycrystalline thin-film solar cells. *Thin Solid Films, 260*(1), 26-31.

Scragg, J. J. (2010). *Studies of Cu_2ZnSnS_4 films prepared by sulfurisation of electrodeposited precursors* (Doctoral dissertation) University of Bath.

Scragg, J. J., Choubrac, L., Lafond, A., Ericson, T., & Platzer-Björkman, C. (2014). A low-temperature order-disorder transition in Cu_2ZnSnS_4 thin films. *Applied Physics Letters, 104*(4), 041911.

Scragg, J. J., Dale, P. J., Peter, L. M., Zoppi, G., & Forbes, I. (2008). New routes to sustainable photovoltaics: evaluation of Cu_2ZnSnS_4 as an alternative absorber material. *Physica Status Solidi (b), 245*(9), 1772-1778.

Senthamilselvi, V., Saravanakumar, K., Anandhi, R., Ravichandran, A., & Ravichandran, K. (2011). Effect of annealing on the stoichiometry of CdS films deposited by SILAR technique. *Optoelectronics and Advanced Materials-Rapid Communications, 5*(10), 1072-1077.

Senthil, K., Mangalaraj, D., Narayandass, S. K., & Adachi, S. (2000). Optical constants of vacuum-evaporated cadmium sulphide thin films measured by spectroscopic ellipsometry. *Materials Science and Engineering: B, 78*(1), 53-58.

Sette, A., Spadavecchia, J., Landoulsi, J., Casale, S., Haye, B., Crociani, O., & Arcangeli, A. (2013). Development of novel anti-Kv 11.1 antibody-conjugated PEG–TiO_2 nanoparticles for targeting pancreatic ductal adenocarcinoma cells. *Journal of Nanoparticle Research, 15*(12), 1-11.

Shiang, J., Risbud, S., & Alivisatos, A. (1993). Resonance Raman studies of the ground and lowest electronic excited state in CdS nanocrystals. *The Journal of Chemical Physics, 98*(11), 8432-8442.

Shimizu, K., Phanopoulos, C., Loenders, R., Abel, M. L., & Watts, J. F. (2010). The characterization of the interfacial interaction between polymeric methylene diphenyl diisocyanate and aluminum: a ToF-SIMS and XPS study. *Surface and Interface Analysis, 42*(8), 1432-1444.

Shin, D., Saparov, B., & Mitzi, D. B. (2017). Defect Engineering in Multinary Earth-Abundant Chalcogenide Photovoltaic Materials. *Advanced Energy Materials, 7*(11), 1602366.

Shin, S. W., Pawar, S., Park, C. Y., Yun, J. H., Moon, J.-H., Kim, J. H., & Lee, J. Y. (2011). Studies on Cu_2ZnSnS_4 (CZTS) absorber layer using different stacking orders in precursor thin films. *Solar Energy Materials and Solar Cells, 95*(12), 3202-3206.

Shockley, W., & Queisser, H. J. (1961). Detailed balance limit of efficiency of p-n junction solar cells. *Journal of Applied Physics, 32*(3), 510-519.

Singh, D. J. (2016). Optical and electronic properties of semiconducting Sn_2S_3. *Applied Physics Letters, 109*(3), 032102.

Singh, P., & Ravindra, N. M. (2012). Analysis of series and shunt resistance in silicon solar cells using single and double exponential models. *Emerging Materials Research, 1*(1), 33-38.

Sivasubramanian, V., Arora, A., Premila, M., Sundar, C., & Sastry, V. (2006). Optical properties of CdS nanoparticles upon annealing. *Physica E: Low-dimensional Systems and Nanostructures, 31*(1), 93-98.

Skelton, J. M., Jackson, A. J., Dimitrievska, M., Wallace, S. K., & Walsh, A. (2015). Vibrational spectra and lattice thermal conductivity of kesterite-structured Cu_2ZnSnS_4 and $Cu_2ZnSnSe_4$. *APL Materials, 3*(4), 041102.

Slonopas, A., Ryan, H., Foley, B., Sun, Z., Sun, K., Globus, T., & Norris, P. (2016). Growth mechanisms and their effects on the opto-electrical properties of CdS thin films prepared by chemical bath deposition. *Materials Science in Semiconductor Processing, 52*, 24-31.

Su, C.-Y., Chiu, C.-Y., & Ting, J.-M. (2015). Cu_2ZnSnS_4 absorption layers with controlled phase purity. *Scientific reports, 5*, 9291.

Sugimoto, H., Liao, C., Hiroi, H., Sakai, N., & Kato, T. (2013, June). *Lifetime improvement for high efficiency Cu_2ZnSnS_4 submodules.* Paper presented at the Photovoltaic Specialists Conference (PVSC), 2013 IEEE 39th (pp. 3208-3211). IEEE.

Tajima, S., Itoh, T., Hazama, H., Ohishi, K., & Asahi, R. (2015). Improvement of the open-circuit voltage of Cu_2ZnSnS_4 solar cells using a two-layer structure. *Applied Physics Express, 8*(8), 082302.

Tajima, S., Kataoka, K., Takahashi, N., Kimoto, Y., Fukano, T., Hasegawa, M., & Hazama, H. (2013). Direct measurement of band offset at the interface between CdS and Cu_2ZnSnS_4 using hard X-ray photoelectron spectroscopy. *Applied Physics Letters, 103*(24), 243906.

Tajima, S., Umehara, M., Hasegawa, M., Mise, T., & Itoh, T. (2017). Cu_2ZnSnS_4 photovoltaic cell with improved efficiency fabricated by high-temperature annealing after CdS buffer-layer deposition. *Progress in Photovoltaics: Research and Applications, 25*(1), 14-22.

Tanaka, T., Kawasaki, D., Nishio, M., Guo, Q., & Ogawa, H. (2006). Fabrication of Cu_2ZnSnS_4 thin films by co-evaporation. *Physica Status Solidi (C), 3*(8), 2844-2847.

Tanaka, T., Yoshida, A., Saiki, D., Saito, K., Guo, Q., Nishio, M., & Yamaguchi, T. (2010). Influence of composition ratio on properties of Cu_2ZnSnS_4 thin films fabricated by co-evaporation. *Thin Solid Films, 518*(21), S29-S33.

Thakur, P., Joshi, S. S., & Patil, K. (2010). Investigations of CdS and Ag–CdS nanoparticles by X-ray photoelectron spectroscopy. *Applied Surface Science, 257*(5), 1390-1394.

Thornton, J. A., & Hoffman, D. (1985). The influence of discharge current on the intrinsic stress in Mo films deposited using cylindrical and planar magnetron sputtering sources. *Journal of Vacuum Science & Technology A: Vacuum, Surfaces, and Films, 3*(3), 576-579.

Thornton, J. A., & Hoffman, D. (1989). Stress-related effects in thin films. *Thin Solid Films, 171*(1), 5-31.

Todorov, T. K., Reuter, K. B., & Mitzi, D. B. (2010). High-efficiency solar cell with earth-abundant liquid-processed absorber. *Advanced materials, 22*(20), E156-E159.

Todorov, T. K., Tang, J., Bag, S., Gunawan, O., Gokmen, T., Zhu, Y., & Mitzi, D. B. (2013). Beyond 11% efficiency: characteristics of state-of-the-art $Cu_2ZnSn(S, Se)_4$ solar cells. *Advanced Energy Materials, 3*(1), 34-38.

Toyama, T., Konishi, T., Tsuji, R., Maenishi, R., Arata, A., Yudate, S., & Shirakata, S. (2015). Impact of water-rinse treatment on Cu_2ZnSnS_4 studied by X-ray absorption near-edge structure analysis. *Physica Status Solidi (C), 12*(6), 721-724.

Valakh, M. Y., Kolomys, O., Ponomaryov, S., Yukhymchuk, V., Babichuk, I., Izquierdo-Roca, V., . . . Schorr, S. (2013). Raman scattering and disorder effect in Cu_2ZnSnS_4. *Physica Status Solidi (RRL)-Rapid Research Letters, 7*(4), 258-261.

Vigil-Galán, O., Courel, M., Espindola-Rodriguez, M., Izquierdo-Roca, V., Saucedo, E., & Fairbrother, A. (2013). Toward a high Cu_2ZnSnS_4 solar cell efficiency processed by spray pyrolysis method. *Journal of Renewable and Sustainable Energy, 5*(5), 053137.

Wang, K., Gunawan, O., Todorov, T., Shin, B., Chey, S., Bojarczuk, N., . . . Guha, S. (2010). Thermally evaporated Cu_2ZnSnS_4 solar cells. *Applied Physics Letters, 97*(14), 143508.

Wang, W., Winkler, M. T., Gunawan, O., Gokmen, T., Todorov, T. K., Zhu, Y., & Mitzi, D. B. (2014). Device characteristics of CZTSSe thin-film solar cells with 12.6% efficiency. *Advanced Energy Materials, 4*(7), 1301465.

Washio, T., Shinji, T., Tajima, S., Fukano, T., Motohiro, T., Jimbo, K., & Katagiri, H. (2012). 6% Efficiency Cu_2ZnSnS_4-based thin film solar cells using oxide precursors by open atmosphere type CVD. *Journal of Materials Chemistry, 22*(9), 4021-4024.

Wei, X., Man, B., Liu, M., Xue, C., Zhuang, H., & Yang, C. (2007). Blue luminescent centers and microstructural evaluation by XPS and Raman in ZnO thin films annealed in vacuum, N_2 and O_2. *Physica B: Condensed Matter, 388*(1), 145-152.

Wei, Z., Newman, M. J., Tsoi, W. C., & Watson, T. M. (2016). Raman mapping analysis for removal of surface secondary phases of CZTS films using chemical etching. *Applied Physics Letters, 109*(12), 123902.

Woollam, J. (2011). CompleteEASE data analysis manual. *JA Woollam Co. Inc, New England. United States of America*.

Wu, C., Hu, Z., Wang, C., Sheng, H., Yang, J., & Xie, Y. (2007). Hexagonal Cu_2SnS_3 with metallic character: Another category of conducting sulfides. *Applied Physics Letters, 91*(14), 143104.

Yang, G., Li, Y.-F., Yao, B., Ding, Z.-H., Deng, R., Qin, J.-M., . . . Liu, L. (2015). Band alignments at interface of Cu_2ZnSnS_4/ZnO heterojunction: An X-ray photoelectron spectroscopy and first-principles study. *Journal of Alloys and Compounds, 628*, 293-297.

Yang, K. J., Sim, J. H., Jeon, B., Son, D. H., Kim, D. H., Sung, S. J., . . . Kim, J. (2015). Effects of Na and MoS_2 on Cu_2ZnSnS_4 thin-film solar cell. *Progress in Photovoltaics: Research and Applications, 23*(7), 862-873.

Yazici, S., Olgar, M. A., Akca, F. G., Cantas, A., Kurt, M., Aygun, G., . . . Ozyuzer, L. (2015). Growth of Cu_2ZnSnS_4 absorber layer on flexible metallic substrates for thin film solar cell applications. *Thin Solid Films, 589*, 563-573.

Yeh, M.-Y., Lei, P.-H., Lin, S.-H., & Yang, C.-D. (2016). Copper-Zinc-Tin-Sulfur Thin Film Using Spin-Coating Technology. *Materials, 9*(7), 526.

Yin, X., Tang, C., Chen, M., Adams, S., Wang, H., & Gong, H. (2013). Hierarchical porous Cu_2ZnSnS_4 films for high-capacity reversible lithium storage applications. *Journal of Materials Chemistry A, 1*(27), 7927-7932.

Yoo, H., Wibowo, R., Manoharan, G., Lechner, R., Jost, S., Verger, A., . . . Hock, R. (2015). The formation mechanism of secondary phases in Cu_2ZnSnS_4 absorber layer. *Thin solid films, 582*, 245-248.

Zelaya-Angel, O., de L Castillo-Alvarado, F., Avendano-Lopez, J., Escamilla-Esquivel, A., Contreras-Puente, G., Lozada-Morales, R., & Torres-Delgado, G. (1997). Raman studies in CdS thin films in the evolution from cubic to hexagonal phase. *Solid state communications, 104*(3), 161-166.

Zhai, Y.-T., Chen, S., Yang, J.-H., Xiang, H.-J., Gong, X.-G., Walsh, A., . . . Wei, S.-H. (2011). Structural diversity and electronic properties of Cu_2SnX_3 (X= S, Se): A first-principles investigation. *Physical Review B, 84*(7), 075213.

VITA

Ayten CANTAŞ BAĞDAŞ was born in İzmir, Turkey, on July 27, 1984, the first daughter of Güler CANTAŞ and Haydar CANTAŞ. After finishing high school, she entered in Ege University in İzmir. In June of 2006, she completed a Bachelor of Science in Physics with having 1st rank among all graduated students. In September 2006, she entered the graduate school at Izmir Institute of Technology. She both received an M.Sc.degree in June 2010 and Ph.D. degree in July 2017 in Physics from Izmir Institute of Technology. During her master education, she received a scholarship from the project with the number of "107T117" supported by TUBITAK. She worked as a research assistant between 2009 and 2017 at department of Physics, Izmir Institute of Technology. She has an expertise on photovoltaics, preparation of thin films by magnetron sputtering technique and fabrication of metal oxide semiconductor (MOS) capacitors. She has also experience on various characterization techniques especially X-Ray Photoelectron Spectroscopy (XPS).

Publications:

1. Growth of Cu_2ZnSnS_4 absorber layer on flexible metallic substrates for thin film solar cell applications, S. Yazici, M.A. Olgar, F.G. Akca, **A. Cantas**, M. Kurt, E. Tarhan, G. Aygun, E. Yanmaz, L. Ozyuzer, Thin Solid Films, 589 (2015).

2. In-situ spectroscopic ellipsometry and structural study of HfO_2 thin films deposited by radio frequency magnetron sputtering, **A. Cantas**, G. Aygun, D.K. Basa, J. Appl. Phys. 116, 083517 (2014).

3. Impact of incorporated oxygen quantity on optical, structural and dielectric properties of reactive magnetron sputter grown HfO_2/Hf/Si high-k thin film, **A. Cantas**, G. Aygun, R. Turan, Appl. Surf. Sci. 318, 199-205 (2014).

4. Effects of physical growth conditions on the structural and optical properties of sputtered grown thin HfO_2 films, G. Aygun, **A. Cantas**, Y. Simsek, R. Turan, Thin Solid Films 519, 5820-5825 (2011).

5. Ge nanocrystals embedded in SiO_2 in MOS based radiation sensors, A. Aktag, E. Yılmaz, N.A.P. Mogaddam, G. Aygun, **A. Cantas**, R. Turan, Nuclear Instruments and Methods in Physics Research B 268, 3417-3420 (2010).